NONLINEAR FINITE ELEMENT ANALYSIS OF MARINE RISERS USING QUINTIC HERMITE SHAPE FUNCTIONS

A Dissertation

by

LIYUN ZHU

Submitted to the Office of Graduate and Professional Studies of
Texas A&M University
in partial fulfillment of the requirements for the degree of

DOCTOR OF PHILOSOPHY

Chair of Committee,	Hamn-Ching Chen
Co-Chair of Committee,	Jun Zhang
Committee Members,	John M. Niedzwecki
	Joseph E. Pasciak
Head of Department,	Sharath Girimaji

December 2020

Major Subject: Ocean Engineering

ABSTRACT

A nonlinear three-dimensional finite element numerical code, called RISER3D, has been developed to perform the static, eigenvalue, and dynamic analyses for slender structures such as beams and marine risers. Distinction with the traditional cubic Hermite finite element method, such as CABLE3D program developed by Prof. J. Zhang and his former graduate students which employed cubic Hermite shape functions, RISER3D adopts quintic Hermite shape functions, six fifth-order polynomials, to interpolate the primary variables including the nodal displacement, slope and curvature. Hence, the new feature of RISER3D program is that it can guarantee the continuity of structure curvatures at the discretized nodes, which can help to make an improvement on the accuracy of numerical simulations. By far, no researcher has ever applied this new numerical scheme to perform finite element analysis for marine risers. Therefore, this dissertation has, for the first time, delved into the new finite element scheme and its application to marine riser problems.

A simplified RISER3D, omitting the axial tension term for riser simulations, can be used to study the static and dynamic problems of Euler-Bernoulli beams which have analytical solutions. Therefore, solving Euler-Bernoulli beam problems, with simplified RISER3D, can not only verify the accuracy and validity of RISER3D, but can also study the effectiveness of the new program by comparing the results to those of by CALBE3D.

Although RISER3D has larger size of element matrices, it shows great advantages over the traditional cubic Hermite finite element method. RISER3D simulation with coarse mesh can produce equivalent accuracy to CABLE3D simulation with fine mesh, which means that it has a

faster convergence speed and higher computational effectiveness, which can enhance the confidence for decision makers for the design and analysis of slender structures.

In this dissertation, the validity, accuracy and robustness of RISER3D have been firstly benchmarked with analytical solutions of Euler Bernoulli beam problems. Moreover, they are double checked by making comparisons of the numerical simulation results among RISER3D, Orcaflex, and CALBE3D for marine riser problems. In summary, since RISER3D shows several better merits to traditional cubic Hermite finite element method and its simulation accuracy has been consistently verified by either analytical analysis or Orcaflex, it should be widely utilized for slender structures design and analyses to improve the simulation accuracy and save computational effort.

DEDICATION

To my deeply honored, revered, and beloved mother Mrs. M. Chen, my father Mr. F.M. Zhu, and my rest family members for their continuous financial and spiritual support for my Ph.D. study abroad for years.

To my previous graduate advisor Prof. Y. Bai and Dr. Q. Bai for their kindhearted help, advice and guidance during my study at US!

To someone who will mean the most in the rest of my lifetime!

ACKNOWLEDGEMENTS

I would like to thank my committee chairs, cochair Prof. Jun Zhang and chair Prof. Hamn-Ching Chen and my committee members, Prof. J. M. Niedzwecki, and Prof. J. E. Pasciak, for their continuous guidance and support throughout the period of this research. Words are insufficient to express my deepest gratitude to Prof. Jun Zhang, for being my graduate advisor, his rigorous requirements and scientific attitude have driven me to pursue and absorb more useful knowledge not only within the domain of my PhD research topic, but also beyond the domain of my doctorate study.

My wholehearted appreciation goes to Prof. Hamn-Ching Chen for being my committee chair. Although the meeting times with him are limited, his brilliant ideas and profound knowledge in numerical simulation techniques have dramatically help me to overcome some obstacles in my research. I would like to extend my very special gratitudes to Prof. J. M. Niedzwecki and Prof. J. E. Pasciak for being my committee members and have given me a lot of positive advice on improving my research during my preliminary exam.

Finally, many thanks also go to my friends, colleagues, the department faculty, and the related staff for making my time at Texas A&M University a great experience. Thanks for the department head Prof. S. Girimaji, graduate coordinators Mrs. L. J. Byrd and Mr. C. Mullins, who have done a lot of favors for working through all my paper works.

CONTRIBUTORS AND FUNDING SOURCES

Contributors

This work was supervised by a dissertation committee consisting of co-chair and advisor Prof. Jun Zhang, chair Prof. Hamn-Ching Chen and Dr. J. M. Niedzwecki of the Department of Civil Engineering and Professor J. E. Pasciak of the Department of mathematics.

All other work conducted for the dissertation was completed by the student independently.

Funding Sources

Graduate study was supported by twice ABS Ocean Engineering scholarships for academic excellence from Texas A&M University, which are greatly appreciated!

No research funding is received for my PhD study and it is financially supported by my family and best friends.

TABLE OF CONTENTS

Page

LIST OF FIGURES

LIST OF TABLES

Page

1 INTRODUCTION

1.1 Marine Riser Overview

1.1.1 Marine Riser Introduction

Marine risers, as key structural components for connecting the subsea well bore and the surface host platform, are widely used in offshore drilling, production, and mining. The first riser was used in 1949 (Ertas and Kozik, 1987). Since then, marine risers have played a more and more important and irreplaceable role for offshore oil and gas resources exploitation and production.

In recent years, as oil and gas drilling and production activities are continuously moving forward to deeper and deeper waters due to the depletion of these resources in shallow water areas, the design and analysis of marine riser systems are facing great challenge due to high pressure and high temperature environment in deep sea, together with higher nonlinearities in the structural mechanics due to large riser deformation under combined effect of ocean wave and current loads. Moreover, in deep waters, the long suspension length of riser between the floater and seabed can greatly increase the top tension of riser. Hence, buoyancy modules are usually designed and attached to certain section of suspended length which can drastically change the configuration and increase the geometric complexity of risers. Therefore, the steady state deformed equilibrium configuration of a marine riser in deep ocean usually takes a form of three-dimensional curve, which can add difficulty to its numerical simulation. Because when stiffness is combined with the strong nonlinearity of the problem, the convergence of any classical iterative technique is mostly a matter of chance (Konuk, 1981).

All concepts of marine riser systems must show strong structural integrity and reliability during their whole designed lifetime. Hence, an accurate prediction of the response of the whole riser system under all possible combined loading scenarios is of paramount importance for a robust

and reliable design. As is known, any unexpected structural failure or riser system malfunction can incur significant and unaffordable financial loss and production deduction, together with potential risks of severe environmental pollution, which can definitely turn a riser loss incident into a real catastrophe.

Although the riser is a simple structure, the effect of the waves, currents, and vessel motions makes its response so involved that it requires a complex analysis to predict its behavior (Ertas and Kozik, 1987). A safe, endurable and reliable riser design is deeply relying on the methodologies for riser study and research. From riser design to fabrication, installation, commissioning, operation, and maintenance, there are many combined load cases should be carefully and conservatively considered.

Generally speaking, the methods for marine riser behavior analysis consist of laboratory experiments, field measurements, and mathematical model simulations. To perform riser model tests, a good laboratory, equipped with necessary facilities such as a water tank, riser samples, wave and current makers, data recording gauges, meters and computers etc., is indispensable. Hence, a large sum of budget is required to conduct varieties of riser model experiments. Similarly, the cost for the establishment of a field measurement system for recoding full-scale riser behaviors under real sea states could be even higher than laboratory tests. Therefore, the most feasible and economical approach for studying the behaviors of marine risers is to establish sound mathematical models by incorporating appropriate assumptions and reasonable simplifications, and then try to seek reasonable solutions of the mathematical models either analytically, numerically, or a combination of the two.

A typical marine riser system mainly consists of top interface, bottom interface, riser pipes and riser components, which is shown in Figure 1.1.

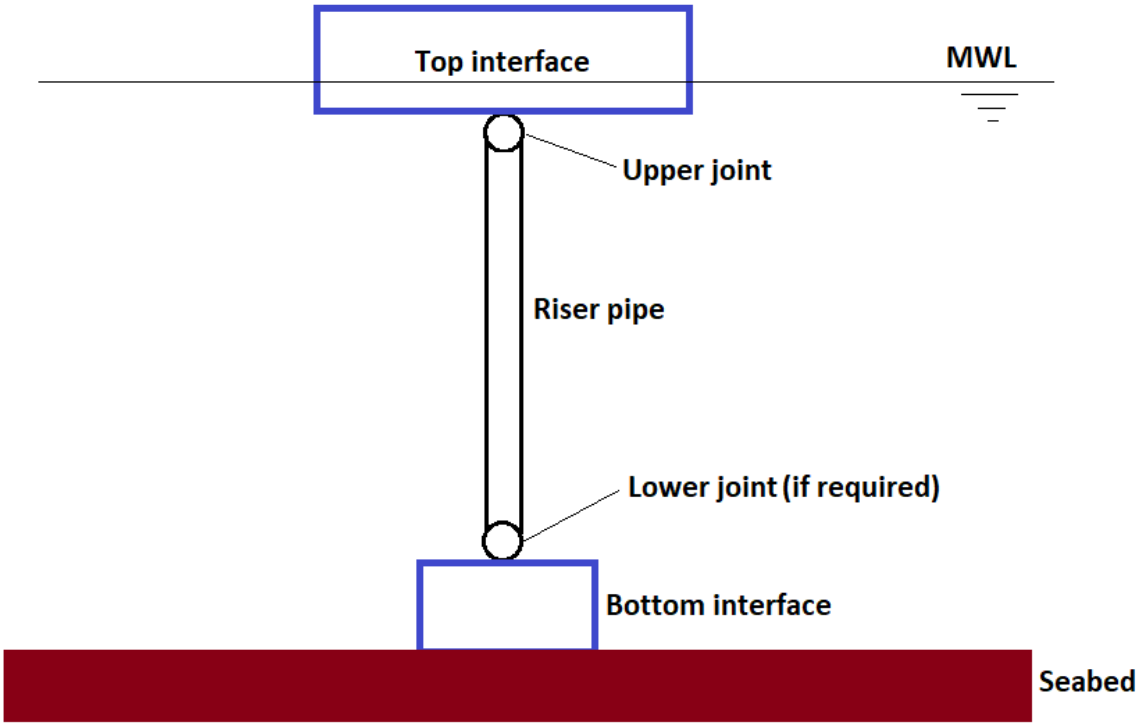

Figure 1.1 Schematic of typical marine riser system

Due to the complexity and nonlinearity of the whole riser system, there is actually no analytical solution which can exactly depict its behavior in the whole problem domain. The commonly used riser analytical approach is the catenary theory, a quite simplified riser model with neglected bending rigidity, which idealizes the riser as a hanging catenary under the effect of its apparent weight with supports at its extremities. The catenary model is only suitable for simple compliant risers such as SCRs or free-hanging flexible risers.

Fortunately, with the rapid development of the digital computer technology in the past decades, numerical solutions for complex mathematical riser model becomes a feasibility. The riser motion governing equations can be solved by either finite difference method, finite element

method, lumped mass method or any other possible numerical methods proposed by former researchers. The main advantages of numerical simulation lie in the possibility of taking all the involved features in a riser mathematical model into appropriate consideration, which include but not limit to the nonlinear boundary conditions, structural nonlinearities due to large bending or torsion, material complexity and nonlinearity, unsteady internal flow, high nonlinearities in external loads, etc. Of all the numerical methods, the finite element method is the most widely adopted technique for the marine riser simulations. The general procedures for the finite element analysis are briefly summarized in Figure 1.2.

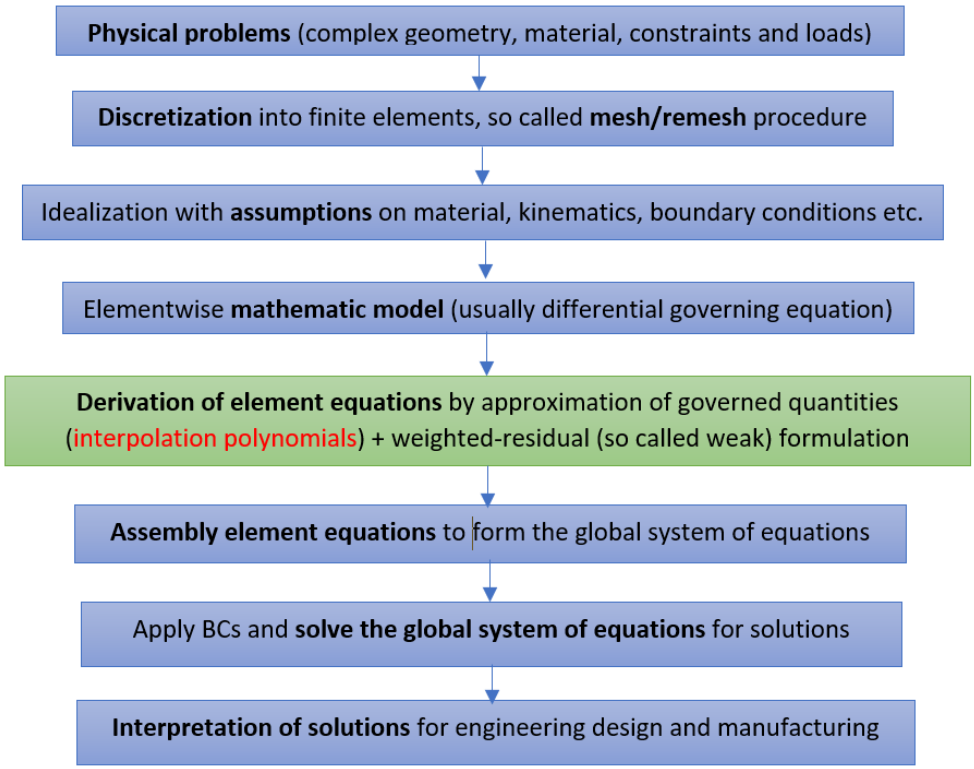

Figure 1.2 The general procedures of a finite element analysis

However, by far, a perfect numerical method or model for marine riser response prediction is nonsexist, which means there are always rooms for technique improvements of marine riser studies. No matter the improvements are obtained with new simulation models or modified techniques on the existing models. Two typical problems were still existing for marine riser studies. The first one is associated with the scarce of reliable prototypes or experimental data on riser motions and stresses in waves. This feature is generally accepted as a serious drawback to the credibility of the large number of finite element computational methods that are available. The second problem arises in the long computer times and large core storage required by the current generation of finite-element riser computations (Patel et al., 1984).

For finite element analysis, the reliability, robustness and efficiency of the model are of paramount importance. A reliable and efficient finite element procedure can help to save computational effort with minimized error for the analysts. A finite element analysis without error is actually an ideal state and several procedures, as shown in Figure 1.2, could probably introduce some errors to the finite element simulations. For instance, procedures of finite element mesh, approximation of concerned dependent variable in an element domain, numerical computation of finite element coefficient matrices, and solving the assembled global system of equations could all introduce certain amount of error to the final numerical solutions. Therefore, to improve the accuracy of the final numerical solution by minimizing all potential errors forms a key part for the research of marine risers using finite element methods.

The present research addresses the adoption of an improved finite element technique, i.e., by using quintic Hermite shape functions, to generate a higher-order approximation for the riser deflection function in an element domain, which can greatly reduce the error for the governed quantity approximation during finite element analysis. So, this dissertation can provide a strong

basis for a better understating, for other riser engineers or analysts, of the marine riser finite element simulation using quintic Hermite interpolation functions.

1.1.2 Marine Riser Categories

The key function of a riser is guaranteeing a safe transportation of fluids and gases between subsea facilities and ocean surface host platforms. Typical metallic riser configurations for different host platforms are shown in Figure 1.3 (DNV-OS-F201, 2010).

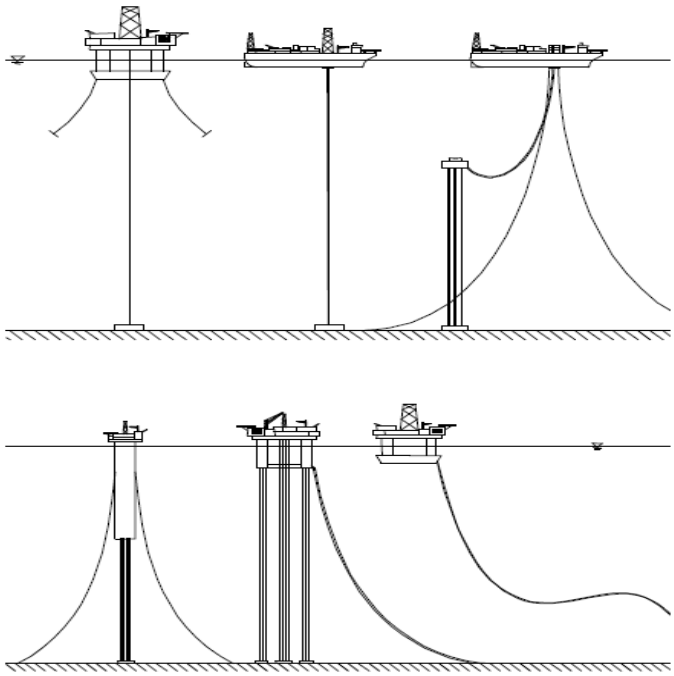

Figure 1.3 Examples of metallic riser configurations and floaters (Reprinted from DNV, 2010)

Consideration there are already so many types of risers, further subdivision of different risers usually depends on the categorizing perspectives that we emphasize on. For instance, risers can be categorized from their applications or functions, physical configurations, materials or even the ways they absorb the motions exerted by host platforms. The following subsections will illustrate this statement one by one in great details (DNV-OS-F201, 2010 and Miller, 2017).

If divided by the riser applications, they can typically be grouped into:

- Drilling riser: utilized during drilling and workover, the main function of which is to provide fluid transportation to and from the subsea wells.
- Workover/completion riser: temporarily used for workover or completion operation.
- Injection riser: transport fluid to the producing reservoir or a convenient disposal or storage formation.
- Production riser: transport fluids, i.e. unprocessed oil or gas, produced from the reservoir.
- Export riser: export processed oil and gas from the platform to subsea pipelines

If divided by riser configurations, they can generally be categorized as:

- Catenary riser: taking on a near catenary shape during service life
- Top-tensioned riser (TTR): near vertical riser which is always kept in a tensile condition by an applied top tension
- Hybrid riser (HR): a combination of catenary riser and top-tensioned riser, which use a vertical riser tower as the main riser body and connect the top of which to the host floater by a flexible catenary shaped riser or jumper at the near surface area

If divided by riser materials, they can be simply differentiated as:

- Metallic riser: which are made of carbon steels such as X65,X70 etc.
- Titanium riser: a new riser concept fits for ultra-deep waters which has a low modulus of elasticity and high yield stress
- Flexible riser: which consists multiple functional layers by using different materials

If divided by the mechanism how the riser absorbs the floater motions, risers can be distinguished as:

- Compliant riser: the floater motions are absorbed by changing of the geometry, with no heave compensation systems, and typical complaint riser configurations comprise of one or multiple free hanging catenaries like steel catenary riser (SCR), Steep-S riser, Lazy-S riser, Steep-wave riser, Lazy-wave riser and pliant wave riser, etc.
- Top tensioned riser: vertical risers which allow for relative riser floater motions in the vertical direction; besides, the riser is constrained to follow the horizontal floater motion at one or several locations.

More detailed characteristics on several high-frequently used riser types are summarized below, the contents of which have mainly referred to the public literatures (DNV-OS-F201, 2010 and Sparks, 2007).

The main characteristics about steel catenary riser (SCR) system, as shown in Figure 1.4, include:

- Structurally simple, easy design and install and therefore can save costs from these aspects
- Can work as production, export and injection risers
- The touch down zone (TDZ) section suffers large tension fluctuations due to host platform movements and offsets, hence fatigue damage at the TDZ is a big issue for this type of riser

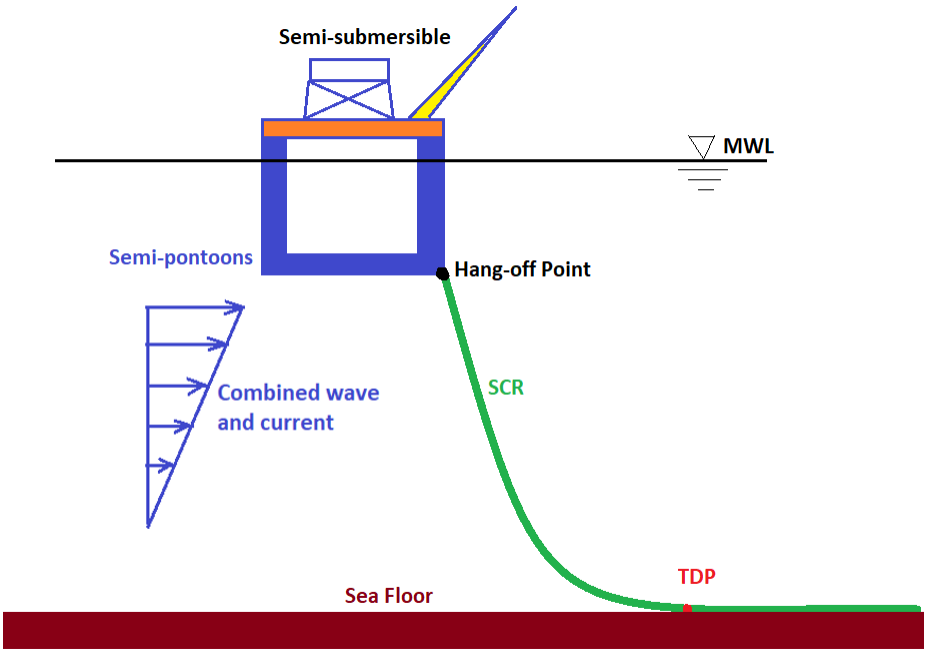

Figure 1.4 A schematic view of typical a SCR system

The main characteristics about steel catenary riser (SLWR) system include:

- Structurally more complex than the SCR, a middle buoyancy module section is required to provide extra net buoyancy which can form an arch bend in the riser, as illustrated in Figure 1.5.
- Can reduce the riser top tension by attaching the buoyancy modules
- Can isolate floater motion effect on the touch down zone (TDZ) and deduce the stress fluctuations in the TDZ section, which can thus extend the riser's fatigue life
- Suitable for more harsher environment than SCR but usually cost more due to the complexities involving of design, analysis and installation

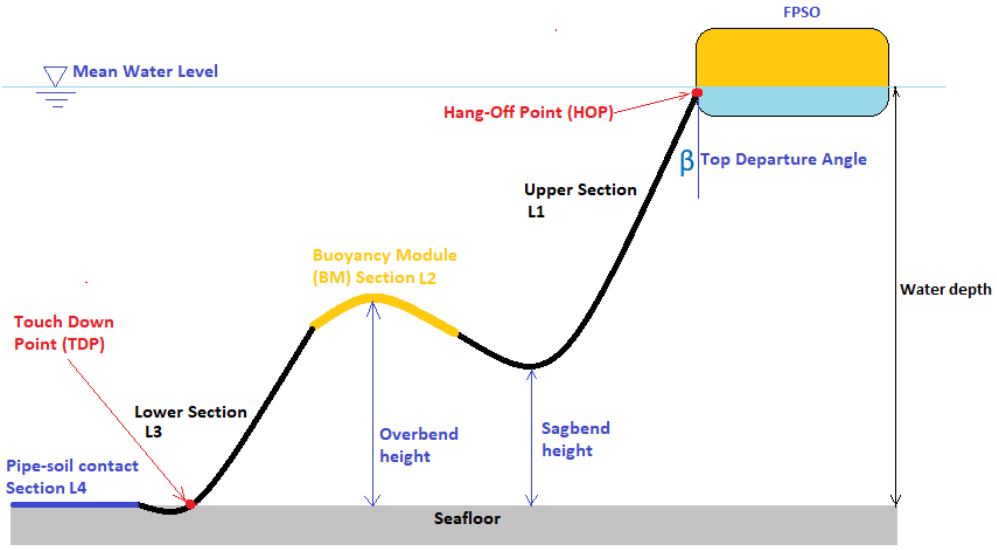

Figure 1.5 A schematic view of a typical SLWR system

The main characteristics of a TTR system mainly include:

- TTR production and injection risers are designed to have direct access to the subsea well, leaving the wellhead on the host platform
- A top tensioner or air can (for SPARs) is required to exert the top tension
- Have a typical of 3 to 6m space gap among different riser centers to avoid potential interactions

The main characteristics of a hybrid riser (HR) system, as shown in Figure 1.6, mainly include:

- The free-standing riser tower is connected to the floater by a flexible catenary jumper
- The buoyancy tank provides a top tension to keep the standing rigid section in tension
- The bottom of the vertical riser tower is usually fixed by a suction pile
- The surface floater motions and dominant wave kinematics can be avoided for the vertical riser part

- Bottom end of the standing rigid riser should be connected to the subsea foundation by a well-designed connector, such as a stress joint

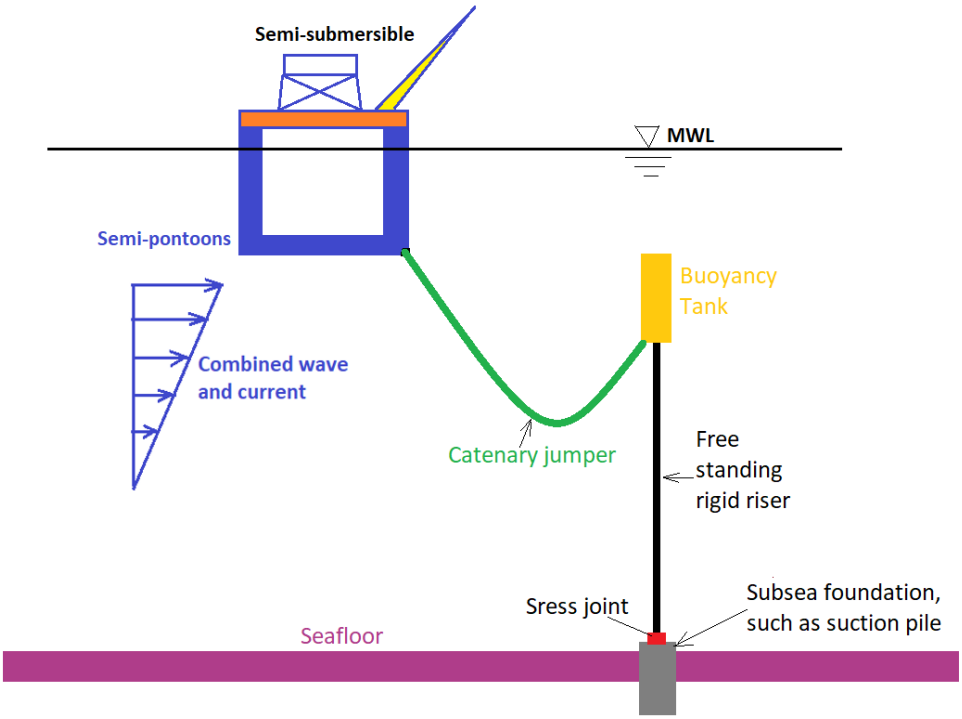

Figure 1.6 A schematic view of a typical HR system

1.2 Research Objective and Scope of Work

Large deformations on deep water risers are almost unavoidable due to its great length, which make them more vulnerable to failure during installation, operation and abandonment. Therefore, the importance of more accurate prediction of the response of marine risers, especially for deep waters, can never be over-exaggerated. Because any blunder or large simulation error over a certain acceptable limit may incur unexpected incidents, unbearable economical loss or even a great catastrophe for our natural environment. To be brief, the pursuit of a more efficient,

safe and reliable simulation method for deep water risers has always be a top concern for a riser engineering researcher in recent years.

Previously, the cubic Hermite interpolation shape functions, normalized forms of which as plotted in Figure 1.7, have been widespreadly used in the finite element formulation for numerical simulation of slender structures such as rods, cables, moorings, pipelines and risers. For instance, the CALBE3D program, developed by Prof. J. Zhang and his previous graduate students for the static and dynamic simulations of moorings and risers, had adopted the cubic Hermite shape functions for the finite element scheme formulation.

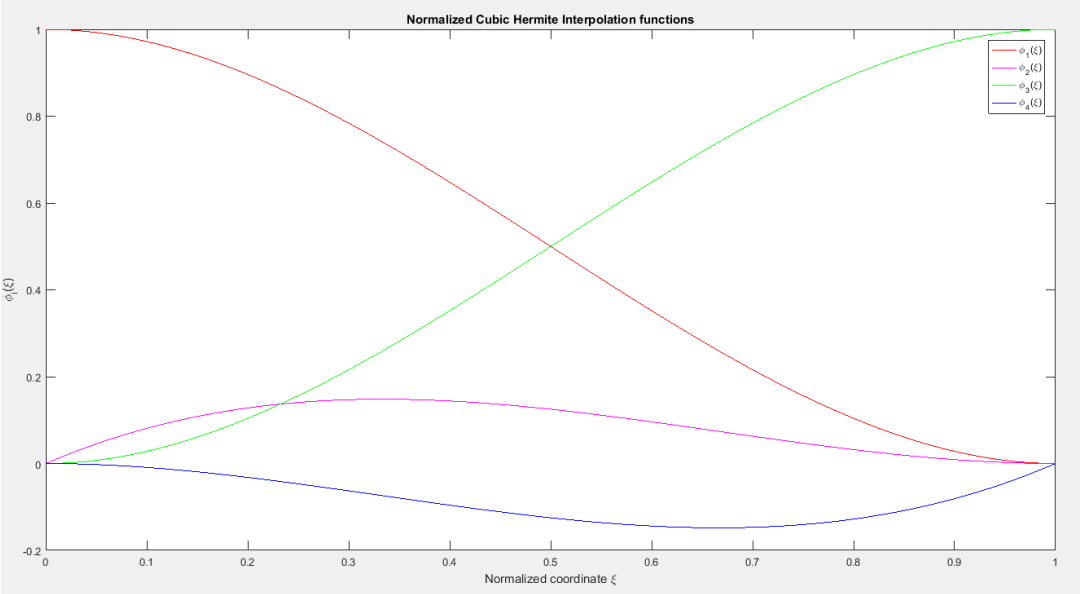

Figure 1.7 Normalized cubic Hermite shape functions

Although cubic Hermite shape function finite element formulation can yield reasonable results by using an appropriate fine element size, some intrinsic shortcomings enrooted in this traditional method are gradually discovered during the research process of solving more tricky marine riser problems, which mainly include

- Only the structure displacement $\boldsymbol{r}$ and slope $\boldsymbol{r}'$ are continuous at nodes, the continuity of structure curvature $\boldsymbol{r}''$ cannot be guaranteed, which means a discontinuous bending stress distribution in the simulation results
- One cannot apply Dirichlet (essential) boundary conditions in terms of the structure curvature $\boldsymbol{r}''$, which will result in a loosely restrained structural model on the boundaries. For instance, large error will occur for the eigenvalue analysis of the slender structures, especially for high vibration modes.
- Since the structure shear force is a related to the rate change of the structure curvatures, it is difficult to be accurately postprocessed in the finite element analysis by only using nodal displacements and slopes. Hence, when slender structures subjected to distributed transverse load with large gradients, the traditional finite element simulation will yield poor shear force prediction in the problem domain.

Therefore, the main objective of this research is to seek an improved numerical technique, especially aimed at a more accurate simulation of challenging marine riser problems, that can be of numerically feasible to overcome those downsides embedded in the traditional cubic Hermite finite element formulation as summarized above. This objective is fulfilled by incorporating the quintic Hermite shape functions to Galerkin's finite element model, which can help to eliminate the mentioned drawbacks in the cubic Hermite finite element method. Therefore, a new finite element program, called RISER3D by using quintic Hermite shape functions, are developed in this research. RISER3D can be a powerful numerical tool for handling challenging engineering problems such as ultra-deep water riser deformation, nonlinearities due to transverse hydrodynamic loads with large gradient, flexible jumpers that are usually subject to large rotation angles, etc. The main reason that RSIER3D can do a better job for solving these tricky problems

lie in the new properties brought into the new finite element model by the six the quintic Hermite shape functions.

In order to verify the validity, accuracy and consistency of RISER3D, static and dynamic benchmark cases of Euler-Bernoulli beam problems under different transversal loads are simulated with RISER3D, the results of which are compared to the exact analytical solutions by using Euler-Bernoulli beam theory. And then, RISER3D program is adopted to solve varieties of static and dynamic marine riser problems, such as the deformation and response of steel catenary risers (SCRs), steel lazy wave risers (SLWRs), steep wave risers (SWRs), the flexible jumper sections of hybrid risers, and the top-tensioned risers, to investigate the advantages of the new program over the previous CABLE3D program.

The scope of work of this research mainly consists of three parts. The first part is developing a new finite element program, called RISER3D, by using quintic Hermite shape functions. This part of research work mainly includes

- Derivation of the expressions of the quintic Hermite shape functions
- Formulation of the new finite element scheme using quintic Hermite shape functions
- Programming the new formulated scheme in both FORTRAN and MATLAB, called the RISER3D program
- Explaining on how to correctly impose typical boundary conditions on the new finite element model
- Proposing appropriate data post processing methods for RISER3D program

The second part of the proposed study is firstly to verify the validity and accuracy of RISER3D program, and then deplore the convergence speed and effectiveness of the new program by solving typical one-dimensional static and dynamic beam problems. The benchmark cases

focus on typical transverse loads types and classical boundary conditions for prismatic Euler Bernoulli beams, two examples of which as shown in Figure 1.8. The numerical results obtained from the RISER3D program are compared with those of obtained by either analytical analyses or CALBE3D program. Based on the comparison of the results among three different methods, we can easily identify whether RISER3D can show some beneficial merits over CABLE3D.

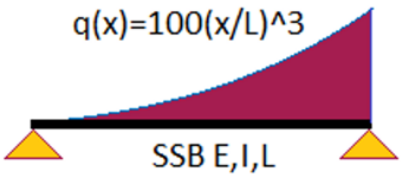

a, An example of polynomial-type transverse load for the beam

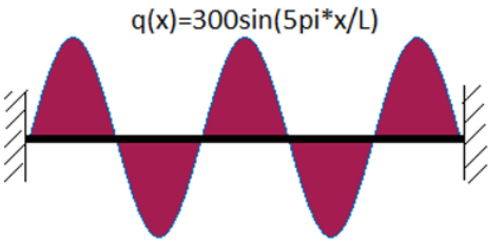

b, An example of sinusodal-type transverse load for the beam

Figure 1.8 Typical transverse load types for Euler Bernoulli beams

For benchmark cases, the compared results mainly include

- The Euler Bernoulli beam displacements and slopes at discrete nodes and within the element domains
- The beam bending moment and shear force at discrete nodes and within the element domain

The third part of the research is the application of RISER3D to eigenvalue, static, and dynamic analyses of different marine riser problems, the objective of which is to seek the advantages of RISER3D over CABLE3D. The proposed study cases mainly include:

- Natural frequency analysis for constant tensioned beams and top-tension risers (TTRs)
- Static in-place analyses of the SCR, SLWR, and SWR
- Static analysis of SLWR and SWR under steady current loads
- Deep-water TTR under linear and nonlinear current loads
- Dynamic analysis of a flexible riser subject to harmonic excitations at the top end
- Parametric studies of concerned parameters for some riser types

All these application cases are both simulated with CABLE3D and RISER3D, the results of which are also compared to those of obtained by Orcaflex (if applicable). The validity, accuracy and advantages of RISER3D should be identified through the results comparison with other numerical methods in these proposed studies.

1.3 Literature Review on Marine Risers

After the birth of the first riser in 1940s, a numerous number of marine risers were designed and installed from shallow waters to deep waters. Many journal papers have been published addressing on varieties of marine riser problems, a combined extensive and intensive reading of these literatures can drastically improve our understanding of the static and dynamic behavior of offshore risers. The main distinctions among these published literatures lie in different treatments on the following factors regarding marine riser design, modelling and analysis:

- Study riser behaviors by either static analysis, dynamic analysis, eigenvalue analysis, scaled model tests at laboratories or full-scale field measurements

- Two-dimensional or three-dimensional simulations depending on the externally applied loads on the riser are in one plane or not
- Small deformation or large deformation, usually based on the water depths
- Axially inextensible or extensible
- Riser torsion include or neglected
- Internal flow considered or neglected, if considered, steady flow or unsteady flow
- Unidirectional steady current or multi-directional steady currents or even unsteady currents
- Treat the vertical current profile as uniformly, linearly, bi-linearly, in power-law distribution, or arbitrarily
- Solving riser governing equations analytically by either simple catenary theory or Bessel functions with neglecting bending stiffness, or numerically by either finite element method (FEM), finite difference method (FDM) or lumped mass method (LMM)
- Varieties of riser-soil interaction models, which include but limited to riser-seabed contact elastically or non-elastically, lateral and longitudinal pipe-soil interaction with friction or frictionless, riser-seabed penetration with small embedment or large embedment at the touch down zone (TDZ), the supporting soil strength with degradation or non-degradation, etc.
- Top end of riser with horizontal offset or no offset
- Take the lift forces induced by vortex-induced vibration (VIV) into consideration or just neglected
- Take the riser fatigue assessment into consideration or neglected

- Hydrodynamic loads due to only current, or only wave, or a combination of wave and current
- Hydrodynamic wave loads by using regular wave or irregular wave, linear wave or nonlinear wave
- Riser and host platform interaction coupled or decoupled
- Using rod, beam, hybrid beam or even three-dimension continuum elements
- Treat the riser model nonlinearities, which may be caused by axial constitutive constraint, non-homogenous material, boundary conditions, external loads, large deformation, etc., as either with neglected, linearization or nonlinearly
- Treat multi-layered riser with one equivalent layer or as what they are
- Treat the riser top end with harmonic excitation boundary conditions or simply with classic boundary conditions such as pinned (hinged), fixed, free with tension, free with linear springs restraint, pinned with rotation springs restraint, etc.
- Focus their analysis on one type or several types of marine risers, which include but not limited to flexible riser, drilling riser, steel catenary riser (SCR), steel lazy-wave riser (SLWR), Steep-S riser, Steep-wave riser, Lazy-S riser, top-tensioned riser (TTR), hybrid riser (HR), multi-layered composite flexible riser, flexible w-shape riser, flexible free-hanging riser (sometimes called flexible jumper), etc.
- Riser analyses at different loading cases, such as during installation, in-plane service, abandonment during unbearable storm conditions, or recovery; as for riser installation, using S-lay method or J-lay method

Considering such a large number of literatures exist, the dissertation cannot numerate all of them one by one. Some of the published literatures, either have a positive effect on this research

or have presented a good model or method for marine risers analysis, are briefly reviewed in the subsections one by one in a chronological sequence.

R.P. Nordgren (1974) developed a computational method for the finite amplitude three-dimensional motion of inextensible elastic rods with equal principal stiffness, which can also be applied to the two-dimensional motion of such rods with unequal principal stiffness. He devised the numerical solution of the formulation by incorporating a consistent finite difference approximation, correct to second order in increments of arc length and time, with a semi-explicit method.

R.D. Young, et al. (1977) developed a computer program for economically predicting the dynamic response of marine risers to lateral forces from waves (regular and random) and currents (vortex shedding). In addition to a technical description of the model, they discussed the differences in response between long and short risers and which physical parameters should be scrutinized in analyzing each of these. They made a conclusion that the random wave provides a method of predicting maximum stresses for strength design and the regular wave provides data which is compatible with fatigue analysis.

I. Konuk (1981) provided a general foundation for developing reliable and rigorous formulations for problems involving pipelines and risers with twist. A continuation technique was developed to solve convergence problems of three-dimensional pipelines.

D.L. Garrett (1982) used a three-dimensional finite element method to model an inextensible elastic rod with equal principal stiffness. This model permits large deflections and finite relations and accounts for tension variation along length of the rod. The author demonstrated the accuracy of the spatial discretization and the stability of the time integration method by comparing the numerical results with exact solutions for certain nonlinear problems.

O. Egeland et al. (1981) performed theoretical analysis by utilizing four different computer programs, covering six different methods. The programs employed either linearized frequency domain solution or time integration techniques with varying degrees of non-linearities included and for either regular waves or irregular sea. The four program analysis results were compared with the field measurements data taken by CONOCO in 1975 on a drilling riser operated from a semisubmersible. They concluded that it was not understood why the irregular sea simulations gave inferior comparisons than those by the regular waves and suggested that this could be due to modelling deficiencies.

M.H. Patel et al. (1984) employed a two-dimensional finite-element computational method for determining marine riser displacements and stresses due to self-weight, buoyancy, internal and external pressures, surface vessel motions and environmental forces arising from currents and waves. A dynamic analysis was performed in the frequency domain for regular waves by linearizing the hydrodynamic damping term.

M.H. Patel and A.S. Jesudasen (1987) did a theoretical and experimental investigation of the lateral dynamics of free hanging marine risers during riser retrieval or in storm conditions. The riser is disconnected from the subsea well head and remains hanging freely from the surface vessel while being subjected to excitation by surface vessel motions, waves and current. They investigated the in-plane behavior of the riser pipe and its hydrodynamic loading by finite element analysis, and the results of which were compared with model test data at 1:28 scale from a specially designed deep-water tank. Some measurements of the out-of-plane behavior of the riser due to vortex shedding effects were also presented.

R. Ghadimi (1988) used the lumped mass discretization method to derive the equations of motion of flexible risers in three-dimensional space. The nonlinear equations describing the riser

motions were solved in the time domain using the tangent stiffness incremental approach combined with the Wilson-theta numerical integration algorithm. Besides, the author also gave a consideration to natural periods and mode shapes for small oscillations about the static equilibrium position of the riser.

J.F. McNamara et al. (1988) developed a method for the static and dynamic analysis of flexible risers and pipelines in the offshore environment under conditions of arbitrarily large motions due to wave loading and vessel movements. A mixed finite element formulation was adopted where the axial force was independently interpolated and only combined with the corresponding axial displacements via a Lagrangian constraint, which produced a hybrid beam element that could be applied to offshore components varying from mooring lines or cables with zero bending stiffness to pipelines with finite bending stiffness subjected to large motions.

N. Vlahopoulos and M.M. Bernitsas (1988) developed a mathematical model of static, dynamic and eigen analysis of non-integral production risers, i.e. a bundle of component risers interconnected along their length by guide arms, based on a small deformation, two dimensional, structurally linear and hydrodynamically nonlinear single riser model. Typical non-integral production riser problems were solved, and results were compared to those of single risers.

P.J. O'Brien and J.F. McNamara (1989) further developed their three-dimensional hybrid beam-column finite element model by addressing the issues of the use of a pre-processor program based on simple cable equations for locating the initial configuration, variable-step static and dynamic solution schemes, seabed contact algorithms and the modelling of finite three-dimensional rigid body rotations. Based on the sample analyses carried out in the paper, they concluded that the model could work as an accurate and robust computational tool for the static and dynamic analysis of three-dimensional flexible riser systems.

M.C. Wu and J.Y.K. Lou (1991) developed a mathematical model for the lateral motion of a marine riser to examine the effect of the internal flow and bending rigidity of the pipe on the dynamic behavior of the riser. The mathematical model, with a relatively small elastic rigidity, included a steady flow inside the pipe together with other factors such as currents, wave excitation, rig motions, etc., which was solved with a singular perturbation technique. They found that the internal flow acts to reduce the effect of the top tension. However, its effect on riser dynamics was not significant when the top tension of the riser is relatively high. For small top tension cases, the perturbation technique is no longer valid and the effect of internal flow on riser dynamics remains to be investigated.

F.B. Seyed and M.H. Patel (1992) presented their derivations for calculation of pressure and internal flow induced forces on flexible risers and other curved pipes using a mathematically rigorous approach. The mathematical identity of these equations with those for effective tension was also illustrated. Moreover, they mathematically showed that internal flow contributes a new term to the expression for effective tension. At the end of this literature, the authors tried to construct the rigorous mathematical model for typical compliant flexible risers, i.e. Steep-S, Steep-wave, Lazy-S and Lazy-W risers.

Ma et al. (1994) improved the finite element elastic rod model, as initially proposed by R.P. Nordgren in 1974, by simulating offshore risers under complex internal and external loading conditions.

T. Sakamoto and R.E. Hobbs (1995) presented a new calculation technique for the static and dynamic analysis of flexible risers, using the Dynamic Relaxation method with a finite difference discretization. Two new features were introduced in the new technique, one was the governing equation was first derived in a local coordinate system, and then transformed into the

global coordinate system; the other one was the exact expressions for bending moments were employed in terms of the rotation angles at nodes. They figured out that these new features could solve efficiently the geometrically nonlinear problem without the very large number of loading steps and elements which the FEM must employ.

C.P. Pesce et al. (1999) derived a simple formula for the natural frequencies and eigenmodes of a catenary riser under no current by WKB general solution. Compared to Bessel's approximations and to numerical results obtained by a standard Finite Element Method formulation, where extensibility was considered, they found that the present solution showed a rather good agreement for typical free-hanging catenary risers.

Chen et al. and Prof. J. Zhang (2002) developed a three-dimensional finite element program, called CALBE3D, to simulate hybrid beam-column element with small axial elongation and mooring line cable element with large elongation by using appropriate constitutive constraint conditions respectively. Thus, in CABLE3D, the riser can be simulated as a hybrid beam-column element with small elongation by considering the external forces such as riser gravity, hydrostatic forces, and hydrodynamic forces.

W. Raman-nair and R.E. Baddour (2003) formulated the equations of the three-dimensional motion of a marine riser undergoing large elastic deformations using Kane’s formalism. The riser is modeled using lumped masses connected by extensional and rotational springs including structural damping. Besides, their model had taken the effects of vortex-induced lift forces and internal flow into consideration.

Torres et al. (2003) used ANFLEX and POSFAL, and an in-house finite element based code for deterministic and random nonlinear time-domain analysis, to verify the structural integrity

of a SLWR attached to a turret-moored FPSO at a water depth of 1800m. The time domain nonlinear analysis was also performed for SLWR fatigue damage calculation.

Y.T. Chai, K.S. Varyani (2006) presented a rather general absolute coordinate formulation for the analysis of flexible pipe structure. In their formulation, the structural response characteristics were expressed in terms of globally based position coordinate and its derivative to allow an accurate nonlinear description of the pipe kinematics, which could be capable of handling of bending-torsion coupling, axial-radial coupling, bend restriction effect, internal flow effect, irregular seabed with friction effect, and the Poisson's ratio effect, thus allowing it a useful general tool to be developed for riser, pipeline and flexible hose analyses.

Roveri et al. (2005) performed a parametric analysis, by using an in-house finite element computer tool, for SLWR by considering riser segment lengths variation and changing the buoyancy module design parameters.

I. Senjanovic et al. (2006) analyzed the natural vibration of deep-water tensioned uniform risers. The riser was considered as both a cable and a beam due to the fairly weak flexural stiffness. The exact and asymptotic solutions of the cable differential equation were presented. The beam vibration was determined by modifying the cable solution for each halfwave of the natural mode, so called segments. They verified their analytical analysis results by the finite element method and presented very valuable conclusions on riser dynamic behavior in the lower and higher frequency domain.

S.T. Santillan (2010) modelled flexible risers and pipelines as slender elastic structures. The theoretical formulation lead to a type of nonlinear boundary value problem that could be solved numerically by finite difference method with appropriate boundary conditions. Two-

dimensional planar problem of steep-wave riser and free-vibration analysis of various deflected equilibrium configuration were considered.

Sun and Qi (2011) studied the static and dynamic behavior of a steep wave flexible riser configuration by using the lumped mass method, in which the riser was divided into a series of massless line segments with loads lumped to nodes at the end of each line.

J.L. Wang and M.L. Duan (2014) established the governing equations for a SLWR by consisting of conventional small deformation beam theory for the portion of pipeline lying on the seabed and a large deformation beam theory for the suspended section. The proposed model, numerically solved by finite difference method, with appropriate boundary conditions could simulate the nonlinear mechanical behavior of SLWR with the effect of pipe–soil interaction, ocean current and internal flow.

Kim et al. (2014) investigated the dynamic behaviors of conventional SCR and Lazy-wave SCR for FPSOs in deep waters by using a hull/mooring/riser fully coupled dynamic analysis program.

Ruan et al. (2016) established a mathematical model based on this elastic rod theory and using finite element method to simulate the dynamic response of SLWR by considering hydrodynamic loading and internal flow.

D.H. Yoo et al. (2017) proposed practical and stable methods of ultimate-strength assessment for flexible pipes using 8-layered and 5-layered finite element models subjected to axial tensile and compressive loads, respectively. For the 5-layered model, four inner layers, i.e. carcass, pressure sheath, pressure armor, and anti-friction tape, are replaced by one equivalent pressure layer to simplify the model and improve numerical convergence.

C. Zhang et al. (2019) proposed a mechanical analysis model based on the absolute nodal coordinate formulation (ANCF) and the theories of continuum mechanics and finite element method to accurately analyze the statics and dynamics of deep-water flexible structures with large deformation. Based on the energy variation principle, the generalized elastic force and stiffness matrix of the element are derived, and the mass matrix and external load matrix of the element are combined to perform the element assembling using the finite element method. The static and dynamic characteristics of a SLWR are analyzed systematically, which verified the effectiveness and practicability of the mechanical model.

Y. Cheng et al. (2020) presented a numerical model based on three-dimensional (3D) large deformation rod theory. The governing equations were established in terms of a global coordinate system, which involves the effects of vessel motion, wave- current loads, riser-seabed interaction and internal flow. The finite element method combined with an Adams-Moulton scheme is applied to discretize the governing equation and update the time integration. The numerical model was verified with the published results and numerical simulations of the SLWR.

To make a clearer comparison among some good literatures regarding marine riser behavior study and analysis, a literature review summary is presented in Table 1.1 with highlights of each paper presented.

Table 1.1 Summary of some highlight literatures comparison among previous riser analyses

Author	Year	Riser Type	Dimension	Study and method	Deformation	Seabed friction	Internal flow	Torsion	Sea loading
R.P. Nordgren	1974	elastic rod	3D	S./D. analysis[4] using FDM	finite-amplitude	NA[1]	NA	NA	NO[3]
D.L. Garrett	1982	elastic rod	3D	S./D. analysis using FEM	large deflection	NA	NA	NO	NO
M.H. Patel et al.	1984	top tensioned risers	2D	S./D. analysis using FEM	large displacement	NA	NA	NO	wave and current
M.H. Patel and A.S. Jesudasen	1987	free hanging risers	2D	S./D., eigenvalue analysis using FEM and model tests	large deflection	NA	NA	NA	wave and current
R. Ghadimi	1988	catenary flexible riser and steep-S	3D	S./D. and eigenvalue analysis using LMM	small strain	NO	NA	NO	wave and current
J.F. McNamara et al.	1988	flexible risers such as catenary and HR	2D	S./D. analysis using a hybrid beam-column FEM	Lagrangian restraint on the axial strain	NA	NA	NA	wave
N. Vlahopoulos and M.M. Bernitsas	1988	non-integral production risers	2D	S./D. analysis and eigen analysis using FEM	small deformation	NA	NO	NO	wave and current
P.J. O'Brien and J.F. McNamara	1989	flexible risers	3D	S./D. analysis using a hybrid beam-column FEM	Lagrangian restraint on the axial strain	YES[2]	NO	YES	wave and current
F.B. Seyed and M.H. Patel	1992	all flexible complaint risers	2D	Analytical analysis by a mathematically rigorous approach	small strain	NA	considered	NA	NA
T. Sakamoto and R.E. Hobbs	1995	flexible risers, steep-wave riser	3D	S./D. analysis by dynamic relaxation method using FDM	small strain	NA	NA	NA	wave and current

Table 1.1 Continued

Author	Year	Riser Type	Dimension	Study and method	Deformation	Seabed friction	Internal flow	Torsion	Sea loading
C.P. Pesce et al.	1999	catenary riser	2D	Eigenvalue analysis by Bessel functions and WKB approximation solution, standard FEM	inextensible	NA	NA	NA	NA
A.C. Fernandes	2001	flexible jumpers of HR	3D	Static analysis by consistent catenary and modal analysis, model tests	inextensible	NA	NA	NA	wind, wave and current
M. Yazdchi and M.A. Crisfield	2002	simple catenary and HR	3D	Dynamic analysis by co-rotational FEM	large deformation	NA	not included	NA	wave and current
M. Yazdchi and M.A. Crisfield	2002	flexible pipes and risers	2D	Dynamic analysis by co-rotational FEM	large deformation	NA	not included	NA	steady current
W. Raman-nair and R.E. Baddour	2003	riser and cantilever beam	3D	Dynamic analysis by Kane's formulism using LMM	large elastic deformation	NA	included	NO	2nd-order Stoke's wave
I. Senjanovic et al.	2006	tensioned risers	2D	Natural vibration by analytical segmentation method	NA	NA	NA	NA	NA
Y.T. Chai and K.S. Varyani	2005	flexible jumper and pipeline on irregular seabed	3D	S./D. analysis by absolute coordinate formulation and Galerkin FEM	mixed-field formation of stress strain and Poisson's ratio	YES	YES	bending-torsion coupling	wave and current
S.T. Santillan et al.	2010	steep-wave flexible riser	2D	S./D. analysis by elastica approach and FDM	inextensible	NA	NO	NO	steady current
I.K. Chatjigeorgiou	2010	catenary riser	3D	S./D. analysis by potential theory for internal flow and FDM	small deformation	NA	YES	YES	NA

Table 1.1 Continued

Author	Year	Riser Type	Dimension	Study and method	Deformation	Seabed friction	Internal flow	Torsion	Sea loading
S.T. Santillan and L.N. Virgin	2011	Lazy-S and steep-S	2D	Static analysis by FDM and experiment	inextensible or small deformation	NA	NA	NA	steady current
J.L. Wang and M.L. Duan	2014	SLWR	2D	Static analysis FDM	coupled small and large deformation	axial friction	YES	NA	steady Current
D.H. Yoo, et al	2017	multi-layer flexible pipe	2D and 3D	2D plain strain and 3D FEM by Ansys	axial tensile and compression	NA	NA	YES	NA
X.W. Zhen et al.	2018	HR with flexible jumper	2D	S./D. analysis by analytical catenary and Orcaflex	small deformation	NA	NA	NA	wave and current
C. Zhang et al.	2019	steel lazy-wave riser (SLWR)	2D	S./D. analysis by absolute nodal coordinate formulation FEM	large deformation	NA	NA	NA	NA
Y. Cheng et al.	2020	SLWR	3D	S./D. analysis by absolute coordinate FEM	NO	linear friction	YES	NO	wave and current
C.T.P. Bomfimsilva, T.A. Netto	2020	free standing and jumper	3D	S./D. analysis by Orcaflex	small deformation	NA	NA	NA	NA

Notes for Table 1.1:

1. NA denotes not applied to;
2. YES denotes considered;
3. NO denotes neglected;
4. S./D. analysis denotes static and dynamic analysis.

For riser eigenvalue analysis, many previous researchers have developed different approaches to study the vibration of the marine risers. Slender marine risers are often subject to vortex-induced vibrations (VIV) and therefore require accurate eigenvalue modelling for prediction of natural frequencies, mode shapes and fatigue damage rate (Cheng et al., 2002). Shear 7 (J. Kim Vandiver 1998), a program developed by Professor J. Kim Vandiver and his research team at MIT, can predict the riser response subjected to spatially varying current loads. By using mode superposition, it is able to evaluate which modes are likely to be excited due to vortex shedding and estimates the VIV response in uniform and sheared flows. For riser dynamic analysis, the determination of riser natural frequencies and mode shapes forms a critical step towards riser dynamic response prediction. Taking the natural frequency calculation of a typical drilling riser as an example, several literatures have proposed different methods. Initially, Dareing and Huang (1976) used an expanded power series to approximate the mode shapes of risers and presented the results of the first five natural frequencies of a drilling riser. Later, Cheng et al. (2002) employed a WKB-based dynamic stiffness method to numerically analyze the natural frequencies of the same drilling riser, it addressed that the first five natural frequencies are accurate to O (10-4) by only using five elements. And then, Chen et al. (2009 and 2015) adopted a differential transformation method and another variational iteration method (VIM) for reanalyzing the natural frequencies and mode shapes of the same drilling riser with different boundary conditions respectively.

Nowadays, especially in offshore engineering industry, many engineering companies prefer using the commercial software Orcaflex for riser in-place and installation analyses. In Orcaflex, the riser is divided into a series of line elements which are modelled as straight massless segments with a node at each end. The segments are used for modelling the axial and torsional properties of the line. Other properties like riser mass, weight and buoyancy etc. are all lumped to

the nodes. Each node is like a straight rod that represents the two half-segments at either side of it. Forces and moments are all applied at the nodes (Orcina, 2011). In this research, the results of some static and dynamic cases by using RISER3D are also compared with those of obtained by Orcaflex.

1.4 Dissertation Organization

In this dissertation, it comprises a total of six chapters, the main content of each chapter is briefly described below.

Chapter 1 starts with a general introduction of marine risers and the popular categories of marine risers, and then the main objective and the scope of work for this research are presented. Finally, the first chapter ended with the literature review of previous researches on marine risers.

Chapter 2 starts with a brief introduction of the CABLE3D program, which has laid a good foundation for this research. After that, the expressions for the quintic Hermite shape functions are presented and their properties are discussed. Most importantly, the detailed derivation for the riser governing equation and the formulation of the new finite element model for riser static and dynamic analyses are presented. The main procedures for solving riser static and dynamic problems with RISER3D are discussed with flowcharts. Then the boundary conditions, especially for the parts different from traditional CABLE3D are addressed. Finally, the numerical integration methods for evaluating the coefficients in RISER3D finite element scheme are proposed and the main methods for data postprocessing of the research are also included.

Chapter 3 starts with derivation of finite element formulation for Euler-Bernoulli beam problems with quintic Hermite shape functions. Then the analytical solutions of the static and dynamic beam problems are derived and presented. Finally, the static and dynamic Euler-Bernoulli

beam problems are simulated with both CABLE3D and RISER3D numerically, the results of which are compared with the exact solutions.

Chapter 4 starts with presenting the analytical analyses on transverse vibration of constant tensioned beams and vertical risers, which is followed by cases study on solving the natural frequencies of slender beams/risers using both analytical analysis and numerical simulations with both CABLE3 and RISER3D. The results by three different methods are compared and useful conclusions are obtained.

Chapter 5 starts with presenting hydrodynamic loads on marine risers, followed by a series of application of RISER3D to practical marine riser problems. Parametric studies are performed for some cases when the change of a parameter can exert a large effect on the riser response. The numerical results of RISER3D are compared to those of by both CABLE3D and Orcaflex. Finally, some useful conclusions are achieved with the application of RISER3D on marine risers.

Chapter 6 makes a final summary of the whole research work. The advantages of RISER3D over the traditional CABLE3D are discussed and summarized. Some future work which can be the extensions of this research are proposed at the end of this dissertation.

2 FORMULATION FOR RISER3D

2.1 Introduction of CABLE3D Program

COUPLE program is a numerical code developed by Professor Jun Zhang and his previous graduate students, which incorporate Hybrid Wave Model for nonlinear wave kinematics for wave load computation. This program can solve the global six degrees of freedom (DoFs) motion of floaters with coupled mooring and riser constraints in both time domain and frequency domain.

CABLE3D, mainly developed by X.H. Chen and Professor J. Zhang (2002), is a key module of COUPLE program, which is used to compute the static and dynamic mooring and riser load. The main theory of CABLE3D originates from early research work on slender rod by Love (1944), Nordgren (1974), Garrett (1982), and Ma and Webster (1994). CABLE3D is a Galerkin's finite element method program which adopted cubic Hermite shape functions to derive the element equations in three-dimensional space. This finite element model has taken the structural displacements and slopes as nodal primary variables. Considering each beam element has two nodes with 12 degrees of freedom (DoFs), together with the Lagrange multiplier approximated with quadratic shape functions in an element domain with 3 DoFs, a total of 15 DoFs are employed for depicting a tension-varied beam element in CABLE3D.

The main functions of CALBE3D comprise of two fold. The first is using small elongation constitutive constraint and nonzero bending stiffness for beam-type riser simulation, the second is using large elongation constitutive constraint and zero bending stiffness for wire-type mooring and cable simulation.

The governing equations, from the dissertation of X.H. Chen (2002), for beam-type element simulation are briefly summarized as

$$\boldsymbol{M}(s,t)\ddot{\boldsymbol{r}}(s,t) + [EI\boldsymbol{r}''(s,t)]'' - \left[\tilde{\lambda}(s,t)\boldsymbol{r}'(s,t)\right]' = \boldsymbol{q}(s,t) \tag{2.1}$$

$$\boldsymbol{r}'(s,t)\cdot\boldsymbol{r}'(s,t)=\left(1+\frac{\tilde{\lambda}(s,t)+P_fA_f-P_iA_i}{EA}\right) \tag{2.2}$$

The governing equations, from X.H. Chen (2002), for wire-type element simulation are briefly summarized as

$$\boldsymbol{M}(s,t)\ddot{\boldsymbol{r}}(s,t)-\left[\tilde{\lambda}\boldsymbol{r}'(s,t)\right]'=\boldsymbol{q}(s,t) \tag{2.3}$$

$$\boldsymbol{r}'(s,t)\cdot\boldsymbol{r}'(s,t)=\left(\frac{EA}{EA-\tilde{\lambda}(s,t)}\right)^2 \tag{2.4}$$

Those who are interested in the physical meaning in each term, omitted here for brevity, of equations from (2.1) to (2.4) can referred to Chen's Ph.D. dissertation (2002). Although CALBE3D can accurately predict the deflection, rotation, and effective tension of slender rods, there are still some shortcomings in this program, which has described in detail in the section 1.2 of the dissertation.

To overcome these shortcomings in CABLE3D, a new finite element program, called RISER3D, by using quintic Hermite interpolation functions is proposed and developed in this research. RISER3D will dramatically mitigate the potential drawbacks in CALBE3D and provide a better alternative for static and dynamic simulation of slender structures such as beams, marine risers and subsea pipelines, especially for those problems which have large gradients in their solutions.

2.2 RIER3D Finite Element Model Formulation and Flowcharts

2.2.1 The Expression and Properties of Quintic Hermite Shape Functions

The main characteristic of the finite element model formulation, using proposed quintic Hermite shape functions, lies in taking the structural curvatures at the two nodes of an element as primary nodal degrees of freedom (DoFs), i.e. primary variables. A one-dimensional beam element, with primary variables of beam displacement, slope and curvature at each end, can be

used to derive the expressions of quintic Hermite shape functions. In this section, the final expressions of the quintic Hermite shape functions are directly presented, the detailed procedures for the mathematic derivations are presented in Appendix A.

The expressions for the normalized quintic Hermite interpolation functions ${\phi_i}^e(\xi)$ $(i = 1\sim6)$,for the e^{th} element, in normalized local coordinate system are six fifth-order polynomials and can be written as

$$
\begin{aligned}
{\phi_1}^e(\xi) &= 1 - 10\xi^3 + 15\xi^4 - 6\xi^5 \\
{\phi_2}^e(\xi) &= \xi - 6\xi^3 + 8\xi^4 - 3\xi^5 \\
{\phi_3}^e(\xi) &= 0.5(\xi^2 - 3\xi^3 + 3\xi^4 - \xi^5) \\
{\phi_4}^e(\xi) &= 10\xi^3 - 15\xi^4 + 6\xi^5 \\
{\phi_5}^e(\xi) &= -4\xi^3 + 7\xi^4 - 3\xi^5 \\
{\phi_6}^e(\xi) &= \tfrac{1}{2}(\xi^3 - 2\xi^4 + \xi^5)
\end{aligned}
\tag{2.5}
$$

where the definition of ξ is $\xi = {(x - x_a)}\Big/{(x_b - x_a)}$ for the element within the domain of $x \in [x_a, x_b]$ and the interval of ξ is $\xi \in [0,1]$, x is the global coordinate.

The plotting for the six normalized quintic Hermite shape functions are shown in Figure 2.1.

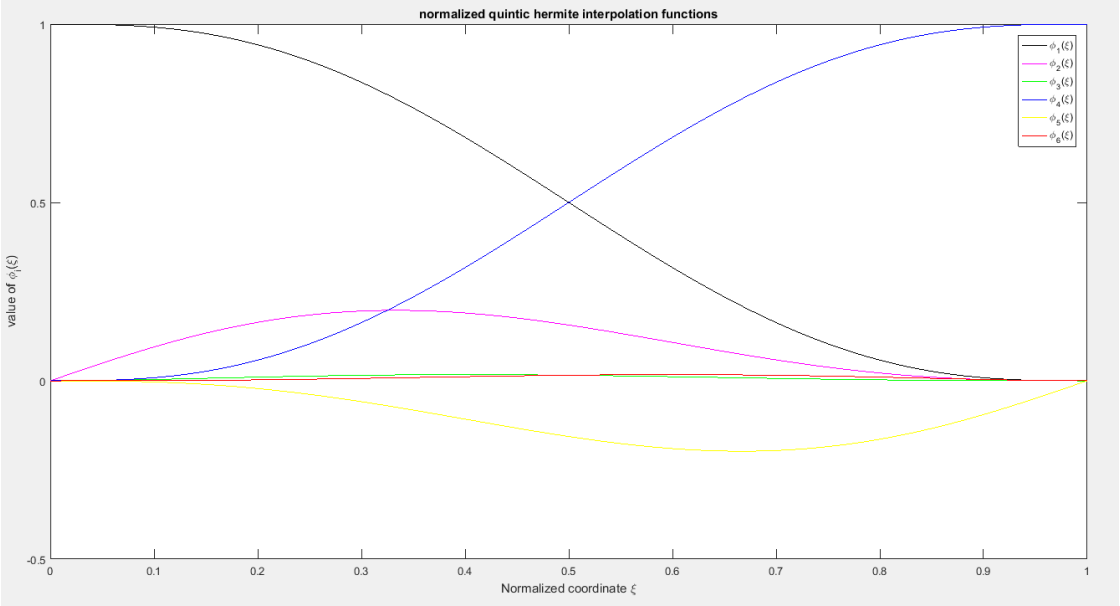

Figure 2.1 Plotting of normalized quintic Hermite shape functions

To get a clearer view of the function $\phi_3(\xi)$ and $\phi_6(\xi)$, the plotting for the third and sixth normalized quintic Hermite shape functions are shown in Figure 2.2.

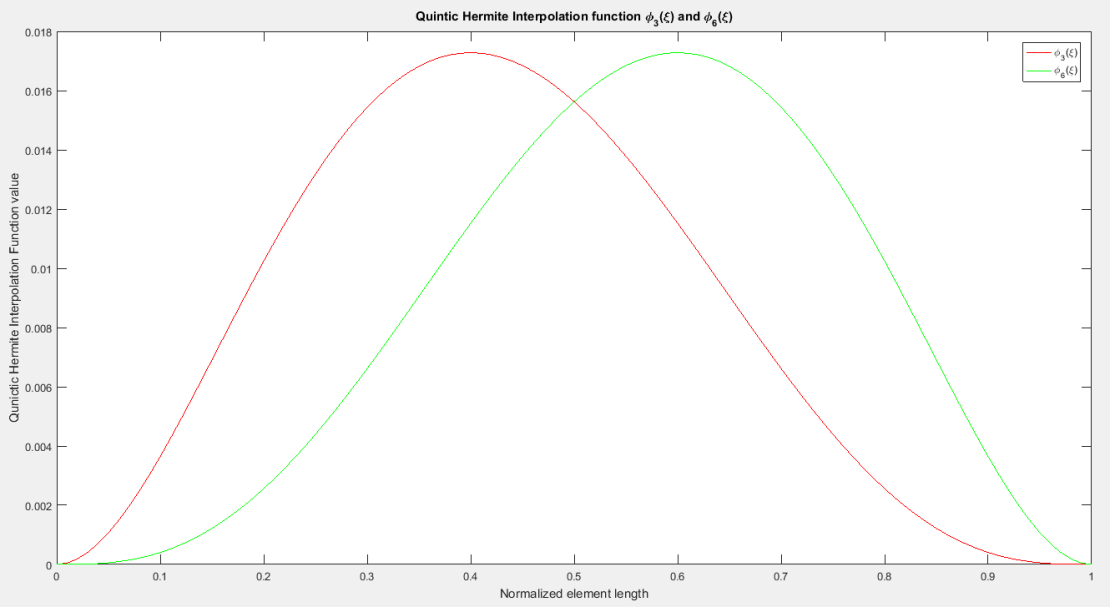

Figure 2.2 Plotting of the third and sixth normalized quintic Hermite shape functions

The general quintic Hermite shape functions, used in the global coordinate system for weak formulation, are related to the normalized quintic Hermite shape functions in normalized local coordinate system by using Jacobian transformation coefficients as

$$a_i{}^e(\xi) = J_i \phi_i{}^e(\xi) \ \ (i = 1\sim 6) \tag{2.6}$$

where J_i are the Jacobian transformation coefficients, relating the normalized local coordinate derivatives to the global coordinate derivatives, are defined by equation (2.7) as a function of the element length h^e of the eth element

$$J_i = \begin{cases} 1 \ (for \ i = 1 \ or \ 4) \\ h^e \ (for \ i = 2 \ or \ 5) \\ h^{e\,2} \ (for \ i = 3 \ or \ 6) \end{cases} \tag{2.7}$$

The main properties of the quintic Hermite shape functions, used for the finite element model development, are all summarized in equation (2.8)

$$\begin{gathered} \phi_1(0) = 1, \phi_i(0) = 0 \ (for \ i = 1\sim 6 \text{ and i} \neq 1) \\ \phi_4(1) = 1, \ \ \phi_i(1) = 0 \ (for \ i = 1\sim 6 \text{ and i} \neq 4) \\ \phi'_2(0) = 1, \ \ \phi'_i(0) = 0 \ \ (for \ i = 1\sim 6 \text{ and i} \neq 2) \\ \phi'_5(1) = 1, \ \ \phi'_i(1) = 0 \ \ (for \ i = 1\sim 6 \text{ and i} \neq 5) \\ \phi''_3(0) = 1, \ \ \phi''_i(0) = 0 \ \ (for \ i = 1\sim 6 \text{ and i} \neq 3) \\ \phi''_6(1) = 1, \ \ \phi''_i(1) = 0 \ \ (for \ i = 1\sim 6 \text{ and i} \neq 6) \end{gathered} \tag{2.8}$$

2.2.2 The Derivation of the Mathematic Model of Marine Riser

To derive the mathematic model for marine risers, the following assumptions have been implemented throughout this research

- The riser is regarded as a slender thin-walled beam which has large length to diameter ratio

- The riser bending rigidity EI is assumed as constant through the overall length. If buoyancy modules are included in the model, the bending rigidity provided by buoyancy modules are neglected
- The undeformed condition of the riser pipe is assumed to be perfect straight and round , with no initial residual stress or out-of-roundness
- The material of riser is homogeneous, isotropic and linear elastic
- The rotatory inertia and Poisson effect are neglected for this study
- The internal flow effect is neglected
- The seabed is treated as flat, frictionless and have elastic support in vertical direction

The main parts of the following derivation for the mathematic model of marine riser have followed the previous work by Nordgren (1974), Garrett (1982), and X.H. Chen (2002). Since the marine riser element has small ratio of characteristic diameter to length, it can be also treated as a kind of slender rod.

In order to appropriately describe the deformed configuration of a marine riser, a global three-dimensional Cartesian coordinate system is used as shown in Figure 2.3. The origin of the coordinate is located at the mean water level with global Y-axis points upward. The instantaneous deformed configuration of the riser can be expressed in terms of a space vector $\boldsymbol{r}(s,t)$. In Figure 2.3, the vectors $\hat{\boldsymbol{t}}$, $\hat{\boldsymbol{n}}$ and $\hat{\boldsymbol{b}}$ are unit vectors in riser tangential, normal and binormal directions respectively, which form a right-handed orthonormal triad.

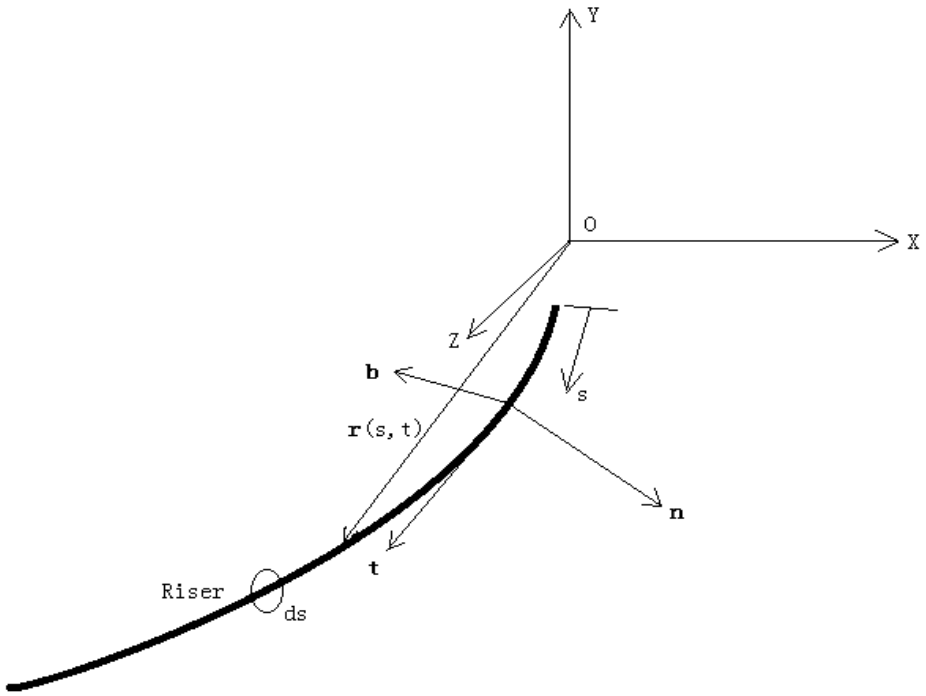

Figure 2.3 Cartesian coordinate system for marine riser

Taking an infinitesimal differential segment ds of the riser, circled in Figure 2.3, as an object for analysis, the free body diagram of which can be drawn in Figure 2.4.

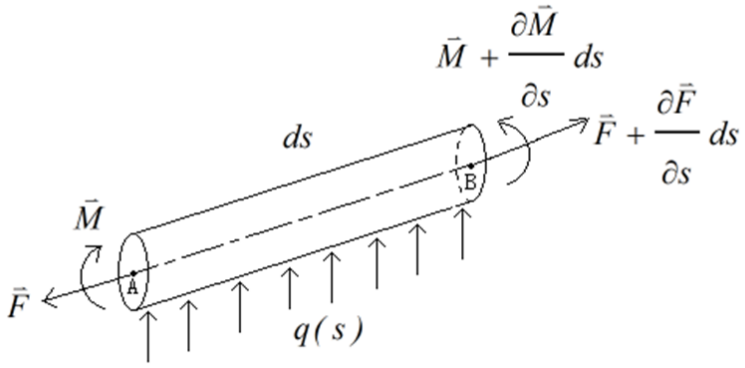

Figure 2.4 Free body diagram of an infinitesimal riser segment

By conservation of linear momentum, the force equilibrium for the differential segment of riser can be established as

$$-\boldsymbol{F} + \boldsymbol{q}ds + \boldsymbol{F} + \frac{\partial \boldsymbol{F}}{\partial s}ds = \rho_m \ddot{\boldsymbol{r}}(s,t)ds \tag{2.9}$$

Further simplification of equation (2.9) leads to the riser motion equation as

$$\boldsymbol{q} + \frac{\partial \boldsymbol{F}}{\partial s} = \rho_m \ddot{\boldsymbol{r}}(s,t) \tag{2.10}$$

where $\boldsymbol{F}$ is the internal resultant force of riser, $\boldsymbol{q}(s,t)$ is distributed external load per unit length, ρ_m is the mass of riser per unit length, $\boldsymbol{r}(s,t)$ is the position vector of the deformed riser centerline curve in space, which is a function of arc length s and time t, $\ddot{\boldsymbol{r}}(s,t)$ is the acceleration of riser, superposed double dot denotes differentiation with respect to time t twice.

Now taking the moments with respect to the point A, as shown in Figure 2.4, the following equilibrium equation can be obtained by using conservation of angular momentum

$$\begin{aligned} &-\boldsymbol{M} + \boldsymbol{M} + \frac{\partial \boldsymbol{M}}{\partial s}ds + \hat{\boldsymbol{t}}ds \times (\boldsymbol{F} + \frac{\partial \boldsymbol{F}}{\partial s}ds) + \boldsymbol{q}ds \cdot \frac{ds}{2} + \boldsymbol{m}ds \\ &= \frac{\partial \boldsymbol{M}}{\partial s}ds + \hat{\boldsymbol{t}}ds \times (\boldsymbol{F} + \frac{\partial \boldsymbol{F}}{\partial s}ds) + \boldsymbol{q}ds \cdot \frac{ds}{2} + \boldsymbol{m}ds = \boldsymbol{0} \end{aligned} \tag{2.11}$$

Omitting the higher order terms including ds^2 and then equation (2.11) can be further simplified as:

$$\boldsymbol{M}' + \hat{\boldsymbol{t}} \times \boldsymbol{F} + \boldsymbol{m} = \boldsymbol{0} \tag{2.12}$$

where $\boldsymbol{M}$ is internal resultant moment of riser, $\boldsymbol{m}$ is the applied external moment per unit length, s is arc length of the deformed riser measured from the top end of riser.

Bold type, superscript symbol '′', superposed symbols '¨' and symbol '^' denote tensor or vector, derivative with respect to deformed arc length s, derivative with respect to time t and unit vector respectively throughout the dissertation unless otherwise specified.

The constitution relationship for bending and torsion of a slender rod is given by Love (1944) as

$$\boldsymbol{M} = B\kappa\hat{\boldsymbol{b}} + H\hat{\boldsymbol{t}} = \hat{\boldsymbol{t}} \times B\kappa\hat{\boldsymbol{n}} + H\hat{\boldsymbol{t}} = \hat{\boldsymbol{t}} \times B\boldsymbol{r}'' + H\hat{\boldsymbol{t}} \tag{2.13}$$

where $B = EI$ is the bending rigidity of riser, E is the Young's modulus, I is the second moment of area, $\kappa = |\boldsymbol{r}''|$ is the curvature of the deformed riser curve, $\hat{\boldsymbol{n}} = \frac{\boldsymbol{r}''}{\kappa}$ is the unit vector in normal direction, $\hat{\boldsymbol{b}}$ is the unit vector in binormal direction, $\hat{\boldsymbol{t}}$ is the unit vector in tangential direction, H is the torsional moment (i.e. axial component of the resultant bending moment, which is proportional to the torsional rigidity and the angle of twist per unit length).

Substitution of the expression of bending moment in Eq (2.13) into Eq (2.12), yields

$$(\hat{\boldsymbol{t}} \times B\boldsymbol{r}'' + H\hat{\boldsymbol{t}})' + \hat{\boldsymbol{t}} \times \boldsymbol{F} + \boldsymbol{m} = \boldsymbol{0} \tag{2.14}$$

Now by employing the Frenet-serret formula for unit vector manipulations

$$\hat{\boldsymbol{t}}' = \kappa\hat{\boldsymbol{n}}$$

$$\hat{\boldsymbol{n}}' = -\kappa\hat{\boldsymbol{t}} + \tau\hat{\boldsymbol{b}} \tag{2.15}$$

Equation (2.14) can be further simplified as

$$\kappa\hat{\boldsymbol{n}} \times B\kappa\hat{\boldsymbol{n}} + \hat{\boldsymbol{t}} \times (B\boldsymbol{r}'')' + H'\hat{\boldsymbol{t}} + H\hat{\boldsymbol{t}}' + \hat{\boldsymbol{t}} \times \boldsymbol{F} + \boldsymbol{m} = \boldsymbol{0} \tag{2.16}$$

Taking the scalar product of equation (2.14) with unit tangential vector $\hat{\boldsymbol{t}}$ yields

$$\hat{\boldsymbol{t}} \cdot [\hat{\boldsymbol{t}} \times (B\boldsymbol{r}'')' + H'\hat{\boldsymbol{t}} + H\kappa\hat{\boldsymbol{n}} + \hat{\boldsymbol{t}} \times \boldsymbol{F} + \boldsymbol{m}] = H' + \hat{\boldsymbol{t}} \cdot \boldsymbol{m} = \boldsymbol{0} \tag{2.17}$$

If the distributed term $\boldsymbol{m}$ is zero, the torque H becomes independent of deformed arc length s. For this research, both $\boldsymbol{m}$ and H are neglected for simplicity of the model. Hence, equation (2.16) can be further simplified as

$$\hat{\boldsymbol{t}} \times (B\boldsymbol{r}'')' + \hat{\boldsymbol{t}} \times \boldsymbol{F} = \hat{\boldsymbol{t}} \times [(B\boldsymbol{r}'')' + \boldsymbol{F}] = \boldsymbol{0} \tag{2.18}$$

Now taking the cross product of equation (2.18) by the unit tangential vector $\hat{\boldsymbol{t}}$, we obtain the following equations with vector manipulations

$$\hat{\boldsymbol{t}} \times \{\hat{\boldsymbol{t}} \times [(B\boldsymbol{r}'')' + \boldsymbol{F}]\} = \boldsymbol{0}$$

$$[-B\kappa^2 + \hat{\boldsymbol{t}} \cdot \boldsymbol{F}]\hat{\boldsymbol{t}} - [(B\boldsymbol{r}'')' + \boldsymbol{F}] = \boldsymbol{0} \tag{2.19}$$

Letting $T = \hat{\boldsymbol{t}} \cdot \boldsymbol{F}$ as the local tangential tension, $\lambda = T - B\kappa^2$ as a Lagrange multiplier, then the internal force of riser can be expressed as

$$\boldsymbol{F} = -(B\boldsymbol{r}'')' + \lambda \boldsymbol{r}' \tag{2.20}$$

Plugging the expression of the internal force $\boldsymbol{F}$ into the motion equation (2.10), the following governing motion equation for marine risers can be eventually obtained

$$-(B\boldsymbol{r}'')'' + \left(\tilde{\lambda}\boldsymbol{r}'\right)' + \boldsymbol{q} = \rho_m \ddot{\boldsymbol{r}} \tag{2.21}$$

For hydrodynamic analysis of marine riser, the added-mass effect should be taken into consideration. Therefore, the governing motion equation for marine riser dynamic analysis can be written as

$$\boldsymbol{M}_m \ddot{\boldsymbol{r}} + (B\boldsymbol{r}'')'' - \left(\tilde{\lambda}\boldsymbol{r}'\right)' = \boldsymbol{q} \tag{2.22}$$

where $\boldsymbol{M}_m$ is the virtual mass matrix, $\boldsymbol{r}(s,t)$ is a space vector for expressing the instantaneous deformed configuration of the riser under external loads.

The small elongation stretching restraint equation for a marine riser can be expressed as

$$\boldsymbol{r}' \cdot \boldsymbol{r}' = (1+\varepsilon)^2 \approx \left(1 + \frac{\tilde{\lambda} - P_f A_f + P_c A_c}{EA}\right)^2 \tag{2.23}$$

where $\boldsymbol{r}'$ is the riser slope vector, ε is the axial strain of the riser, E is the Young's Modulus of riser material, A is the riser tube cross-sectional area, A_f is the riser outer cross-sectional area, A_c is the riser internal cross-sectional area, P_f is the local external pressure and P_c is the local internal pressure.

2.2.3 RISER3D Finite Element Model Formulation

The Galerkin's method is adopted to discretize the partial differential equations (PDEs) of the riser motion equation (2.22) and constraint equation (2.23). For approximation of the unknown primary variables, two types of shape functions are employed in RISER3D. One is the general quintic Hermite shape functions $a_i(s)$ (i=1~6), as presented in equation (2.6), for approximating the deformed state of the riser configuration $\boldsymbol{r}(s,t)$ in element domain; the other is the quadratic shape functions $p_m(s)$, as defined in equation (2.24) below, for discretizing remaining parameters of $\tilde{\lambda}$, B, $\boldsymbol{q}$, $\boldsymbol{M}_m$, etc.

$$p_m(\xi) = \begin{cases} 1 - 3\xi + 2\xi^2 \ \ for\ m = 1 \\ 4\xi(1-\xi)\ for\ m = 2 \\ \xi(2\xi - 1)\ for\ m = 3 \end{cases} \tag{2.24}$$

The weak form of the governing equation (2.22) can be obtained by pre-multiplying the equation with general quintic Hermite shape functions $a_i(s)$ $(i = 1\sim6)$, integrating over a typical element domain from 0 to L and then performing integration by parts three times to trade the differentiation from the dependent variable $\boldsymbol{r}$ to the shape functions, which results in a weaken continuity of the dependent variable in the governing motion equation of marine risers as

$$\int_0^L [\boldsymbol{M_m}\ddot{\boldsymbol{r}}a_i(s) - (B\boldsymbol{r}')a_i'''(s) + \left(\tilde{\lambda}\boldsymbol{r}'\right)a_i'(s) - \boldsymbol{q}a_i(s)]ds = a_i(s)\left(-B\boldsymbol{r}''' + \tilde{\lambda}\boldsymbol{r}'\right)\Big|_0^L +$$

$$a_i{}'(s)B\boldsymbol{r}''\Big|_0^L - a_i{}''(s)B\boldsymbol{r}'\Big|_0^L \qquad \text{(i=1~6)} \tag{2.25}$$

where $a_i(s)$ $(i = 1\sim6)$ are the general non-normalized quintic Hermite interpolation functions in global coordinate system, as presented by equation (2.6), L is the element length of marine risers.

The right-hand side integrated terms in equation (2.25) are usually called the generalized forces, which are denoted as $\boldsymbol{F}_i$ hereafter. The specification of the generalized forces at the riser

extremities, i.e. the riser top and bottom ends, constitutes the natural boundary conditions for the finite element model of a marine riser.

$$\boldsymbol{F}_i = a_i(s)\left(-B\boldsymbol{r}''' + \tilde{\lambda}\boldsymbol{r}'\right)\Big|_0^L + a_i'(s)B\boldsymbol{r}''\Big|_0^L - a_i''(s)B\boldsymbol{r}'\Big|_0^L \quad \text{(i=1~6)} \tag{2.26}$$

The riser deflection $\boldsymbol{r}(s,t)$, effective tension $\tilde{\lambda}$, bending stiffness B, transverse distributed loading $\boldsymbol{q}(s,t)$ and the virtual mass matrix $\boldsymbol{M_m}(s,t)$ are approximated below by using vector or tensor summation rules as

$$\boldsymbol{r}(s,t) = u_{kn}(t)a_k(s)\boldsymbol{e}_n$$

$$\boldsymbol{r}^{(n)}(s,t) = \frac{d^n[u_{kn}(t)a_k(s)]}{ds^n}\boldsymbol{e}_n = u_{kn}(t)a_k{}^{(n)}(s)\boldsymbol{e}_n$$

$$\tilde{\lambda}(s,t) = \tilde{\lambda}_m(t)p_m(s)$$

$$B(s) = B_m p_m(s)$$

$$\boldsymbol{M}(s,t) = \boldsymbol{M}_m(t)p_m(s) \tag{2.27}$$

By substituting all the approximated expressions in equation (2.27) into the weak form of the riser governing equation (2.25), the following set of algebraic equations can be obtained for a typical riser element in the global coordinate system as

$$\gamma_{ikm}M_{njm}\ddot{u}_{kj} - \alpha_{ikm}B_m u_{kn} + \beta_{ikm}\tilde{\lambda}_m u_{kn} = q_{in} + F_{in}$$

$$(for\ i,k = 1\sim6; m,n,j = 1\sim3) \tag{2.28}$$

For the convenience of coding, the coefficients in equation (2.28) are usually transformed into the normalized local coordinate system ξ by incorporating the Jacobian transformation coefficients as defined in equation (2.7), which can lead to the final finite element model of marine risers using quintic Hermite shape functions as

$$L\overline{\gamma}_{ikm}M_{njm}\ddot{\bar{u}}_{kj} - \frac{1}{L^3}\overline{\alpha}_{ikm}B_m\bar{u}_{kn} + \frac{1}{L}\overline{\beta}_{ikm}\tilde{\lambda}_m\bar{u}_{kn} = L\overline{q}_{in} + \frac{F_{in}}{J_i}$$

$$(for\ i,k = 1\sim6; m,n,j = 1\sim3) \tag{2.29}$$

where $\bar{u}_{kn} = J_k u_{kn} (k = 1{\sim}6)$, J_k are the Jacobian transformation coefficients.

A similar derivation procedures can be applied to the riser constraint equation (2.23), omitted here for brevity, which can be finally discretized as three algebraic equations in a typical riser element domain

$$\frac{1}{L}\overline{\beta}_{ikm}\bar{u}_{in}\bar{u}_{kn} - L\bar{\tau}_m - 2L\bar{\eta}_{lm}\varepsilon_l - L\bar{\phi}_{jlm}\varepsilon_j\varepsilon_l = 0 \quad (i,k = 1{\sim}6; j,l,m = 1{\sim}3) \tag{2.30}$$

The riser axial strain in equation (2.30) is defined as

$$\varepsilon_l = \left(\frac{T}{EA}\right)_l = \left(\frac{\tilde{\lambda} + \rho_f g y A_f - \rho_c g y A_c}{EA}\right)_l = \frac{\tilde{\lambda}_l}{EA} + \frac{\rho_f g A_f - \rho_c g A_c}{EA} y_l$$

$$y_l = \begin{cases} \bar{u}_{12} \quad (for\ l = 1) \\ \frac{1}{2}\bar{u}_{12} + \frac{5}{32}\bar{u}_{22} + \frac{1}{64}\bar{u}_{32} + \frac{1}{2}\bar{u}_{42} - \frac{5}{32}\bar{u}_{52} + \frac{1}{64}\bar{u}_{62} \quad (for\ l = 2) \\ \bar{u}_{42} \quad (for\ l = 3) \end{cases} \tag{2.31}$$

where ρ_c is the density of internal content of riser if any, A_c is the internal cross-sectional area of riser, ρ_f is the external fluid density, A_f is the outer cross-sectional area of riser, y_l is the vertical elevation of any point in a typical riser element domain, and the element starting point ($s = 0$), middle point ($s = L/2$) and end point ($s = L$) correspond to the subscript $l = 1,2,3$ respectively.

All the coefficients in equations (2.29) and (2.30) can be summarized and evaluated in the normalized local coordinate system, with an overbar symbol of "¯" over them. The reason for transforming the coefficients from global coordinate system to normalized local coordinate system is for the convenience of numerical coding for a program. All readers should pay attention to this point and know how to do the derivatives transformation with the help of Jacobian transformation coefficients. Because numerical calculations for the coefficients of the finite element model are seldom performed in global coordinate system due to element mesh uncertainty and complexity.

$$\alpha_{ikm} = \int_0^{\mathrm{L}} a_i'''(\mathrm{s}) a_k'(s) p_m(s) ds = \frac{1}{L^3} J_i J_k \overline{\alpha}_{ikm} = \frac{1}{L^3} J_i J_k \int_0^1 \phi_i'''(\xi)\phi_k'(\xi) p_m(\xi) d\xi$$

$$\beta_{ikm} = \int_0^{\mathrm{L}} a_i'(s)a_k'(s)p_m(s)ds = \frac{1}{L}J_iJ_k\overline{\beta}_{ikm} = \frac{1}{L}J_iJ_k\int_0^1 \phi_i{}'(\xi)\phi_k{}'(\xi)p_m(\xi)d\xi$$

$$\gamma_{ikm} = \int_0^{L} a_i(s)a_k(s)p_m(s)ds = LJ_iJ_k\overline{\gamma}_{ikm} = LJ_iJ_k\int_0^1 \phi_i(\xi)\phi_k(\xi)p_m(\xi)d\xi$$

$$q_{in} = \int_0^{\mathrm{L}} a_i(s)q_n(s)ds = LJ_i\overline{q}_{in} = LJ_i\int_0^1 \phi_i(\xi)q_n(\xi)d\xi$$

$$\mu_{im} = \int_0^{\mathrm{L}} a_i(s)p_m(s)ds = LJ_i\overline{\mu}_{im} = LJ_i\int_0^1 \phi_i(\xi)p_m(\xi)d\xi$$

$$\tau_m = L\int_0^1 p_m(\xi)d\xi = L\bar{\tau}_m$$

$$\eta_{lm} = L\int_0^1 p_l(\xi)p_m(\xi)d\xi = L\bar{\eta}_{lm}$$

$$\phi_{jlm} = L\int_0^1 p_j(\xi)p_l(\xi)p_m(\xi)d\xi = L\bar{\phi}_{jlm} \tag{2.32}$$

Since the quintic Hermite shape functions are six fifth-order polynomials, the analytical integration for the coefficients of $\bar{\alpha}_{ikm}$, $\bar{\beta}_{ikm}$, and $\bar{\gamma}_{ikm}$, in the normalized local coordinate system, are quite complicated to perform. The Gaussian Legendre quadrature is adopted, the details of which can be referred to section 2.4. The detailed numerical values of these coefficient matrices are presented in compact matrices forms Appendix B.

2.2.4 Finite Element Analysis Procedures and Flowcharts for RISER3D

The finite element analysis procedures in RISER3D have been decomposed into two modules: the first module is for marine riser static analysis, which should omit the unsteady term in the finite element model equation (2.29); the second module is for marine riser dynamic analysis, which should take the unsteady term in the finite element model equation (2.29) into consideration.

For RISER3D static analysis, the discretized riser motion equation (2.29) and the constraint equation (2.30), together with equation (2.31), can be rewritten in two residual forms by omitting the inertia term as

$$\boldsymbol{R}^1 = -\frac{1}{L^3}\overline{\alpha}_{ikm}B_m\bar{u}_{kn} + \frac{1}{L}\overline{\beta}_{ikm}\tilde{\lambda}_m\bar{u}_{kn} - L\overline{q}_{in} - \frac{F_{in}}{J_i}$$

$$(for\ i,k = 1\sim6; m,n = 1\sim3) \tag{2.33}$$

$$\boldsymbol{R}^2 = \frac{1}{L}\overline{\beta}_{ikm}\bar{u}_{in}\bar{u}_{kn} - L\bar{\tau}_m - 2L\bar{\eta}_{lm}\left(\frac{\tilde{\lambda}_l}{EA} + \frac{\rho_f g A_f - \rho_c g A_c}{EA}y_l\right)$$

$$- L\bar{\phi}_{jlm}\left(\frac{\tilde{\lambda}_j}{EA} + \frac{\rho_f g A_f - \rho_c g A_c}{EA}y_j\right)\left(\frac{\tilde{\lambda}_l}{EA} + \frac{\rho_f g A_f - \rho_c g A_c}{EA}y_l\right)$$

$$(i,k = 1\sim6; j,l,m = 1\sim3) \tag{2.34}$$

To obtain the solution of the coupled unknown 21 primary degrees of freedom (DoFs), i.e. $\bar{u}_{kn}(6 \times 3 = 18$ entries, as k=1~6, n=1~3) and $\tilde{\lambda}_l$ (three entries as l=1~3), Newton-Raphson iteration method is used to solve the coupled nonlinear system of equations, for the r^{th} iteration step we have

$$\begin{bmatrix} \frac{\partial \boldsymbol{R}^{1,r-1}}{\partial \bar{u}} & \frac{\partial \boldsymbol{R}^{1,r-1}}{\partial \tilde{\lambda}} \\ \frac{\partial \boldsymbol{R}^{2,r-1}}{\partial \bar{u}} & \frac{\partial \boldsymbol{R}^{2,r-1}}{\partial \tilde{\lambda}} \end{bmatrix} \begin{Bmatrix} \delta\bar{u}^r \\ \delta\tilde{\lambda}^r \end{Bmatrix} = \begin{Bmatrix} -\boldsymbol{R}^{1,r-1} \\ -\boldsymbol{R}^{2,r-1} \end{Bmatrix} \tag{2.35}$$

By implementing equation (2.35) to equation (2.33) and (2.34) respectively, we obtain the rth step iteration algorithm with the obtained previous iteration step solutions as

$$\left(-\frac{1}{L^3}\overline{\alpha}_{ikm}B_m + \frac{1}{L}\overline{\beta}_{ikm}\tilde{\lambda}_m{}^{(r-1)}\right)\delta\bar{u}_{kn}{}^{(r)} + \left(\frac{1}{L}\overline{\beta}_{ikm}\bar{u}_{kn}{}^{(r-1)}\right)\delta\tilde{\lambda}_m{}^{(r)} = \frac{1}{L^3}\overline{\alpha}_{ikm}B_m\bar{u}_{kn}{}^{(r-1)} - \frac{1}{L}\overline{\beta}_{ikm}\tilde{\lambda}_m{}^{(r-1)}\bar{u}_{kn}{}^{(r-1)} + L\overline{q}_{in} + \frac{F_{in}}{J_i} \quad (for\ i,k = 1\sim6; m,n = 1\sim3) \qquad (2.36)$$

$$\left[\frac{1}{L}\overline{\beta}_{ikm}\bar{u}_{in}{}^{(r-1)}\right]\delta\bar{u}_{kn}{}^{(r)} - L\frac{\rho_f gA_f - \rho_c gA_c}{EA}\left[\bar{\eta}_{lm} + \bar{\phi}_{jlm}\left(\frac{\tilde{\lambda}_j{}^{(r-1)}}{EA} + \frac{\rho_f gA_f - \rho_c gA_c}{EA}y_j{}^{(r-1)}\right)\right]\delta y_l{}^{(r)} - \frac{L}{EA}\left[\bar{\eta}_{lm} + \bar{\phi}_{jlm}\left(\frac{\tilde{\lambda}_j{}^{(r-1)}}{EA} + \frac{\rho_f gA_f - \rho_c gA_c}{EA}y_j{}^{(r-1)}\right)\right]\delta\tilde{\lambda}_l{}^{(r)} = \frac{1}{2}\left[-\frac{1}{L}\overline{\beta}_{ikm}\bar{u}_{in}{}^{(r-1)}\bar{u}_{kn}{}^{(r-1)} + L\bar{\tau}_m + 2L\bar{\eta}_{lm}\left(\frac{\tilde{\lambda}_l{}^{(r-1)}}{EA} + \frac{\rho_f gA_f - \rho_c gA_c}{EA}y_l{}^{(r-1)}\right) + L\bar{\phi}_{jlm}\left(\frac{\tilde{\lambda}_j{}^{(r-1)}}{EA} + \frac{\rho_f gA_f - \rho_c gA_c}{EA}y_j{}^{(r-1)}\right)\left(\frac{\tilde{\lambda}_l{}^{(r-1)}}{EA} + \frac{\rho_f gA_f - \rho_c gA_c}{EA}y_l{}^{(r-1)}\right)\right] \quad (for\ i,k = 1\sim6; j,l,m = 1\sim3) \qquad (2.37)$$

where δy_l should be calculated based on equation (2.31) as

$$y_l = \begin{cases} \delta\bar{u}_{12} & (for\ l = 1) \\ \frac{1}{2}\delta\bar{u}_{12} + \frac{5}{32}\delta\bar{u}_{22} + \frac{1}{64}\delta\bar{u}_{32} + \frac{1}{2}\delta\bar{u}_{42} - \frac{5}{32}\delta\bar{u}_{52} + \frac{1}{64}\delta\bar{u}_{62} & (for\ l = 2) \\ \delta\bar{u}_{42} & (for\ l = 3) \end{cases}$$

According to the iteration algorithm presented in equation (2.36) and (2.37), the detailed finite element procedures for marine riser static analysis can be summarized as:

Guess initial displacement and force vector as $\{\bar{u}_{kn}{}^{(0)}\}$ and $\{\tilde{\lambda}_l{}^{(0)}\}$

***Loop r=1:itmax** (itmax is the preset maximum iteration steps)*

Initialize the global stiffness matrix [GLK] and global force vector {GLF} as zeros

***Loop ie=1:ne** (ne is the total element number)*

Initialize the element stiffness matrix [K$^{(ie)}$] and the force vector {F$^{(ie)}$}as zeros

Calculate the stiffness matrix [K$^{(ie)}$] and the force vector {F$^{(ie)}$} for each element

Assemble all the element stiffness matrix and the force vector to global stiffness matrix [GLK] and global force vector {GLF}

End loop ie

Impose boundary conditions to the global system equations

Solve the global system equations by using Gauss elimination for $\delta\bar{u}_{kn}{}^{(r)}$ *and* $\delta\tilde{\lambda}_{l}{}^{(r)}$

Update the displacement and force vectors using $\bar{u}_{kn}{}^{(r)} = \bar{u}_{kn}{}^{(r-1)} + \lambda_r \delta\bar{u}_{kn}{}^{(r)}$ *and* $\tilde{\lambda}_{m}{}^{(r)} = \tilde{\lambda}_{m}{}^{(r-1)} + \lambda_r \delta\tilde{\lambda}_{m}{}^{(r)}$*, where* λ_r *is the relaxation coefficient, usually taken as 0.8*

Check if $max\{\delta\bar{u}_{kn}{}^{(r)}\} < \varepsilon$*, here* ε *is a preset convergence limit; if the condition is satisfied, then the code is considered as convergent and write results to output files and exit the loop r, otherwise continue for the next iteration step*

End loop r

If when r=itmax and condition $max\{\delta\bar{u}^r, \delta\tilde{\lambda}^r\} < \varepsilon$ *still does not satisfied, print divergence message and terminate the code.*

For RISER3D dynamic analysis, the riser dynamic motion equation (2.29) and constraint equation (2.30), together with equation (2.31), can be rewritten in residual form as

$$\boldsymbol{R}^1 = L\overline{\gamma}_{ikm} M_{njm} \ddot{\bar{u}}_{kj}(t) - \frac{1}{L^3}\overline{\alpha}_{ikm} B_m \bar{u}_{kn}(t) + \frac{1}{L}\overline{\beta}_{ikm} \tilde{\lambda}_m(t) \bar{u}_{kn}(t) - L\overline{q}_{in}(t) - \frac{F_{in}(t)}{J_i}$$

$$(for\ i,k = 1\sim 6; m,n,j = 1\sim 3) \tag{2.38}$$

$$\boldsymbol{R}^2 = \frac{1}{L}\overline{\beta}_{ikm} \bar{u}_{in}(t) \bar{u}_{kn}(t) - L\bar{\tau}_m - 2L\bar{\eta}_{lm}\left(\frac{\tilde{\lambda}_l}{EA} + \frac{\rho_f g A_f - \rho_c g A_c}{EA} y_l\right)$$

$$- L\bar{\phi}_{jlm}\left(\frac{\tilde{\lambda}_j}{EA} + \frac{\rho_f g A_f - \rho_c g A_c}{EA} y_j\right)\left(\frac{\tilde{\lambda}_l}{EA} + \frac{\rho_f g A_f - \rho_c g A_c}{EA} y_l\right)$$

$$(i,k = 1\sim 6; j,l,m = 1\sim 3) \tag{2.39}$$

By implementation of the Newmark-beta scheme for the dynamic time integration, applying the Newton-Raphson iteration scheme, as shown in equation (2.35), to equation (2.38) and (2.39), for the r^{th} iteration step and s^{th} time step, lead to

$$\left(L\overline{\gamma}_{ikm}M_{njm}\frac{1}{\beta h^2}\right)\delta\bar{u}_{kj}{}^{(s,r)}+\left(-\frac{1}{L^3}\overline{\alpha}_{ikm}B_m+\frac{1}{L}\overline{\beta}_{ikm}\tilde{\lambda}_m{}^{(s,r-1)}\right)\delta\bar{u}_{kn}{}^{(s,r)}$$

$$+\left(\frac{1}{L}\overline{\beta}_{ikm}\bar{u}_{kn}{}^{(s,r-1)}\right)\delta\tilde{\lambda}_m{}^{(s,r)}$$

$$=L\overline{q}_{in}{}^{(s,r)}+\frac{F_{in}{}^{(s,r)}}{J_i}-L\overline{\gamma}_{ikm}M_{njm}\ddot{\bar{u}}_{kj}{}^{(s,r-1)}+\frac{1}{L^3}\overline{\alpha}_{ikm}B_m\bar{u}_{kn}{}^{(s,r-1)}$$

$$-\frac{1}{L}\overline{\beta}_{ikm}\tilde{\lambda}_m{}^{(s,r-1)}\bar{u}_{kn}{}^{(s,r-1)}$$

$$(i,k=1\sim6;j,l,m=1\sim3;s=1\sim itstep) \tag{2.40}$$

$$\left[\frac{1}{L}\overline{\beta}_{ikm}\bar{u}_{in}{}^{(s,r-1)}\right]\delta\bar{u}_{kn}{}^{(s,r)}-L\frac{\rho_f gA_f-\rho_c gA_c}{EA}\left[\bar{\eta}_{lm}+\bar{\phi}_{jlm}\left(\frac{\tilde{\lambda}_j{}^{(s,r-1)}}{EA}+\right.\right.$$

$$\left.\left.\frac{\rho_f gA_f-\rho_c gA_c}{EA}y_j{}^{(s,r-1)}\right)\right]\delta y_l{}^{(s,r)}-\frac{L}{EA}\left[\bar{\eta}_{lm}+\bar{\phi}_{jlm}\left(\frac{\tilde{\lambda}_j{}^{(s,r-1)}}{EA}+\frac{\rho_f gA_f-\rho_c gA_c}{EA}y_j{}^{(s,r-1)}\right)\right]\delta\tilde{\lambda}_l{}^{(s,r)}=$$

$$\frac{1}{2}\left[-\frac{1}{L}\overline{\beta}_{ikm}\bar{u}_{in}{}^{(s,r-1)}\bar{u}_{kn}{}^{(s,r-1)}+L\bar{\tau}_m+2L\bar{\eta}_{lm}\left(\frac{\tilde{\lambda}_l{}^{(s,r-1)}}{EA}+\frac{\rho_f gA_f-\rho_c gA_c}{EA}y_l{}^{(s,r-1)}\right)+\right.$$

$$\left.L\bar{\phi}_{jlm}\left(\frac{\tilde{\lambda}_j{}^{(s,r-1)}}{EA}+\frac{\rho_f gA_f-\rho_c gA_c}{EA}y_j{}^{(s,r-1)}\right)\left(\frac{\tilde{\lambda}_l{}^{(s,r-1)}}{EA}+\frac{\rho_f gA_f-\rho_c gA_c}{EA}y_l{}^{(s,r-1)}\right)\right](for\ i,k=$$

$$1\sim6;j,l,m=1\sim3;s=1\sim itstep) \tag{2.41}$$

where the symbol δ represents the iteration incremental of the unknown primary variables for the r^{th} iteration step at the s^{th} time step, h is the discretized time step, β and γ are the Newmark-beta scheme control parameters, different combinations of these two parameters yield different Newmark-beta schemes. For instance, the average constant acceleration scheme requires $\beta=0.25$ and $\gamma=0.5$, which is widely used due to its unconditional stability.

According to the time marching and iteration algorithm presented in equation (2.40) and (2.41), the detailed finite element procedures for marine riser dynamic analysis in RISER3D can be summarized as:

Determine initial displacement, velocity and force vector as $\{\bar{u}_{kn}{}^{(0)}\}$ $\{\ddot{\bar{u}}_{kn}{}^{(0)}\}$ *and* $\{\tilde{\lambda}_m{}^{(0)}\}$ *according to initial conditions, the initial acceleration vector* $\{\ddot{\bar{u}}_{kn}{}^{(0)}\}$ *can be solved using the discretized governing motion equation (2.29)*

Loop s=1:itstep *(itstep is the total time steps, which is determined by the total simulation time and time step increment* Δt *)*

Loop r=1:itmax *(itmax is the preset maximum iteration steps, such as itmax=500)*

Initialize the global stiffness matrix [GLK] and global force vector {GLF} as zeros

Loop ie=1:ne *(ne is the total riser element number)*

If r=1

If s=1

Update the displacement vector by $\bar{u}_{kn}{}^{(1,1)} = \bar{u}_{kn}{}^{(0)} + h\dot{\bar{u}}_{kn}{}^{(0)} + \frac{h^2}{2}\ddot{\bar{u}}_{kn}{}^{(0)}$ $(here\ h = \Delta t)$

Update the velocity vector by $\dot{\bar{u}}_{kn}{}^{(1,1)} = \dot{\bar{u}}_{kn}{}^{(0)} + h\ddot{\bar{u}}_{kn}{}^{(0)}$

Update the effective tension by $\{\tilde{\lambda}_m{}^{(1,1)}\}=\{\tilde{\lambda}_m{}^{(0)}\}$

Else

Update the displacement vector by $\bar{u}_{kn}{}^{(s,1)} = \bar{u}_{kn}{}^{(s-1,N_{s-1})} + h\dot{\bar{u}}_{kn}{}^{(s-1,N_{s-1})} + \frac{h^2}{2}\ddot{\bar{u}}_{kn}{}^{(s-1,N_{s-1})}$

Update the velocity vector by $\dot{\bar{u}}_{kn}{}^{(s,1)} = \dot{\bar{u}}_{kn}{}^{(s-1,N_{s-1})} + h\ddot{\bar{u}}_{kn}{}^{(s-1,N_{s-1})}$

Update the effective tension by $\{\tilde{\lambda}_m{}^{(s,1)}\}=\{\tilde{\lambda}_m{}^{(s-1,N_{s-1})}\}$

endif

Endif

Initialize the element stiffness matrix [$K^{(ie)}$] and the force vector {$F^{(ie)}$}as zeros

Calculate the element stiffness matrix [$K^{(ie)}$] and the force vector {$F^{(ie)}$}

Assemble the element stiffness matrix and the force vector to form the global stiffness matrix [GLK] and global force vector {GLF}

End loop ie

Impose boundary conditions to the assembled global system of equations

Solve the global system of equations using a banded-matrix solver for $\delta\bar{u}_{kn}{}^{(s,r)}$ *and* $\delta\tilde{\lambda}_m{}^{(s,r)}$

Update the riser nodal displacement, velocity and acceleration by using formulas

$$\bar{u}_{kn}{}^{(s,r+1)} = \bar{u}_{kn}{}^{(s,r)} + \lambda_r \delta\bar{u}_{kn}{}^{(s,r)}$$

$$\dot{\bar{u}}_{kn}{}^{(s,r+1)} = \dot{\bar{u}}_{kn}{}^{(s,r)} + \frac{\gamma}{\beta h}\lambda_r \delta\bar{u}_{kn}{}^{(s,r)}$$

$$\delta\tilde{\lambda}_m{}^{(s,r+1)} = \tilde{\lambda}_m{}^{(s,r)} + \delta\tilde{\lambda}_m{}^{(s,r)}$$

If r=1 then

$$\ddot{\bar{u}}_{kn}{}^{(s,r+1)} = \ddot{\bar{u}}_{kn}{}^{(s-1,N_{s-1})} + \frac{1}{\beta h^2}\lambda_r \delta\bar{u}_{kn}{}^{(s,r)}$$

Else

$$\ddot{\bar{u}}_{kn}{}^{(s,r+1)} = \ddot{\bar{u}}_{kn}{}^{(s,r)} + \frac{1}{\beta h^2}\lambda_r \delta\bar{u}_{kn}{}^{(s,r)}$$

endif

if $max\left\{\delta\bar{u}_{kn}{}^{(s,r)}, \delta\tilde{\lambda}_m{}^{(s,r)}\right\} < \varepsilon$ ***and*** $r < itmax$

The time step s is convergent, mark down the current iteration step $r = N_s$*, exit the iteration loop and start the simulation for the next time step s+1. Therefore, the convergent*

displacement, velocity and acceleration for the time step s are $\bar{u}_{kn}{}^{(s,N_s)}$, $\bar{\ddot{u}}_{kn}{}^{(s,N_s)}$ *and* $\bar{\ddot{u}}_{kn}{}^{(s,N_s)}$

if $max\left\{\delta\bar{u}_{kn}{}^{(s,r)}, \delta\tilde{\lambda}_m{}^{(s,r)}\right\} > \varepsilon$ ***and*** $r < itmax$

Continue for the next iteration loop until the convergent criteria for the time step s are satisfied

if $max\left\{\delta\bar{u}_{kn}{}^{(s,r)}, \delta\tilde{\lambda}_m{}^{(s,r)}\right\} > \varepsilon$ ***and*** $r \geq itmax$

print scheme divergence warning message to the computer screen for the analyst, check all the input data and code control parameters to restart the overall analysis

endif

End loop r

End loop s

A flow chart for RISER3D static finite element analysis procedures by Newton Raphson iteration is shown in Figure 2.5 and the dynamic finite element analysis procedures by Newmark-beta scheme is shown in Figure 2.6.

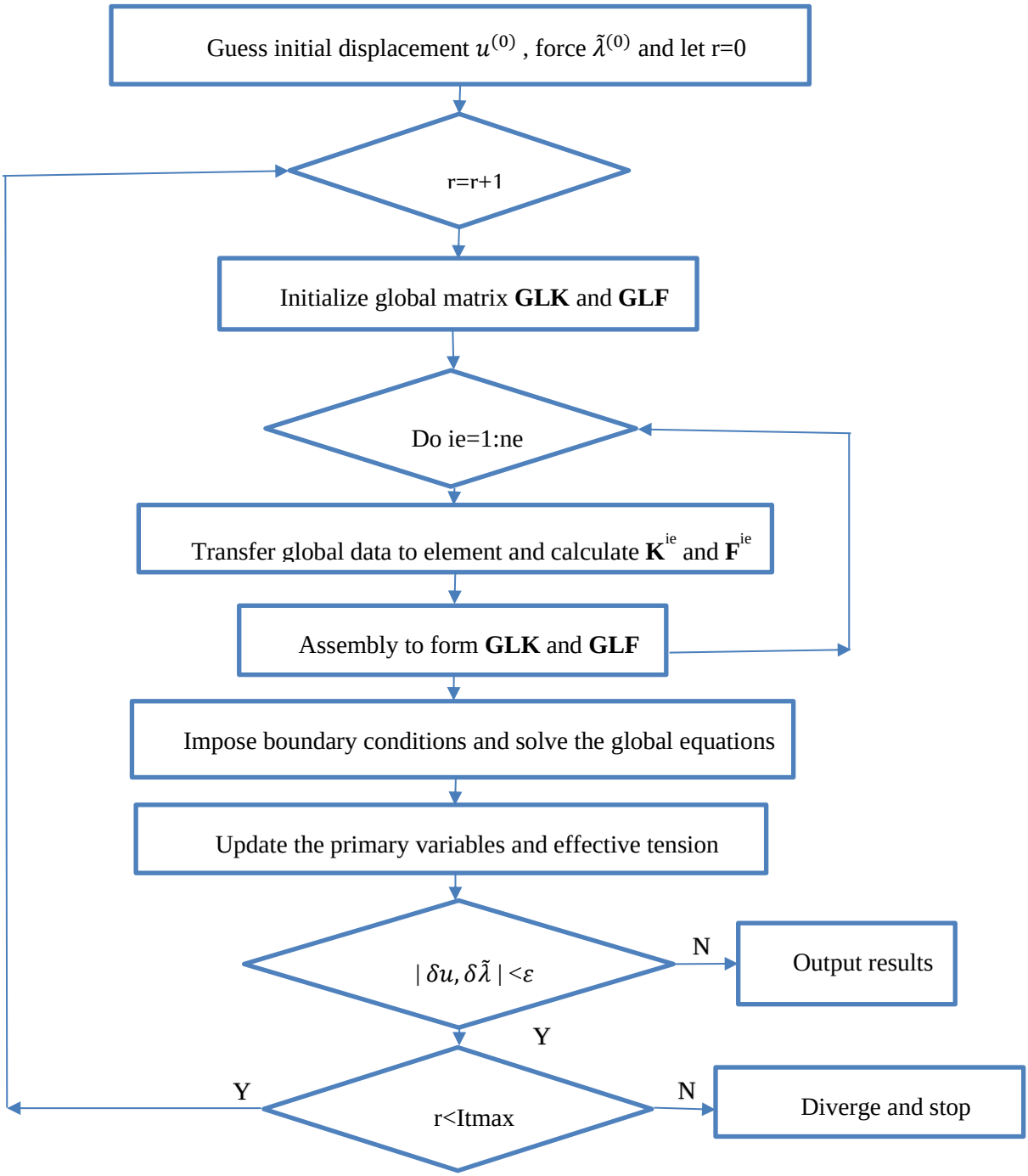

Figure 2.5 Static analysis flow chart for RISER3D

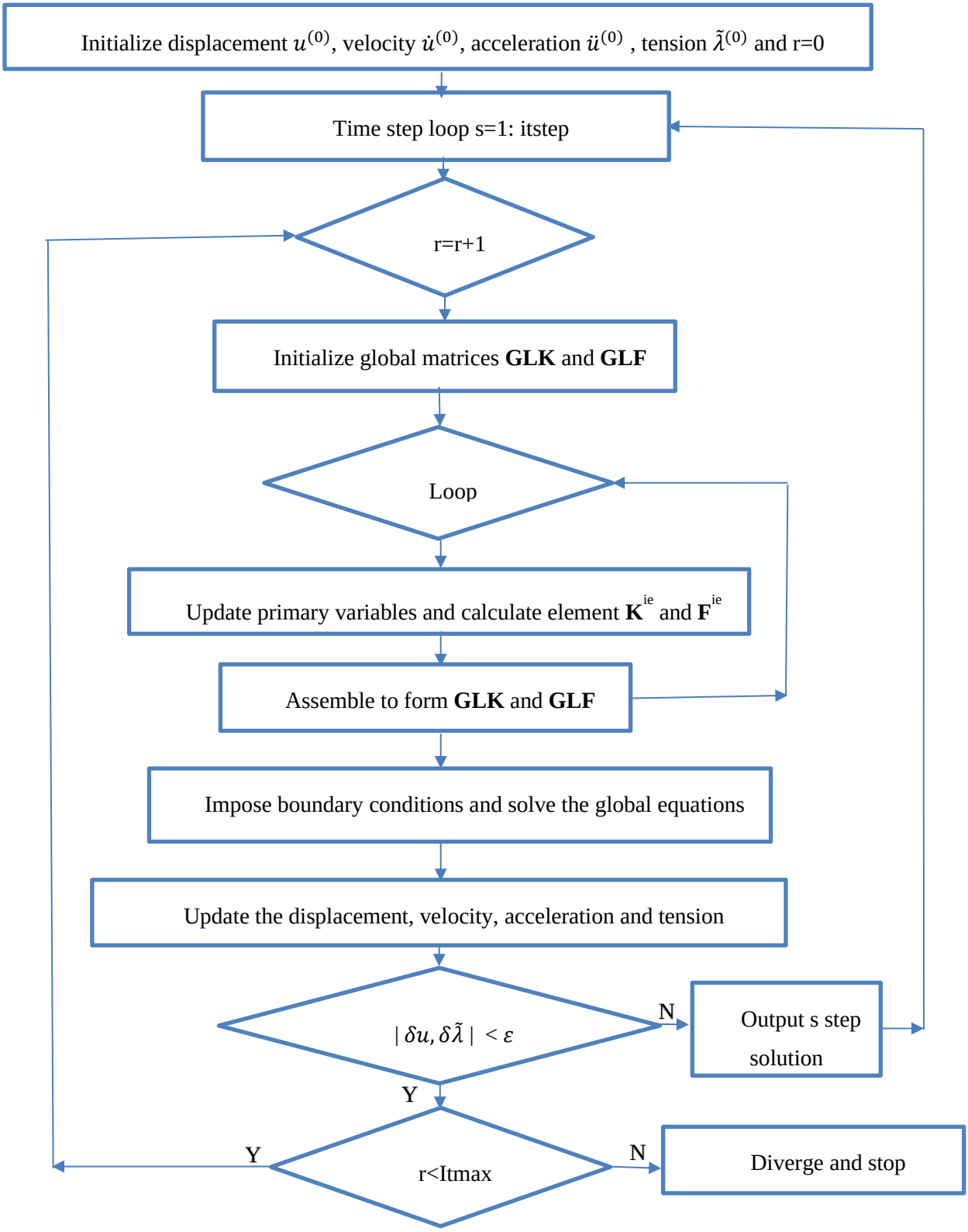

Figure 2.6 Dynamic analysis flow chart for RISER3D

2.3 RIER3D Boundary Conditions and Seabed Support Model

2.3.1 Typical Beam Boundary Conditions of RISER3D

By using finite element method for solving engineering problems of slender structures, specific boundary conditions (BCs) must be correctly specified and imposed. For boundary conditions of marine risers, it can be started with the generalized force equation (2.26). As a general rule for finite element analysis, the dependent unknowns $\boldsymbol{r}(s,t)$ in the same form as the shape function $a_i(s)$ appearing in the generalized force expression (2.26) is termed as a primary variable (PV), and the specification of which constitutes the Dirichlet (essential) boundary conditions; the coefficients of the shape function $a_i(s)$ in the generalized force expression (2.26) are termed as a secondary variables (SVs), the specification of which constitutes the Neumann (natural) boundary conditions. And the primary and secondary variables always appear in pairs (J.N. Reddy, 2006). For riser finite element model by using quintic Hermite shape functions, there are a total of three pairs of primary and secondary variables (PV_i, SV_i) $(i = 1\sim3)$, i.e. $(PV_1, SV_1) = (\boldsymbol{r}, -B\boldsymbol{r}''' + \tilde{\lambda}\boldsymbol{r}')$, $(PV_2, SV_2) = (\boldsymbol{r}' , B\boldsymbol{r}'')$, $(PV_3, SV_3) = (\boldsymbol{r}'' , B\boldsymbol{r}')$ respectively.

As for the boundary conditions of internal elements of RISER3D, the continuity of the generalized displacements and balance of the generalized forces should be guaranteed, which is illustrated in Figure 2.7.

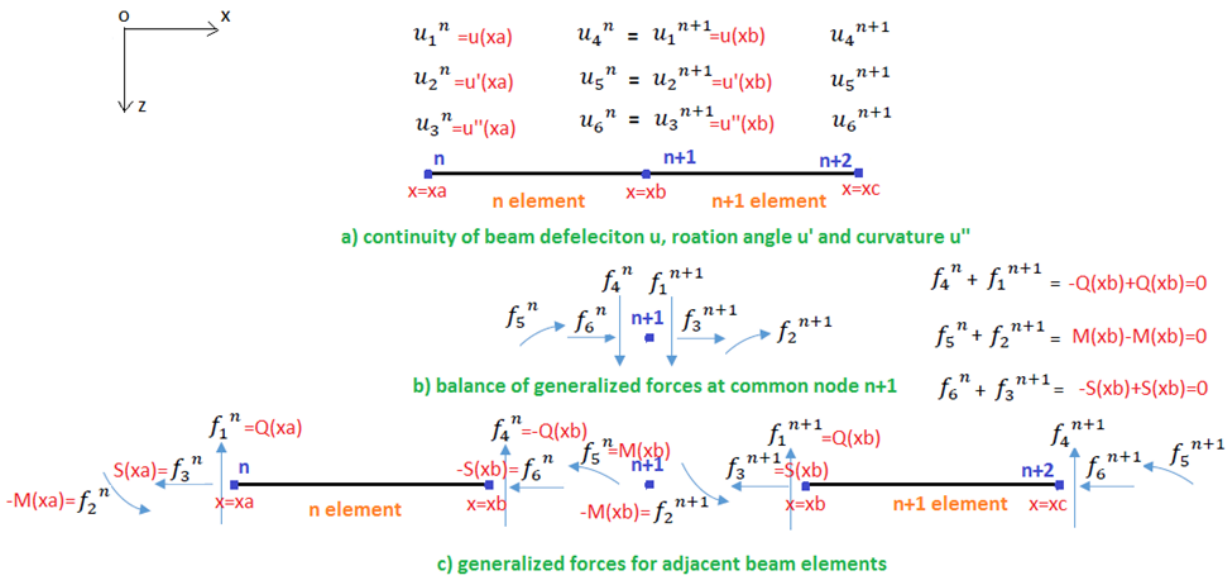

Figure 2.7 The boundary conditions for the internal nodes of RISER3D

For typically supported beam elements at the end of the domain, the boundary conditions are summarized in Figure 2.8. With distinction to the cubic Hermite finite element method, the quintic Hermite finite element method has a third pair of the primary and secondary variable $(PV_3, SV_3) = (\boldsymbol{r}''\ ,\ B\boldsymbol{r}')$, which can help to impose Dirichlet boundary condition for the riser curvature and Neumann boundary condition for the bending slope of riser. This point is the key difference on boundary conditions part between the new RISER3D and traditional CABLE3D.

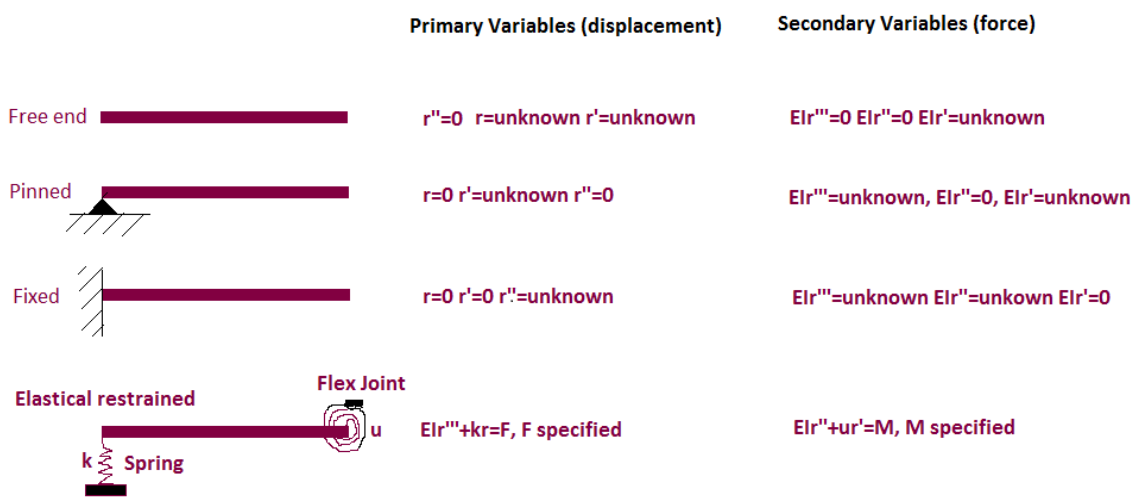

Figure 2.8 Typical boundary conditions for RISER3D

Take the pinned end and the fixed end boundary condition as examples, the imposition of the classical boundary conditions in RISER3D is shown in Figure 2.9 below.

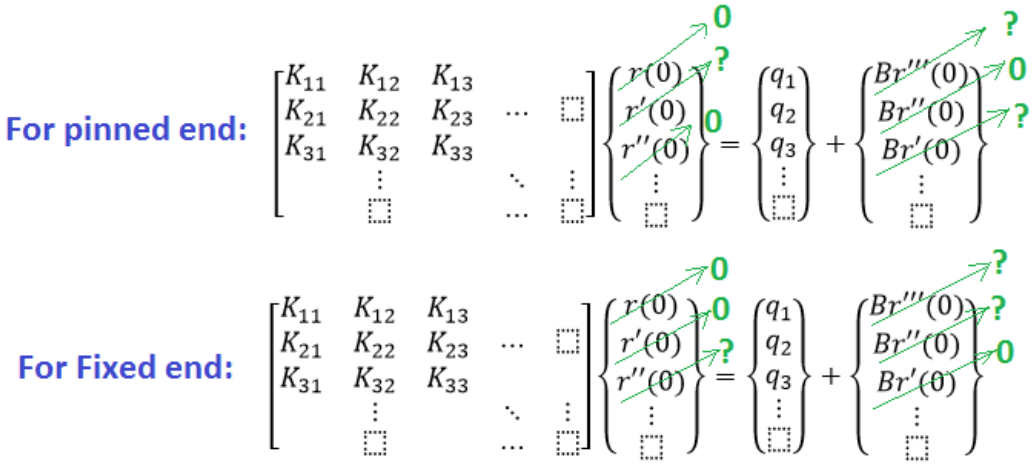

Figure 2.9 Typical boundary condition examples for RISER3D

As for the beam or riser has a rotational stiffness restraint at the boundary, this type of boundary conditions is quite different from the traditional finite element method by using RISER3D. Now taking the one-dimensional beam element as an example, assuming that the beam is subject to a rotational stiffness k_θ restraint at the starting end (i.e. $\xi = 0$) and we can express the generalized forces of the beam bending moment and beam slop as

$$-Br'' = -k_\theta (r' - r'_0) \tag{2.42}$$

$$Br' = -k_\kappa (r'' - r''_0) \tag{2.43}$$

where B is the bending rigidity of the beam, r, r' and r'' are the nodal displacement, slope and curvature respectively, $k_\kappa$is an assumed constant representing stiffness related to the curvature, r'_0 is a referred neutral angle where the external bending moment applied by the rotational stiffness is zero, r''_0 is a referred curvature which can be solved later.

Now solving the expression of the beam slope r' by equation (2.42) and substituting it to the left hand side of equation (2.43), the following two relationships hold

$$k_\kappa = -\frac{B^2}{k_\theta} \tag{2.44}$$

$$k_k\, r''_0 = Br'_0 \tag{2.45}$$

Therefore, the related entries in the global stiffness matrix and force vector for the rotational stiffness boundary condition should be updated as

$$\begin{aligned} K_{22} &\leftarrow K_{22} + k_\theta \\ F_2 &\leftarrow F_2 + k_\theta r'_0 \\ K_{33} &\leftarrow K_{33} - \frac{B^2}{k_\theta} \\ F_3 &\leftarrow F_3 + Br'_0 \end{aligned} \tag{2.46}$$

Form equation (2.46), it can be seen that, for RISER3D, all the equations related to the unknown beam slope and beam curvature should be updated if a rotational stiffness is applied to at the end of an element. This part is quite different to traditional finite element method by using cubic Hermite shape functions, analysts should pay great attention to this kind of boundary conditions to avoid mistakes for finite element analysis.

2.3.2 Linear Spring-damper Seabed Model for RISER3D

The seabed is modeled as a spring system in riser static analysis and a spring-damping system in riser dynamic analysis, this section has mainly followed the work of X.H. Chen (2002) with minor modifications to be consistent with this dissertation, reader can also refer to her dissertation if interested.

The reaction force, in vertical direction, per unit length exerted by the elastic seabed on the riser can be modeled as

$$q^{soil} = \begin{cases} \frac{w_{sub}}{R_f}\left[R_f - (\boldsymbol{r}\cdot\hat{\boldsymbol{j}} - H_b)\right] & ,for\ (\boldsymbol{r}\cdot\hat{\boldsymbol{j}} - H_b) < R_f \\ 0 & ,otherwise \end{cases} \tag{2.47}$$

where R_f is the distance from the centerline of the riser to the outermost surface of the riser; H_b is the vertical coordinate of seabed in three-dimensional riser coordinate system; w_{sub} is the submerged (also called apparent) weight of riser per unit length, which can be calculated by

$$w_{sub} = \begin{cases} (\rho_t A_t + \rho_i A_i - \rho_f A_f)\, g & (product\ filled) \\ (\rho_t A_t - \rho_f A_f)\, g & (empty\ pipe) \end{cases} \tag{2.48}$$

The equivalent nodal force exerted by seabed support can be computed by multiplying both sides of equation (2.47) by quintic Hermite shape functions $a_i(s)$ $(i = 1\sim6)$ and integrating with respect to arc length s from 0 to L in an element domain

$$\int_0^L q^{soil} a_i(s)\, ds = \int_0^L \frac{w_{sub}}{R_f}\left[R_f - (\boldsymbol{r}\cdot\hat{\boldsymbol{j}} - H_b)\right] a_i(s)\, ds = \mu_{im}\left(w_{sub} + \frac{H_b}{R_f}\right)_m -$$

$$\gamma_{ikm}\left(\frac{w_{sub}}{R_f}\right)_m u_{k2} \tag{2.49}$$

where the integration coefficients μ_{im} and can γ_{ikm} be referred to equation (2.32).

The distributed force due to soil damping is also considered in vertical direction

$$q^{sd} = \begin{cases} -C_{sd}\dot{\boldsymbol{r}}\cdot\hat{\boldsymbol{j}} & ,for\ (\boldsymbol{r}\cdot\hat{\boldsymbol{j}} - H_b) < R_f \\ 0 & ,otherwise \end{cases} \tag{2.50}$$

where C_{sd} is the soil damping coefficient which can be calculated as

$$C_{sd} = 2\sqrt{\frac{w_{sub}\rho_m}{R_f}} \tag{2.51}$$

The nodal equivalent damping force can be evaluated by multiplying both sides of equation (2.50) by quintic Hermite shape functions $a_i(s)$ $(i = 1\sim6)$ and integrating with respect to arc length s from 0 to L in an element domain

$$\int_0^L q^{sd} a_i(s)\, ds = \int_0^L (-C_{sd}\dot{\boldsymbol{r}}\cdot\hat{\boldsymbol{j}}) a_i(s)\, ds = -(C_{sd})_m \gamma_{ikm}\dot{u}_{k2} \tag{2.52}$$

2.4 Calculation of Coefficient Matrices Using Gaussian Legendre Quadrature

The n-point Gauss Legendre quadrature approach is a numerical integration rule constructed to yield an exact result for a polynomial of degree 2n-1 or less by using corresponding nodes x_i and weight w_i (i=1~n). In other words, a polynomial of degree p can be integrated exactly by employing [(p+1)/2] Gauss points, here the symbol '[ ]' denotes taking integer.

The n-point Gauss Legendre quadrature formula can be expressed as

$$\int_a^b f(x)dx = \int_{-1}^1 f\left(\frac{b-a}{2}t + \frac{b+a}{2}\right)\frac{b-a}{2}dt \approx \frac{b-a}{2}\sum_{i=1}^n f\left(\frac{b-a}{2}x_i + \frac{b+a}{2}\right)w_i \tag{2.53}$$

where the Gauss nodes x_i in the formula are defined as the roots of the Legendre polynomial $P_n(x)$, and the integration weights w_i can be calculated by function:

$$w_i = \frac{2}{(1-x_i^2)[P_n'(x_i)]^2} \tag{2.54}$$

In order to guarantee the accuracy of all the coefficients in equation (2.32), an eleven-point Gauss Legendre quadrature is adopted in RISER3D program. The nodes and weights are referred to data cited from the website *https://pomax.github.io/bezierinfo/legendre-gauss.html*, which are shown in the Figure 2.10.

The Gauss Legendre weights and nodes for n=11

i	weight - w_i	abscissa - x_i
1	0.2729250867779006	0.0000000000000000
2	0.2628045445102467	-0.2695431559523450
3	0.2628045445102467	0.2695431559523450
4	0.2331937645919905	-0.5190961292068118
5	0.2331937645919905	0.5190961292068118
6	0.1862902109277343	-0.7301520055740494
7	0.1862902109277343	0.7301520055740494
8	0.1255803694649046	-0.8870625997680953
9	0.1255803694649046	0.8870625997680953
10	0.0556685671161737	-0.9782286581460570
11	0.0556685671161737	0.9782286581460570

Figure 2.10 11-Point Gauss Legendre weights and nodes abscissa (Reprinted from Kamermans, 2011)

2.5 Data Postprocessing Methods for CABLE3D and RISER3D

For CABLE3D, the riser deflection function within an element domain is a cubic polynomial function, whose second and third derivative are piecewise linear and constant within the element domain. Therefore, the calculation of riser bending moment ($B\boldsymbol{r}''$) and shear force ($B\boldsymbol{r}'''$), in an element domain, suffers considerable error by directly taking differentiations of the

riser deflection function. A better alternative for bending moment and shear force computation is using the five-point finite difference method (marked as 5pFDM in the legend of figures in this dissertation), the formulas of which are summarized as three schemes from equation (2.55) to (2.57).

Five-point forward asymmetric scheme for first and second derivative with uniform grid length Δx is

$$f'(x_i) = \frac{-25f_i + 48f_{i+1} - 36f_{i+2} + 16f_{i+3} - 3f_{i+4}}{12\Delta x} + o(\Delta x^4)$$

$$f''(x_i) = \frac{35f_i - 104f_{i+1} + 114f_{i+2} - 56f_{i+3} + 11f_{i+4}}{12\Delta x^2} + o(\Delta x^3) \tag{2.55}$$

where $f_i = f(x_i)$, $f_{i+\mathrm{j}} = f(x_i + j\Delta x)(j = 1{\sim}4)$.

Five-point backward asymmetric scheme for first and second derivative with uniform grid length Δx is

$$f'(x_i) = \frac{3f_{i-4} - 16f_{i-3} + 36f_{i-2} - 48f_{i-1} + 25f_i}{12\Delta x} + o(\Delta x^4)$$

$$f''(x_i) = \frac{11f_{i-4} - 56f_{i-3} + 114f_{i-2} - 104f_{i-1} + 35f_i}{12\Delta x^2} + o(\Delta x^3) \tag{2.56}$$

where $f_i = f(x_i)$, $f_{i-\mathrm{j}} = f(x_i - j\Delta x)(j = 1{\sim}4)$.

Five-point central symmetric scheme for first and second derivative with uniform grid length Δx is

$$f'(x_i) = \frac{f_{i-2} - 8f_{i-1} + 8f_{i+1} - f_{i+2}}{12\Delta x} + o(\Delta x^4)$$

$$f''(x_i) = \frac{-f_{i-2} + 16f_{i-1} - 30f_i + 16f_{i+1} - f_{i+2}}{12\Delta x^2} + o(\Delta x^4) \tag{2.57}$$

What is worth mentioning is that five-point uniform grid finite difference method works well for a lot of general cases. However, this approximation scheme cannot yield good prediction at the near boundary nodes if the function has large gradient there; besides, if the problem subjected

to harmonic type loads with very high frequencies, this scheme may also yield poor results for approximating the structure bending moment and shear force.

For RISER3D program, the riser deflection function, in an element domain, is a fifth-order polynomial function, whose second and third derivatives are cubic and quadratic functions. For instance, the one-dimensional beam deflection function, in the normalized local coordinate system, of the eth element can be expressed as

$$r^e(\xi) = \sum_{i=1}^{6} {u_i}^e J_i {\phi_i}^e(\xi) = A_{q5}\xi^5 + A_{q4}\xi^4 + A_{q3}\xi^3 + A_{q2}\xi^2 + A_{q1}\xi + A_{q0}$$

$$for\ \xi \in [0,1] \qquad (2.58)$$

where the constant coefficients are calculated by the following expressions using the obtained nodal primary variable vector $\{{u_1}^e \quad {u_2}^e \quad {u_3}^e \quad {u_4}^e \quad {u_5}^e \quad {u_6}^e\}^T$, here ${u_1}^e$ and ${u_4}^e$ denotes the nodal displacements, ${u_2}^e$ and ${u_5}^e$ denotes the nodal slopes, ${u_3}^e$ and ${u_6}^e$ denotes the nodal curvatures.

$$A_{q5} = -6{u_1}^e - 3h^e{u_2}^e - \frac{h^{e2}}{2}{u_3}^e + 6{u_4}^e - 3h^e{u_5}^e + \frac{h^{e2}}{2}{u_6}^e$$

$$A_{q4} = 15{u_1}^e + 8h^e{u_2}^e + \frac{3h^{e2}}{2}{u_3}^e - 15{u_4}^e + 7h^e{u_5}^e - h^{e2}{u_6}^e$$

$$A_{q3} = -10{u_1}^e - 6h^e{u_2}^e - \frac{3h^{e2}}{2}{u_3}^e + 10{u_4}^e - 4h^e{u_5}^e + \frac{h^{e2}}{2}{u_6}^e$$

$$A_{q2} = \frac{h^{e2}}{2}{u_3}^e$$

$$A_{q1} = h^e{u_2}^e$$

$$A_{q0} = {u_1}^e \qquad (2.59)$$

The slope of the beam for eth element can be calculated by

$$\frac{dr^e(s)}{ds} = \frac{1}{h^e}\frac{dr^e(\xi)}{d\xi} = \frac{1}{h^e}\left(5A_{q5}\xi^4 + 4A_{q4}\xi^3 + 3A_{q3}\xi^2 + 2A_{q2}\xi + A_{q1}\right) \qquad (2.60)$$

The bending moment of the beam for eth element can be calculated by

$$M^e(s) = -EI\frac{d^2r^e(s)}{ds^2} = -\frac{EI}{h^{e2}}\left(20A_{q5}\xi^3 + 12A_{q4}\xi^2 + 6A_{q3}\xi + 2A_{q2}\right) \quad (2.61)$$

The shear force of the beam for eth element can be calculated by

$$Q^e(s) = -EI\frac{d^3r^e(s)}{ds^3} = -\frac{EI}{h^{e3}}\left(60A_{q5}\xi^2 + 24A_{q4}\xi + 6A_{q3}\right) \quad (2.62)$$

where h^e denotes the e^{th} element length from equation (2.59) to (2.62)

Therefore, equations from (2.58) to (2.62) form a very effective and easy method for postprocessing the riser deflection, slope, bending moment and shear force. This method is called quintic Hermite interpolation method, the bending moment and shear force can be directly obtained by taking differentiations of the riser deflection function within an element domain.

3 VALIDITY BENCHMARK AND EFFECTIVENESS STUDY FOR RISER3D

3.1 Quintic Hermite Finite Element Model Formulation for Beam Problems

The governing equation of transverse deflection of one-dimensional Euler Bernoulli beam with length L, subject to static transverse loads, is a fourth order differential equation as

$$\frac{d^2}{dx^2}\left(EI\frac{d^2u}{dx^2}\right) + K_s u = q(x) \;\; x \in [0, L] \tag{3.1}$$

where E is modulus of elasticity of the beam material, I is the second moment of area, K_s is the elastic foundation stiffness if any, $q(x)$ is distributed transverse load and u is transverse deflection of Euler Bernoulli beam (the governed dependent variable), the global positive x direction is aligned with the axial center line of the beam.

For problems in solid mechanics, the weak formulation derivation can be either by principle of virtual work or by weighted residual method, i.e. by integration of the governing equation with weight functions. For the present study, the second one is adopted.

For weak form derivation for the differential equation (3.1), moving all terms to the left-hand-side and multiplying with the general quintic Hermite shape functions (in global coordinate system) as

$$\left[\frac{d^2}{dx^2}\left(EI\frac{d^2u}{dx^2}\right) + K_s u - q(x)\right] a_i(x) = 0 \;\; x \in [0, L] \tag{3.2}$$

Taking integration of equation (3.2) over a typical beam element domain $[x_a, x_b]$ and performing integration by parts three times, lead to weak form equation as

$$0 = \int_{x_a}^{x_b}\left[-\left(EI\frac{du}{dx}\right)a'''_i(x) + K_s u a_i(x) - q(x)a_i(x)\right]dx + \left[a_i(x)\frac{d}{dx}\left(EI\frac{d^2u}{dx^2}\right)\right]\Big|_{x_a}^{x_b} -$$

$$\left[a_i'(x)\left(EI\frac{d^2u}{dx^2}\right)\right]\Big|_{x_a}^{x_b} + \left[a_i''(x)\left(EI\frac{du}{dx}\right)\right]\Big|_{x_a}^{x_b} \tag{3.3}$$

where $a_i(x)$ $(i = 1\sim6)$ are the general quintic Hermite interpolation functions as presented in equation (2.6), and $a_i{}'(x)$, $a_i{}''(x)$, $a_i{}'''(x)$ are the first, second and third derivatives of the quintic Hermite shape functions respectively.

Three integrated terms in the weak form equation (3.3) are due to integration by parts three times, which correspond to three primary variable and secondary variable pairs as $\left(u, \frac{d}{dx}\left(EI\frac{d^2u}{dx^2}\right)\right)$, $\left(\frac{du}{dx}, EI\frac{d^2u}{dx^2}\right)$ and $\left(\frac{d^2u}{dx^2}, EI\frac{du}{dx}\right)$. Therefore, the essential (Dirichlet) boundary conditions involve the specification of the beam primary variables, i.e. the beam deflection u, the beam rotation angle $\frac{du}{dx}$ and the beam curvature $\frac{d^2u}{dx^2}$; the natural (Newman) boundary conditions involve the specification of the secondary variables, i.e. the beam shear force $\frac{d}{dx}\left(EI\frac{d^2u}{dx^2}\right)$, the beam bending moment $EI\frac{d^2u}{dx^2}$ and the beam slope $EI\frac{du}{dx}$. It is worth mentioning that the third natural boundary condition, which does not appear when cubic Hermite shape functions are adopted in traditional weak formulation. The physical meaning of this term is straightforward, it is the beam slope and can be denoted as $S(x) = EI\frac{du}{dx}$.

With the weak form equation (3.3), the generalized force vector , for the nth element, can be expressed as

$$f_i{}^n = -\left[a_i(x)\frac{d}{dx}\left(EI\frac{d^2u}{dx^2}\right)\right]\Big|_{x_a}^{x_b} + \left[a_i'(x)\left(EI\frac{d^2u}{dx^2}\right)\right]\Big|_{x_a}^{x_b} - \left[a_i''(x)\left(EI\frac{du}{dx}\right)\right]\Big|_{x_a}^{x_b} (i = 1\sim6) \tag{3.4}$$

The entries of the generalized force vector can be obtained by applying the quintic Hermite shape function properties, given in equation (2.8), to equation (3.4) as

$$f_1{}^n = -\left[a_1(x)\frac{d}{dx}\left(EI\frac{d^2u}{dx^2}\right)\right]\Big|_{x_a}^{x_b} + 0 + 0 = \frac{d}{dx}\left(EI\frac{d^2u}{dx^2}\right)\Big|_{x_a}$$

$$f_2{}^n = 0 + \left[a'_2(x)\left(EI\frac{d^2u}{dx^2}\right)\right]\Big|_{x_a}^{x_b} + 0 = -\left(EI\frac{d^2u}{dx^2}\right)\Big|_{x_a}$$

$$f_3{}^n = 0 + 0 - \left[a''_3(x)\left(EI\frac{du}{dx}\right)\right]\Big|_{x_a}^{x_b} = \left(EI\frac{du}{dx}\right)\Big|_{x_a}$$

$$f_4{}^n = -\left[a_4(x)\frac{d}{dx}\left(EI\frac{d^2u}{dx^2}\right)\right]\Big|_{x_a}^{x_b} + 0 + 0 = -\frac{d}{dx}\left(EI\frac{d^2u}{dx^2}\right)\Big|_{x_b}$$

$$f_5{}^n = 0 + \left[a'_5(x)\left(EI\frac{d^2u}{dx^2}\right)\right]\Big|_{x_a}^{x_b} + 0 = \left(EI\frac{d^2u}{dx^2}\right)\Big|_{x_b}$$

$$f_6{}^n = 0 + 0 - \left[a''_6(x)\left(EI\frac{du}{dx}\right)\right]\Big|_{x_a}^{x_b} = -\left(EI\frac{du}{dx}\right)\Big|_{x_b} \quad (3.5)$$

where the generalized force $f_1{}^n$ and $f_4{}^n$ denote the beam shear force of the nth element; $f_2{}^n$ and $f_5{}^n$ denote the beam bending moment of the nth element; $f_3{}^n$ and $f_6{}^n$ denote the beam slope of the nth element.

The function of the beam transverse deflection, for the nth element, can be approximated by employing general quintic Hermite shape functions as

$$u^n(x) \approx u_{ap}{}^n(x) = \sum_{j=1}^{6} u_j{}^n a_j\,(x)\; for\; (j = 1{\sim}6) \quad (3.6)$$

Substituting equation (3.6) into the beam weak form equation (3.3), we obtain

$$\int_{x_a}^{x_b}\left[-\left(EI\frac{d(\sum_{j=1}^{6} u_j{}^n a_j(x))}{dx}\right)a'''_i(x) + K_s\left(\sum_{j=1}^{6} u_j{}^n a_j\,(x)\right)a_i(x) - q(x)a_i(x)\right]dx = f_i{}^n \quad (3.7)$$

Further simplification of equation (3.7) can yield the nth element finite element model, using quintic Hermite shape functions, for prismatic Euler Bernoulli beams as

$$\sum_{j=1}^{6} K_{ij}{}^n u_j{}^n = f_i{}^n + q_i{}^n\;(i = 1{\sim}6) \quad (3.8)$$

where the beam element stiffness matrix and the external transverse load vector can be expressed as follow

$$K_{ij}{}^n = \int_{x_a}^{x_b}\left[-EIa'''_i(x)a'_j(x) + K_s a_i(x)a_j(x)\right]dx \quad (3.9)$$

$$q_i{}^n = \int_{x_a}^{x_b} [q(x)a_i(x)]dx \tag{3.10}$$

By incorporating the Jacobian transformation coefficient, as defined in equation (2.7), the beam element stiffness matrix integration can be transformed from the global coordinate system to the normalized local coordinate system as

$$K_{ij}{}^n = \int_{x_a}^{x_b} \left[-EIa'''_i(x)a'_j(x) + K_s a_i(x)a_j(x)\right]dx = \int_0^1 \left[-EIa'''_i(\xi)\frac{J_i}{(h^n)^3}a'_j(\xi)\frac{J_j}{h^n} + K_s J_i J_j a_i(\xi)a_j(\xi)\right] h^n \, d\xi = -\frac{EI}{(h^n)^3}J_i J_j \alpha_{ij} + K_s h^n J_i J_j \eta_{ij} \tag{3.11}$$

where $\xi = \frac{x-x_a}{h^n}$ and h^n is the element length of the nth beam element.

By plugging in the analytical results of coefficient matrices of α_{ij} and η_{ij}, the stiffness matrix of the Euler-Bernoulli beam using quintic Hermite shape functions becomes

$$K_{ij}{}^n = -\frac{1}{70}\frac{EI}{h^{n3}}J_i J_j \begin{bmatrix} -1200 & -600 & -30 & 1200 & -600 & 30 \\ -600 & -384 & -22 & 600 & -216 & 8 \\ -30 & -92 & -6 & 30 & -8 & -1 \\ 1200 & 600 & 30 & -1200 & 600 & -30 \\ -600 & -216 & -8 & 600 & -384 & 22 \\ 30 & 8 & -1 & -30 & 92 & -6 \end{bmatrix} + \frac{1}{55440} K_s J_i J_j \begin{bmatrix} 21720 & 3732 & 281 & 6000 & -1812 & 181 \\ 3732 & 832 & 69 & 1812 & -532 & 52 \\ 281 & 69 & 6 & 181 & -52 & 5 \\ 6000 & 1812 & 181 & 21720 & -3732 & 281 \\ -1812 & -532 & -52 & -3732 & 832 & -69 \\ 181 & 52 & 5 & 281 & -69 & 6 \end{bmatrix} \tag{3.12}$$

where the stiffness matrix is unsymmetrical although it looks like symmetrical at first glance, analyst should pay attention to this point during programming using quintic Hermite shape functions because it cannot be stored or manipulated as symmetrical stiffness matrices.

The evaluation of the distributed load vector in equation (3.10) can also be changed from global coordinate system to normalized local coordinate system as

$$q_i{}^n = \int_{x_a}^{x_b} [q(x)a_i(x)]dx = \int_0^1 [q(\xi)J_i a_i(\xi)]h^n d\xi = J_i \, h^n \int_0^1 q(\xi)a_i(\xi)d\xi \tag{3.13}$$

For instance, if a case $q(\xi) = q_0$, i.e. the load is uniformly distributed, the force vector can be evaluated as

$$q_i{}^n = J_i h^n q_0 \int_0^1 a_i(\xi) d\xi = J_i h^n q_0 \mu_i = \frac{J_i h^n q_0}{120} \{60 \quad 12 \quad 1 \quad 60 \quad -12 \quad 1\}^T \quad (3.14)$$

where the superscript symbol ' ^{T} ' denotes the transpose of a vector or matrix in this dissertation.

3.2 Analytical Solutions of Euler-Bernoulli Beam Problems

3.2.1 Euler-Bernoulli Beam Subject to Static Transverse Load

3.2.1.1 Static Polynomial Distributed Load

For a one-dimensional prismatic Euler-Bernoulli beam, i.e. EI is a constant, with its axial direction oriented in positive x-axis, subjected to distributed polynomial load transversely, the governing equation is a fourth order differential equation as

$$EIu''''(x) = q_0 \left(\frac{x}{L}\right)^n \ (for\ x \in [0, L]) \quad (3.15)$$

where EI is the beam bending rigidity, q_0 is a constant indicating the magnitude of the distributed load intensity, L is the length of the beam, n is an integer indicates the order of the polynomial for loads (for instance, if $n = 0$, the beam is subjected to uniform load; if $n = 1$, the beam is subjected to linearly distributed load), $u(x)$ is the transverse deflection of the beam.

Performing integration of equation (3.15) with respect to x once yields beam shear force as

$$Q(x) = EIu'''(x) = q_0 \frac{L}{n+1} \left(\frac{x}{L}\right)^{n+1} + C_1 \quad (3.16)$$

Performing integration of equation (3.15) with respect to x twice yields beam bending moment as

$$M(x) = EIu''(x) = q_0 \frac{L^2}{(n+1)(n+2)} \left(\frac{x}{L}\right)^{n+2} + C_1 x + C_2 \quad (3.17)$$

Performing integration of equation (3.15) with respect to x three times yields beam slope as

$$S(x) = EIu'(x) = q_0 \frac{L^3}{(n+1)(n+2)(n+3)} \left(\frac{x}{L}\right)^{n+3} + C_1 \frac{x^2}{2} + C_2 x + C_3 \tag{3.18}$$

Performing integration of equation (3.15) with respect to x four times yields beam transverse deflection as

$$EIu(x) = q_0 \frac{L^4}{(n+1)(n+2)(n+3)(n+4)} \left(\frac{x}{L}\right)^{n+4} + C_1 \frac{x^3}{6} + C_2 \frac{x^2}{2} + C_3 x + C_4 \tag{3.19}$$

where the constant q_0 is the load magnitude coefficient, C_i $(i = 1 \sim 4)$ are unknown integration constants which should be determined according to the four boundary conditions of the beam at both ends.

There are many possible boundary condition combinations for Euler-Bernoulli beams, for simplicity, this research is only focused on addressing problems of three types of commonly-used Euler Bernoulli beams in engineering field, i.e. simply supported beam, cantilever beam (fixed-free beam) and fixed-fixed beam hereafter, for both static analysis or dynamic analysis.

For the simply supported beam case, the boundary conditions are shown in Figure 3.1 in global coordinate system.

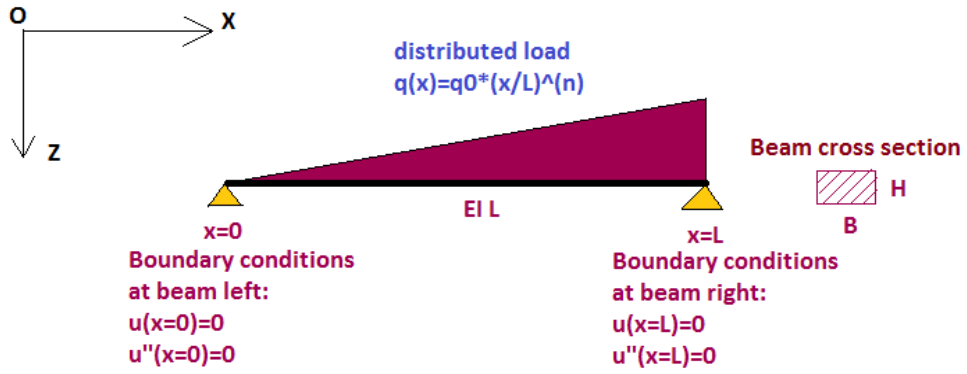

Figure 3.1 Schematic of boundary conditions for a simply supported beam

By imposing the simply supported beam boundary conditions, as shown in Figure 3.1, onto equation (3.17) and (3.19), the unknown constants C_2 and C_4 can be easily determined to be zeros, and the remaining unknown constants C_1 and C_3 can be calculated using equation (3.20) and (3.21) as

$$C_1 = -\frac{q_0 L}{(n+1)(n+2)} \tag{3.20}$$

$$C_3 = -\frac{q_0 L^3}{(n+1)(n+2)(n+3)(n+4)} + \frac{q_0 L^3}{6(n+1)(n+2)} = \frac{q_0 L^3 (n^2+7n+6)}{6(n+1)(n+2)(n+3)(n+4)} \tag{3.21}$$

When the polynomial order index n for loads in equation (3.15) is designated to different values, the result of the integration constants C_1 C_3 are summarized in Table 3.1.

Table 3.1 Integration constants for a simply supported beam

Value of n	**Distributed load type**	C_1		C_2	C_3	C_4
0	Constant	$-\frac{q_0 L}{2}$		0	$\frac{q_0 L^3}{24}$	0
1	Linear	$-\frac{q_0 L}{6}$		0	$\frac{7 q_0 L^3}{360}$	0
2	Quadratic	$-\frac{q_0 L}{12}$		0	$\frac{q_0 L^3}{90}$	0
3	Cubic	$-\frac{q_0 L}{20}$		0	$\frac{q_0 L^3}{140}$	0
5	Quintic	$-\frac{q_0 L}{42}$		0	$\frac{11 q_0 L^3}{3024}$	0
7	Septic	$-\frac{q_0 L}{72}$		0	$\frac{13 q_0 L^3}{5940}$	0

For the cantilever beam case, the boundary conditions of the beam are shown in Figure 3.2.

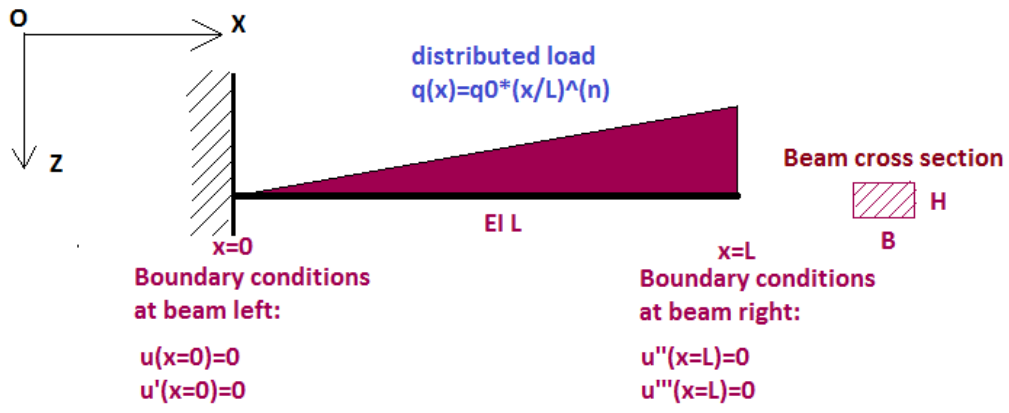

Figure 3.2 Schematic of boundary conditions for a cantilever beam

By applying the boundary conditions, as shown in Figure 3.2, to equation (3.18) and (3.19), both the constants C_3 and C_4 can be easily determined to be zeros, and the remaining constants C_1 and C_2 can be evaluated using equation (3.22) and (3.23) as

$$C_1 = -\frac{q_0 L}{n+1} \tag{3.22}$$

$$C_2 = -\frac{q_0 L^2}{(n+1)(n+2)} + \frac{q_0 L^2}{n+1} = \frac{q_0 L^2}{n+2} \tag{3.23}$$

When the polynomial order n in equation (3.15) is designated to different values, the result of the integration constants $C_1$and C_2 are summarized in Table 3.2 for the cantilever beam case.

Table 3.2 Integration constants for a cantilever beam

Value of n	**Distributed load type**	C_1	C_2	C_3	C_4
0	Constant	$-q_0 L$	$\frac{q_0 L^2}{2}$	0	0
1	Linear	$-\frac{q_0 L}{2}$	$\frac{q_0 L^2}{3}$	0	0
2	Quadratic	$-\frac{q_0 L}{3}$	$\frac{q_0 L^2}{4}$	0	0
3	Cubic	$-\frac{q_0 L}{4}$	$\frac{q_0 L^2}{5}$	0	0
5	Quintic	$-\frac{q_0 L}{6}$	$\frac{q_0 L^2}{7}$	0	0
7	Septic	$-\frac{q_0 L}{8}$	$\frac{q_0 L^2}{9}$	0	0

For the fixed-fixed beam case, the boundary conditions of the beam are shown in Figure 3.3 below.

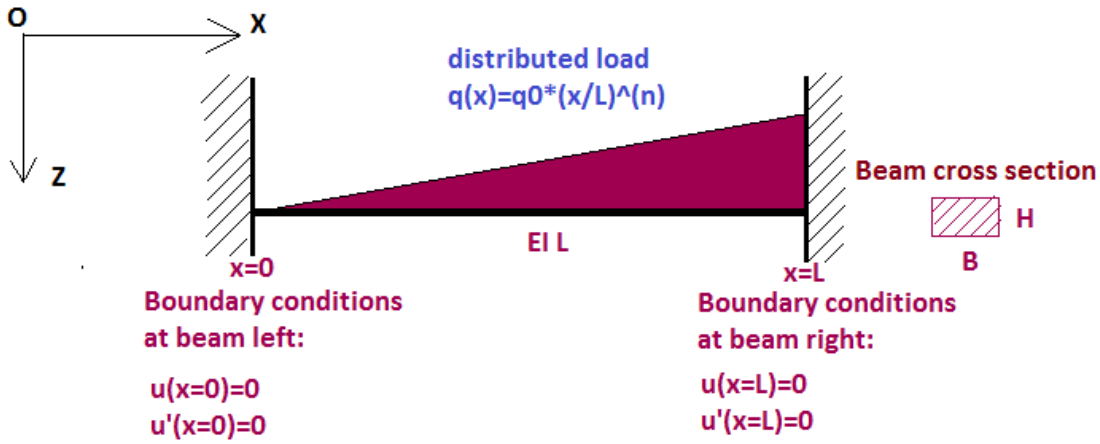

Figure 3.3 Schematic of boundary conditions for a fixed-fixed beam

By applying the boundary conditions, as shown in Figure 3.3, to equation (3.18) and (3.19), the constants C_3 and C_4 can be easily determined as zeros, and the remaining constants C_1 and C_2 can be computed by using equation (3.24) as

$$\begin{cases} C_1 = \frac{-6A_n+12B_n}{L} \\ C_2 = 2A_n - 6B_n \end{cases} \tag{3.24}$$

where the constants $A_n = \frac{q_0 L^2}{(n+1)(n+2)(n+3)}$, $B_n = \frac{q_0 L^2}{(n+1)(n+2)(n+3)(n+4)}$

When the polynomial order n in equation (3.15) is designated to different values, the result of the integration constants $C_1$and C_2 are shown in Table 3.3 for the fixed-fixed beam case.

Table 3.3 Integration constants for a fixed-fixed beam

Value of n	**Distributed load type**	C_1	C_2	C_3	C_4
0	Constant	$-\frac{q_0 L}{2}$	$\frac{q_0 L^2}{12}$	0	0
1	Linear	$-\frac{3q_0 L}{20}$	$\frac{q_0 L^2}{30}$	0	0
2	Quadratic	$-\frac{q_0 L}{15}$	$\frac{q_0 L^2}{60}$	0	0
3	Cubic	$-\frac{q_0 L}{28}$	$\frac{q_0 L^2}{105}$	0	0
5	Quintic	$-\frac{q_0 L}{72}$	$\frac{q_0 L^2}{252}$	0	0
7	Septic	$-\frac{3q_0 L}{440}$	$\frac{q_0 L^2}{495}$	0	0

Hence, for different types of Euler Bernoulli beams subject to nth degree polynomial load, by substitution of the results of the integration constants $C_1 \sim C_4$, summarized in the above three tables, back into equations (3.16-3.19), the analytical solutions for the beam shear force, bending moment, slope and deflection can be eventually obtained.

3.2.1.2 Static Sinusoidal Distributed Load

For a one-dimensional prismatic Euler-Bernoulli beam subjected to a transverse sinusoidal distributed load, the governing equation of the beam is a fourth order differential equation of

$$EIu''''(x) = q_0 sin\left(\frac{n\pi x}{L}\right) \ (for \text{ n} = 1,2,3,\dots;\ x \in [0, L]) \tag{3.25}$$

where EI is the beam bending rigidity, q_0 is a constant of the sinusoidal load amplitude, L is the length of the beam, n is an integer indicates the shape of the sinusoidal load and the axial direction of the beam points in positive global x-axis.

Taking integration of equation (3.25) with respect to x once yields beam shear force as

$$Q(x) = EIu'''(x) = -q_0 \frac{L}{n\pi} \cos\left(\frac{n\pi x}{L}\right) + C_1 \tag{3.26}$$

Taking integration of equation (3.25) with respect to x twice yields beam bending moment as

$$M(x) = EIu''(x) = -q_0 \left(\frac{L}{n\pi}\right)^2 \sin\left(\frac{n\pi x}{L}\right) + C_1 x + C_2 \tag{3.27}$$

Taking integration of equation (3.25) with respect to x three times yields beam slope as

$$S(x) = EIu'(x) = q_0 \left(\frac{L}{n\pi}\right)^3 \cos\left(\frac{n\pi x}{L}\right) + C_1 \frac{x^2}{2} + C_2 x + C_3 \tag{3.28}$$

Taking integration of equation (3.25) with respect to x four times yields beam transverse deflection as

$$EIu(x) = q_0 \left(\frac{L}{n\pi}\right)^4 \sin\left(\frac{n\pi x}{L}\right) + C_1 \frac{x^3}{6} + C_2 \frac{x^2}{2} + C_3 x + C_4 \tag{3.29}$$

For a simply supported beam case, by implementation of boundary conditions through equation (3.26) to (3.29), the four unknown integration constants can be easily determined as

$$C_1 = C_2 = C_3 = C_4 = 0 \tag{3.30}$$

Similarly, for a cantilever beam case and a fixed-fixed beam case, after implementation of the boundary conditions, the expressions of the four unknown integration constants can be solved out and summarized as shown in equation (3.31) and (3.32) respectively.

$$\begin{cases} C_1 = q_0 \frac{L}{n\pi} \ (for\ n = 2,4,6\ldots);\ C_1 = -q_0 \frac{L}{n\pi} \ (for\ n = 1,3,5\ldots) \\ C_2 = -q_0 \frac{L^2}{n\pi} \ (for\ n = 2,4,6\ldots);\ C_2 = q_0 \frac{L^2}{n\pi} \ (for\ n = 1,3,5\ldots) \\ C_3 = -q_0 \left(\frac{L}{n\pi}\right)^3 \quad (for\ n = 1,2,3,\ldots) \\ C_4 = 0 \quad (for\ n = 1,2,3,\ldots) \end{cases} \tag{3.31}$$

$$\begin{cases} C_1 = -\frac{12q_0}{L^2}\left(\frac{L}{n\pi}\right)^3 \ (for\ n = 2,4,6\ldots);\ C_1 = 0 \quad (for\ n = 1,3,5\ldots) \\ C_2 = \frac{6q_0}{L}\left(\frac{L}{n\pi}\right)^3 \ (for\ n = 2,4,6\ldots);\ C_2 = \frac{2q_0}{L}\left(\frac{L}{n\pi}\right)^3 \ (for\ n = 1,3,5\ldots) \\ C_3 = -q_0 \left(\frac{L}{n\pi}\right)^3 \quad (for\ n = 1,2,3,\ldots) \\ C_4 = 0 \quad (for\ n = 1,2,3,\ldots) \end{cases} \tag{3.32}$$

Therefore, for the three different types of Euler Bernoulli beams mentioned above, by substitution of the results of the integration constants $C_1 \sim C_4$ back into equations (3.26-3.29), the analytical solutions for the beam shear force, bending moment, slope and deflection can be definitely obtained.

3.2.2 Euler-Bernoulli Beam Subject to Dynamic Transverse Loads

Now considering the transversal vibration of a prismatic Euler-Bernoulli beam (EI =constant) excited by a distributed transverse dynamic force $q(x,t)$, the governing motion equation of the beam can be expressed as

$$\rho A \frac{\partial^2 y(x,t)}{\partial t^2} + EI \frac{\partial^4 y(x,t)}{\partial x^4} = q(x,t) \ (x \in [0,L]) \tag{3.33}$$

where E is modulus of elasticity of the beam material, I is the second moment of area about y-axis of the beam, ρ is the density of the beam material, A is the beam cross-sectional area, $q(x,t)$ is distributed transverse dynamic load and $y(x,t)$ denotes transverse deflection of the beam in space and time, L is the total length of the beam and the axial direction of the beam points in positive global x-axis.

The homogeneous form of equation (3.33) can be obtained by omitting the external load term, i.e. $q(x,t) = 0$, which can be written as

$$\rho A \frac{\partial^2 y(x,t)}{\partial t^2} + EI \frac{\partial^4 y(x,t)}{\partial x^4} = 0 \tag{3.34}$$

By using the separation of variables approach, the solution of the homogenous equation can be assumed in form of $y^h(x,t) = X(x)\varphi(t)$. Substituting $y^h(x,t)$ into the equation (3.34) leads to

$$\rho A X \frac{d^2 \varphi}{dt^2} + EI\varphi \frac{d^4 X}{dx^4} = 0 \tag{3.35}$$

Equation (3.35) can be further decomposed into two isolated equations by separation of variables, one is a function in time t and the other one is a function in space x, as

$$\frac{d^2 \varphi}{dt^2} + {\omega_n}^2 \varphi = 0 \tag{3.36}$$

$$EI \frac{d^4 X}{dx^4} - \rho A {\omega_n}^2 X = 0 \tag{3.37}$$

By solving these two separated equations mathematically, the general form of the solution for equation (3.36) is

$$\varphi(t) = A cos(\omega_n t) + B sin(\omega_n t) \tag{3.38}$$

where A and B are unknown constants which should be determined by initial conditions, ω_n is the nth mode natural frequency of the beam.

The general form of the solution for equation (3.37) can be written as

$$X(x) = C[\cos(\alpha x) + \cosh(\alpha x)] + D[\cos(\alpha x) - \cosh(\alpha x)]$$
$$+E[\sin(\alpha x) + \sinh(\alpha x)] + F[\sin(\alpha x) - \sinh(\alpha x)] \tag{3.39}$$

where C, D, E, F are four unknown constants which should be determined by specific boundary conditions, α are constants related to the natural frequencies by equation

$$\alpha^4 = \frac{\rho A {\omega_n}^2}{EI} \tag{3.40}$$

As mentioned early, this research only focuses on three types of Euler Bernoulli beams, i.e. the simply supported beam, fixed-free cantilever beam and fixed-fixed beam. The boundary conditions for these three scenarios can be summarized as

Scenarios 1, Simply supported beam boundary conditions:

$$X(0) = X''(0) = 0$$

$$X(L) = X''(L) = 0 \tag{3.41}$$

Scenarios 2, Fixed-free cantilever beam boundary conditions:

$$X(0) = X'(0) = 0$$

$$X''(L) = X'''(L) = 0 \tag{3.42}$$

Scenarios 3, Fixed-fixed beam boundary conditions:

$$X(0) = X'(0) = 0$$

$$X(L) = X'(L) = 0 \tag{3.43}$$

Now taking the first, second and third derivatives of the general solution function $X(x)$ with respect to x respectively, the following three expressions can be obtained straightforwardly

$$\begin{aligned}
X'(x) = \alpha[&C(-\sin(\alpha x) + \sinh(\alpha x)) + D(-\sin(\alpha x) - \sinh(\alpha x)) + E(\cos(\alpha x) + \cosh(\alpha x)) \\
&+ F(\cos(\alpha x) - \cosh(\alpha x))] \\
X''(x) = \alpha^2[&C(-\cos(\alpha x) + \cosh(\alpha x)) + D(-\cos(\alpha x) - \cosh(\alpha x)) \\
&+ E(-\sin(\alpha x) + \sinh(\alpha x)) + F(-\sin(\alpha x) - \sinh(\alpha x))] \\
X'''(x) = \alpha^3[&C(\sin(\alpha x) + \sinh(\alpha x)) + D(\sin(\alpha x) - \sinh(\alpha x)) + E(-\cos(\alpha x) + \cosh(\alpha x)) \\
&+ F(-\cos(\alpha x) - \cosh(\alpha x))]
\end{aligned} \tag{3.44}$$

To solve the dynamic response $X(x)$ of the forced vibration of a Euler-Bernoulli beam in space, now considering equation (3.37) as an eigenvalue problem of (Some steps of the following

derivations in section 3.2.2 have mainly followed the work by Timoshenko, 1974. Readers can also find solutions of transverse vibrations of prismatic beams in the chapter 5 of his book.)

$$X'''' - \frac{\rho A \omega^2}{EI} X = X'''' - \alpha^4 X = 0 \tag{3.45}$$

By letting $\lambda = \alpha^4$ and taking the two distinct subscripts n and m into consideration, where n and m are two integers, we have

$$X_n{}'''' = \lambda_n X_n \, (for\ mode\ n) \tag{3.46}$$

$$X_m{}'''' = \lambda_m X_m \, (for\ mode\ m) \tag{3.47}$$

If multiplying equation (3.46) by X_m and equation (3.47) by X_n and performing integration over the domain of the beam, i.e. from 0 to the beam length L, we can reach

$$\int_0^L X_n{}'''' \, X_m \, dx = \lambda_n \int_0^L X_n \, X_m \, dx \, (for\ mode\ n) \tag{3.48}$$

$$\int_0^L X_m{}'''' \, X_n \, dx = \lambda_m \int_0^L X_m \, X_n \, dx (for\ mode\ m) \tag{3.49}$$

Integrating by parts twice for the left-hand sides of equation (3.48) and (3.49) respectively leads to

$$(X_n{}''' X_m) \Big|_0^L - (X_n{}'' X'_m) \Big|_0^L + \int_0^L X_n{}'' \, X''_m \, dx = \lambda_n \int_0^L X_n \, X_m \, dx \, (for\ mode\ n) \tag{3.50}$$

$$(X_m{}''' X_n) \Big|_0^L - (X_m{}'' X'_n) \Big|_0^L + \int_0^L X_m{}'' \, X''_n \, dx = \lambda_m \int_0^L X_m \, X_n \, dx (for\ mode\ m) \tag{3.51}$$

For all the three types of beams considered in this research, by applying the boundary conditions summarized in equation (3.41) to equation (3.43), it is easy to find out that the integrated terms in equation (3.50) and (3.51) are all zeros. Thus, the following relationship holds by subtracting of equation (3.51) from equation (3.50)

$$(\lambda_n - \lambda_m) \int_0^L X_n \, X_m \, dx = 0 \tag{3.52}$$

If $n \neq m$, the eigenvalues $\lambda_n \neq \lambda_m$, an orthogonality relationship holds between the normal response functions, for three scenarios considered, as

$$\int_0^L X_n X_m \, dx = 0 \; (for \; n \neq m) \tag{3.53}$$

Besides, another two orthogonality relationships also hold straightforwardly as

$$\int_0^L {X_n}'''' X_m \, dx = \int_0^L {X_n}'' {X''}_m \, dx = \lambda_n \int_0^L X_n X_m \, dx = 0 \; (for \; n \neq m \,) \tag{3.54}$$

If $n = m$, the integral in equation (3.52) can be an arbitrary constant, say C_n. Usually, the mode shapes are normalized to make $C_n = 1.0$, i.e.

$$\int_0^L {X_n}^2 \, dx = C_n = 1 \tag{3.55}$$

Hence, the following functions hold

$$\int_0^L {X_n}'''' X_n \, dx = \int_0^L {X_n}''^2 \, dx = \lambda_n \int_0^L {X_n}^2 \, dx = \lambda_n = {\alpha_n}^4 \;\; (for \; n = m \,) \tag{3.56}$$

Considering the homogenous form of the Euler-Bernoulli beam motion equation (3.34), the homogenous solution can be superimposed in terms of the mode shape functions $X_n(x)$ and time functions φ_n(t), i.e.

$$y^h(x,t) = \sum_{n=1}^{\infty} X_n(x)[A_n cos(\omega_n t) + B_n sin(\omega_n t)] \;\; (for \; n = 1,2,3, \dots, \infty) \tag{3.57}$$

The constants A_n and B_n can be easily derived using the orthogonality relationship equation (3.55) together with the beam initial conditions. For instance, if assuming the initial transverse displacement and velocity of a beam as given functions $u_0(x)$ and $v_0(x)$ respectively, i.e.

$$y^h(x,0) = \sum_{n=1}^{\infty} A_n X_n(x) = u_0(x)$$

$$\dot{y}^h(x,0) = \sum_{n=1}^{\infty} \omega_n B_n X_n(x) = v_0(x) \tag{3.58}$$

By using the orthogonality relationship, the constants A_n and B_n can be easily figured out as

$$A_n = \int_0^L u_0(x) X_n(x) \, dx$$

$$B_n = \frac{1}{\omega_n} \int_0^L v_0(x) X_n(x) \, dx \tag{3.59}$$

As for the non-homogenous form of the Euler-Bernoulli beam motion equation (3.33), the general solution can be assumed in form of

$$y(x,t) = \sum_{n=1}^{\infty} X_n(x)\varphi_n(\mathrm{t}) \ \ (for\ n = 1,2,3,\dots,\infty) \tag{3.60}$$

Substitution of the solution equation (3.60) into equation (3.33), we can have

$$\sum_{n=1}^{\infty}[\rho A X_n(x)\ddot{\varphi}_n(t) + EI{X_n}''''(x)\varphi_n(\mathrm{t})] = q(x,t) \quad (x \in [0,L]) \tag{3.61}$$

Multiplying this equation by normal function $X_m(x)$ and integrating over the whole domain of the beam, leads to

$$\sum_{n=1}^{\infty}\int_0^L [\rho A X_n(x)\ddot{\varphi}_n(t) + EI{X_n}''''(x)\varphi_n(\mathrm{t})]\, X_m(x)dx = \int_0^L q(x,t)X_m(x)dx \quad (x \in [0,L]) \tag{3.62}$$

By implementation of the orthogonality properties, as presented in equation (3.54), of the beam normal functions to this equation, the non-homogenous motion equation can be transformed into a form of

$$\ddot{\varphi}_n(t) + \lambda_n \frac{EI}{\rho A}\varphi_n(\mathrm{t}) = \int_0^L \frac{q(x,t)}{\rho A} X_n(x)dx \quad (x \in [0,L]) \tag{3.63}$$

By incorporation the relationship of $\lambda_n = {\alpha_n}^4 = \frac{\rho A {\omega_n}^2}{EI}$, the non-homogenous motion equation of the beam can be further simplified as

$$\ddot{\varphi}_n(t) + {\omega_n}^2\varphi_n(\mathrm{t}) = \int_0^L \bar{q}(x,t)X_n(x)dx \quad (x \in [0,L]) \tag{3.64}$$

where $\bar{q}(x,t) = q(x,t)/\rho A$.

The transverse response of the nth mode can be found by applying the Duhamel integral as

$$\varphi_n(\mathrm{t}) = \frac{1}{\omega_n}\int_0^L X_n(x)\int_0^t \bar{q}(x,\tau)\sin(\omega_n(t-\tau))d\tau dx \tag{3.65}$$

Hence, the total transverse response of the beam deflection under excitation can be expressed as

$$y(x,t) = \sum_{n=1}^{\infty}\frac{X_n(x)}{\omega_n}\int_0^L X_n(x)\int_0^t \bar{q}(x,\tau)\sin(\omega_n(t-\tau))d\tau dx \ \ (for\ n = 1,2,3,\dots,\infty) \tag{3.66}$$

3.2.2.1 Transverse Vibration of Simply Supported Beams

Implementation of the left end boundary conditions, the first relationship of equation (3.41), onto the beam general form of solution in equation (3.39) leads to

$$X(0) = C \cdot 2 + D \cdot 0 + E \cdot 0 + F \cdot 0 = 0$$

$$X''(0) = \alpha^2 C \cdot 0 + \alpha^2 D \cdot (-2) + \alpha^2 E \cdot 0 - \alpha^2 F \cdot 0 = 0 \tag{3.67}$$

Thus, for a simply supported beam, the unknow constants C and D can be determined as $C = D = 0$.

Implementation of the right end boundary conditions, the second relationship of equation (3.41), onto the beam general form of solution in equation (3.39) results in

$$X(L) = E\big(sin(\alpha L) + sinh(\alpha L)\big) + F\big(sin(\alpha L) - sinh(\alpha L)\big) = 0$$

$$X''(L) = \alpha^2 E\big(-sin(\alpha L) + sinh(\alpha L)\big) + \alpha^2 F\big(-sin(\alpha L) - sinh(\alpha L)\big) = 0 \tag{3.68a}$$

Rewriting these two equations in equation (3.68a) into a compact matrix form as

$$\begin{bmatrix} sin(\alpha L) + sinh(\alpha L) & sin(\alpha L) - sinh(\alpha L) \\ -sin(\alpha L) + sinh(\alpha L) & -sin(\alpha L) - sinh(\alpha L) \end{bmatrix} \begin{Bmatrix} E \\ F \end{Bmatrix} = \begin{Bmatrix} 0 \\ 0 \end{Bmatrix} \tag{3.68b}$$

For achieving a nontrivial solution, the determinant of the coefficient matrix in equation (3.68b) must be equal to zero, which requires that

$$sin(\alpha L) sinh(\alpha L) = 0 \tag{3.69}$$

Considering $\alpha L \neq 0$, hence $sinh(\alpha L) \neq 0$. The only possible condition satisfying equation (3.69) is that

$$sin(\alpha L) = 0 \tag{3.70}$$

Equation (3.70) is the, so called, frequency equation for transverse vibration of a simply supported beam. Obviously, there are infinite solutions to the frequency equation due to the periodical property of sine function, i.e.

$$\alpha L = n\pi \ (n = 1,2,3, \dots, \infty) \tag{3.71}$$

Therefore, the following relationships hold for the simply supported beam case

$$\alpha_n{}^4 = \frac{\rho A \omega_n{}^2}{EI} = \left(\frac{n\pi}{L}\right)^4 \tag{3.72}$$

Finally, the natural frequencies of the simply supported Euler Bernoulli beam can be expressed as

$$\omega_n = \sqrt{\frac{EI}{\rho A}}\left(\frac{n\pi}{L}\right)^2 \tag{3.73}$$

The normal response function of the simply supported Euler Bernoulli beam can be further simplified as

$$X(x) = E(sin\alpha x + sinh\alpha x) + E(sin\alpha x - sinh\alpha x) = 2Esin\alpha x = 2Esin\left(\frac{n\pi x}{L}\right) \tag{3.74}$$

By incorporating the orthogonality property, as shown in function (3.55), to normalize the expression for the function $X(x)$, we have

$$2E = \left(\frac{2}{L}\right)^{0.5} \tag{3.75}$$

Therefore, we can eventually obtain the nth mode normal function for the transverse vibration of a simply supported Euler-Bernoulli beam as

$$X_n = \left(\frac{2}{L}\right)^{0.5} sin\left(\frac{n\pi x}{L}\right) \tag{3.76}$$

First dynamic case for a simply supported beam:

For the first dynamic case of a simply-supported beam, let us consider a transversal dynamic load in form of $q(x,t) = f_0 sin\frac{n^*\pi x}{L}\sin(\omega t)$ $(for\ n^* = 1,3,5,7,9)$, where f_0 is an arbitrary given constant which indicates the load amplitude, ω is a given excitation frequency. By utilizing Duhamel integral as shown in equation (3.65), the nth mode response function can be obtained as

$$\varphi_n(\mathrm{t}) = \frac{1}{\omega_n}\int_0^L X_n(x)\int_0^t \frac{f_0 sin\frac{n^*\pi x}{L}\sin(\omega\tau)}{\rho A}\sin(\omega_n(t-\tau))d\tau dx = \frac{f_0}{\rho A{\omega_n}^2}\mathrm{H}_n(\omega)\left[\sin(\omega t) - \frac{\omega}{\omega_n}\sin(\omega_n t)\right]\int_0^L X_n(x) sin\frac{n^*\pi x}{L}dx \quad (3.77)$$

The total transverse dynamic response of the beam deflection can be computed using equation (3.66) as

$$y(x,t) = \sum_{n=1}^{\infty} X_n(x)\frac{f_0}{\rho A{\omega_n}^2}\mathrm{H}_n(\omega)\left[\sin(\omega t) - \frac{\omega}{\omega_n}\sin(\omega_n t)\right]\int_0^L X_n(x) sin\frac{n^*\pi x}{L}dx =$$

$$sin\left(\frac{n^*\pi x}{L}\right)\frac{f_0}{\rho A{\omega_{n^*}}^2}\mathrm{H}_{n^*}(\omega)\left[\sin(\omega t) - \frac{\omega}{\omega_{n^*}}\sin(\omega_{n^*} t)\right] \quad (\text{for } n^* = 1,3,5,7,9) \quad (3.78)$$

In equation (3.78), $\mathrm{H}_{n^*}(\omega) = \frac{1}{1-\omega^2/{\omega_{\mathrm{n}^*}}^2}$ is called the n^{*th} mode magnification factor, the plotting of which against excitation to natural frequency ratio is shown in Figure 3.4.

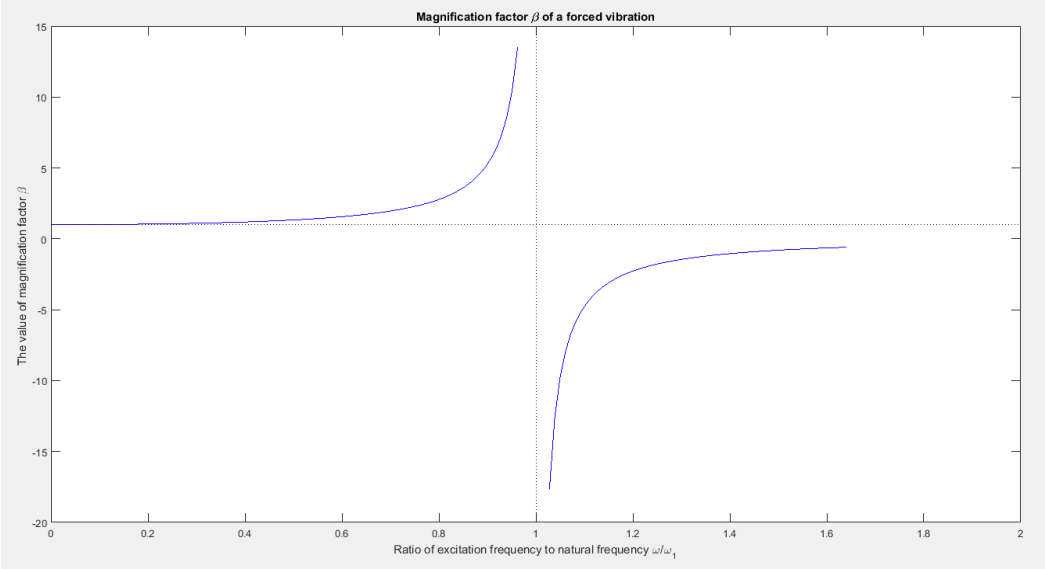

Figure 3.4 The magnification factor of a forced vibration

From Figure 3.4, it can be seen that when the ration of excitation frequency to the dominant natural beam frequency ω_1 approaches unity form left hand side, the amplitude of the response in

equation (3.62) will be amplified to positive infinity $+\infty$, while the frequency ratio approaches unity form the right hand side, the amplitude of the response in equation (3.62) will be amplified to negative infinity $-\infty$. If the frequency ratio equals to unity, the amplitude of the particular solution is infinity, which is known as the phenomenon of resonance for structural vibrations in engineering.

The dynamic response of the beam bending moment can be calculated by

$$M(x,t) = -EIy''(x,t) = EI\left(\frac{n^*\pi}{L}\right)^2 sin\left(\frac{n^*\pi x}{L}\right)\frac{f_0}{\rho A{\omega_{n^*}}^2}\mathrm{H}_{n^*}(\omega)\left[\sin(\omega t) - \frac{\omega}{\omega_{n^*}}\sin(\omega_{n^*}t)\right] (\text{for } n^* = 1,3,5,7,9) \quad (3.79)$$

The dynamic response of the beam shear force can be calculated by

$$V(x,t) = -EIy'''(x,t) = EI\left(\frac{n^*\pi}{L}\right)^3 cos\left(\frac{n^*\pi x}{L}\right)\frac{f_0}{\rho A{\omega_{n^*}}^2}\mathrm{H}_{n^*}(\omega)\left[\sin(\omega t) - \frac{\omega}{\omega_{n^*}}\sin(\omega_{n^*}t)\right] (\text{for } n^* = 1,3,5,7,9) \quad (3.80)$$

Second dynamic case for a simply supported beam:

For the second simply-supported beam vibration case, considering a pulsating load $q(x,t) = f_0\,\delta(\mathrm{x} - \mathrm{x}_0)\sin(\omega t)$ applied at an arbitrary beam position $x = x_0$. By using Duhamel integral formulas as presented in equation (3.65), the nth mode response contribution can be integrated as

$$\varphi_n(\mathrm{t}) = \frac{X_n(x=x_0)}{\omega_n}\int_0^t \frac{f_0\sin(\omega\tau)}{\rho A}\sin(\omega_n(t-\tau))d\tau = \frac{X_n(x=x_0)}{\omega_n}\frac{f_0}{\rho A}\mathrm{H}_n(\omega)\left[\frac{1}{\omega_n}\sin(\omega t) - \frac{\omega}{{\omega_n}^2}\sin(\omega_n t)\right] \quad (3.81)$$

where f_0 is a given constant indicating the amplitude the pulsating load, ω is the angular frequency of the pulsating load, ω_n is the natural frequency of the beam for the nth vibration mode.

The total dynamic transverse response of the beam deflection can be computed using equation (3.66) as

$$y(x,t) = \sum_{n=1}^{\infty} X_n(x) \frac{X_n(x=x_0)}{\omega_n} \frac{f_0}{\rho A} \mathrm{H}_n(\omega) \left[\frac{1}{\omega_n} \sin(\omega t) - \frac{\omega}{{\omega_n}^2} \sin(\omega_n t)\right] =$$

$$\frac{2}{L} \sum_{n=1}^{\infty} sin\left(\frac{n\pi x}{L}\right) sin\left(\frac{n\pi x_0}{L}\right) \frac{f_0}{\rho A {\omega_n}^2} \mathrm{H}_n(\omega) \left[\sin(\omega t) - \frac{\omega}{\omega_n} \sin(\omega_n t)\right] \quad (3.82)$$

The dynamic responses of the beam bending moment and shear force can be computed by the following two equations respectively

$$M(x,t) = \frac{2EI}{L} \left(\frac{n\pi}{L}\right)^2 \sum_{n=1}^{\infty} sin\left(\frac{n\pi x}{L}\right) sin\left(\frac{n\pi x_0}{L}\right) \frac{f_0}{\rho A {\omega_n}^2} H_n(\omega) \left[sin(\omega t) - \frac{\omega}{\omega_n} sin(\omega_n t)\right] \quad (3.83)$$

$$V(x,t) = \frac{2EI}{L} \left(\frac{n\pi}{L}\right)^3 \sum_{n=1}^{\infty} cos\left(\frac{n\pi x}{L}\right) sin\left(\frac{n\pi x_0}{L}\right) \frac{f_0}{\rho A {\omega_n}^2} H_n(\omega) \left[sin(\omega t) - \frac{\omega}{\omega_n} sin(\omega_n t)\right] \quad (3.84)$$

3.2.2.2 Transverse Vibration of Cantilever Beams

By implementation of the four boundary conditions in equation (3.42), for a cantilever beam, to the general form of the solution in equation (3.39), the following four relationships hold

$$C = E = 0$$

$$\alpha^2 D\big(-cos(\alpha L) - cosh(\alpha L)\big) + \alpha^2 F\big(-sin(\alpha L) - sinh(\alpha L)\big) = 0$$

$$\alpha^3 D\big(sin(\alpha L) - sinh(\alpha L)\big) + \alpha^3 F\big(-cos(\alpha L) - cosh(\alpha L)\big) = 0 \quad (3.85)$$

To achieve a nontrivial solution for the system of equations regarding the four unknown constants of equation (3.85), i.e. C, D, E and F should not be all equal to zero simultaneously. Hence, the following relationship must be held to avoid a trivial solution based on the related linear algebra theorem

$$[-cos(\alpha L) - cosh(\alpha L)]^2 - [sin(\alpha L) - sinh(\alpha L)][-sin(\alpha L) - sinh(\alpha L)] = 0 \quad (3.86)$$

Further simplification of equation (3.86) yields the frequency equation for the fixed-free cantilever beam as

$$cos(\alpha L)\cosh(\alpha L) = -1.0 \quad (3.87)$$

Obviously, this frequency equation for a cantilever beam is a transcendental equation which should be solved numerically, for instance by using Newton-Raphson iteration method adopted in this dissertation. The smallest twenty-seven real positive roots of equation (3.87) are listed in Table 3.4 below. Many significant figures for the presented roots are kept due to the existence of a hyperbolic cosine term in the transcendental equation. For the remaining even larger real roots, they are not frequently used due to trivial contributions and are omitted here for brevity.

Table 3.4 Frequency equation solutions for a fixed-free cantilever beam

αL	Value R_n	αL	Value R_n	αL	Value R_n
$\alpha_1 L$	1.875104069	$\alpha_{10} L$	29.845130209	$\alpha_{19} L$	58.119464091
$\alpha_2 L$	4.694091133	$\alpha_{11} L$	32.986722863	$\alpha_{20} L$	61.261056745
$\alpha_3 L$	7.854757438	$\alpha_{12} L$	36.128315516	$\alpha_{21} L$	64.402649399
$\alpha_4 L$	10.995540735	$\alpha_{13} L$	39.269908170	$\alpha_{22} L$	67.544242052
$\alpha_5 L$	14.137168391	$\alpha_{14} L$	42.411500823	$\alpha_{23} L$	70.685834706
$\alpha_6 L$	17.278759532	$\alpha_{15} L$	45.553093477	$\alpha_{24} L$	73.827427359
$\alpha_7 L$	20.420352251	$\alpha_{16} L$	48.694686131	$\alpha_{25} L$	76.969020013
$\alpha_8 L$	23.561944902	$\alpha_{17} L$	51.836278784	$\alpha_{26} L$	80.110612667
$\alpha_9 L$	26.703537556	$\alpha_{18} L$	54.977871438	$\alpha_{27} L$	83.252205320

By using the following relationship

$$\alpha_n{}^4 = \left(\frac{R_n}{L}\right)^4 = \frac{\rho A \omega_n{}^2}{EI} \tag{3.88}$$

The nth mode natural frequency for a fixed-free cantilever beam can be expressed as

$$\omega_n = \sqrt{\frac{EI}{\rho A}}\left(\frac{R_n}{L}\right)^2 \tag{3.89}$$

Now expressing the unknown constant F in terms of D as

$$F = -D\,\frac{cos(\alpha L)+cosh(\alpha L)}{sin(\alpha L)+sinh(\alpha L)} \tag{3.90}$$

Then the nth mode normal function of a fixed-free cantilever beam can be written as

$$X_n(x) = D_n\left[\left(cos(\alpha_n x) - cosh(\alpha_n x)\right) - C_c(\alpha_n L)\left(sin(\alpha_n x) - sinh(\alpha_n x)\right)\right] \tag{3.91}$$

where the coefficient $C_c(\alpha_n L) = \frac{cos(\alpha_n L)+cosh(\alpha_n L)}{sin(\alpha_n L)+sinh(\alpha_n L)}$.

Using the orthogonality relationship in equation (3.55) to normalize the normal function $X_n(x)$ of the fixed-free cantilever beam, which leads to

$$\int_0^L X_n(x)^2 dx = {D_n}^2 \int_0^L \left[\left(cos(\alpha_n x) - cosh(\alpha_n x)\right) - C_c(\alpha_n L)\left(sin(\alpha_n x) - sinh(\alpha_n x)\right)\right]^2 dx =$$

$${D_n}^2 * L = 1 \tag{3.92}$$

The unknown constant D_n can be easily determined by the normalization relationship in equation (3.92) as

$$D_n = \frac{1}{\sqrt{L}} \tag{3.93}$$

Finally, the nth mode normal function for the fixed-free cantilever beam becomes

$$X_n(x) = \frac{1}{\sqrt{L}}\left[\left(cos(\alpha_n x) - cosh(\alpha_n x)\right) - C_c(\alpha_n L)\left(sin(\alpha_n x) - sinh(\alpha_n x)\right)\right] \tag{3.94}$$

The first five mode normal functions for a fixed-free cantilever beam are plotted in Figure 3.5 below.

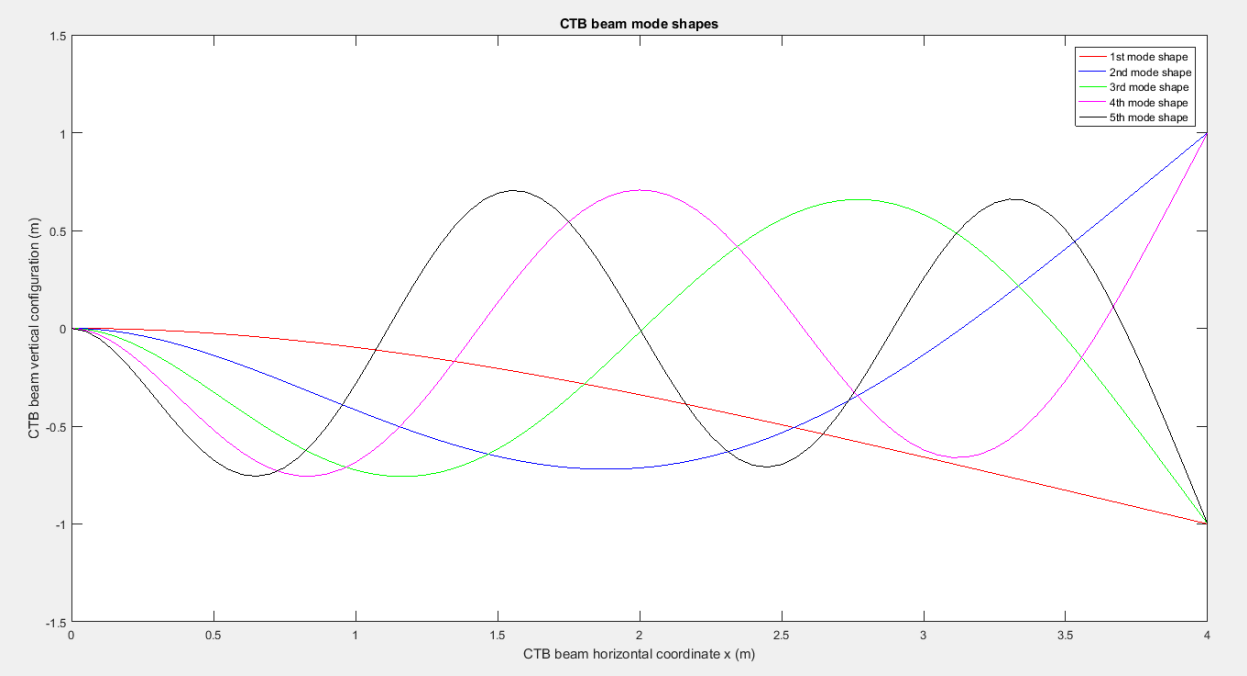

Figure 3.5 The first five mode shapes for the fixed-free cantilever beam

First dynamic case for a fixed-free cantilever beam:

For the first transverse vibration case of a fixed-free cantilever beam, assuming that $q(x,t) = f_0 X_{n^*}(x)\sin(\omega t)$ $(for\ n^* = 1,3,5,7,9)$, here f_0 is a given constant, $X_{n^*}(x)$ is the n^{*th} normalized normal function of the fixed-free beam, ω is a given excitation frequency. Taking the Duhamel integration for this case by using equation (3.65), we obtain the response contribution by the nth mode as

$$\varphi_n(\mathrm{t}) = \frac{1}{\omega_n}\int_0^L X_n(x)\int_0^t \frac{f_0 X_{n^*}(x)\sin(\omega\tau)}{\rho A}\sin(\omega_n(t-\tau))d\tau dx = \frac{f_0}{\rho A{\omega_n}^2}\mathrm{H}_n(\omega)\left[\sin(\omega t) - \frac{\omega}{\omega_n}\sin(\omega_n t)\right]\int_0^L X_n(x)X_{n^*}(x)\,dx \quad (n^* = 1,3,5,7,9; n = 1,2,3,\ldots) \tag{3.95}$$

The total transverse response of the beam deflection due to vibration, for the fixed-free cantilever beam, can be computed by using equation (3.66) as

$$y(x,t) = \sum_{n=1}^{\infty} X_n(x) \frac{f_0}{\rho A {\omega_n}^2} \mathrm{H}_n(\omega) \left[\sin(\omega t) - \frac{\omega}{\omega_n} \sin(\omega_n t)\right] \int_0^L X_n(x) X_{n^*}(x)\, dx =$$

$$\frac{1}{\sqrt{L}} \big[\big(cos(\alpha_{n^*} x) - cosh(\alpha_{n^*} x)\big) - C_c(\alpha_{n^*} L)\big(sin(\alpha_{n^*} x) -$$

$$sinh(\alpha_{n^*} x)\big)\big] \frac{f_0}{\rho A {\omega_{n^*}}^2} \mathrm{H}_{n^*}(\omega) \left[\sin(\omega t) - \frac{\omega}{\omega_{n^*}} \sin(\omega_{n^*} t)\right] (n^* = 1,3,5,7,9) \quad (3.96)$$

The total transverse response of the bending moment, for the fixed-free cantilever beam, can be calculated as

$$M(x,t) = -EIy''(x,t) = -\frac{{\alpha_{n^*}}^2}{\sqrt{L}} \big[\big(-cos(\alpha_{n^*} x) - cosh(\alpha_{n^*} x)\big) - C_c(\alpha_{n^*} L)\big(-sin(\alpha_{n^*} x) -$$

$$sinh(\alpha_{n^*} x)\big)\big] \frac{f_0}{\rho A {\omega_{n^*}}^2} \mathrm{H}_{n^*}(\omega) \left[\sin(\omega t) - \frac{\omega}{\omega_{n^*}} \sin(\omega_{n^*} t)\right] (n^* = 1,3,5,7,9) \quad (3.97)$$

The total transverse response of the shear force, for the fixed-free cantilever beam, can be calculated as

$$V(x,t) = -EIy'''(x,t) = -\frac{{\alpha_{n^*}}^3}{\sqrt{L}} \big[\big(sin(\alpha_{n^*} x) - sinh(\alpha_{n^*} x)\big) - C_c(\alpha_{n^*} L)\big(-cos(\alpha_{n^*} x) -$$

$$cosh(\alpha_{n^*} x)\big)\big] \frac{f_0}{\rho A {\omega_{n^*}}^2} \mathrm{H}_{n^*}(\omega) \left[\sin(\omega t) - \frac{\omega}{\omega_{n^*}} \sin(\omega_{n^*} t)\right] (n^* = 1,3,5,7,9) \quad (3.98)$$

where the coefficient $C_c(\alpha_{n^*} L) = \frac{cos(\alpha_{n^*} L) + cosh(\alpha_{n^*} L)}{sin(\alpha_{n^*} L) + sinh(\alpha_{n^*} L)}$ $(n^* = 1,3,5,7,9)$ applies throughout this subcase, $\mathrm{H}_{n^*}(\omega) = \frac{1}{1 - \omega^2 / {\omega_{\mathrm{n}^*}}^2}$.

Second dynamic case for a fixed-free cantilever beam:

For the second dynamic case study of the fixed-free cantilever beam, assuming the external excitation is a pulsating force $q(x,t) = f_0\, \delta(x - x_0) \sin(\omega t)$ applied at the position of $x = x_0$, here f_0 and ω are given data of the problem. By using Duhamel integral as presented in equation (3.65), we obtain the response contribution by the nth mode as

$$\varphi_n(\mathrm{t}) = \frac{X_n(x = x_0)}{\omega_n} \int_0^t \frac{f_0 \sin(\omega \tau)}{\rho A} \sin\left(\omega_n (t - \tau)\right) d\tau = \frac{X_n(x = x_0)}{\omega_n} \frac{f_0}{\rho A} \mathrm{H}_n(\omega) \left[\frac{1}{\omega_n} \sin(\omega t) -\right.$$

$$\left. \frac{\omega}{{\omega_n}^2} \sin(\omega_n t)\right] \quad (3.99)$$

Thus, the total transverse dynamic response of fixed-free cantilever beam deflection can be computed using equation (3.66) as

$$y(x,t) = \sum_{n=1}^{\infty} X_n(x) \frac{X_n(x=x_0)}{\omega_n} \frac{f_0}{\rho A} \mathrm{H}_n(\omega) \left[\frac{1}{\omega_n} \sin(\omega t) - \frac{\omega}{{\omega_n}^2} \sin(\omega_n t)\right] = \frac{1}{L} \sum_{n=1}^{\infty} \Big[\big(cos(\alpha_n x) - cosh(\alpha_n x)\big) - C_c(\alpha_n L)\big(sin(\alpha_n x) - sinh(\alpha_n x)\big)\Big]\Big[\big(cos(\alpha_n x_0) - cosh(\alpha_n x_0)\big) - C_c(\alpha_n L)\big(sin(\alpha_n x_0) - sinh(\alpha_n x_0)\big)\Big] \frac{f_0}{\rho A {\omega_n}^2} \mathrm{H}_n(\omega) \left[\sin(\omega t) - \frac{\omega}{\omega_n} \sin(\omega_n t)\right] \quad (3.100)$$

The total transverse response of the bending moment, for the fixed-free cantilever beam, can be calculated as

$$M(x,t) = -\frac{EI{\alpha_n}^2}{L} \sum_{n=1}^{\infty} \Big[\big(-cos(\alpha_n x) - cosh(\alpha_n x)\big) - C_c(\alpha_n L)\big(-sin(\alpha_n x) - sinh(\alpha_n x)\big)\Big]\Big[\big(cos(\alpha_n x_0) - cosh(\alpha_n x_0)\big) - C_c(\alpha_n L)\big(sin(\alpha_n x_0) - sinh(\alpha_n x_0)\big)\Big] \frac{f_0}{\rho A {\omega_n}^2} \mathrm{H}_n(\omega) \left[\sin(\omega t) - \frac{\omega}{\omega_n} \sin(\omega_n t)\right] \quad (3.101)$$

The total transverse response of the shear force, for the fixed-free cantilever beam, can be calculated as

$$V(x,t) = -\frac{EI{\alpha_n}^3}{L} \sum_{n=1}^{\infty} \Big[\big(sin(\alpha_n x) - sinh(\alpha_n x)\big) - C_c(\alpha_n L)\big(-cos(\alpha_n x) - cosh(\alpha_n x)\big)\Big]\Big[\big(cos(\alpha_n x_0) - cosh(\alpha_n x_0)\big) - C_c(\alpha_n L)\big(sin(\alpha_n x_0) - sinh(\alpha_n x_0)\big)\Big] \frac{f_0}{\rho A {\omega_n}^2} \mathrm{H}_n(\omega) \left[\sin(\omega t) - \frac{\omega}{\omega_n} \sin(\omega_n t)\right] \quad (3.102)$$

where the coefficient $C_c(\alpha_n L) = \frac{cos(\alpha_n L) + cosh(\alpha_n L)}{sin(\alpha_n L) + sinh(\alpha_n L)}$ $(n = 1,2,3, \dots)$ applies throughout this case, $\mathrm{H}_n(\omega) = \frac{1}{1 - \omega^2/{\omega_n}^2}$.

3.2.2.3 Transverse Vibration of Fixed-Fixed Beams

By implementation the four boundary conditions in equation (3.43) to the general form of the solution in equation (3.39), the following four relationships hold

$$C = E = 0$$

$$D\big(cos(\alpha L) - cosh(\alpha L)\big) + F\big(sin(\alpha L) - sinh(\alpha L)\big) = 0$$

$$\alpha D\big(-sin(\alpha L) - sinh(\alpha L)\big) + \alpha F\big(cos(\alpha L) - cosh(\alpha L)\big) = 0 \qquad (3.103)$$

To obtain a nontrivial solution for the four unknown coefficients in equation (3.103), the determinant of the coefficient matrix should be equal to zero according to the related linear algebra theorem, which leads to

$$[cos(\alpha L) - cosh(\alpha L)]^2 - [sin(\alpha L) - sinh(\alpha L)][-sin(\alpha L) - sinh(\alpha L)] = 0 \qquad (3.104)$$

Further simplification of equation (3.104) yields the frequency equation for the fixed-fixed beam as

$$cos(\alpha L)\cosh(\alpha L) = 1.0 \qquad (3.105)$$

The frequency equation (3.105) is also a transcendental equation like the cantilever beam case, thus the same method is utilized for seeking the roots of the equation. The smallest twenty-seven real positive roots of the equation are obtained and summarized in Table 3.5, and many significant figures are reserved here due to the existence of a hyperbolic cosine term in the frequency equation. For the remaining even larger positive roots, they are seldom used due to negligible contributions and are omitted here for brevity.

Table 3.5 Frequency equation solutions for a fixed-fixed Euler-Bernoulli beam

αL	Value R_n	αL	Value R_n	αL	Value R_n
$\alpha_1 L$	4.730040745	$\alpha_{10} L$	32.986722863	$\alpha_{19} L$	61.261056745
$\alpha_2 L$	7.853204624	$\alpha_{11} L$	36.128315516	$\alpha_{20} L$	64.402649399
$\alpha_3 L$	10.995607838	$\alpha_{12} L$	39.269908170	$\alpha_{21} L$	67.544242052
$\alpha_4 L$	14.137165491	$\alpha_{13} L$	42.411500823	$\alpha_{22} L$	70.685834706
$\alpha_5 L$	17.278759657	$\alpha_{14} L$	45.553093477	$\alpha_{23} L$	73.827427359
$\alpha_6 L$	20.420352246	$\alpha_{15} L$	48.694686131	$\alpha_{24} L$	76.969020013
$\alpha_7 L$	23.561944902	$\alpha_{16} L$	51.836278784	$\alpha_{25} L$	80.110612667
$\alpha_8 L$	26.703537556	$\alpha_{17} L$	54.977871438	$\alpha_{26} L$	83.252205320
$\alpha_9 L$	29.845130209	$\alpha_{18} L$	58.119464091	$\alpha_{27} L$	86.393797974

The nth mode natural frequency of the fixed-fixed Euler-Bernoulli beam can be calculated similarly as of the fixed-free beam by using equation (3.89), however the values of R_n should be referred to Table 3.5.

Based on equation (3.103), the unknown constant F can be expressed in terms of D as

$$F = -D\frac{cos(\alpha L)-cosh(\alpha L)}{sin(\alpha L)-sinh(\alpha L)} \tag{3.106}$$

Then the nth mode normal function of the fixed-fixed beam can be written as

$$X_n(x) = D_n\left[\left(cos(\alpha_n x) - cosh(\alpha_n x)\right) - C_f(\alpha_n L)\left(sin(\alpha_n x) - sinh(\alpha_n x)\right)\right] \tag{3.107}$$

where the coefficient $C_f(\alpha_n L) = \frac{cos(\alpha_n L)-cosh(\alpha_n L)}{sin(\alpha_n L)-sinh(\alpha_n L)}$.

By normalization of the normal function $X_n(x)$ in terms of equation (3.55), we have

$$\int_0^L X_n(x)^2 dx = {D_n}^2 \int_0^L \left[\left(cos(\alpha_n x) - cosh(\alpha_n x)\right) - C_f(\alpha_n L)\left(sin(\alpha_n x) - sinh(\alpha_n x)\right)\right]^2 dx =$$

$${D_n}^2 * L = 1 \tag{3.108}$$

Thus, the constant D_n can be determined based on equation (3.108) as

$$D_n = \frac{1}{\sqrt{L}} \tag{3.109}$$

Finally, the nth mode normal function for a fixed-fixed beam can be written as

$$X_n(x) = \frac{1}{\sqrt{L}}\left[\left(cos(\alpha_n x) - cosh(\alpha_n x)\right) - C_f(\alpha_n L)\left(sin(\alpha_n x) - sinh(\alpha_n x)\right)\right] \tag{3.110}$$

The first five modes of the normal functions for the fixed-fixed Euler-Bernoulli beam are plotted in Figure 3.6 below.

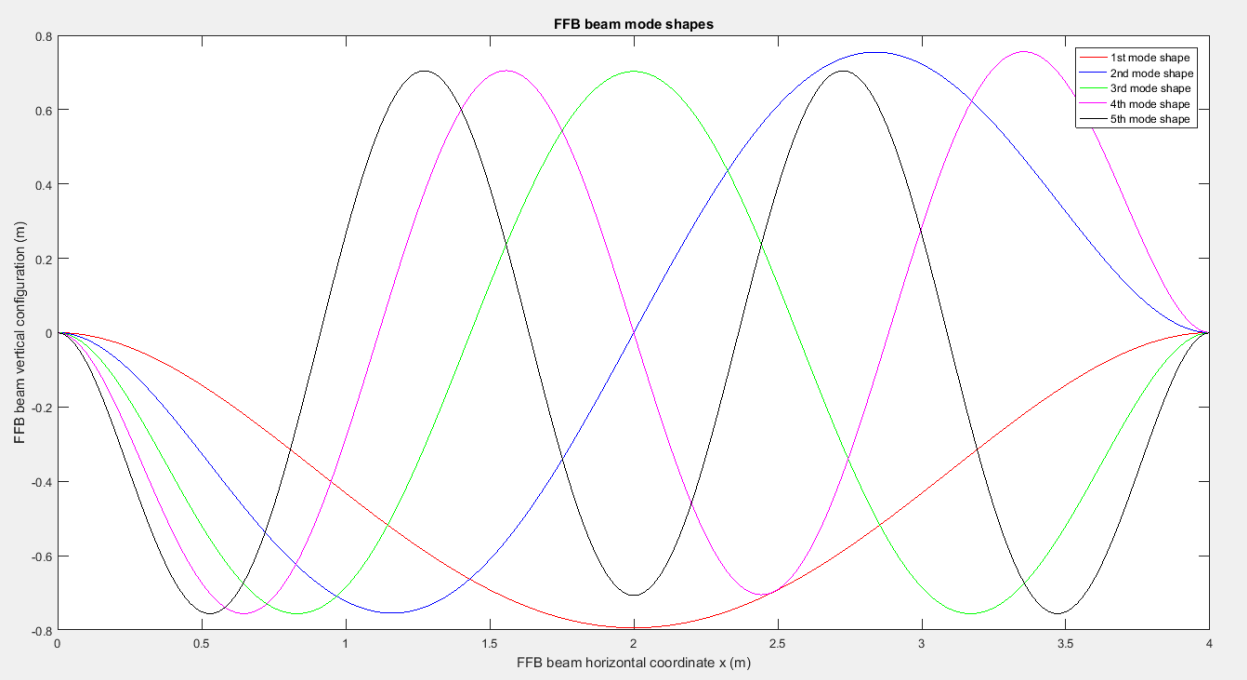

Figure 3.6 The first five mode shapes for a fixed-fixed Euler-Bernoulli beam

First dynamic case for fixed-fixed beams:

For the first vibration case study of a fixed-fixed beam, let the external load $q(x,t) = f_0 X_{n^*}(x)\sin(\omega t)\ \ (for\ n^* = 1,3,5,7,9)$, here $X_{n^*}(x)$ is the n^{*th} normalized normal function of the fixed-fixed beam, f_0 and ω are both given problem data. Taking the Duhamel integration for this case by utilizing equation (3.65), the nth mode response can be obtained as

$$\varphi_n(\mathrm{t}) = \frac{1}{\omega_n}\int_0^L X_n(x)\int_0^t \frac{f_0 X_{n^*}(x)\sin(\omega\tau)}{\rho A}\sin(\omega_n(t-\tau))d\tau dx = \frac{f_0}{\rho A{\omega_n}^2}\mathrm{H}_n(\omega)\left[\sin(\omega t) - \frac{\omega}{\omega_n}\sin(\omega_n t)\right]\int_0^L X_n(x)X_{n^*}(x)\,dx \qquad (3.111)$$

The total transverse response of the deflection, for a fixed-fixed beam, can be computed by using equation (3.66) as

$$y(x,t) = \sum_{n=1}^{\infty} X_n(x)\frac{f_0}{\rho A{\omega_n}^2}\mathrm{H}_n(\omega)\left[\sin(\omega t) - \frac{\omega}{\omega_n}\sin(\omega_n t)\right]\int_0^L X_n(x)X_{n^*}(x)\,dx = \frac{1}{\sqrt{L}}\left[\left(cos(\alpha_{n^*}x) - cosh(\alpha_{n^*}x)\right) - C_f(\alpha_{n^*}L)\left(sin(\alpha_{n^*}x) - sinh(\alpha_{n^*}x)\right)\right]\frac{f_0}{\rho A{\omega_{n^*}}^2}\mathrm{H}_{n^*}(\omega)\left[\sin(\omega t) - \frac{\omega}{\omega_{n^*}}\sin(\omega_{n^*}t)\right]\ (for\ n^* = 1,3,5,7,9) \qquad (3.112)$$

where the coefficient $C_f(\alpha_{n^*}L) = \frac{cos(\alpha_{n^*}L) - cosh(\alpha_{n^*}L)}{sin(\alpha_{n^*}L) - sinh(\alpha_{n^*}L)}$.

The dynamic response of the bending moment, for the fixed-fixed beam, can be easily calculated with the expression presented in equation (3.112) as

$$M(x,t) = -EIy''(x,t) = -\frac{{\alpha_{n^*}}^2}{\sqrt{L}}\left[\left(-cos(\alpha_{n^*}x) - cosh(\alpha_{n^*}x)\right) - C_f(\alpha_{n^*}L)\left(-sin(\alpha_{n^*}x) - sinh(\alpha_{n^*}x)\right)\right]\frac{f_0}{\rho A{\omega_{n^*}}^2}\mathrm{H}_{n^*}(\omega)\left[\sin(\omega t) - \frac{\omega}{\omega_{n^*}}\sin(\omega_{n^*}t)\right]\ (for\ n^* = 1,3,5,7,9) \qquad (3.113)$$

The dynamic response of the shear force, for the fixed-fixed beam, can be easily calculated with the expression presented in equation (3.112) as

$$V(x,t) = -EIy'''(x,t) = -\frac{{\alpha_{n^*}}^3}{\sqrt{L}}\left[\left(sin(\alpha_{n^*}x) - sinh(\alpha_{n^*}x)\right) - C_f(\alpha_{n^*}L)\left(-cos(\alpha_{n^*}x) - cosh(\alpha_{n^*}x)\right)\right]\frac{f_0}{\rho A{\omega_{n^*}}^2}\mathrm{H}_{n^*}(\omega)\left[\sin(\omega t) - \frac{\omega}{\omega_{n^*}}\sin(\omega_{n^*}t)\right] \ (for\ n^* = 1,3,5,7,9) \qquad (3.114)$$

where the coefficient $C_f(\alpha_{n^*}L) = \frac{cos(\alpha_{n^*}L) - cosh(\alpha_{n^*}L)}{sin(\alpha_{n^*}L) - sinh(\alpha_{n^*}L)}$ applies throughout the equations in this case, $\mathrm{H}_{n^*}(\omega) = \frac{1}{1-\omega^2/{\omega_{n^*}}^2}$.

Second dynamic case fixed-fixed beams:

For the second dynamic case study, a pulsating load $q(x,t) = f_0\delta(x - x_0)\sin(\omega t)$ is applied at the position of $x = x_0$ of a fixed-fixed beam, here f_0 and ω are given problem data. By using Duhamel integral, the response contribution by nth mode can be calculated as

$$\varphi_n(\mathrm{t}) = \frac{X_n(x=x_0)}{\omega_n}\int_0^t \frac{f_0 \sin(\omega\tau)}{\rho A}\sin\left(\omega_n(t-\tau)\right)d\tau = \frac{X_n(x=x_0)}{\omega_n}\frac{f_0}{\rho A}\mathrm{H}_n(\omega)\left[\frac{1}{\omega_n}\sin(\omega t) - \frac{\omega}{{\omega_n}^2}\sin(\omega_n t)\right] \qquad (3.115)$$

The total transverse response of the deflection, for the fixed-fixed beam, can be computed by using equation (3.66) as

$$y(x,t) = \sum_{n=1}^{\infty} X_n(x)\frac{X_n(x=x_0)}{\omega_n}\frac{f_0}{\rho A}\mathrm{H}_n(\omega)\left[\frac{1}{\omega_n}\sin(\omega t) - \frac{\omega}{{\omega_n}^2}\sin(\omega_n t)\right] = \frac{1}{L}\sum_{n=1}^{\infty}\left[\left(cos(\alpha_n x) - cosh(\alpha_n x)\right) - C_f(\alpha_n L)\left(sin(\alpha_n x) - sinh(\alpha_n x)\right)\right]\left[\left(cos(\alpha_n x_0) - cosh(\alpha_n x_0)\right) - C_f(\alpha_n L)\left(sin(\alpha_n x_0) - sinh(\alpha_n x_0)\right)\right]\frac{f_0}{\rho A{\omega_n}^2}\mathrm{H}_n(\omega)\left[\sin(\omega t) - \frac{\omega}{\omega_n}\sin(\omega_n t)\right] \ (for\ n = 1,2,3,\dots) \qquad (3.116)$$

The response of the bending moment, for the fixed-fixed beam, can be calculated with the expression presented in equation (3.116) as

$$M(x,t) = -\frac{EI{\alpha_n}^2}{L}\sum_{n=1}^{\infty}\Big[\big(-cos(\alpha_n x) - cosh(\alpha_n x)\big) - C_f(\alpha_n L)\big(-sin(\alpha_n x) - sinh(\alpha_n x)\big)\Big]\Big[\big(cos(\alpha_n x_0) - cosh(\alpha_n x_0)\big) - C_f(\alpha_n L)\big(sin(\alpha_n x_0) - sinh(\alpha_n x_0)\big)\Big]\frac{f_0}{\rho A{\omega_n}^2}\mathrm{H}_n(\omega)\left[\sin(\omega t) - \frac{\omega}{\omega_n}\sin(\omega_n t)\right] \ (for\ n = 1,2,3,\dots) \quad (3.117)$$

The response of the shear force, for the fixed-fixed beam, can be calculated with the expression presented in equation (3.116) as

$$V(x,t) = -\frac{EI{\alpha_n}^3}{L}\sum_{n=1}^{\infty}\Big[\big(sin(\alpha_n x) - sinh(\alpha_n x)\big) - C_f(\alpha_n L)\big(-cos(\alpha_n x) - cosh(\alpha_n x)\big)\Big]\Big[\big(cos(\alpha_n x_0) - cosh(\alpha_n x_0)\big) - C_f(\alpha_n L)\big(sin(\alpha_n x_0) - sinh(\alpha_n x_0)\big)\Big]\frac{f_0}{\rho A{\omega_n}^2}\mathrm{H}_n(\omega)\left[\sin(\omega t) - \frac{\omega}{\omega_n}\sin(\omega_n t)\right] \ (for\ n = 1,2,3,\dots) \quad (3.118)$$

where the coefficient $C_f(\alpha_n L) = \frac{cos(\alpha_n L) - cosh(\alpha_n L)}{sin(\alpha_n L) - sinh(\alpha_n L)}$ applies throughout this case, $\mathrm{H}_n(\omega) = \frac{1}{1-\omega^2/{\omega_\mathrm{n}}^2}$.

3.3 Static Benchmark Cases Study for RISER3D

For Euler Bernoulli beam static benchmark cases, two types of transverse loads are used for simply supported and fixed-fixed beam finite element simulation respectively. One type is high degrees polynomial distributed load, the other type is sinusoidal load with high frequencies. The results of the beam deflection, slope, bending moment and shear force are compared among RISER3D, CALBE3D and analytical analysis.

3.3.1 Static Benchmark Cases Subjected Transverse Polynomial-type Loads

For transverse polynomial-type distributed loads, the governing equation for a prismatic Euler Bernoulli beam with linear foundation is a fourth order differential equation as

$$EIu'''' + K_a u = q_0\left(\frac{x}{L}\right)^n \ for\ x \in [0, L] \quad (3.119)$$

where the constants $K_a$is the linear foundation stiffness.

The first static benchmark case is for one-dimensional simply supported beam with zero foundation stiffness and subjected to a fifth-order polynomial distributed load (n=5), the main properties of the beam are summarized in Table 3.6. A total of eight elements are adopted for the discretization of the beam domain. The concerned results of this cases, including the simply-supported beam deflection, slope, bending moment and shear force, are presented from Figure 3.7 to Figure 3.10.

In the plotted figures of this study, the legend '**QH FEA**' denotes Quintic Hermite Finite Element Method, '**CH FEA**' denotes Cubic Hermite Finite Element Method, '**Analytical**' denotes results calculated based on the Euler Bernoulli beam theory as presented in section 3.2, '**5PFDM CH FEA**' denotes using five-point finite difference method for postprocessing the concerned results based on nodal information obtained by Cubic Hermite Finite Element analysis. Unless otherwise specified, these legend titles are applied throughout all study cases in this dissertation.

For the first benchmark case, with 1m element mesh, the maximum bending moment computed by Analytical, QH FEA and 5PFDM CH FEA methods are 46.9727Nm, 46.9764Nm and 47.1967Nm respectively. The relative difference of the maximum bending moment between Analytical and QH FEA method is 0.0081%, while the relative difference between Analytical and 5PFDM is 0.4771%. As of the maximum shear force, the corresponding value are -57.1429N, -57.0381N and -50.2645N respectively. The corresponding relative differences become -0.1833% and -12.0371% respectively.

Table 3.6 Case data for simply supported beam with no foundation

Designate	Symbol	Value	Unit
Beam length	L	8	m
Beam width	W	0.05	m
Beam height	H	0.02	m
Young's Modulus	E	2.07E+11	N/m^2
Bending rigidity	EI	6.90E+03	Nm^2
Axial stiffness	EA	2.07E+08	N
Lateral load factor	q_0	50.0	N/m

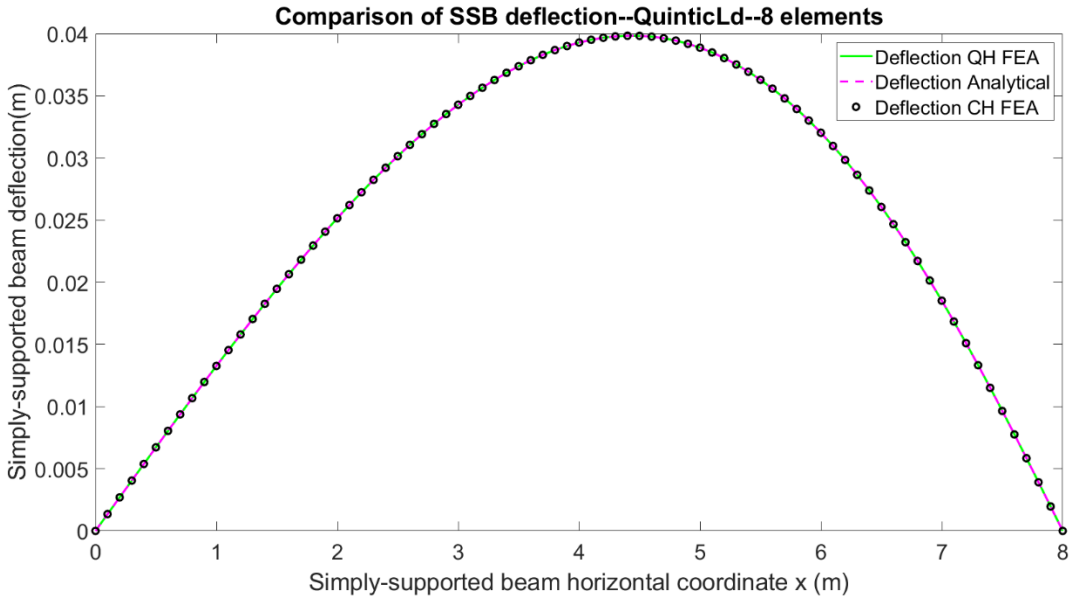

Figure 3.7 Simply supported beam deflection for case n=5

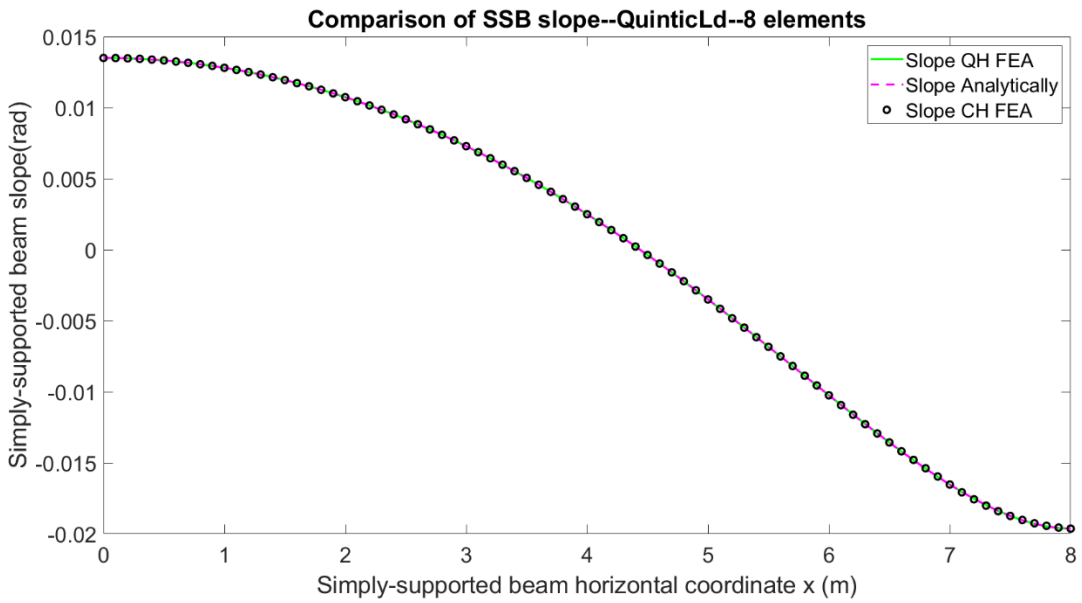

Figure 3.8 Simply supported beam slope for case n=5

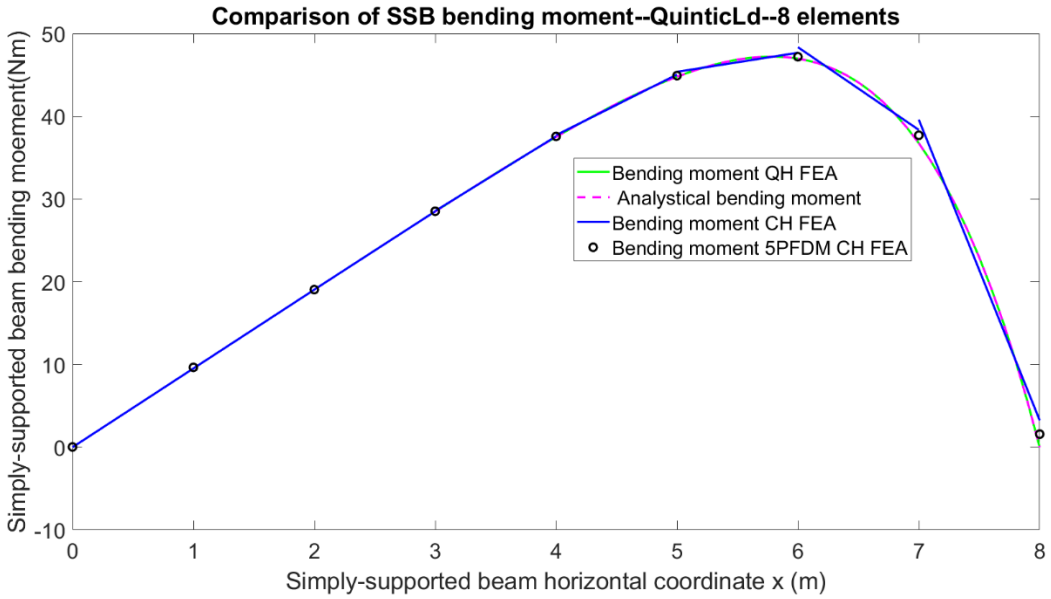

Figure 3.9 Simply supported beam bending moment for case n=5

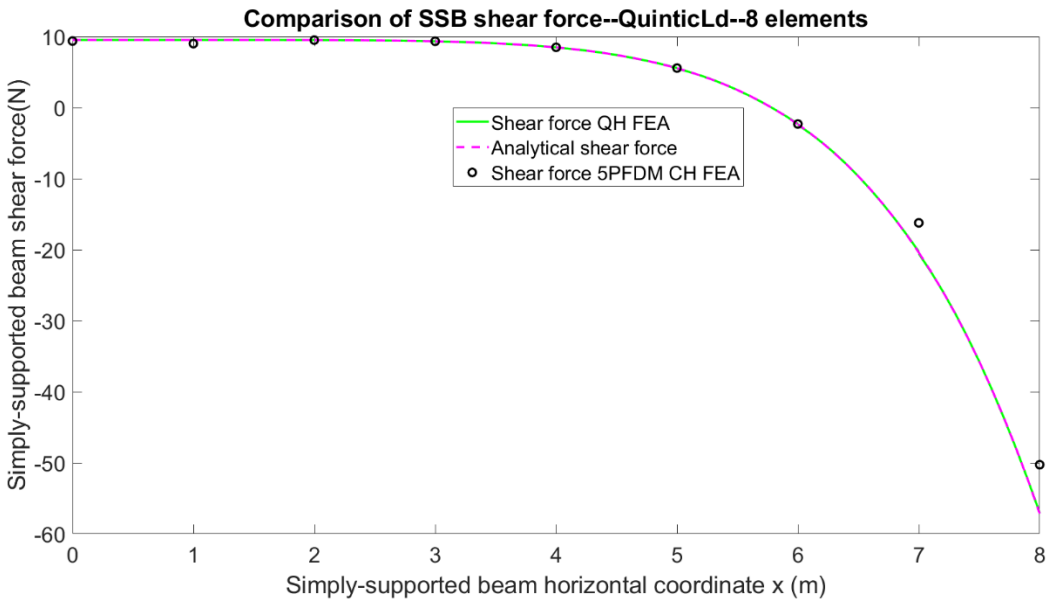

Figure 3.10 Simply supported beam shear force for case n=5

The second static benchmark case is for a fixed-fixed beam with zero foundation stiffness, subjected to a cubic polynomial distributed load n=3, the case input data are the same with the first benchmark case except using a larger load factor $q_0 = 2000N/m$. A total of eight elements are adopted for meshing the problem domain. The concerned results of this cases, including the fixed-fixed beam deflection, slope, bending moment and shear force, are plotted form Figure 3.11 to Figure 3.14.

For the second benchmark case, the maximum bending moment computed by Analytical, QH FEA and 5PFDM CH FEA are -3047.6190Nm, -3047.5122Nm and -3017.9315Nm respectively. The relative difference of the maximum bending moment between Analytical and QH FEA method is -0.0035%, while the relative difference between Analytical and 5PFDM is -0.9741%. As of the maximum shear force, the corresponding critical value are -3428.5714N, -3426.4330N and -3303.3110N respectively. And the corresponding relative differences become as -0.0624% and -3.6534% respectively.

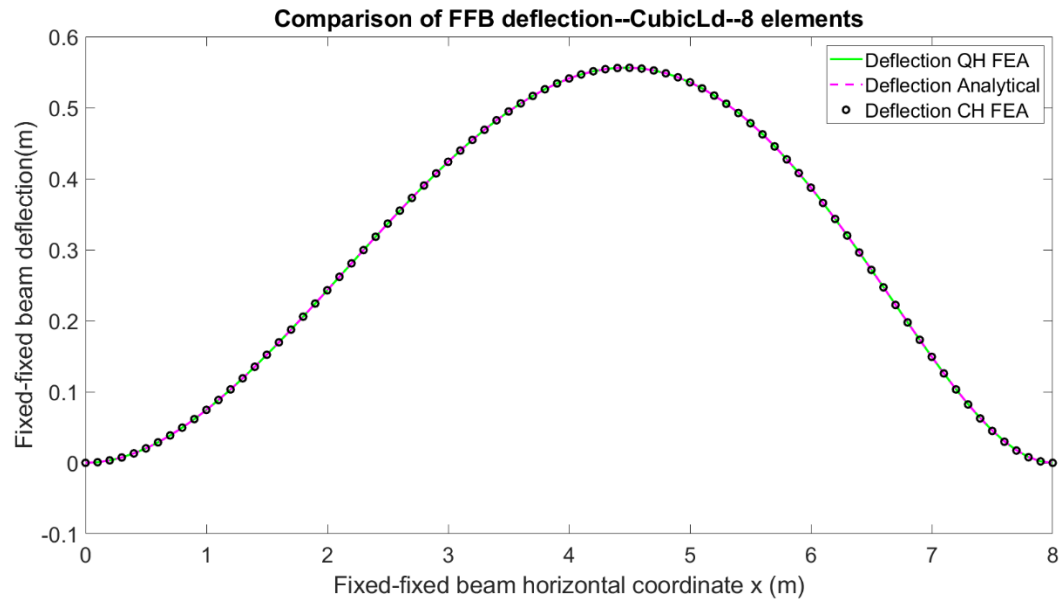

Figure 3.11 Fixed-fixed beam deflection for case n=3

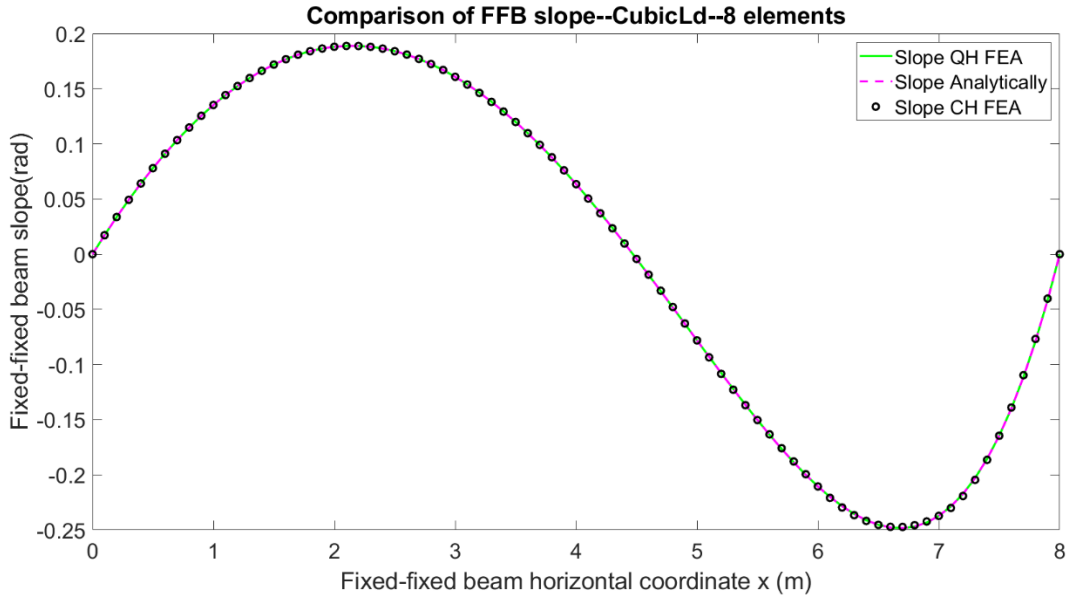

Figure 3.12 Fixed-fixed beam slope for case n=3

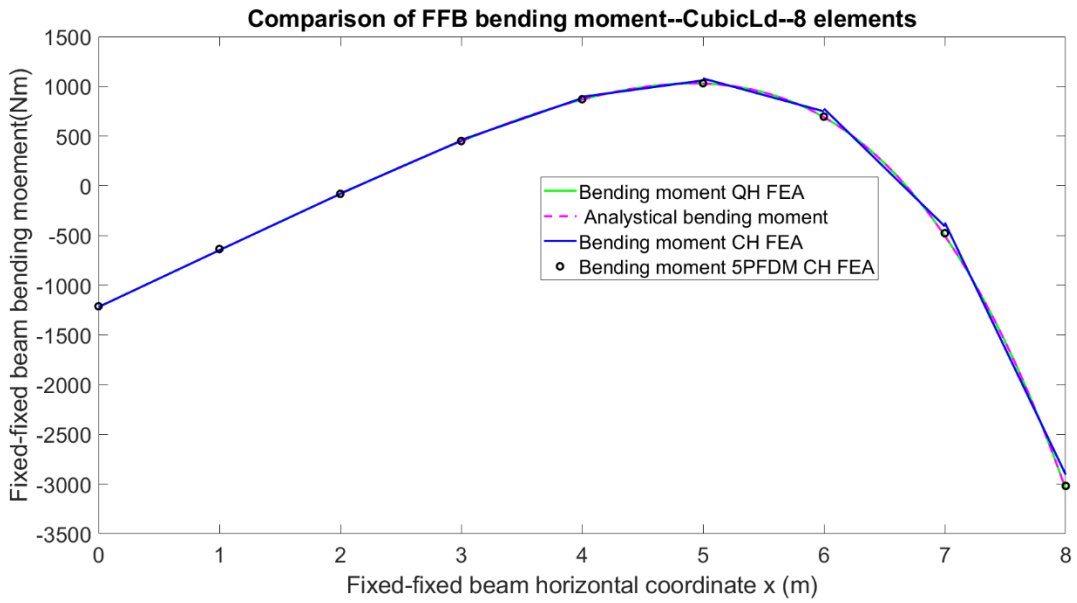

Figure 3.13 Fixed-fixed beam bending moment for case n=3

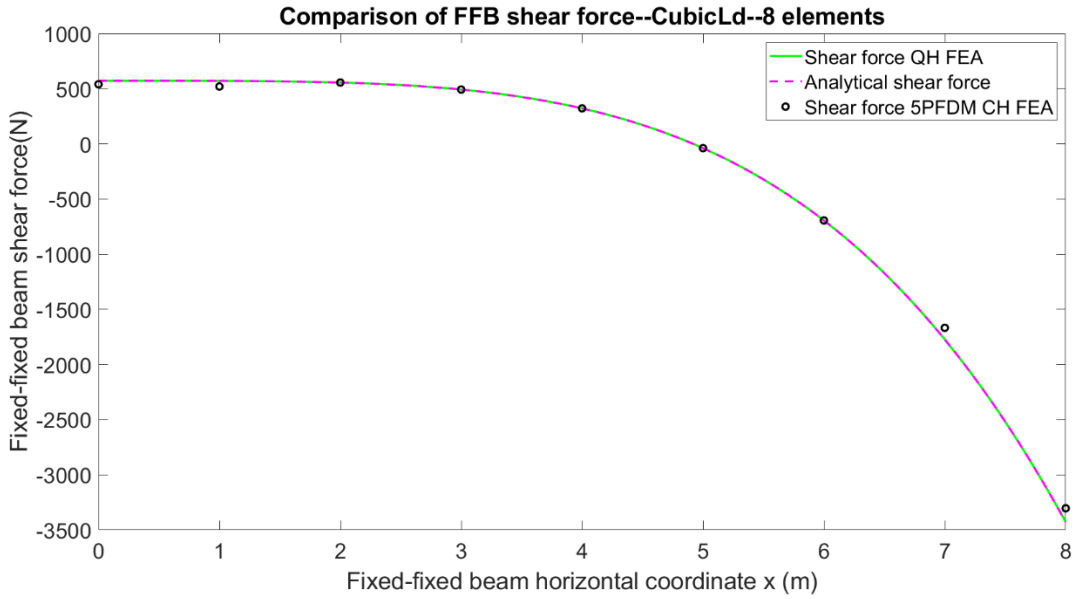

Figure 3.14 Fixed-fixed beam slope for case n=3

A third case is studied for the fixed-fixed beam with linear elastic foundation, i.e. $K_a = 1.0e4\mathrm{N/m/m}$, subjected to fifth-order polynomial distributed load n=5. The case input data are

the same with the first benchmark case except using a larger load factor $q_0 = 2000N/m$. A total of eight elements are utilized for meshing the problem domain. The concerned results of this case, including the fixed-fixed beam deflection, slope, bending moment and shear force, are plotted form Figure 3.15 to Figure 3.18 respectively.

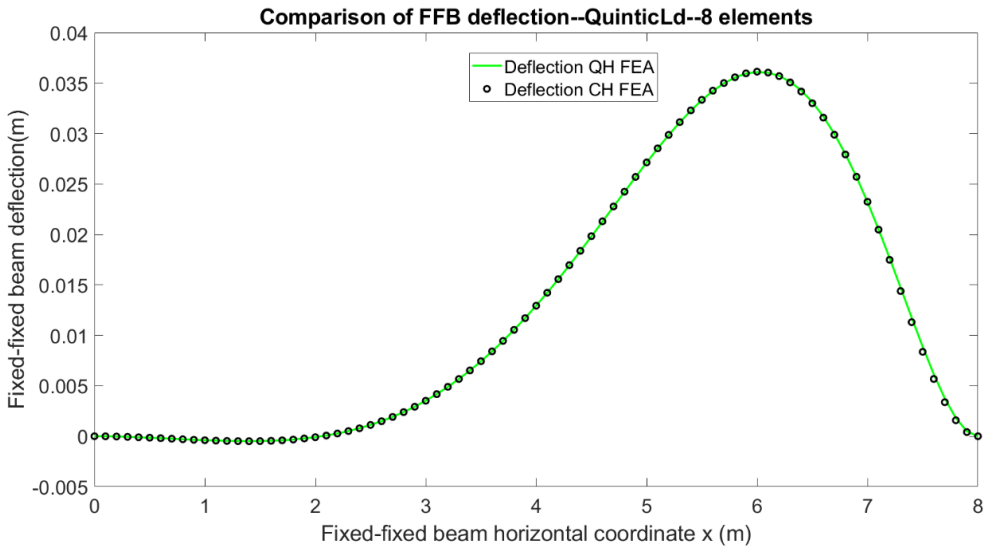

Figure 3.15 Fixed-fixed beam deflection for case n=5 with linear foundation

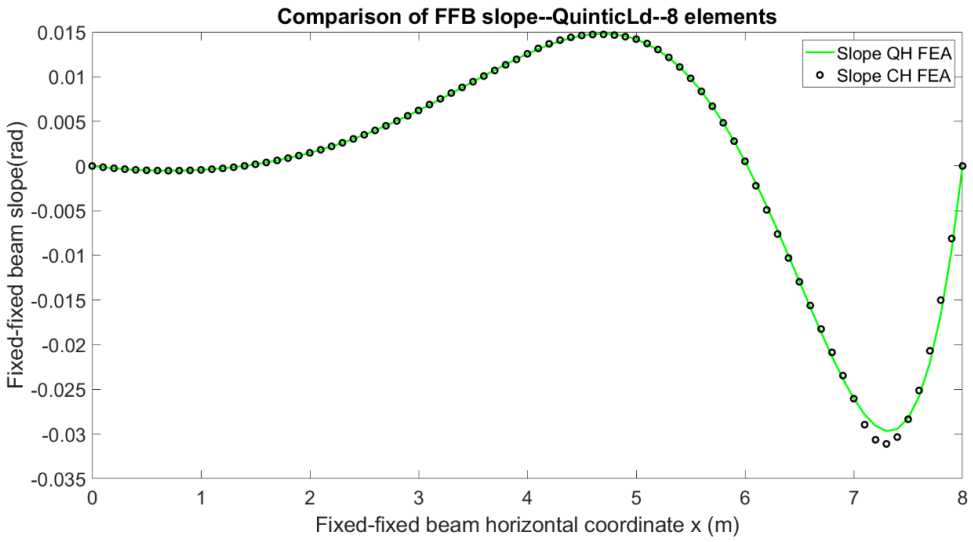

Figure 3.16 Fixed-fixed beam slope for case n=5 with linear foundation

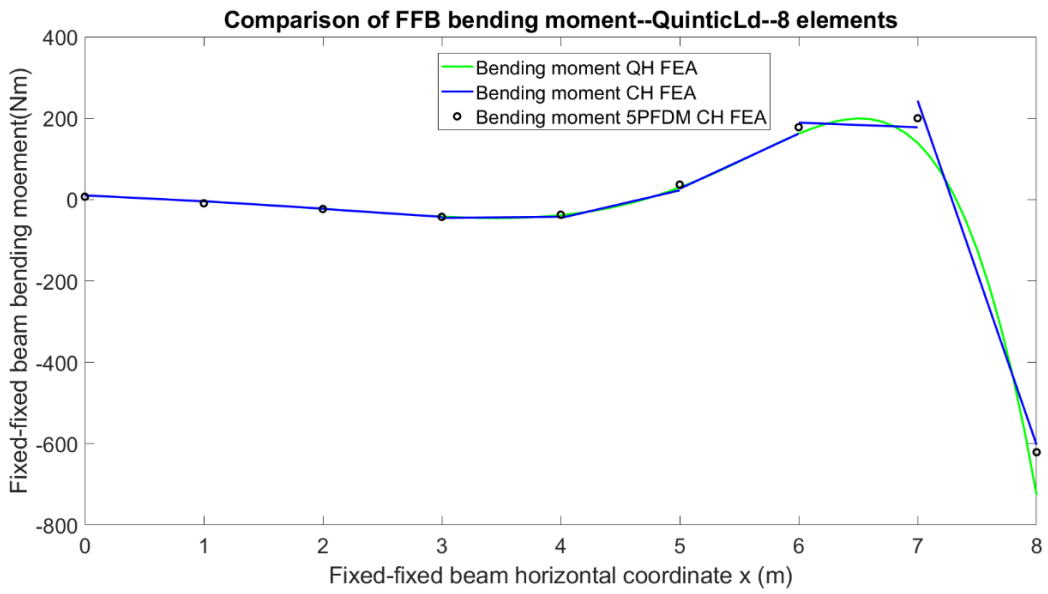

Figure 3.17 Fixed-fixed beam bending moment for case n=5 with linear foundation

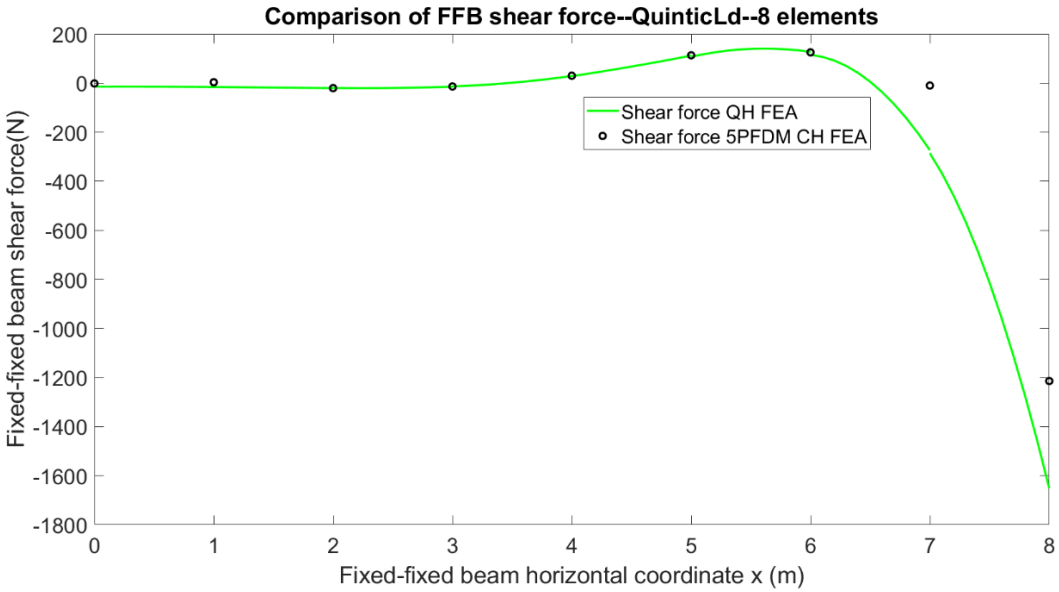

Figure 3.18 Fixed-fixed beam shear force for case n=5 with linear foundation

3.3.2 Static Benchmark Cases Subjected Transverse Sinusoidal-type Loads

For transverse sinusoidal-type loads, the governing equation for a prismatic Euler Bernoulli beam (EI=constant) with linear foundation is a fourth order differential equation as

$$EIu'''' + K_a u = q_0 sin\left(\frac{n\pi x}{L}\right) \ (for \text{ n} = 1,2,3, \dots; \ x \in [0, L]) \tag{3.120}$$

For this type of loads, the first benchmark case is for a simply supported beam with zero foundation stiffness ($K_a = 0N/m/m$), the particulars of which are also presented in Table 3.6. Case specific data include n=7 and $q_0 = 6.0e3N/m$. A total of 16 equal size elements are used for the problem domain meshing. The results of RISER3D, including the deflection, slope , bending moment and shear force of the simply-supported beam, are compared to those of obtained by analytical analysis and CABLE3D program from Figure 3.19 to Figure 3.22 respectively.

For this benchmark case, the bending moments, at the middle point of the beam, computed by Analytical, QH FEA and 5PFDM CH FEA method are -794.0272Nm, -791.4754Nm and -718.6285Nm respectively. The relative difference of the bending moment between Analytical and QH FEA method is -0.3214%, while the relative difference between Analytical and 5PFDM is -9.4957%.

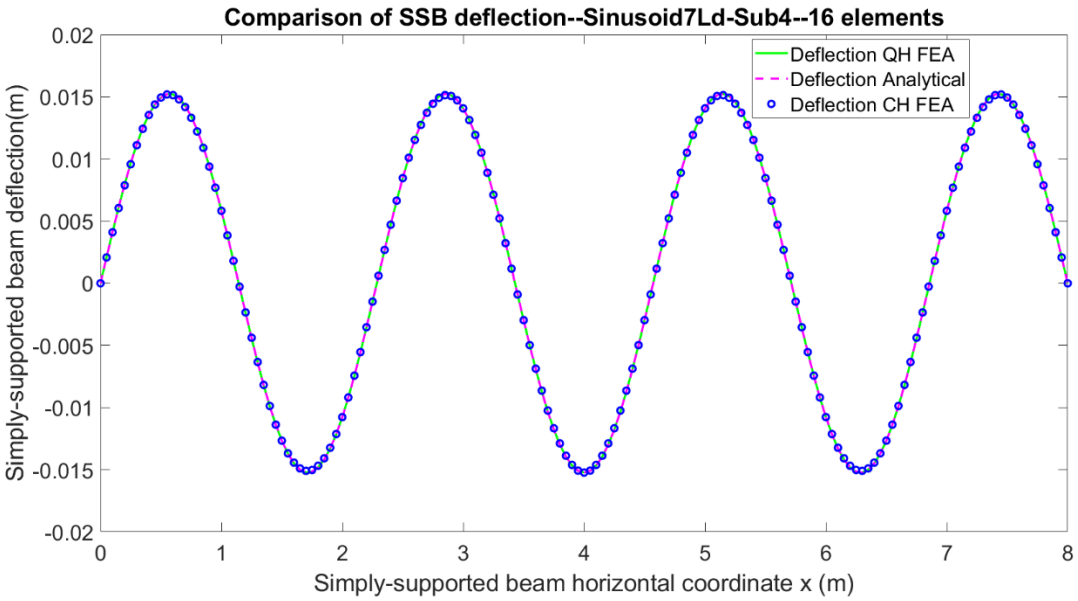

Figure 3.19 Simply supported beam deflection for case n=7

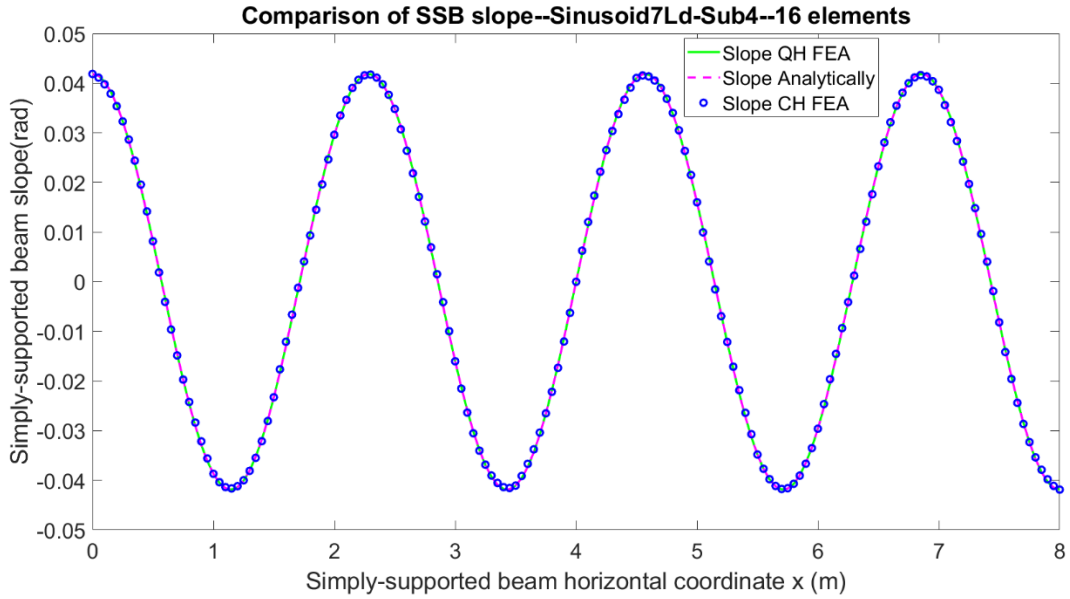

Figure 3.20 Simply supported beam slope for case n=7

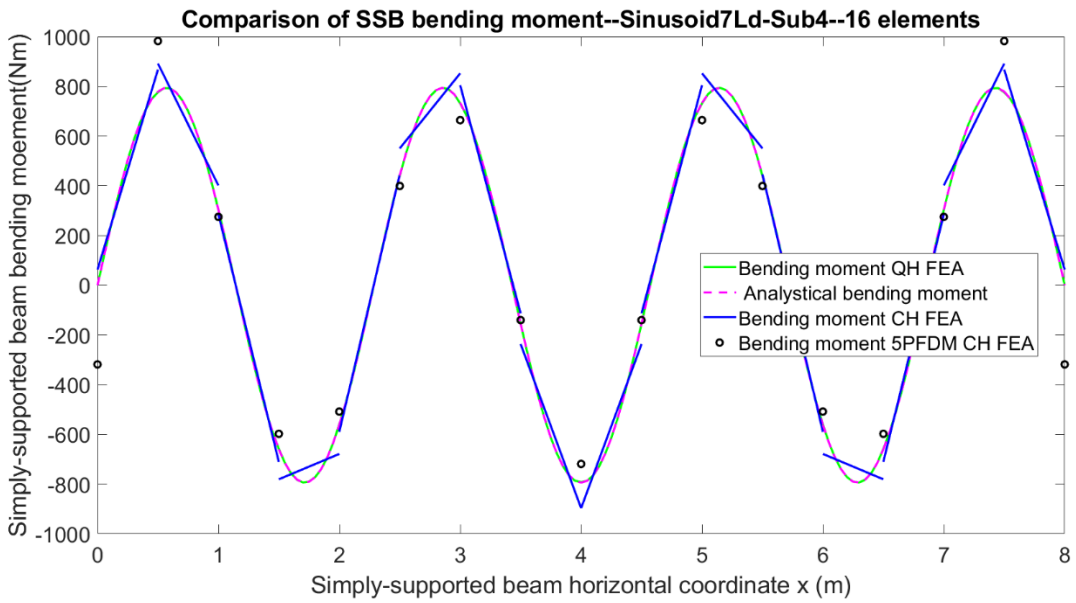

Figure 3.21 Simply supported beam bending moment distribution for case n=7

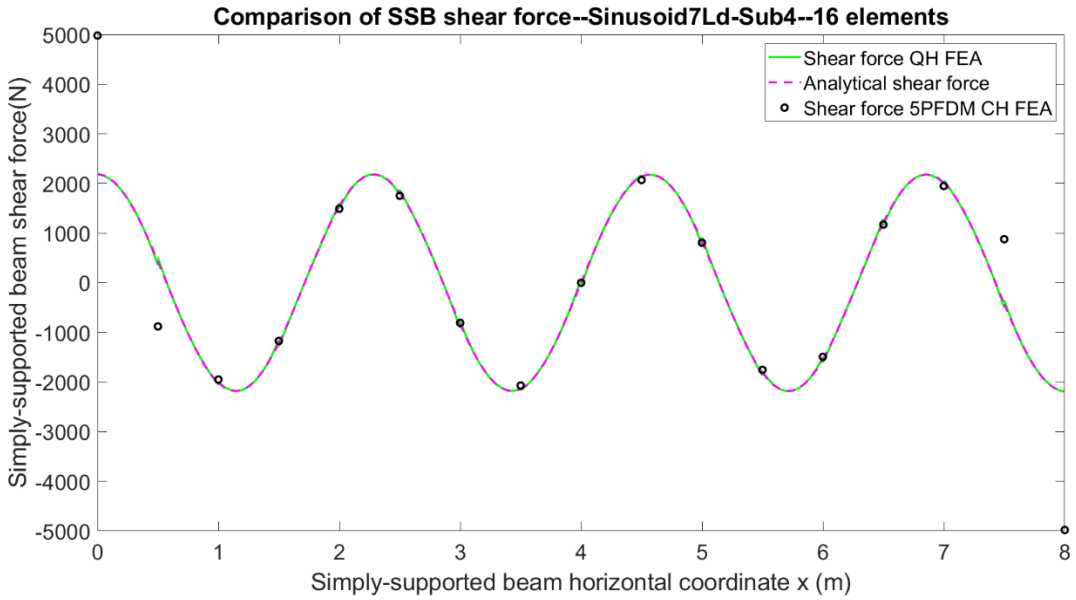

Figure 3.22 Simply supported beam shear force distribution for case n=7

For the same beam with zero foundation but fixed-fixed boundary conditions, the second static benchmark case for sinusoidal-type load is studied with specific case data n=9 and $q_0 =$

$6.0e3N/m$. A total of 16 equal size elements are used for the problem domain meshing. The main results of RISER3D for this case, including the deflection, slope, bending moment and shear force of the fixed-fixed beam, are compared to those of by analytical analysis and CABLE3D program from Figure 3.23 to Figure 3.26 respectively.

For this benchmark case, the maximum bending moments predicted by Analytical, QH FEA and 5PFDM CH FEA methods are -513.9441Nm, -515.8828Nm and -378.3928Nm respectively. The relative difference of the bending moment between Analytical and QH FEA method is 0.3772%, while the relative difference between Analytical and 5PFDM is -26.3747%.

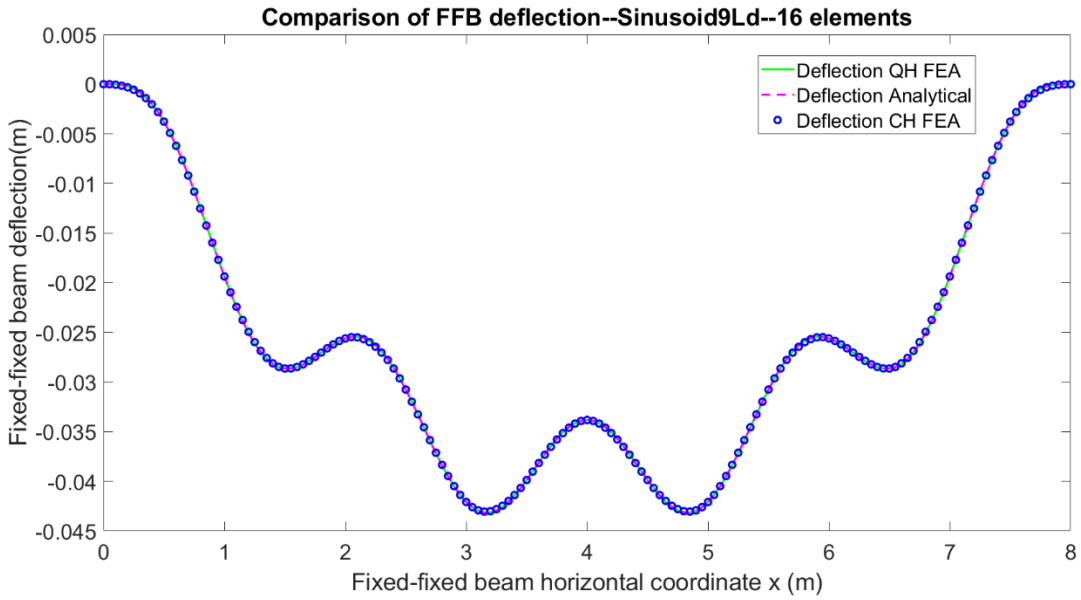

Figure 3.23 Fixed-fixed beam deflection for case n=9

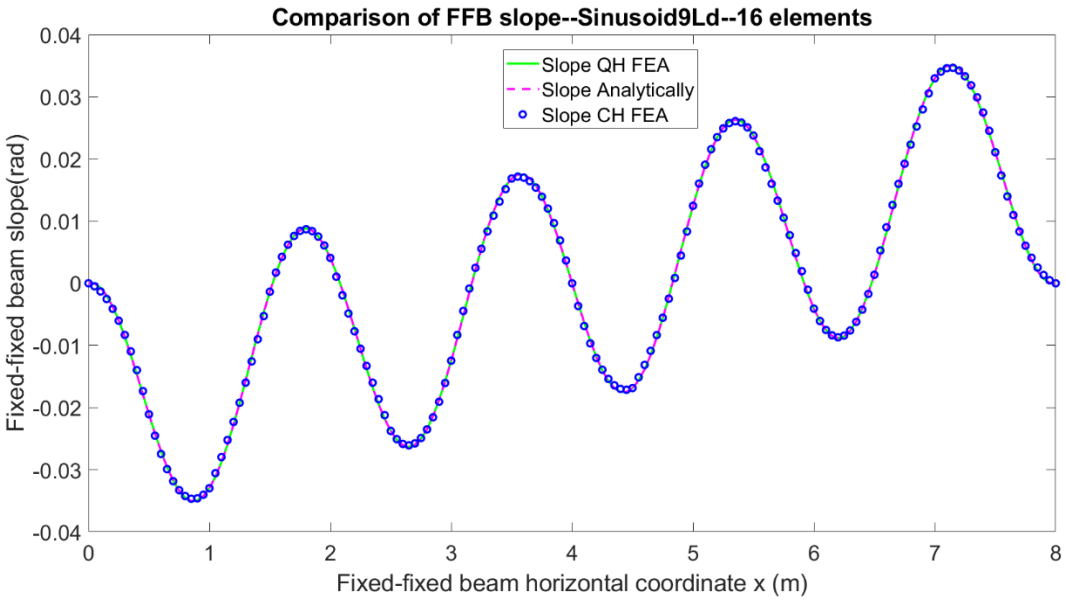

Figure 3.24 Fixed-fixed beam slope for case n=9

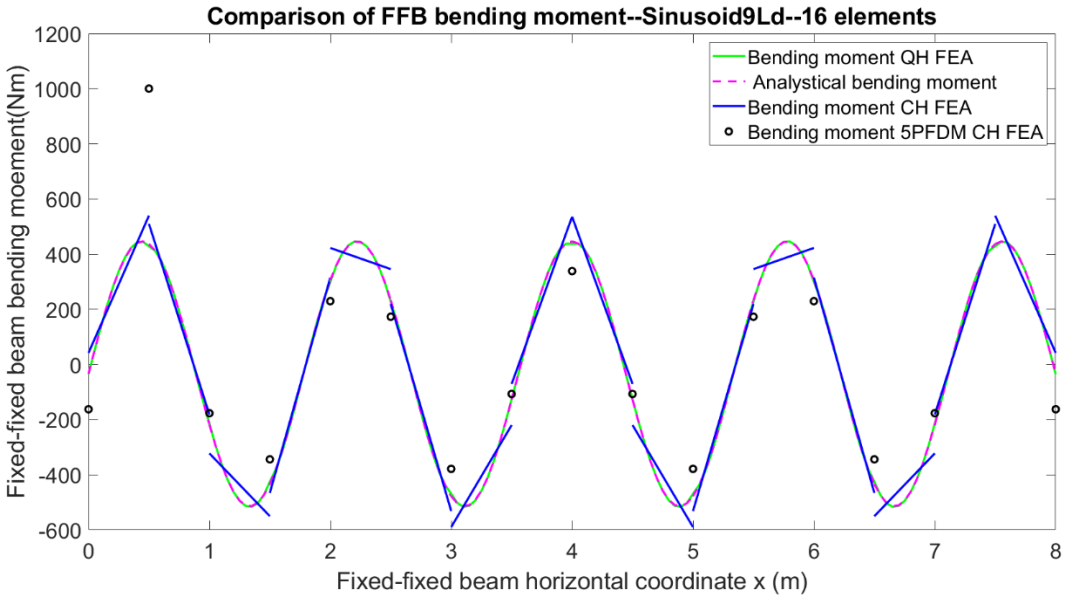

Figure 3.25 Fixed-fixed beam bending moment distribution for case n=9

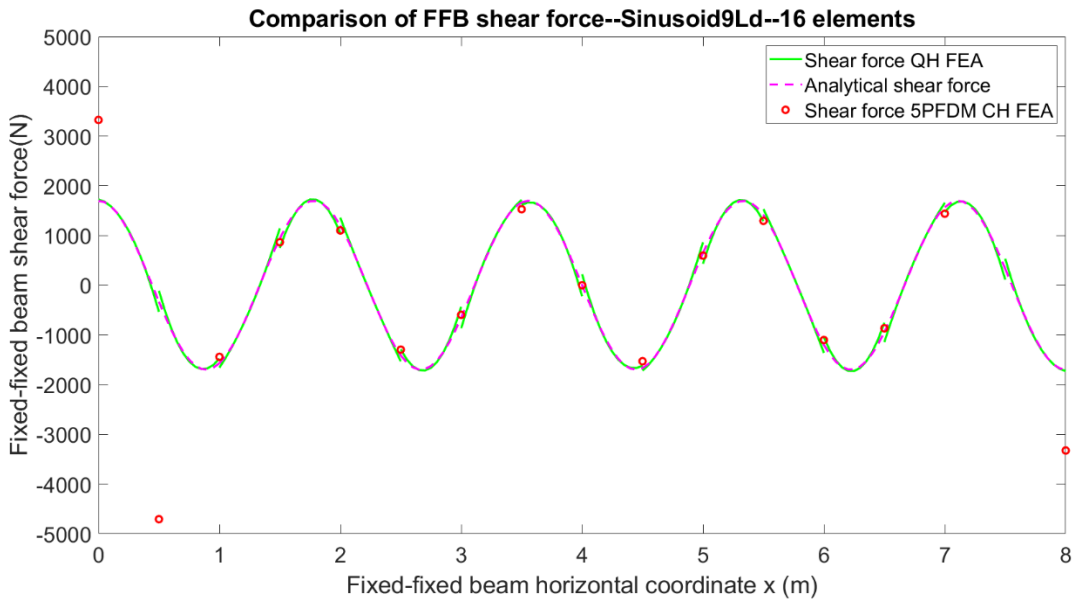

Figure 3.26 Fixed-fixed beam shear force distribution for case n=9

Based on the plotted results of above static benchmark cases, it can be seen that both the traditional method, i.e. the cubic Hermite finite element method, and the new quintic Hermite finite element method can yield good simulation results for the beam deflection and slope. However, for the bending moment and shear force prediction, especially at the section where the solution gradient is large, the new method can yield much higher accuracy than the traditional method.

3.4 Dynamic Benchmark Cases Study for RISER3D

For dynamic benchmark cases study of Euler Bernoulli beams, forced transverse vibration of simply supported beam, cantilever beam and fixed-fixed beam are studied respectively. For brevity, only a few selected cases are presented in the dissertation. Two types of loads are considered since the analytical responses can be derived using Duhamel integral. The first dynamic load type is pulsating load exerted at arbitrary position $x = x_0$ ($x_0 \in [0, L]$) with load amplitude f_0

$$\rho A \frac{\partial^2 y(x,t)}{\partial t^2} + EI \frac{\partial^4 y(x,t)}{\partial x^4} = f_0 \delta(x - x_0) sin(\omega t) \quad (3.121)$$

The second dynamic load type is a distributed varying force in form of the beam's natural mode shape functions, say n^{*th} mode, with load amplitude of f_0

$$\rho A \frac{\partial^2 y(x,t)}{\partial t^2} + EI \frac{\partial^4 y(x,t)}{\partial x^4} = f_0 X_{n^*}(x) sin\,(\omega t) \quad (3.122)$$

If taking the three types of beam and two types of dynamic loads into consideration, a total of six dynamic cases have to be performed in this section. For simplicity, only three dynamic cases are studied here.

The first dynamic benchmark case is a simply supported beam subjected to a transverse excitation load in form of $q(x,t) = 200 sin\left(\frac{5\pi x}{L}\right) sin\,(182t)$. The beam particulars for this dynamic benchmark case are summarized in Table 3.7.

Table 3.7 The Euler Bernoulli beam particulars for the dynamic benchmark cases

Designate	**Symbol**	**Value**	**Unit**
Beam length	L	4	m
Beam width	W	0.02	m
Beam height	H	0.01	m
Young's Modulus	E	2.07E+11	N/m^2
Bending rigidity	EI	345	Nm^2
Axial stiffness	EA	4.14E+07	N

For this case study, a total of 12 equal size elements are used for the domain mesh. The main results for the first dynamic cases, including the time series of the beam middle point

deflection, the beam middle point bending moment, the local zoom in of the beam middle point bending moment, and the beam left end shear force , are presented from Figure 3.27 to Figure 3.30 respectively. The time series selected for comparison among RISER3D, CALBE3D and analytical analysis mainly consist of the beam middle point deflection, middle point bending moment and left end point shear force.

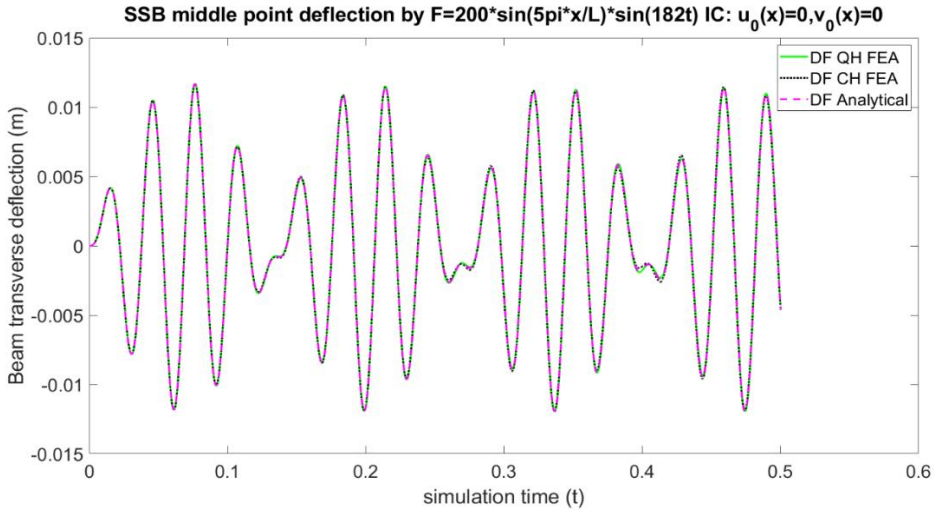

Figure 3.27 Time series of the middle point deflection of the simply supported beam

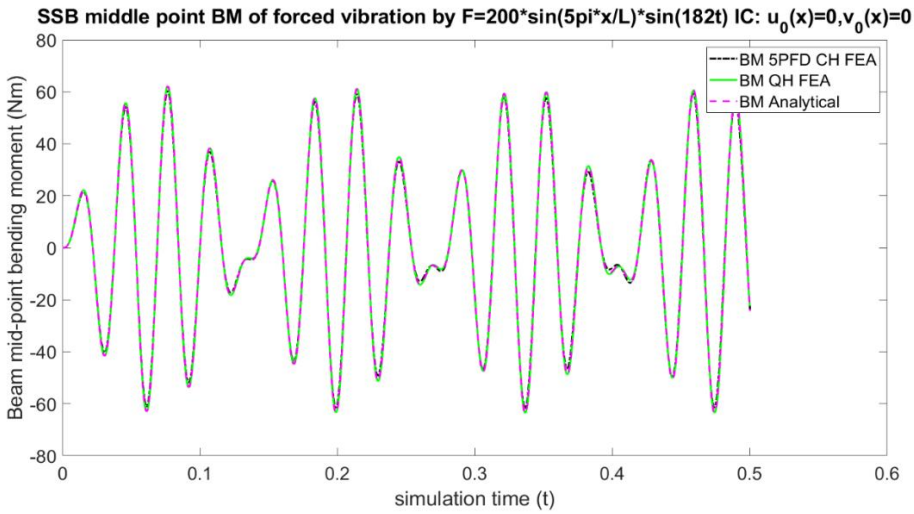

Figure 3.28 Time series of the middle point bending moment of the simply supported beam

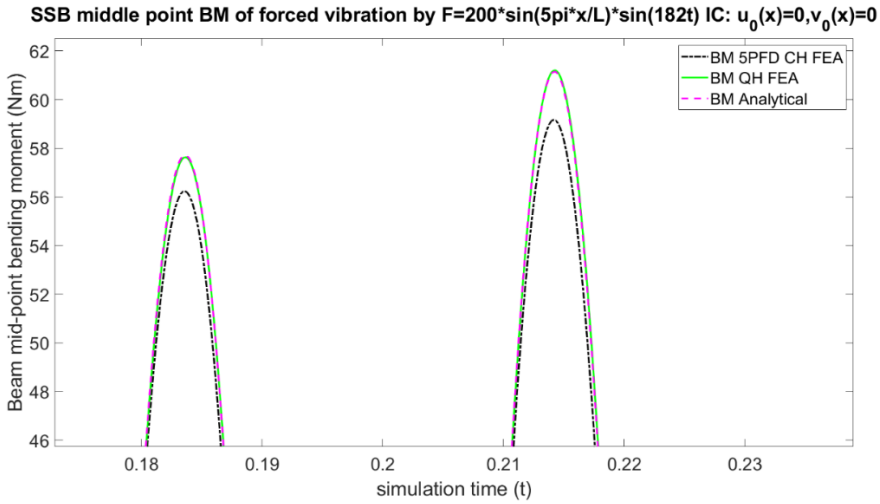

Figure 3.29 Time series of the SSB middle point bending moment with local zoom in

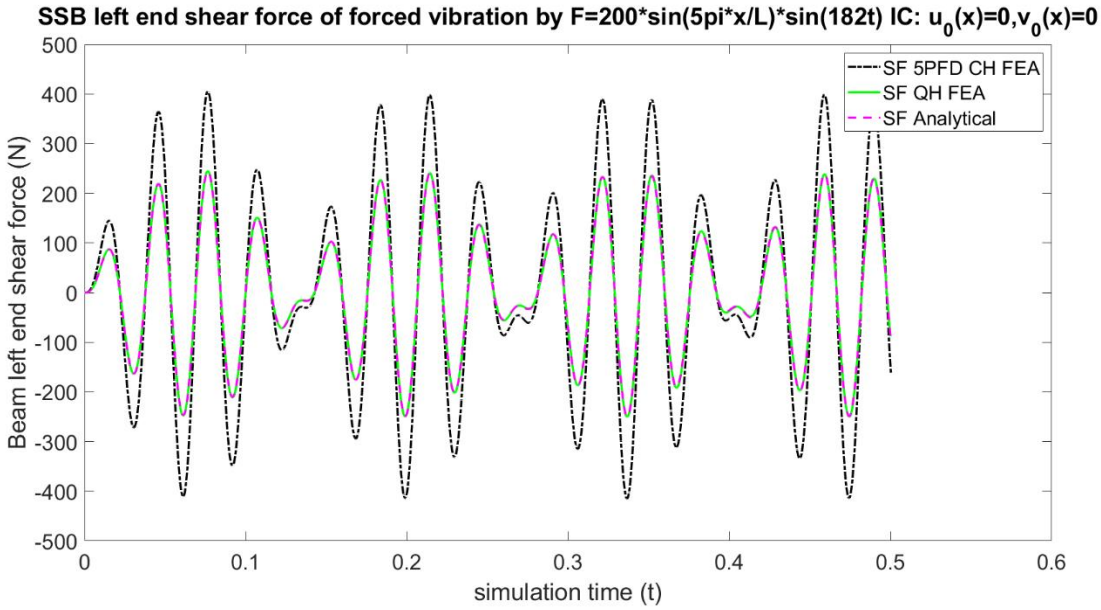

Figure 3.30 Time series of the left end shear force of the simply supported beam

The second dynamic benchmark case is a fixed-free cantilever beam subjected to a pulsating load, in form of $q(x,t) = 200\delta(x-2.05)sin\,(148t)$, at the point x_0=2.05m closing to the middle point of the beam. The analytical results of the beam deflection, bending moment and

shear force are derived by Duhamel integral and summarized in equation (3.100) to (3.102) respectively, which are truncated high to 27^{th} mode for this case.

For the second case study, a total of 12 equal size elements are used for the domain mesh. The concerned time series, including the time series of the beam deflection at the right free end, the bending moment at the left fixed end, the local zoom in the bending moment, the shear force at the left end and the local zoom in the shear force, are plotted from Figure 3.31 to Figure 3.35 respectively. The Figure 3.33 and Figure 3.35 are the local zoom in plots for an amplified view of the response differences among the three different methods.

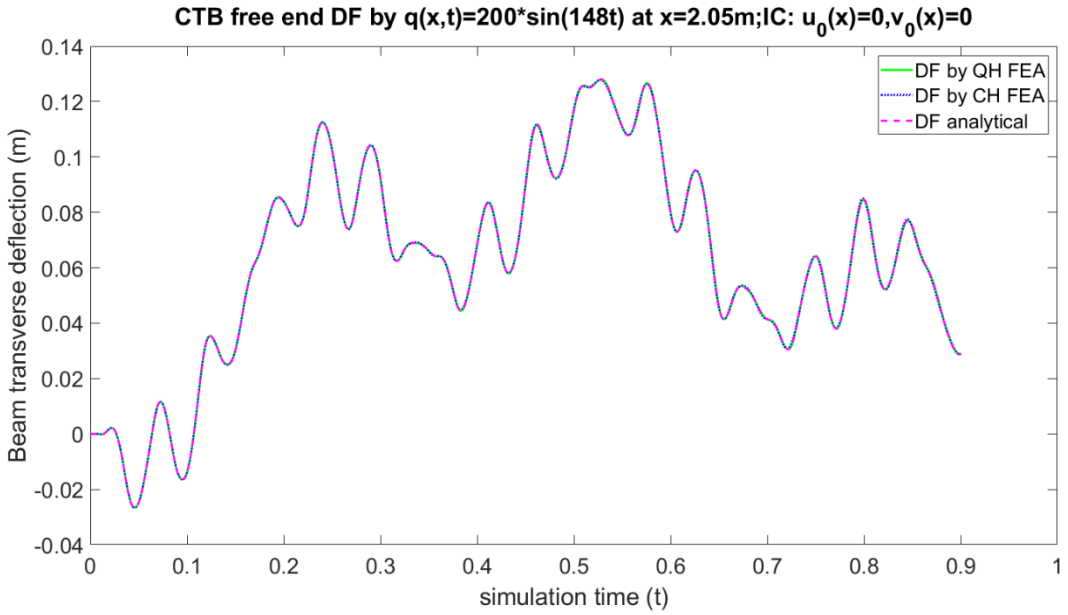

Figure 3.31 Comparison of the time series of free end deflection of the cantilever beam

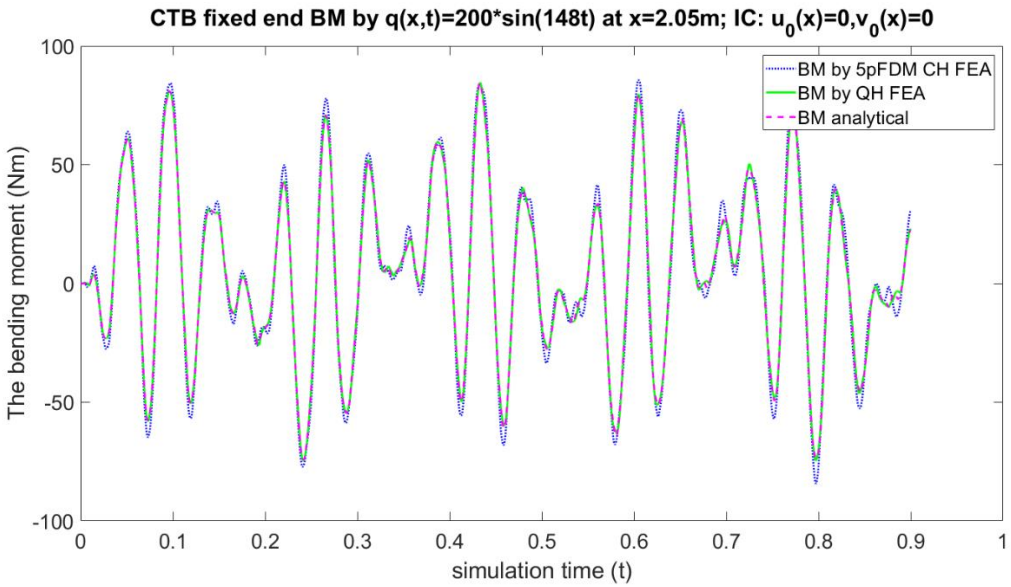

Figure 3.32 Time series of the cantilever beam bending moment at left end

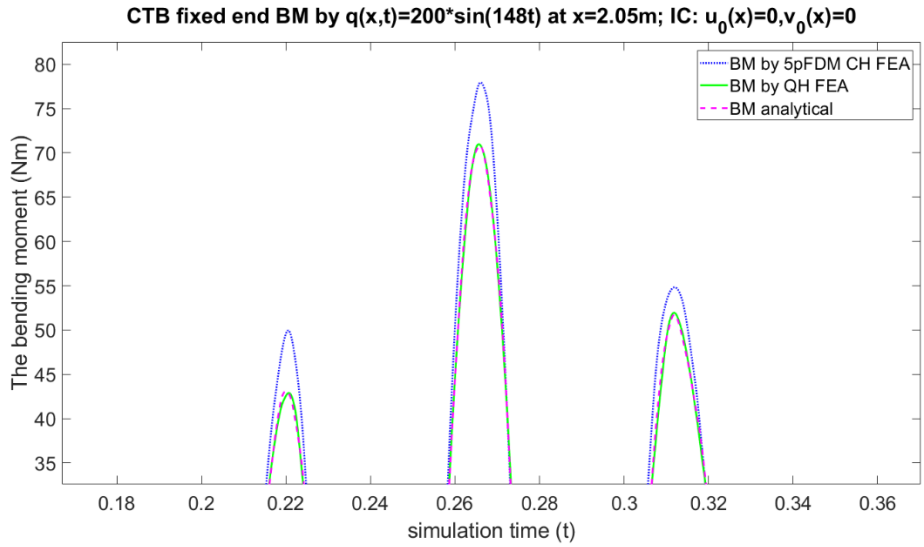

Figure 3.33 Time series of local zoom in of the cantilever beam bending moment at left end

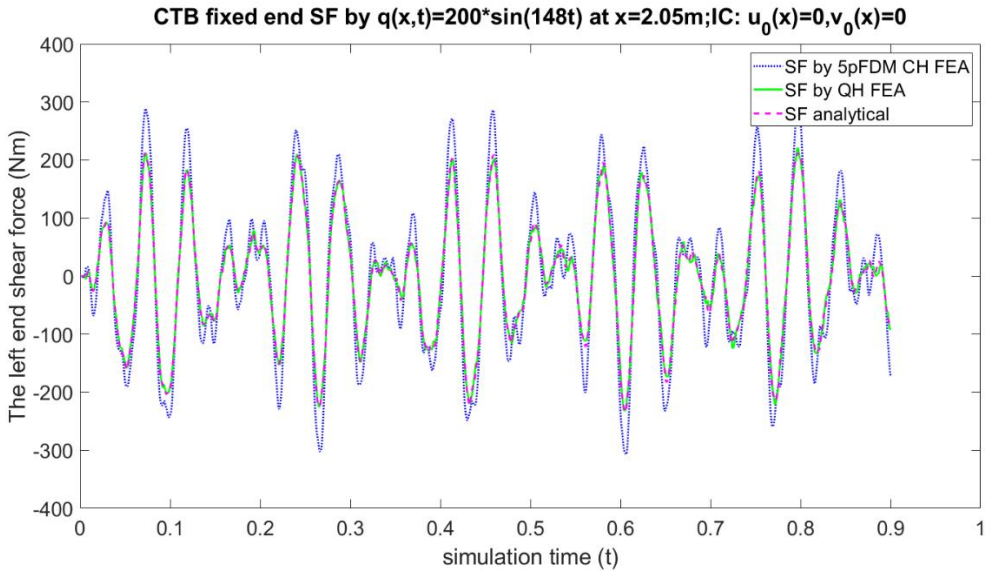

Figure 3.34 Time series of the shear force of the cantilever beam at left fixed end

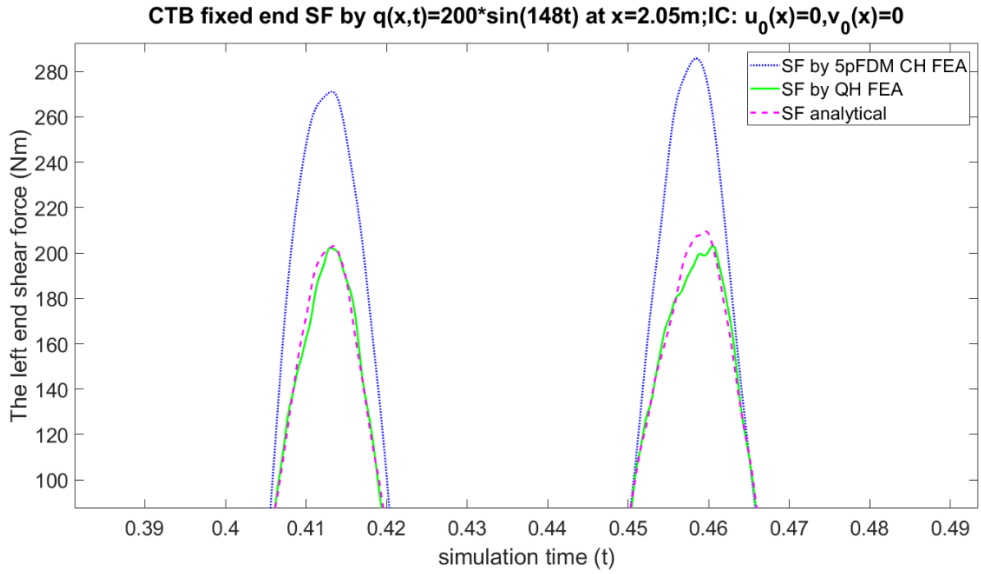

Figure 3.35 Time series of the local zoom in of the cantilever beam shear force at left end

The third dynamic benchmark case is for the beam, with fixed-fixed boundary conditions, subjected to a dynamic pulsating load in form of $q(x,t) = 100\delta(x-2.05)sin\,(89t)$. The analytical results for the beam transverse deflection, bending moment and shear force are

calculated based on equation (3.116), (3.117) and (3.118) respectively, which are truncated high to 27th mode in this study.

For this case, a total of 12 uniform length elements are used for the beam mesh. The time series of the deflection at the middle point of the beam, the bending moment at the middle point of the beam and the shear force at the left end of the beam are plotted from Figure 3.36 to Figure 3.40. Figure 3.38 and 3.40 are the local zoom in plots for getting a better view of the response differences among the three different approaches, i.e. RISER3D, CALBE3D and Analytical analysis.

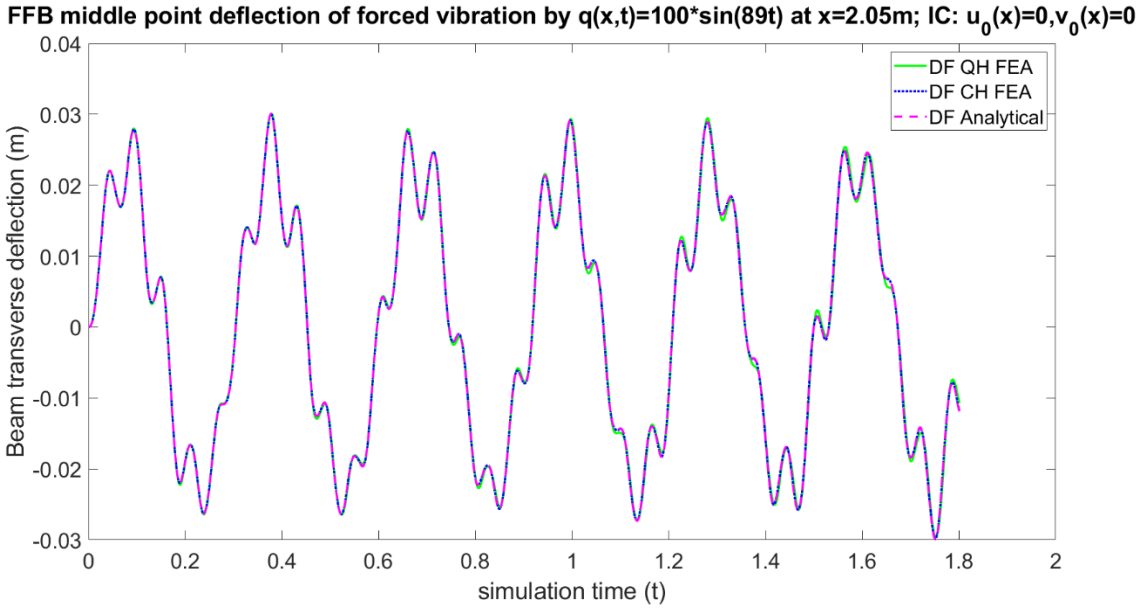

Figure 3.36 Time series of the fixed-fixed beam transverse deflection at the middle point

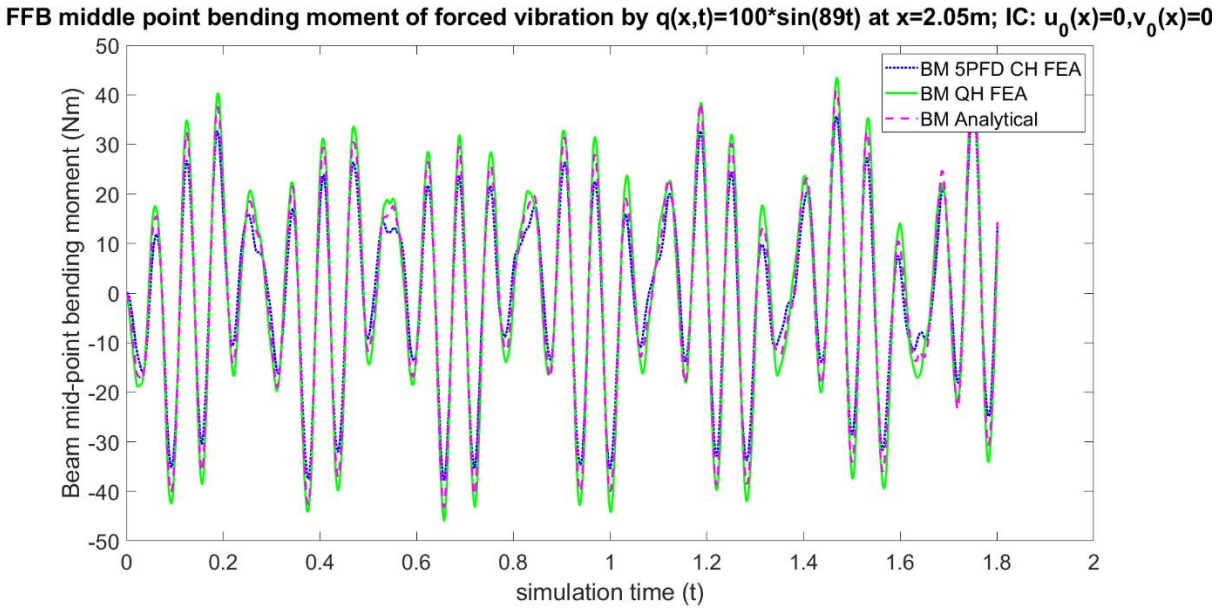

Figure 3.37 Time series of the fixed-fixed beam bending moment at the middle point

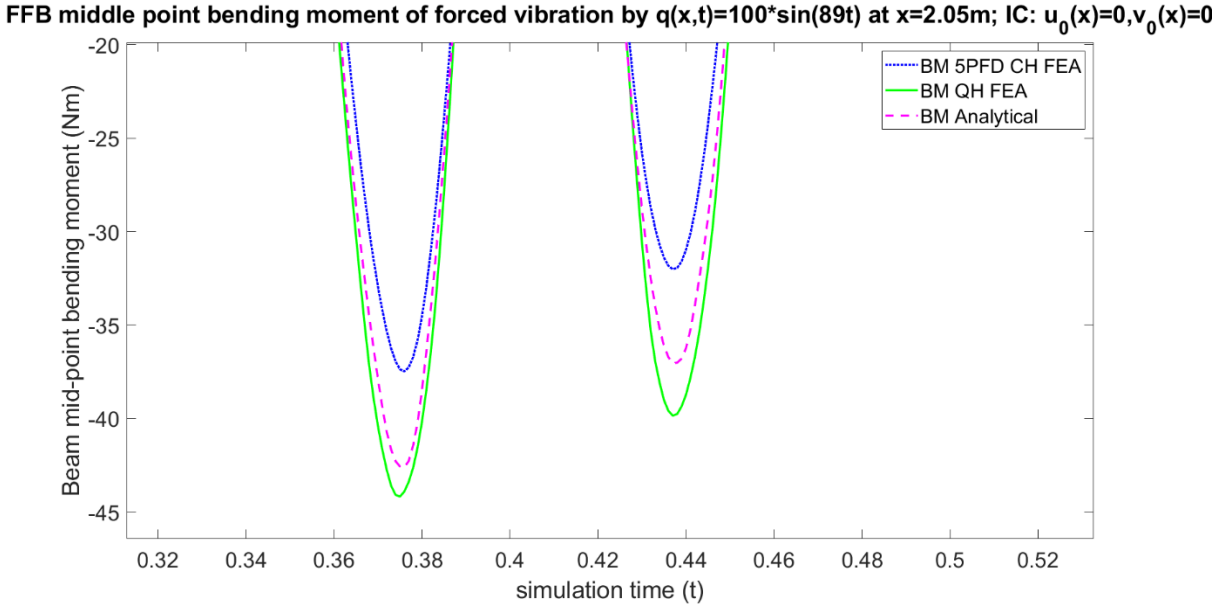

Figure 3.38 Local room in for fixed-fixed beam bending moment at the middle point

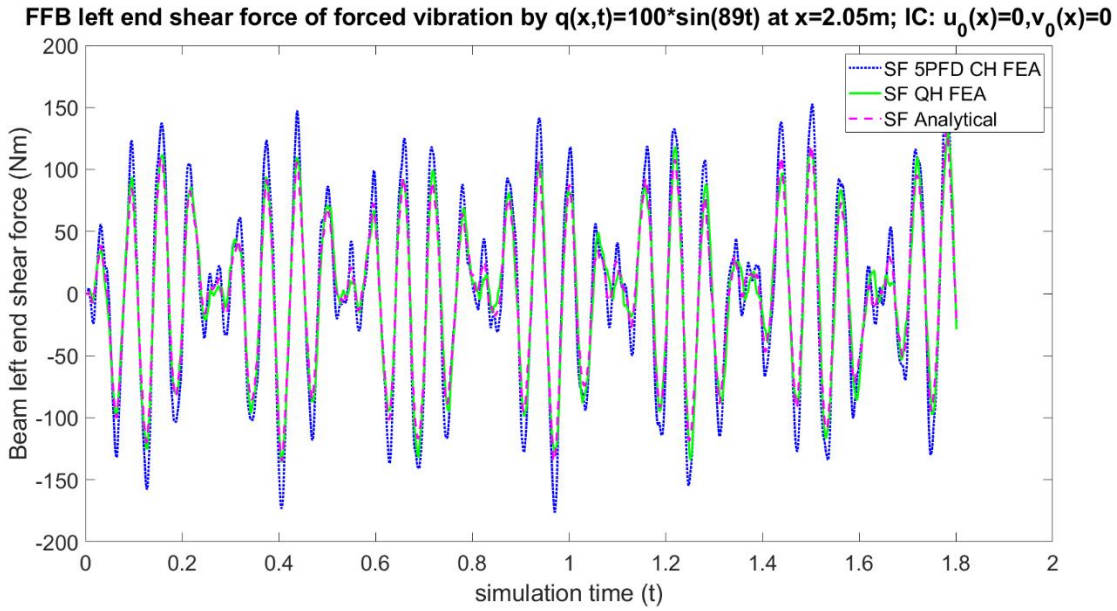

Figure 3.39 Time series of the fixed-fixed beam shear force at left fixed end

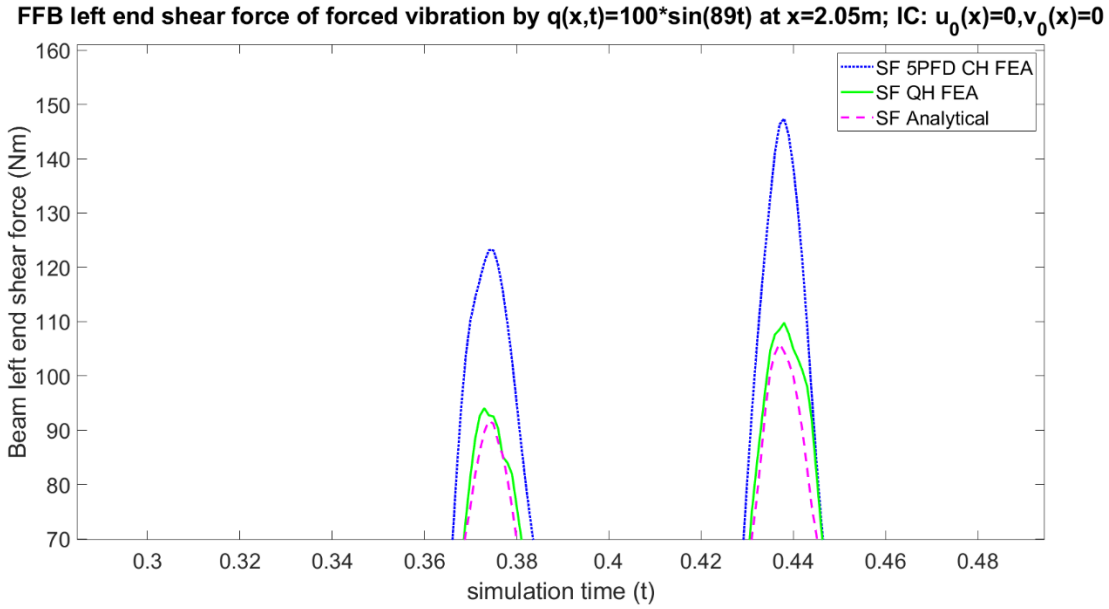

Figure 3.40 Time series of the local zoom in of the fixed-fixed beam shear force at left end

Based on the results of all the static and dynamic benchmark cases, several conclusions can be drawn as below

- For the traditional cubic Hermite finite element analyses, such as CABLE3D, they can produce good accuracy for the simulation of the beam deflection and beam slope. However, the beam bending moment and shear force always have discernable difference to the analytical results either postprocessed by using the cubic Hermite interpolation method or the five-point finite difference method, especially for cases subjected to transverse high-orders of polynomial loads and high-modes of sinusoidal loads.
- For the new quintic Hermite finite element analysis, it can not only produce good accuracy for the simulation of the beam deflection and beam slope, but also for the simulation of the beam bending moment and shear force within the whole problem domain.
- For the quintic Hermite finite element analysis, the results of the bending moment curves are continuous piecewise cubic-polynomial functions in the whole problem domain, which can dramatically facilitate the identification of the maximum bending moment position and magnitude. On the contrary, the results by cubic Hermite finite element analysis are not continuous and the maximum bending moment are either underestimated or overestimated, the error which is depending on the mesh size.

3.5 The Effectiveness Study of RISER3D

In this section, the effectiveness study of the new finite element method is performed by using different element mesh sizes for several simply-supported beam problems. The numerical simulation results obtained by CABLE3D, i.e. by cubic Hermite finite element method, and the new method RISER3D are compared to those of obtained by analytical solution.

A total of three subcases for a simply-supported beam subject to different transverse loads or restraints are analyzed in this section. The beam properties used for the effectiveness study are

shown in Table 3.6. The governing differential equation for these subcases is the equation (3.119). The objective of each subcase is to identify the beam maximum bending moment (denoted as **MBM**), the position of the maximum bending moment (denoted as **MBMPos**) and the beam maximum shear force(denoted as **MSF**) with both finite element methods, i.e. cubic Hermite finite element method (CH) and quintic Hermite finite element method (QH), using three types of element mesh, i.e. 1.0m, 0.5m and 0.33m respectively.

The first subcase assumes that the beam is subjected to a static cubic polynomial-type distributed load with problem data $f_0 = 50N/m$, $n = 3$, and $K_a = 0N/m/m$ in equation (3.119). The concerned results are summarized and compared in Table 3.8 and Table 3.9 respectively.

Table 3.8 The comparison of the beam MBM and its position for subcase1

SSB_FEM	Element No.	Mesh Size (m)	MBM_ANA (Nm)	MBM (Nm)	MBM_Rdif (%)	MBMPos_ANA (m)	MBMPos (m)	MBMPos_Rdif (%)
CH	8	1	85.5988	84.8389	-0.8877	5.3499	5.0000	-6.5403
	16	0.5	85.5988	85.4323	-0.1945	5.3499	5.5000	2.8057
	24	0.33	85.5988	85.5980	-0.0009	5.3499	5.3333	-0.3103
QH	8	1	85.5988	85.5989	0.0001	5.3499	5.3504	0.0093
	16	0.5	85.5988	85.5987	-0.0001	5.3499	5.3499	0.0000
	24	0.33	85.5988	85.5988	0.0000	5.3499	5.3499	0.0000

Table 3.9 The comparison of the beam MSF for subcase1

SSB_FEM	Element No.	Mesh Size (m)	MSF_ANA (N)	MSF (N)	MSF_Rdif (%)	GDoFs
CH	8	1	80	76.8685	-3.9144	18
	16	0.5	80	79.5601	-0.5499	34
	24	0.33	80	79.8649	-0.1689	50
QH	8	1	80	79.9659	-0.0426	27
	16	0.5	80	79.9956	-0.0055	51
	24	0.33	80	79.9987	-0.0016	75

Notes applied for all the effectiveness study cases in section 3.5:

SSB= simply-supported beam; Ana=analytical;
Rdif= relative difference;
GDoFs= global degrees of freedom;
Ana= analytical solutions;
Best= the solutions of the 0.33 element size case using RISER3D program.

The second subcase assumes that the simply supported beam is subjected to a static septic polynomial-type distributed load with problem data $f_0 = 50N/m$, $n = 7$, and $K_a = 0N/m/m$ in equation (3.119). The concerned results are summarized and compared in Table 3.10 and Table 3.11 respectively.

Table 3.10 The comparison of the beam MBM and its position for subcase2

SSB_FEM	Element No.	Mesh Size (m)	MBM_ANA (Nm)	MBM (Nm)	MBM_Rdif (%)	MBMPos_ANA (m)	MBMPos (m)	MBMPos_Rdif (%)
CH	8	1	30.0182	30.2731	0.8492	6.0787	6.0000	-1.2947
	16	0.5	30.0182	30.0127	-0.0183	6.0787	6.0000	-1.2947
	24	0.33	30.0182	29.9995	-0.0623	6.0787	6.0000	-1.2947
QH	8	1	30.0182	30.0172	-0.0033	6.0787	6.0727	-0.0987
	16	0.5	30.0182	30.0181	-0.0003	6.0787	6.0786	-0.0016
	24	0.33	30.0182	30.0182	0.0000	6.0787	6.0788	0.0016

Table 3.11 The comparison of the beam MSF for subcase2

SSB_FEM	Element No.	Mesh Size (m)	MSF_ANA (N)	MSF (N)	MSF_Rdif (%)	GDoFs
CH	8	1	44.4444	34.6261	-22.0912	18
	16	0.5	44.4444	42.3829	-4.6384	34
	24	0.33	44.4444	43.7201	-1.6297	50
QH	8	1	44.4444	44.2451	-0.4484	27
	16	0.5	44.4444	44.4165	-0.0628	51
	24	0.33	44.4444	44.4359	-0.0191	75

The third subcase assumes that the simply supported beam is subjected to a static septic polynomial-type distributed load with problem data $f_0 = 50N/m$, $n = 7$, and $K_a = 1.0e4N/m/m$ in equation (3.119). The concerned results are summarized and compared in Table 3.12 and Table 3.13 respectively.

Table 3.12 The comparison of the beam MBM and its position for subcase3

SSB_FEM	Element No.	Mesh Size (m)	MBM_Best (Nm)	MBM (Nm)	MBM_Rdif (%)	MBMPos_Best (m)	MBMPos (m)	MBMPos_Rdif (%)
CH	8	1	7.8935	8.6720	9.8625	7.2145	7.0000	-2.9732
	16	0.5	7.8935	7.6295	-3.3445	7.2145	7.0000	-2.9732
	24	0.33	7.8935	7.7854	-1.3695	7.2145	7.3333	1.6467
QH	8	1	7.8935	7.8833	-0.1292	7.2145	7.2180	0.0485
	16	0.5	7.8935	7.8938	0.0038	7.2145	7.2149	0.0055
	24	0.33	7.8935	7.8935	0.0000	7.2145	7.2145	0.0000

Table 3.13 The comparison of the beam MSF for subcase3

SSB_FEM	Element No.	Mesh Size (m)	MSF_Best (N)	MSF (N)	MSF_Rdif (%)	GDoFs
CH	8	1	24.5121	9.1803	-62.5479	18
	16	0.5	24.5121	21.3997	-12.6974	34
	24	0.3333	24.5121	23.5183	-4.0543	50
QH	8	1	24.5121	24.2792	-0.9501	27
	16	0.5	24.5121	24.5061	-0.0245	51
	24	0.3333	24.5121	24.5121	0.0000	75

According to the effectiveness studies in this section, it can be seen that, compared to traditional cubic Hermite finite element method, the new quintic Hermite finite element method can:

- show better effectiveness by converging to the true solutions with large mesh size
- yield much more accurate results, especially for the coarse element cases
- save computational effort by produce more accurate simulation results while solving even smaller global system of equations

4 RISER3D APPLICATION TO EIGENVALUE PROBLEMS OF RISERS

Another typical problem that frequently encountered in structural engineering filed is that a governing differential equation which governs the dependent variable also contains unknown parameters. Both the dependent variable and the unknown parameters in the equation should be determined simultaneously such that all involved boundaries are also satisfied. This type of engineering problem is the called eigenvalue problem. As for marine risers, the study of the axial and transverse vibrations, triggered by three-dimensional host platform translational movements under combined effect of the wind, wave and current, is of great importance for a better understanding of riser dynamics. The riser transverse vibrations are also known as vortex-induced vibrations (VIVs), which are widely researched and analyzed in recent decades because they can cause severe fatigue damage to the risers.

This chapter mainly address on the application of RISER3D on the transverse modal vibrations of near vertical marine risers, i.e. top-tensioned risers (TTRs). To validate the accuracy and robustness of the eigenvalue module of RISER3D program, the transverse vibration of simple Euler Bernoulli beams subject to a constant tension are firstly studied, which consist of analytical results that can help to verify the numerical simulation results. The essential difference between the simple beam mathematical model and the vertical riser mathematical model is that the tension in the former is a constant while varies with respect to the vertical elevation for the latter.

4.1 Analytical Natural Frequency Analysis on a Constant Tension Beam

This section studies the transverse vibration of a simple prismatic Euler Bernoulli beam subject to a constant tension. The free-body diagram of the problem is illustrated in Figure 4.1.

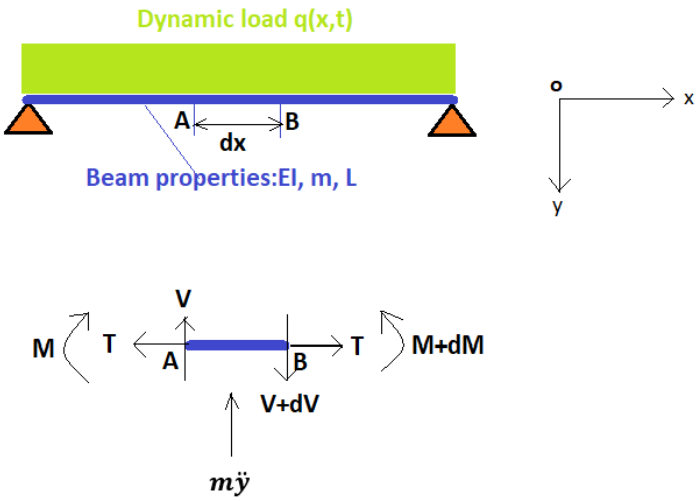

Figure 4.1 The free-body diagram of a tensioned beam subject to dynamic load

Assuming the constant tension T is in the axial direction of the beam and the positive beam slopes at point A and point B are denoted as $\frac{\partial y}{\partial x}$ and $\frac{\partial y}{\partial x}+\frac{\partial}{\partial x}\left(\frac{\partial y}{\partial x}\right)dx$ respectively. For an infinitesimal element dx in the beam, as shown in Figure 4.1, the following force equilibrium equation can be established in the vertical direction by assuming the transverse deflection is small.

$$-V+\left(V+\frac{\partial V}{\partial x}dx\right)-T\frac{\partial y}{\partial x}+T\left[\frac{\partial y}{\partial x}+\frac{\partial}{\partial x}\left(\frac{\partial y}{\partial x}\right)dx\right]-m\frac{\partial^2 y}{\partial t^2}dx=0\ (x\in[0,L]) \tag{4.1}$$

where V is the beam shear force, T is the constant axial tension, $y(x,t)$ is the transverse displacement of the beam, m is mass of the beam per unit length, L is the total length of the beam.

Besides, implementing the conservation of angular momentum can lead to the following equilibrium equation

$$-M+M+\frac{\partial M}{\partial x}dx-\left(V+\frac{\partial V}{\partial x}dx\right)dx+m\frac{\partial^2 y}{\partial t^2}dx\cdot dx=0 \tag{4.2}$$

Further simplification of equation (4.1) by omitting higher order terms yields

$$\frac{\partial V}{\partial x}+T\frac{\partial}{\partial x}\left(\frac{\partial y}{\partial x}\right)-m\frac{\partial^2 y}{\partial t^2}=0 \tag{4.3}$$

Further simplification of equation (4.2) by omitting higher order terms yields

$$\frac{\partial M}{\partial x} = V \tag{4.4}$$

According to structural mechanics in Euler Bernoulli beam theory, together with the shear force and bending moment sign convention as shown in Figure 4.1, the bending moment of a simple beam with constant bending stiffness EI can be expressed as

$$M = -EI\frac{\partial^2 y}{\partial x^2} \tag{4.5}$$

Substitution of equation (4.4) and (4.5) into equation (4.3) can generate the governing differential equation of the small deflection transverse free vibration of the beam as

$$\frac{\partial^2}{\partial x^2}\left(-EI\frac{\partial^2 y}{\partial x^2}\right) + T\frac{\partial}{\partial x}\left(\frac{\partial y}{\partial x}\right) - m\frac{\partial^2 y}{\partial t^2} = 0 \tag{4.6}$$

When the beam vibrates in one of its natural modes, the transverse deflection of beam varies harmonically with time in the beam domain as

$$y(x,t) = X(x)\varphi(t) = X(x)(A cos\omega t + B sin\omega t) \tag{4.7}$$

where the subscript n for the n^{th} mode has been omitted for brevity, A, B are unknown constants here, ω is the beam vibration natural frequency, $X(x)$ is the mode shape function.

Plugging equation (4.7) into equation (4.6) leads to

$$EIX'''' - TX'' - m\omega^2 X = 0 \tag{4.8}$$

By letting $S = \frac{T}{2EI}$ and $U^2 = \frac{m\omega^2}{EI}$, equation (4.8) can be rewritten as

$$X'''' - 2SX'' - U^2 X = 0 \tag{4.9}$$

Hence, the general form of the solution of equation (4.9) can be solved mathematically as

$$X(x) = Csinh(\alpha x) + Dcosh(\alpha x) + Esin(\beta x) + Fcos(\beta x) \tag{4.10}$$

where $\alpha = \sqrt{S + \sqrt{S^2 + U^2}}$, $\beta = \sqrt{-S + \sqrt{S^2 + U^2}}$ are positive real parameters, parameters C, D, E, F are unknown constants which can be determined by the four boundary conditions at both ends of the beam.

Now taking a simply-supported beam as an example, the four boundary conditions at the ends of the beam can be expressed as

$$X(0) = 0; X(L) = 0; X''(0) = 0; X''(L) = 0 \tag{4.11}$$

Substitution of the beam general solution function (4.10) into the four the boundary conditions in equation (4.11) respectively, the following system of equations can be obtained

$$\begin{bmatrix} 0 & 1 & 0 & 1 \\ \alpha & 0 & \beta & 0 \\ sinh\,(\alpha L) & cosh\,(\alpha L) & sin(\beta L) & cos(\beta L) \\ \alpha cosh\,(\alpha L) & \alpha sinh\,(\alpha L) & \beta cos(\beta L) & -\beta sin(\beta L) \end{bmatrix} \begin{Bmatrix} C \\ D \\ E \\ F \end{Bmatrix} = \begin{Bmatrix} 0 \\ 0 \\ 0 \\ 0 \end{Bmatrix} \tag{4.12}$$

To achieve a set of nontrivial solution for the four unknown constants, the determinant of the four by four coefficient matrix in equation (4.12) must be equal to zero, which leads to

$$(\alpha^4 + 2\alpha^2\beta^2 + \beta^4) sin\,h(\alpha L) sin(\beta L) = 0 \tag{4.13}$$

Considering that the parameters α, β and L are all real and positive numbers, the following relationship must be held

$$sin(\beta L) = 0 \tag{4.14}$$

Equation (4.14) is called the frequency equation of the transverse vibration of a simply-supported constant-tension beam. Therefore, all the positive roots of the parameter β can be obtained by solving the frequency equation as $\beta_n = \frac{n\pi}{L}$ $(n = 1,2,3, \dots)$. By incorporation of the expressions for β, S and U^2 mentioned above, the final expression for the beam natural frequencies can be written as

$$\omega_n = \frac{n\pi}{L}\sqrt{\frac{T^*}{m}} \quad (n = 1,2,3, \dots) \tag{4.15}$$

where $T^* = T + EI\left(\frac{n\pi}{L}\right)^2$.

Therefore, if the beam bending stiffness EI is zero, the beam model will descend to a cable or wire model subject to constant tension with fixed boundary conditions, the natural frequencies of which can be simply obtained as

$$\omega_n = \frac{n\pi}{L}\sqrt{\frac{T}{m}} \ (n = 1,2,3,\dots) \tag{4.16}$$

Back substitution of equation (4.14) into equation (4.12), it can be obtained that, among the four unknown constants, the only nonzero constant is E; C, D and F are all zeros. Hence, the solution of the simply-supported beam mode shape function (4.9) can be simplified as

$$X(x) = Esin\left(\frac{n\pi}{L}x\right) \tag{4.17}$$

Finally, by superposition of the solution for different vibrational modes of the differential governing equation, the response of the simply-supported Euler Bernoulli beam can be expressed as

$$y(x,t) = E_n sin\left(\frac{n\pi}{L}x\right)(A_n cos\omega_n t + B_n sin\omega_n t) \ (n = 1,2,3,\dots) \tag{4.18}$$

where the constants E_n can be obtained by normalization of the product of two distinct mode shape functions to unity, unknown constants A_n and B_n should be determined according the initial conditions of the beam, i.e. the initial beam position and velocity before the start of the vibration.

4.2 Analytical Analysis on Transverse Vibration of Vertical Marine Risers

4.2.1 Bessel Function Approximation of a Vertical Riser

For the analytical analysis of a tensioned near-vertical marine riser subject to transverse vibration, we can start with the free-body diagram as illustrated in Figure 4.2.

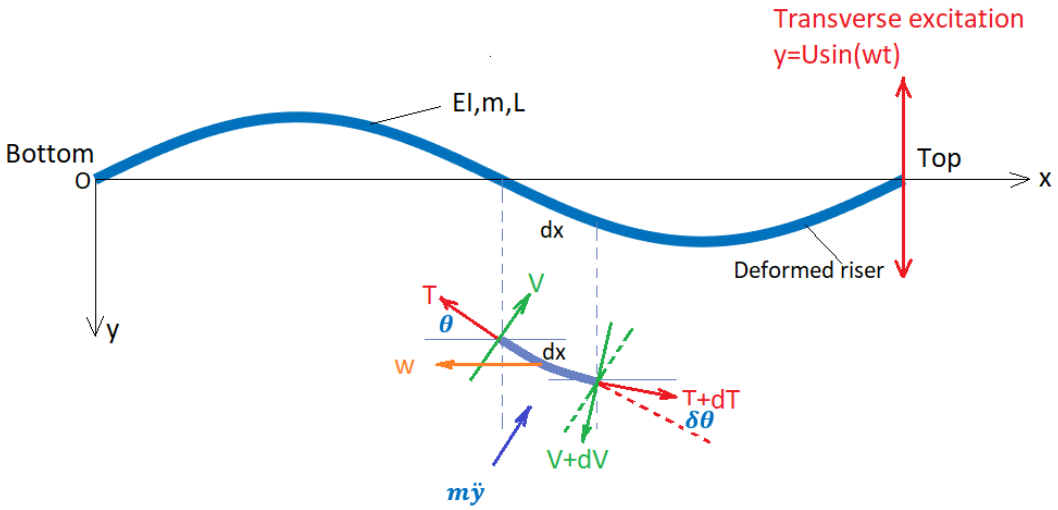

Figure 4.2 The free body diagram for a vertical riser in the global coordinate system

From Figure 4.2, the riser element under free vibration is subject to shear force, axial effective tension, submerged weight and inertial force, denoted as V, T, w and $m\ddot{y}$ respectively. By application of the conservation of linear momentum, the following force equilibrium equation can be established for an infinitesimal length dx as

$$-V + \left(V + \frac{\partial V}{\partial x}dx\right) + wdx \cdot sin\theta - (T + \delta T)\sin(-\delta\theta) - mdx \cdot \ddot{y} = 0 \tag{4.19}$$

By assuming the rotation angle θ is a small for the riser model, then the two relationships of $\theta \approx sin\theta \approx tan\theta = \frac{dy}{dx}$, $\delta\theta = \frac{\partial\theta}{\partial x}dx \approx \frac{\partial}{\partial x}\left(\frac{\partial y}{\partial x}\right)dx$ can hold straightforwardly. Incorporating these two relationships, together with relationships in equation (4.4) and (4.5), to equation (4.19) and omitting the higher order terms, the governing motion equation can be obtained for a vertical riser as

$$\frac{\partial^2}{\partial x^2}\left(-EI\frac{\partial^2 y}{\partial x^2}\right) + T\frac{\partial}{\partial x}\left(\frac{\partial y}{\partial x}\right) + w\frac{dy}{dx} - m\frac{\partial^2 y}{\partial t^2} = 0 \tag{4.20}$$

For the case without bending rigidity, i.e. $EI = 0$, equation (4.20) descends to

$$T\frac{\partial}{\partial x}\left(\frac{\partial y}{\partial x}\right)+w\frac{dy}{dx}-m\frac{\partial^2 y}{\partial t^2}=0 \tag{4.21}$$

The subsequent derivations in section 4.2 have mainly followed previous literature work of Senjanovic et al. (2006) and Sparks (2007), for a linearly varied effective tension TTR, by letting

$$z_x=\frac{2\sqrt{mT_x}}{w}\omega_n \tag{4.22}$$

$$y(x,t)=Y_x sin(\omega_n t) \tag{4.23}$$

where m is the mass of the riser per unit length in air, w is the submerged weight of riser per unit length, $T_x=T_b+wx$ is the effective tension at elevation x, ω_n are the natural frequencies of transverse modal vibration, Y_x is the mode shape function of the riser.

By substitution of equation (4.22) and (4.23) into the equation (4.21), the follow equation can be obtained after some math derivation

$$\frac{d^2Y_x}{dz_x{}^2}+\frac{1}{z_x}\frac{dY_x}{dz_x}+Y_x=0 \tag{4.24}$$

Obviously, the equation (4.24) has the form of the Bessel differential equation. Therefore, its solution can be written as

$$Y_x=AJ_0(z_x)+BY_0(z_x) \tag{4.25}$$

where $J_0(z_x)$ and $Y_0(z_x)$ are zero-order Bessel functions of the first and second kind for order zero. A and B are unknown constants which should be determined by the boundary conditions at the riser extremities.

Although equation (4.25) is exactly the analytical solution of equation (4.21), this equation has little practical application due to the complexity of evaluating the Bessel functions (Sparks, 2007).

4.2.2 Simple Cable Analysis Method for a Vertical Riser

For simplicity, a simplified simple cable analysis method, compared to the Bessel cable analysis, is introduced by a minor modification of the second term in equation (4.21). The modification is halving the second term which will not take a great hit the final solution. The valid reasons to make this modification include

- Compared to the length of the near-vertical riser, the amplitude of the modal vibration is very small; Hence, dy/dx is very small
- The second term changes sign at the crest of the modal wave, i.e. at the antinodes as illustrated in Figure 4.2, when integrated over adjacent nodes, the results is zero.

After this modification, equation (4.21) can be simplified as

$$T\frac{\partial^2 y}{\partial x^2} + \frac{w}{2}\frac{dy}{dx} - m\frac{\partial^2 y}{\partial t^2} = 0 \tag{4.26}$$

Substitution of equation (4.22) and (4.23) into equation (4.26) can yield

$$\frac{d^2 Y_x}{dz_x{}^2} + Y_x = 0 \tag{4.27}$$

The general solution of equation (4.27) can be written as

$$Y_x = Y_a sin(z_x - z_b) \tag{4.28}$$

where Y_a is the amplitude of modal shape (a constant), z_b is the value of z_x at the bottom end of the riser.

Compared to equation (4.25), the solution in equation (4.28) is much simpler with constant amplitudes at the antinodes, while for equation (4.25), the amplitude at antinodes decrease from the bottom end to top end. Since experimental data show that under VIV lock-in conditions, the riser amplitude auto-limited to about one diameter, the simple cable analysis method can be a better approach to illustrate this point than the Bessel cable analysis method (Sparks, 2007).

For the n^{th} mode, both the top and bottom end of the riser are node points, i.e. $Y_x = 0$; Hence, the following relationship can be obtained straightforwardly

$$z_t - z_b = \frac{2\sqrt{mT_t}}{w}\omega_n - \frac{2\sqrt{mT_b}}{w}\omega_n = n\pi \tag{4.29}$$

where T_t and T_b are the riser top and bottom end effective tension, which satisfies the relationship of $T_t - T_b = wL$.

Therefore, the n^{th} mode natural frequency can be computed by equation (4.29) as

$$\omega_n = \frac{n\pi w}{2\sqrt{m}(\sqrt{T_t}-\sqrt{T_b})} \tag{4.30}$$

The n^{th} mode natural period can be computed by

$$T_n = \frac{2\pi}{\omega_n} = \frac{4\sqrt{m}(\sqrt{T_t}-\sqrt{T_b})}{nw} = \frac{4L/n}{\sqrt{T_t/m}+\sqrt{T_b/m}} \tag{4.31}$$

4.2.3 Simple Beam Analysis Method for a Vertical Riser with Bending Rigidity

In section 4.2.1 and 4.2.2, the bending rigidity are assumed to be zero, this section takes the bending rigidity of the riser into consideration. For a vertical uniformly varied tension marine riser, the differential motion equation can be obtained by adding the bending term to equation (4.26) as

$$\frac{\partial^2}{\partial x^2}\left(-EI\frac{\partial^2 y}{\partial x^2}\right) + T_x\frac{\partial^2 y}{\partial x^2} + \frac{w}{2}\frac{dy}{dx} - m\frac{\partial^2 y}{\partial t^2} = 0 \tag{4.32}$$

By comparing the natural frequencies as shown in equation (4.15) and (4.16), it can be concluded that, from cable model to beam model, the effect of bending rigidity is an increment of cable tension by an amount of $(n\pi/L)^2 EI$. By similarity, we can assume that

$$-EI\frac{\partial^4 y}{\partial x^4} = Q_x\frac{\partial^2 y}{\partial x^2} \tag{4.33}$$

$$T_x{}^* = T_x + Q_x \tag{4.34}$$

where Q_x is an unknown mean constant effective tension to be determined.

By substitution of equation (4.33) and (4.34) into equation (4.32) lead to

$$T_x{}^* \frac{\partial^2 y}{\partial x^2} + \frac{w}{2}\frac{dy}{dx} - m\frac{\partial^2 y}{\partial t^2} = 0 \tag{4.35}$$

which has exactly the same form of equation (4.26). In order to be distinguish with the results of the simple cable analysis method, all relevant parameters, in this section, are superscripted with a star symbol '*' for the simple beam analysis method.

By analogy to the simple cable analysis results, it can be assumed that the solution between the kth and (k+1)th node of equation (4.35) has a form of

$$y(x,t) = Y_a sin(z_x{}^* - z_k{}^*) sin(\omega_n{}^* t) \tag{4.36}$$

where $z_x{}^* = \frac{2\sqrt{mT_x{}^*}}{w}\omega_n{}^*$, Y_a is the mode shape amplitude.

Integrating equation (4.33) twice with respect to x can lead to

$$-EI\frac{\partial^2 y}{\partial x^2} = Q_x y \tag{4.37}$$

By integrating both sides of equation (4.37) with respect to x over the interval $[z_k{}^*, z_{k+1}{}^*]$, which can be expressed as

$$\int_{z_k{}^*}^{z_{k+1}{}^*} \left(-EI\frac{\partial^2 y}{\partial x^2}\right) dx = \int_{z_k{}^*}^{z_{k+1}{}^*} (Q_x y) dx \tag{4.38}$$

For uniformly varied tension riser, the following differentiation relationship hold

$$\frac{dz_x{}^*}{dx} = \frac{2}{a^* z_x{}^*} \tag{4.39}$$

where $a^* = \frac{w}{m(\omega_n{}^*)^2}$.

Substituting equation (4.36) and (4.39) into equation (4.38) and performing the integration lead to

$$\frac{2Y_a EI}{a^*}\frac{z_k{}^* + z_{k+1}{}^*}{z_k{}^* z_{k+1}{}^*} sin(\omega_n{}^* t) = \frac{Y_a Q_x a^*}{2}(z_k{}^* + z_{k+1}{}^*) sin(\omega_n{}^* t) \tag{4.40}$$

Hence, Q_x can be evaluated by equation (4.40) as

$$Q_x = \frac{4EI}{z_k{}^* z_{k+1}{}^* a^{*2}} = \left(\frac{2m\omega_n{}^{*2}}{w}\right)^2 \frac{EI}{z_k{}^* z_{k+1}{}^*} = m\omega_n{}^{*2}\frac{EI}{\sqrt{T_k{}^* T_{k+1}{}^*}} \tag{4.41}$$

Since the transmission time between adjacent nodes is equal to half of the modal period, the following relationship hold

$$t^*_{k,k+1} = \frac{L^*_{k,k+1}}{c_k^*} = \frac{T_n^*}{2} = \frac{\pi}{\omega_n^*} \tag{4.42}$$

where $L^*_{k,k+1}$is the riser length between the kth and k+1th node, $c_k^*$is the mean celerity between the k^{th} and $k+1^{th}$ node, $T_n^*$is the n^{th} mode natural modal period.

Therefore, by equation (4.42), the nth mode natural frequency can be expressed as

$$\omega_n^* = \frac{\pi c_k^*}{L^*_{k,k+1}} = \frac{\pi\left(\sqrt{T_k^*/m}+\sqrt{T_{k+1}^*/m}\right)}{2L^*_{k,k+1}} \tag{4.43}$$

Substitution of equation (4.43) into equation (4.41) leads to

$$Q_x = \frac{\left(\sqrt{T_k^*}+\sqrt{T_{k+1}^*}\right)^2}{4\sqrt{T_k^* T_{k+1}^*}} EI \left(\frac{\pi}{L^*_{k,k+1}}\right)^2 \tag{4.44}$$

The mean celerity between adjacent nodes can therefore be expressed as

$$c_k^* = \frac{\sqrt{T_k+Q_x}+\sqrt{T_{k+1}+Q_x}}{2\sqrt{m}} = \frac{2L^*_{k,k+1}}{T_n^*} \tag{4.45}$$

The total riser length can be computed by

$$L = \sum_{k=1}^{n} L^*_{k,k+1} = \sum_{k=1}^{n} \frac{c_k^* T_n^*}{2} = \frac{T_n^*}{2}\sum_{k=1}^{n} c_k^* \tag{4.46}$$

Finally, the nth mode natural period can be computed as

$$T_n^* = \frac{2L}{\sum_{k=1}^{n} c_k^*} = \frac{2L}{\sum_{k=1}^{n} \frac{\sqrt{T_k+Q_x}+\sqrt{T_{k+1}+Q_x}}{2\sqrt{m}}} \tag{4.47}$$

The length between adjacent node can be computed as

$$L^*_{k,k+1} = \frac{c_k^* T_n^*}{2} = \frac{\sqrt{T_k+Q_x}+\sqrt{T_{k+1}+Q_x}}{\sum_{k=1}^{n}\left(\sqrt{T_k+Q_x}+\sqrt{T_{k+1}+Q_x}\right)} L \tag{4.48}$$

Although the simple beam analysis can yield reasonable accuracy, it is involved of great complexity due to there is no explicit expressions for either the mean constant tension Q_x and

length $L^*_{k,k+1}$, two key parameters are need to be solved by a iteration procedure by using their coupled relationship as given by equation (4.44) and (4.48).

4.3 Comparison of Analytical Solutions with both CALBE3D and RISER3D

4.3.1 Eigenvalue Finite Element Model Formulation for Tensioned Beam and Riser

For a prismatic Euler Bernoulli beam under a constant tension, the weak form of the equation (4.8), for a typical element with length h, can be derived by using Galerkin's finite element method and the general quintic Hermite shape functions $a_i(x)$ $(i = 1{\sim}6)$ as

$$\int_0^h (EIX'''' - TX'' - m\omega^2 X)\, a_i(x) dx = 0 \tag{4.49}$$

Integration by parts three times for the first term of the integrand and once for the second term, leads to

$$\int_0^h [-EIX' a_i'''(x) + TX' a_i'(x) - m\omega^2 X a_i(x)] dx = \{[-EIX''' + TX']a_i(x) + EIX'' a_i'(x) - EIX' a_i''(x)\}\Big|_0^h \tag{4.50}$$

For Galerkin's finite element model, the beam transverse mode shape function can be approximated using the general quintic Hermite shape functions as

$$X(x) = \sum_{j=1}^{6} u_j a_j(x) \;\; (j = 1{\sim}6) \tag{4.51}$$

where $a_j(x)$ are non-normalized quintic Hermite shape functions.

By substitution of equation (4.51) into the weak form equation (4.50), the quintic Hermite finite element model for the beam natural frequency analysis can be written in a compact form of

$$[K_{ij}]\{u_j\} - {\omega_n}^2[M_{ij}]\{u_j\} = \{F_i\} \tag{4.52}$$

where the element matrices are defined by the following equations

$$K_{ij} = -EI\alpha_{ij} + T\beta_{ij} \tag{4.53}$$

$$M_{ij} = m\eta_{ij} \tag{4.54}$$

$$\alpha_{ij} = \int_0^h a_i'''(x)\, a_j(x)dx = \frac{J_i J_j}{h^3}\int_0^1 \phi_i'''(\xi)\, \phi_j(\xi)d\xi = \frac{J_i J_j}{h^3}\bar{\alpha}_{ij} \tag{4.55}$$

$$\beta_{ij} = \int_0^h a_i'(x)\, a'_j(x)dx = \frac{J_i J_j}{h}\int_0^1 \phi_i'(\xi)\, \phi'_j(\xi)d\xi = \frac{J_i J_j}{h}\bar{\beta}_{ij} \tag{4.56}$$

$$\eta_{ij} = \int_0^h a_i(x)a_j(x)dx = J_i J_j h\int_0^1 \phi_i(\xi)\phi_j(\xi)d\xi = J_i J_j h\bar{\eta}_{ij} \tag{4.57}$$

After obtaining the typical element matrices, they are assembled to form the global stiffness matrix **GLK** and mass matrix **GLM**. Apply the specified boundary conditions to the finite element model and solving the assembled system of equations using an eigen-solver, the natural frequencies ω_n $(n = 1,2,3, \dots)$ of the beam can be obtained. By substituting each natural frequency to the assembled global system of equations, the eigenvectors corresponding to each natural frequency can be computed, which can be used to compute the corresponding mode shapes of the beam.

For natural frequency computation of a near-vertical riser using quintic Hermite finite element method, it is analogy to the procedures for the constant tension beam. For example, the governing motion equation of a Top-tensioned Riser (TTR), a schematic hinged-hinged model as illustrated in Figure 4.3, with a linearly varying effective tension can be written as

$$m\frac{\partial^2 y}{\partial t^2} + EI\frac{\partial^4 y}{\partial x^4} - \frac{\partial}{\partial x}\left[(T_c + T_L x)\frac{\partial y}{\partial x}\right] = q(x,t) \tag{4.58}$$

where $y(x,t)$ is the riser lateral deflection, virtual mass $m = \rho_s(A_e - A_i) + \rho_i A_i + C_a\rho_f A_e$, $T_c = T_b + Lg(\rho_f A_e - \rho_i A_i)$, $T_L = w + g(\rho_i A_i - \rho_f A_e)$, ρ_s, ρ_i and ρ_f are the density of the riser pipe, the density of the internal content, the density of sea water respectively, $C_a$is the added-mass coefficient, $A_e$and A_i are the external and internal cross-sectional area respectively, T_b is the TTR bottom tension at the ball joint, g is the gravitational constant, w is the effective weight of riser per unit length, L is the total length of the TTR, t is time, $q(x,t)$ is the external transverse loads.

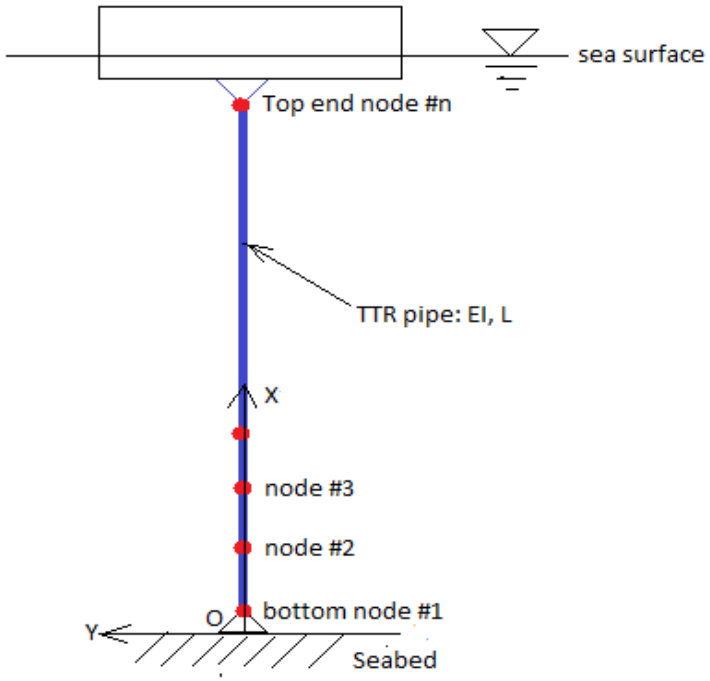

Figure 4.3 A schematic finite element model for a hinged-hinged TTR

Following the same procedures from equation (4.49) to (4.52), the final finite element model for the TTR natural frequency analysis can be written as

$$[K_{ij}]\{u_j\} - \omega^2[M_{ij}]\{u_j\} = \{F_i\} \tag{4.59}$$

where the element matrices for this equation are defined as

$$K_{ij} = EI\alpha_{ij} + {\beta_{ij}}^* \tag{4.60}$$

$$M_{ij} = m\eta_{ij} \tag{4.61}$$

$${\beta_{ij}}^* = \int_0^L (T_c + T_L x) a_i'(x)\, a'_j(x) dx = \frac{J_i J_j}{h} \int_0^1 [T_c + T_L(ie - 1 + \xi)h] \phi_i'(\xi)\, \phi'_j(\xi) d\xi = \frac{J_i J_j}{h} \bar{\beta}_{ij} \tag{4.62}$$

α_{ij} and η_{ij} are defined in equation (4.55) and (4.57) respectively.

The same procedures of the constant-tension beam eigenvalue problem can be followed to compute the natural frequencies of the TTR, which are omitted here for brevity.

4.3.2 Constant Tension Beam Natural Frequencies Analysis by RISER3D

The key objective of this case study is to benchmark the simulation results for the eigenvalue problem module of RISER3D program. The natural frequencies of a prismatic Euler Bernoulli beam, subject to a constant tension in axial direction, are computed with both analytical analyses and two numerical methods, i.e. CABLE3D and RISER3D.

Two cases are studied in this section. The first case is for the computation of the natural frequencies of a short prismatic rectangular Euler Bernoulli beam, the properties of which are summarized in Table 4.1. The second case is for the computation of the natural frequencies of a long steel wire, the properties of which are summarized in table 4.2. In both cases, the slender structures are subject to constant tension T and pinned-pinned boundary conditions at the boundaries.

Table 4.1 The properties of a constant tension beam

Designation	**Value**	**Unit**
Beam Length L	3.00	m
Beam Width bw	0.02	m
Beam Height bh	0.015	m
Cross Sectional Area A_b	3.00E-04	m2
Young's Modulus E	2.07E+11	N/m2

Table 4.1 Continued

Designation	Value	Unit
Second moment Inertia I	5.625-09	m4
Bending rigidity B	1164.375	Nm2
Material density ρ	7850.0	kg/m3
Axial tensile force T	2.00E+02	N

Table 4.2 The properties of a constant tension steel cable

Designation	Value	Unit
Steel cable Length L	100.0	m
Cable diameter D	0.01	m
Cross-sectional Area A_b	7.8540E-05	m2
Young's Modulus E	2.07E+11	N/m2
Second moment Inertia I	4.9087E-10	m4
Bending rigidity B	101.61	Nm2
Material density ρ	7850.0	kg/m3
Mass per unit length m	0.6165	Kg/m
Axial tensile force T	3.00E+02	N

For the first case, two types of element size are used, the first one is using a total of 6 uniform length elements to mesh the 3m length beam, with an element length of 0.5m; the second one is using a total of 12 uniform length elements with an element length of 0.25m. The natural frequencies for the first ten vibrational modes by two types of mesh size are presented in Table 4.3

and Table 4.4 respectively. Analytical results are calculated by using equation (4.15), CALBE3D denotes the traditional finite element method by using cubic Hermite shape functions, RISER3D denotes the new finite element method by using quintic Hermite shape functions.

Table 4.3 0.5m mesh size results for the beam case

Natural Frequencies (1/sec)	**Analytical**	**CABLE3D**	**RISER3D**	**Dif_CABLE3D (%)**	**Dif_RISER3D (%)**
ω1	26.2244	26.2256	26.2244	0.0045	0.0000
ω2	99.4281	99.5056	99.4281	0.0780	0.0000
ω3	221.3591	222.2186	221.3593	0.3883	0.0001
ω4	392.0520	396.6446	392.0566	1.1714	0.0012
ω5	611.5113	627.6541	611.5609	2.6398	0.0081
ω6	879.7382	976.0617	880.3645	10.9491	0.0712
ω7	1196.7331	1319.3502	1198.0724	10.2460	0.1119
ω8	1562.4962	1813.3711	1566.6355	16.0560	0.2649
ω9	1977.0276	2450.6669	1987.2820	23.9571	0.5187
ω10	2440.3273	3243.2130	2462.2271	32.9007	0.8974

Table 4.4 0.25m mesh size results for the beam case

Natural Freq. (1/sec)	**Analytical**	**CABLE3D**	**RISER3D**	**Dif_CABLE 3D (%)**	**Dif_RISER3 D (%)**
ω1	26.2244	26.2245	26.2244	0.0003	0.0000
ω2	99.4281	99.4330	99.4281	0.0050	0.0000
ω3	221.3591	221.4156	221.3591	0.0255	0.0000
ω4	392.0520	392.3664	392.0520	0.0802	0.0000
ω5	611.5113	612.6925	611.5114	0.1932	0.0000
ω6	879.7382	883.1961	879.7391	0.3931	0.0001
ω7	1196.7331	1205.2451	1196.7377	0.7113	0.0004
ω8	1562.4962	1580.9236	1562.5150	1.1794	0.0012
ω9	1977.0276	2013.0896	1977.0932	1.8241	0.0033
ω10	2440.3273	2505.0160	2440.5261	2.6508	0.0081

For the second cable case, two types of element size are used, the first one is using a total of 10 uniform length elements to mesh the 100m length steel cable, with an element length of 10m; the second one is using a total of 25 uniform length elements to mesh the problem domain, with an element length of 4m. The natural frequencies for the first eighteen modes by two types of mesh size are presented in Table 4.5 and Table 4.6 respectively.

Table 4.5 10m mesh size results for the steel cable case

Natural Freq. (1/sec)	**Analytical**	**CABLE3D**	**RISER3D**	**Dif_CABLE 3D (%)**	**Dif_RISER3 D (%)**
ω1	0.6931	0.6931	0.6931	0.0000	0.0000
ω2	1.3869	1.3869	1.3869	0.0001	0.0000
ω3	2.0821	2.0821	2.0821	0.0011	0.0000
ω4	2.7794	2.7795	2.7794	0.0051	0.0000
ω5	3.4794	3.4800	3.4794	0.0168	0.0000
ω6	4.1829	4.1847	4.1829	0.0428	0.0000
ω7	4.8905	4.8951	4.8905	0.0926	0.0001
ω8	5.6030	5.6130	5.6030	0.1784	0.0004
ω9	6.3208	6.3408	6.3209	0.3155	0.0016
ω10	7.0448	7.1159	7.0455	1.0092	0.0090
ω11	7.7756	7.8449	7.7764	0.8916	0.0109
ω12	8.5138	8.6317	8.5157	1.3852	0.0226
ω13	9.2599	9.4557	9.2638	2.1137	0.0415
ω14	10.0147	10.3313	10.0217	3.1608	0.0697
ω15	10.7788	11.2760	10.7906	4.6132	0.1094
ω16	11.5526	12.3034	11.5715	6.4983	0.1635
ω17	12.3369	13.4012	12.3659	8.6269	0.2356
ω18	13.1321	14.4850	13.1754	10.3021	0.3299

Table 4.6 4m mesh size results for the steel cable case

Natural Freq. (1/sec)	**Analytical**	**CABLE3D**	**RISER3D**	**Dif_CABLE 3D (%)**	**Dif_RISER3 D (%)**
ω1	0.6931	0.6931	0.6931	0.0000	0.0000
ω2	1.3869	1.3869	1.3869	0.0000	0.0000
ω3	2.0821	2.0821	2.0821	0.0000	0.0000
ω4	2.7794	2.7794	2.7794	0.0001	0.0000
ω5	3.4794	3.4794	3.4794	0.0002	0.0000
ω6	4.1829	4.1829	4.1829	0.0005	0.0000
ω7	4.8905	4.8906	4.8905	0.0013	0.0000
ω8	5.6030	5.6031	5.6030	0.0028	0.0000
ω9	6.3208	6.3212	6.3208	0.0055	0.0000
ω10	7.0448	7.0455	7.0448	0.0100	0.0000
ω11	7.7756	7.7769	7.7756	0.0170	0.0000
ω12	8.5138	8.5161	8.5138	0.0275	0.0000
ω13	9.2599	9.2639	9.2599	0.0426	0.0000
ω14	10.0147	10.0211	10.0147	0.0636	0.0000
ω15	10.7788	10.7887	10.7788	0.0921	0.0000
ω16	11.5526	11.5676	11.5526	0.1298	0.0001
ω17	12.3369	12.3589	12.3369	0.1785	0.0002
ω18	13.1321	13.1636	13.1321	0.2404	0.0003

Based on the results of natural frequencies obtained by different methods from Table 4.3 to 4.6, it can be summarized that:

- For both type of element mesh, CABLE3D can give good prediction only for the natural frequencies of several lower modes, but not for the higher modes. Besides, the error increases rapidly as modes go higher.
- For the coarse mesh size of the short beam case, CABLE3D can cause large error as shown in Table 4.3, which means by using CALBE3D to predict the natural frequencies of short slender structures, especially for very modes vibrations, very fine mesh size is indispensable to improve the simulation accuracy.
- RISER3D can converge to the true values of the natural frequencies much faster than CABLE3D. Even for the cases of coarse mesh size, RISER3D can still produce unbelievably accurate results for the natural frequencies of all presented modes.
- It can be reasonable to predict that for slender structures, RISER3D can always yield good numerical simulation results for the evaluation of their natural frequencies. Moreover, if the same element size is used in the simulation, results by RISER3D are much more reliable than those of by CABLE3D.
- Compared to traditional CABLE3D, RISER3D can solve much smaller global system of equations to obtain equivalent accuracy, which can, therefore, save computational effort of our computers.

4.3.3 Shallow Water Drilling Riser Natural Frequencies Calculation by RISER3D

In this section, the eigenvalue problem of a TTR drilling riser, the problem data of which originated from (Dareing and Huang, 1976), has been solved using two finite element methods,

i.e. cubic Hermite FEM and quintic Hermite FEM. The original data are in US units, which are converted to SI units in Table 4.7.

Table 4.7 TTR parameters for natural frequency analysis (Dareing and Huang, 1976)

Riser Particulars	**Value**	**US Unit**	**Value Converted**	**SI Unit**
TTR Length L	500	ft	152.40050	m
Effective weight per unit length w	214	lb/ft	3123.08525	m
External cross section area A_e	3.14	ft^2	0.29172	m
Internal cross-sectional area A_i	2.99	ft^2	0.27778	m^2
Young's Modulus E	3.00E+07	psi	2.06843E+11	N/m^2
Second moment Inertia I	3136.9	in^4	1.30568E-03	m^4
TTR bottom tension T_b	2.86E+05	lb	1.27219E+06	Nm^2
Fluid density ρ_f	64.8	pcf	1037.99640	kg/m^3
Internal fluid density ρ_i	85.0	pcf	1361.56936	N
Virtual mass per unit length m	20.8	slugs/ft	9.95906E+02	kg/m
Flexural rigidity EI	9.41E+10	$lb{\cdot}in^2$	2.70070E+08	Nm^2

For the finite element analysis, only 7 elements are used for the discretization of the riser domain. The simulation results of the two numerical finite element simulations, compared with the results by previous literatures using different methods, are summarized in Table 4.8.

Table 4.8 The comparison of the TTR natural frequencies with other literatures

NFs (1/s)	**Power series (Dareing, 1976)**	**WKB_DSM (Cheng et al. 2002, 5 elements)**	**Differential Transformation (Chen et al. 2009)**	**VIM (Chen et al., 2015)**	**Cubic Hermite FEA (7 elements)**	**Quintic Hermite FEA (7 elements)**
ω1	0.8150	0.8150	0.8150	0.8150	0.8150	0.8150
ω2	1.8036	1.8037	1.8038	1.8038	1.8040	1.8038
ω3	3.0876	3.0878	3.0879	3.0879	3.0909	3.0879
ω4	4.7375	4.7377	4.7377	4.7377	4.7561	4.7377
ω5	6.7890	6.7896	6.7899	6.7899	6.8615	6.7896

Based on the results shown in Table 4.8, the following conclusions can be made for the first five modal frequencies:

- Power series method (1976) gives good prediction for the fundamental natural frequency, but not for the higher modes.
- WKB_DSM (2002) yields very good results for the first, forth and fifth mode, but a little bit errors exist for the second and third modes for some reason.
- Both differential transformation (2009) and VIM (2014) yields good prediction for the first four modal natural frequencies, but a tiny error starts to occur for the fifth mode.
- Cubic Hermite FEA (based on 7 element mesh) gives good prediction for the fundamental natural frequency, but not the higher modes. Besides, the errors increase as the modes go higher.

- Quintic Hermite FEA (based on 7 element mesh) can already give excellent prediction of the natural frequencies for the first five modes, at least all accurate to four decimal places.

To compare the convergent speed between CABLE3D and RIASER3D, more natural frequencies were studied and the results of which are presented in Table 4.9. Two types of mesh size were used, one is 7 uniform-length elements and the other is 14 uniform-length elements. Due to the lack of analytical results, the best results of natural frequencies, as highlighted with bold type, are used for benchmark. The results by CALBE3D and coarse mesh case by RISER3D are compared to the benchmark natural frequencies.

Table 4.9 The comparison of TTR natural frequencies between CABLE3D and RISER3D

NFs (1/s)	**CABLE3D_7**	**CABLE3D_14**	**RISER3D_7**	**RISER3D_14**	**Dif_CABLE3D7 (%)**	**Dif_CABLE3D14 (%)**	**Dif_RISER3D7 (%)**
ω1	0.8150	0.8150	0.8150	**0.8150**	0.0004	0.0000	0.0000
ω2	1.8040	1.8038	1.8038	**1.8038**	0.0120	0.0007	0.0000
ω3	3.0909	3.0881	3.0879	**3.0879**	0.0967	0.0061	0.0000
ω4	4.7561	4.7389	4.7377	**4.7377**	0.3882	0.0251	0.0002
ω5	6.8615	6.7944	6.7896	**6.7895**	1.0601	0.0717	0.0015
ω6	9.4706	9.2768	9.2624	**9.2617**	2.2551	0.1629	0.0080
ω7	13.2512	12.2023	12.1707	**12.1636**	8.9411	0.3178	0.0581
ω8	16.7713	15.5867	15.5132	**15.5003**	8.1998	0.5571	0.0829
ω9	21.6926	19.4485	19.3108	**19.2747**	12.5442	0.9013	0.1869

Table 4.9 Continued

NFs (1/sec)	**CABLE3D_7**	**CABLE3D_14**	**RISER3D_7**	**RISER3D_14**	**Dif_CABLE3D7 (%)**	**Dif_CABLE3D14 (%)**	**Dif_RISER3D7 (%)**
ω10	27.8282	23.8102	23.5726	**23.4887**	18.4747	1.3690	0.3572
ω11	35.3978	28.6985	28.3145	**28.1435**	25.7761	1.9720	0.6078
ω12	44.2138	34.1373	33.5579	**33.2404**	33.0123	2.6985	0.9552

4.3.4 Deep-water TTR Natural Frequencies Calculation by RISER3D

In this section, the natural frequencies of a deep water 2000m TTR, the problem data of which are cited from (C.P. Sparks, 2007), has been solved numerically by using two finite element methods, i.e. cubic Hermite FEM (CABLE3D) and quintic Hermite FEM (RISER3D). The key input data are summarized in Table 4.10, all of which are referred to (C.P. Sparks, 2007) except those highlighted with note 1.

Table 4.10 2000m length riser data

Riser Particulars	**Value [Sparks 2007]**	**Units**
Riser length, L	2000	m
Bending stiffness, EI	318,600	kNm^2
Top tension, T_t	7553.7	kN
Total apparent weight, wL	6,867.0	kN
Mass with added mass included, m	1.2	tonnes/m
Amplitude of vibrations, Y_a	1.0	m
Bottom tension[1], Tc	6.867e5	N
Tension increment[1], T_L	3.4335e3	N/m

Note 1: These parameters are calculated based on the riser data provided by Sparks (2007) in order to be consistent with the finite element model as presented in preceding section 4.4.1.

The finite element model in equation (4.59) is used as the programming basis for both finite element methods. The calculated natural modal periods are summarized in Table 4.11. Only two decimal places are kept in order to make a comparison with the results presented by Sparks (2007).

Table 4.11 2000m TTR modal periods comparison among different methods

Modal periods (s)	**Bessel cable [Sparks 2007]**	**Simple cable [Sparks 2007]**	**Simple beam [Sparks 2007]**	**Numerical [Sparks 2007]**	**CABLE3D_40**	**RISER3D_40**
1	78.79	77.47	77.45	78.71	78.71	78.71
2	38.92	38.74	38.69	38.84	38.84	38.84
3	25.88	25.82	25.75	25.78	25.78	25.78
4	19.39	19.37	19.26	19.27	19.27	19.27
5	15.51	15.49	15.36	15.37	15.37	15.37
10	-	7.75	7.52	7.52	7.52	7.52
20	-	3.87	3.54	3.55	3.54	3.54
30	-	2.58	2.21	2.21	2.18	2.21
40	-	1.94	1.54	1.55	1.50	1.54
50	-	1.55	1.15	1.15	1.08	1.15

From the results shown in Table 4.11, the following conclusions can be made:

- First five modal periods by Bessel cable analytical method are a little bit larger than all the numerical simulation results. Typically, the relative differences are less than 1%.
- Simple cable method yields the largest error to the true values among all the methods
- Simple beam method yields a good prediction for the high modal periods, but some errors exist for the lower modes, especially for the fundamental mode.

- Numerical results of CABLE3D by utilizing a forty uniform length element mesh, marked as CABLE3D_40 in Table 4.11, produce good predictions for the previous 20 modal periods, but errors start to occur for the higher modes, i.e. over 30 modes.
- Numerical results of RISER3D by utilizing a forty uniform length element mesh, marked as RISER3D_40 in Table 4.11, can produce very good predictions for all the modal periods. Therefore, RISER3D shows great merits to both simplified analytical method and traditional CABLE3D for accurately predicting the natural frequencies of beams and marine risers, no matter for lower or higher modes.

5 RISER3D APPLICATIONS TO MARINE RISRES PROBLEMS

For marine riser system design and analysis, accurate prediction for the riser configuration and internal forces is of utmost importance. In this chapter, the RISER3D program are applied to static and dynamic problems of several commonly-used marine risers, which mainly include some compliant risers, such as steel catenary riser (SCR), steel lazy wave riser (SLWR), steep wave riser (SWR); steel top-tensioned risers (TTRs) and free-hanging flexible risers. The main objective of this chapter is to address the validity and accuracy of the RISER3D for numerical simulation of marine risers and identify the advantages of RISER3D over the traditional CABLE3D. The RISER3D simulation results are either compared and verified with previous literature results or other alternative numerical methods such as CABLE3D and Orcaflex. For some cases, the hydrodynamic loads include linear or nonlinear current are considered, the theory of which are presented in section 5.1 below.

5.1 Hydrodynamic Loads on Marine Risers

Generally speaking, the hydrodynamic loadings can be categorized as

- Inertia forces, proportional to the acceleration of the water particles
- Nonlinear drag forces, proportional to the square of the water particle velocity
- Oscillating lift forces on the riser when the vortex shedding frequency of the passing flow is close enough to one of the natural frequencies of the designed riser system

These listed hydrodynamic loadings are highly dependent on the riser dimensions; water depth, wave related parameters such as wave height, wave period and wave direction; current velocity and direction along the riser section from surface to sea bottom. In the subsequent sections of this work, only the drag force due to steady current load is taken into consideration, and the

oscillating lift force are excluded in all the case studies. The wave force derivation is presented below but not considered in the case studies of this research.

5.1.1 Steady Current Loads on Fixed Marine Risers

For static analysis, the current load can be calculated using a modified Morison equation, the detailed formulation is presented hereafter. For marine riser analysis by using RISER3D, the equivalent nodal forces due to steady current can be evaluated by

$$\boldsymbol{F}_i = \int_0^L a_i(s)\boldsymbol{q}(s)ds \ \ (i = 1{\sim}6, n = 1{,}3) \tag{5.1}$$

where $a_i(s)$ are the general quintic Hermite shape functions, $\boldsymbol{q}(s)$ is the transverse distributed current load, s is the arc length of the deformed riser, measured form the top end of riser to the bottom extremity.

According to Morison equation, the expression for three dimensional steady current load $\boldsymbol{q}(s)$ on a differential arc length of riser can be written as

$$\boldsymbol{q}(s) = \frac{1}{2}\rho_f C_{dn} D_f(s)\left|\boldsymbol{N}\boldsymbol{v}_f(s)\right|\boldsymbol{N}\boldsymbol{v}_f(s) + \frac{1}{2}\rho_f C_{dt} D_f(s)\left|\boldsymbol{T}\boldsymbol{v}_f(s)\right|\boldsymbol{T}\boldsymbol{v}_f(s) \tag{5.2}$$

where ρ_f is the seawater fluid density, C_{dn} is the normal drag coefficient for cylindrical pipe of riser, C_{dt} is the tangential drag coefficient for cylindrical pipe of riser, D_f is local outer diameter of the riser (the buoyancy module effect should be taken into consideration if exists), $\boldsymbol{N}$ is a transformation matrix which can transfer the current velocity to riser normal direction, $\boldsymbol{T}$ is a transformation matrix which can transfer the current velocity to riser tangential direction, $\boldsymbol{v}_f(s)$ is the column vector of local current velocity expressed in global GXYZ coordinate system, which is placed on the mean water level with X-axis points to the right hand side, Y-axis points upward in vertical direction and Z-axis is the cross-product direction of the positive vectors in X and Y axis direction.

The tangential transformation matrix $\boldsymbol{T}$ can be calculated by

$$\boldsymbol{T} = (\hat{\boldsymbol{t}})^T\hat{\boldsymbol{t}} = \begin{bmatrix} t_1t_1 & t_1t_2 & t_1t_3 \\ t_2t_1 & t_2t_2 & t_2t_3 \\ t_3t_1 & t_3t_2 & t_3t_3 \end{bmatrix} = \begin{bmatrix} t_{11} & t_{12} & t_{13} \\ t_{21} & t_{22} & t_{23} \\ t_{31} & t_{32} & t_{33} \end{bmatrix} \tag{5.3}$$

where the superposed symbol ˆ denotes unit vector, the superscript T denotes vector or matrix transpose, $\hat{\boldsymbol{t}} = t_1\hat{\boldsymbol{\imath}} + t_2\hat{\boldsymbol{\jmath}} + t_3\hat{\boldsymbol{k}} = (t_1, t_2, t_3)$ is the three-dimensional riser tangential vector for eth element, which is, for small elongation risers, related to the nodal slope by

$$\hat{\boldsymbol{t}} = \frac{\boldsymbol{r'}_e}{|\boldsymbol{r'}|} = \frac{\boldsymbol{r'}_e}{1+\varepsilon} = \frac{1}{1+\varepsilon}(r'_{e1}, r'_{e2}, r'_{e3}) = (t_1, t_2, t_3) \quad (e = 1{\sim}ie) \tag{5.4}$$

where $\varepsilon = \frac{T}{EA}$ is the axial strain of riser subject to local axial tension T , EA is the riser stretching rigidity, the subscript e denotes the eth element, the number ie denotes the total number of discretized elements.

The local tangential and normal particle velocity for marine riser due to steady current can be calculated by

$$\boldsymbol{v}_{ft}(s) = \left(\boldsymbol{v}_f(s) \cdot \hat{\boldsymbol{t}}\right)\hat{\boldsymbol{t}} = \boldsymbol{T}\boldsymbol{v}_f(s)$$

$$\boldsymbol{v}_{fn}(s) = \boldsymbol{v}_f(s) - \boldsymbol{v}_{ft}(s) = (\boldsymbol{I}_{3\times3} - \boldsymbol{T})\boldsymbol{v}_f(s) = \boldsymbol{N}\boldsymbol{v}_f(s) \tag{5.5}$$

where the local current velocity vector is expressed in the global GXYZ coordinate system as $\boldsymbol{v}_f(s) = (v_{f1}(s), v_{f2}(s), v_{f3}(s))^T$ and $v_{f1}(s)$, $v_{f2}(s)$ and $v_{f3}(s)$ are the components of the local current velocity vector in global X, Y and Z direction respectively, $\boldsymbol{I}_{3\times3}$ is a three by three identity matrix.

Therefore, the entries of the transformation matrix $\boldsymbol{N}$ is related to three dimensional riser nodal slopes by

$$\boldsymbol{N} = \begin{bmatrix} n_{11} & n_{11} & n_{11} \\ n_{21} & n_{22} & n_{23} \\ n_{31} & n_{32} & n_{33} \end{bmatrix} = \begin{bmatrix} 1 - \frac{r'_{e1}}{1+\varepsilon}\frac{r'_{e1}}{1+\varepsilon} & -\frac{r'_{e1}}{1+\varepsilon}\frac{r'_{e2}}{1+\varepsilon} & -\frac{r'_{e1}}{1+\varepsilon}\frac{r'_{e3}}{1+\varepsilon} \\ -\frac{r'_{e2}}{1+\varepsilon}\frac{r'_{e1}}{1+\varepsilon} & 1 - \frac{r'_{e2}}{1+\varepsilon}\frac{r'_{e2}}{1+\varepsilon} & -\frac{r'_{e2}}{1+\varepsilon}\frac{r'_{e3}}{1+\varepsilon} \\ -\frac{r'_{e3}}{1+\varepsilon}\frac{r'_{e1}}{1+\varepsilon} & -\frac{r'_{e3}}{1+\varepsilon}\frac{r'_{e2}}{1+\varepsilon} & 1 - \frac{r'_{e3}}{1+\varepsilon}\frac{r'_{e3}}{1+\varepsilon} \end{bmatrix} \tag{5.6}$$

For example, if the steady current flows only in positive X-direction and the horizontal component of X-direction of the velocity at arbitrary elevation can be calculated by equation

$$v_{f1}(y) = (v_u - v_b)\left(\frac{y-y_b}{y_u-y_b}\right)^{1/n_c} \quad (y \in [y_b, 0]) \tag{5.7}$$

where y is the global Y-coordinate of the deformed riser, y_u is elevation of sea surface, y_b is the elevation of the sea bottom, v_u is the upper surface current velocity, v_b is current velocity at seabed, n_c is an integer index for current velocity distribution (for instance $n_c =$ 0 for uniform distribution, 1 for linear distribution, 4 for one forth decay distribution, etc.).

5.1.2 Combined Wave and Current Loads on Marine Risers

For riser dynamic analysis, the hydrodynamic loads on riser pipe due to combined wave and current can be calculated by using a modified Morison equation, the expression of the distributed external load intensity $\boldsymbol{q}(s,t)$ on a differential arc length ds in three-dimensional space can be expressed as

$$\boldsymbol{q}(s,t) = \frac{1}{2}\rho_f C_{dn} D_f(s)\left|\boldsymbol{N}\left(\boldsymbol{v}_f(s,t) - \dot{\boldsymbol{r}}(s,t)\right)\right|\boldsymbol{N}\left(\boldsymbol{v}_f(s,t) - \dot{\boldsymbol{r}}(s,t)\right) + \frac{1}{2}\rho_f C_{dt} D_f(s)\left|\boldsymbol{T}\left(\boldsymbol{v}_f(s,t) - \dot{\boldsymbol{r}}(s,t)\right)\right|\boldsymbol{T}\left(\boldsymbol{v}_f(s,t) - \dot{\boldsymbol{r}}(s,t)\right) + (\boldsymbol{I} + C_{an}\boldsymbol{N} + C_{at}\boldsymbol{T}) m_{dw}\boldsymbol{a}_w(s,t) \tag{5.8}$$

where $\boldsymbol{v}_f(s,t) = \boldsymbol{v}_c(s,t) + \boldsymbol{v}_w(s,t)$ is a column vector by adding the velocity vector of wave $\boldsymbol{v}_w(s,t)$ to that of current $\boldsymbol{v}_c(s,t)$, C_{an} and C_{at} are the normal and tangential added-mass coefficient, $m_{dw} = \rho_f A_f \cdot 1 = \rho_f \frac{\pi}{4} {D_f}^2$ is the mass of water displaced by unit length of riser, $\boldsymbol{a}_w(s,t)$ is the local water particle acceleration vector induced by wave.

If the external load intensity $\boldsymbol{q}(s,t)$ on a differential length is decomposed into wave and current loading respectively, it can be expressed as

$$\boldsymbol{q}(s,t) = \boldsymbol{q}_c(s,t) + \boldsymbol{q}_w(s,t) \tag{5.9}$$

where

$$\boldsymbol{q}_c(s,t) = \frac{1}{2}\rho_f C_{dn} D_f(s)|\boldsymbol{N}(\boldsymbol{v}_c(s,t) - \dot{\boldsymbol{r}}(s,t))|\boldsymbol{N}(\boldsymbol{v}_c(s,t) -$$

$$\dot{\boldsymbol{r}}(s,t)) + \frac{1}{2}\rho_f C_{dt} D_f(s)|\boldsymbol{T}(\boldsymbol{v}_c(s,t) - \dot{\boldsymbol{r}}(s,t))|\boldsymbol{T}(\boldsymbol{v}_c(s,t) - \dot{\boldsymbol{r}}(s,t))$$

(5.10)

$$\boldsymbol{q}_w(s,t) = \frac{1}{2}\rho_f C_{dn} D_f(s)|\boldsymbol{N}(\boldsymbol{v}_w(s,t) - \dot{\boldsymbol{r}}(s,t))|\boldsymbol{N}\boldsymbol{v}_w(s,t) -$$

$$\dot{\boldsymbol{r}}(s,t) + \frac{1}{2}\rho_f C_{dt} D_f(s)|\boldsymbol{T}(\boldsymbol{v}_w(s,t) - \dot{\boldsymbol{r}}(s,t))|\boldsymbol{T}(\boldsymbol{v}_w(s,t) - \dot{\boldsymbol{r}}(s,t)) + (C_{mn}\boldsymbol{N} +$$

$$C_{mt}\boldsymbol{T}) m_{dw} \boldsymbol{a}_w(s,t) \qquad (5.11)$$

where C_{mn} and C_{mt} are the riser normal and tangential inertia coefficient, which are related to the normal and tangential added-mass coefficient by relationships of

$$C_{mn} = 1 + C_{an}$$

$$C_{mt} = C_{at} \qquad (5.12)$$

According to some previous literatures on hydrodynamic coefficients, the approximated ranges for the values of hydrodynamic coefficients are summarized based on experiment results of some published literatures as

$$C_{dn} \in [1.0,1.9]$$

$$C_{dt} \in [0.03,0.25]$$

$$C_{an} \in [1.0,1.5]$$

$$C_{at} \in [0.0,0.1] \qquad (5.13)$$

For dynamic finite element analysis, the major steps for riser hydrodynamic force updating can be summarized as

- Determine the instantaneous water particle velocity and acceleration in space-fixed global coordinate system GXYZ

- According to the riser configuration at instant time t, calculate the transformation matrix $\boldsymbol{N}$ and $\boldsymbol{T}$ by the unit tangential vector $\hat{\boldsymbol{t}}$ of the riser element in space-fixed global coordinate system GXYZ
- Using the transform matrix $\boldsymbol{N}$ and $\boldsymbol{T}$ to calculate the components of riser normal and tangential water particle velocity and accelerin, which are functions of deformed riser arc length s and time t
- Compute the equivalent nodal force for each element

5.2 Application of RISER3D to Compliant Risers

5.2.1 Typical SCR Static In-place Analysis

In this section, a deep-water 1800m water depth 8'' SCR static analysis is performed with RISER3D. The main particulars of the SCR are referred to the literature (Celso, 2006) and summarized in the Table 5.1. The related environmental parameters for this case are presented in Table 5.2.

Table 5.1 8'' 1800 water depth SCR Particulars

Designation	Symbol	Value	SI Unit
Outer diameter	D_o	0.2032	m
Internal diameter	D_i	0.1651	m
Young's modulus	E	2.100E+11	Pa
Outer cross-sectional area	A_f	3.2429E-02	m^2
Internal cross section	A_i	2.1408E-02	m^2
Weight in air	W_{air}	85.434	kg/m
Buoyancy	B	325.97	N/m
Steel density	ρ_s	7752	kg/m^3
Moment of inertia	I	4.7216E-05	m^4
Bending stiffness	EI	9.9154E+06	Nm^2
Axial stiffness	EA	2.3144E+09	N
Internal fluid density	ρ_i	1250.00	kg/m^3
Submerged weight	W_{sub}	727.0	N/m
Riser total length	L_r	3200.00	m

Table 5.2 Environmental parameters for the 1800m water depth SCR

Designation	Value	Unit
Sea water density	1025	kg/m^3
Water depth	1800.0	m
Seabed soil stiffness	35.216	$kN/m/m^2$

The following assumptions, unless otherwise specified, are employed for all marine riser analysis in this dissertation

- The steel pipe of marine riser is thin-walled, perfect round and homogenous pipe, no damage, no initial residual stress
- The material of marine riser is assumed to isotropic within elastic deformation range
- The seabed axial and lateral friction is neglected due to small contribution
- The Poisson ratio effect is neglected for the simplicity of the mathematical model
- The structural damping effect, VIV suppress auxiliaries, and riser torsion are neglected
- Corrosion allowance, water absorption and marine growth effect are neglected
- The seabed is assumed to be a flat and linear elastic foundation
- No consideration of the internal flow effect
- Small axial extensibility has been employed

The results extracted from the RISER3D numerical simulation, including the SCR configuration, the horizontal component of riser slope, the distribution of the riser effective tension, the distribution of the riser bending moment, the local zoom in of the maximum bending moment section, the local zoom in of the bending moment section at the TDP, and the riser shear

force distribution, are illustrated from Figure 5.1 to Figure 5.7 respectively. These results by RISER3D are compared to those of obtained by two alternative numerical methods, one is CABLE3D and the other is Orcaflex (Orcina, 2019).

For this case, a total number of 400 uniform-length elements are utilized to discretize the whole riser length of 3200m, so each element has a length of 8m. For Newton iteration method, the relaxation coefficient adopted is 0.7. The riser is assumed to be water filled during the analysis, and a top tension of 1986.9kN are exactly matched among the three different numerical methods.

The touch down tension predicted by CABLE3D and RISER3D is 680.5kN, which is a little bit higher than that of by Orcaflex 679.7kN. The top departure angle predicted by CABLE3D and RISER3D are both 20.03deg, which is close to Orcaflex result of 20.05deg.

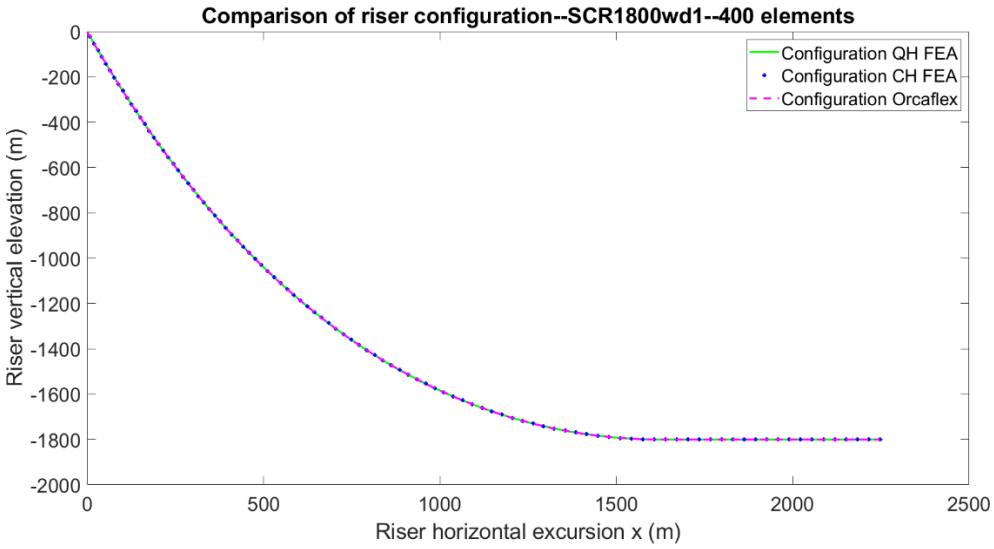

Figure 5.1 The 8'' SCR configuration

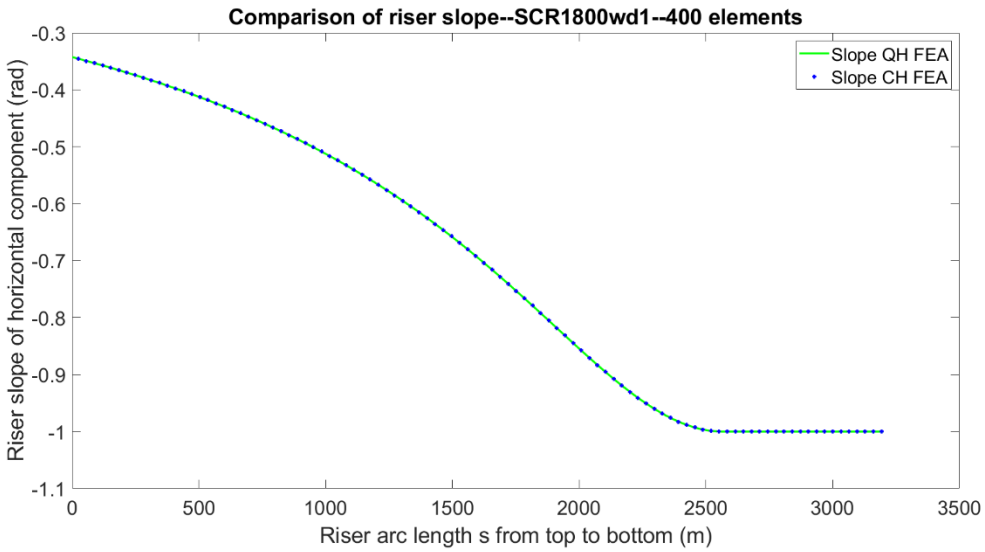

Figure 5.2 The 8'' SCR horizontal component of slope

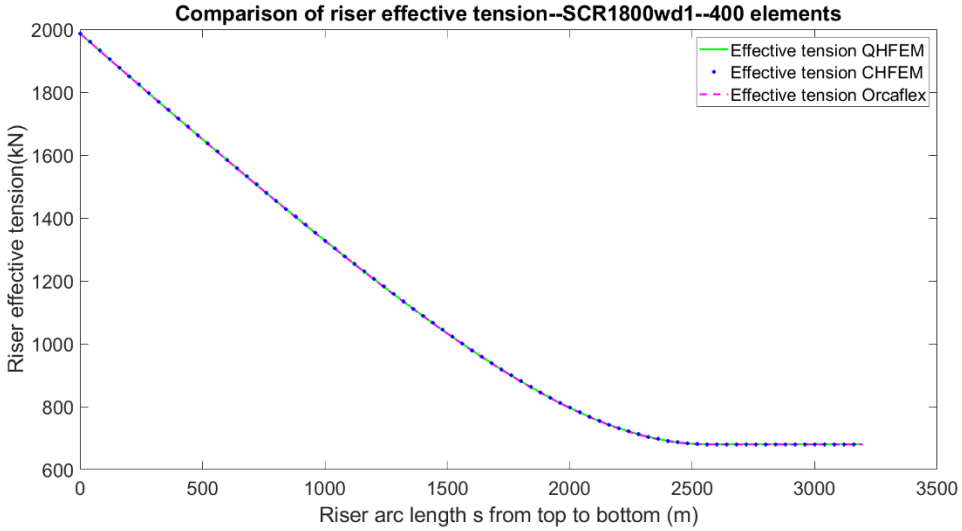

Figure 5.3 The 8'' SCR effective tension distribution

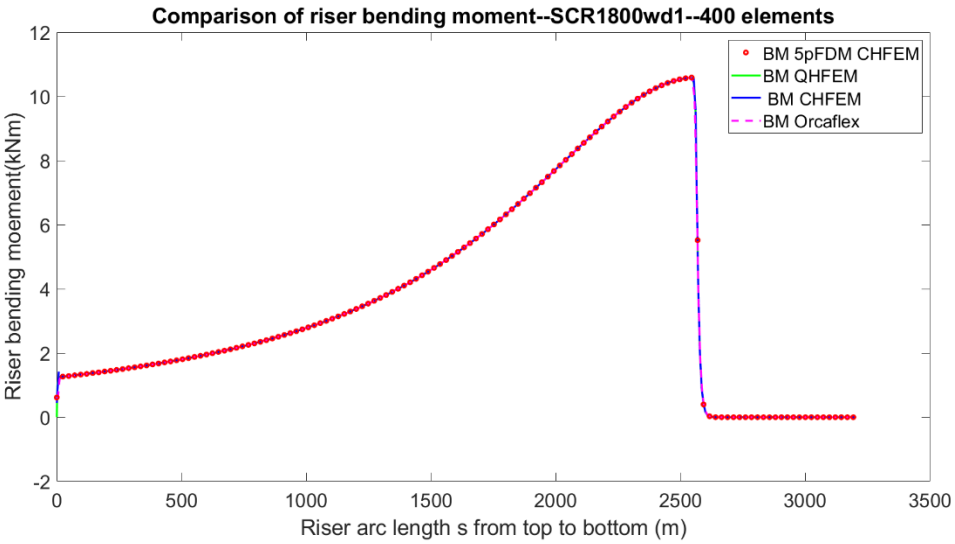

Figure 5.4 The 8'' SCR overall bending moment distribution

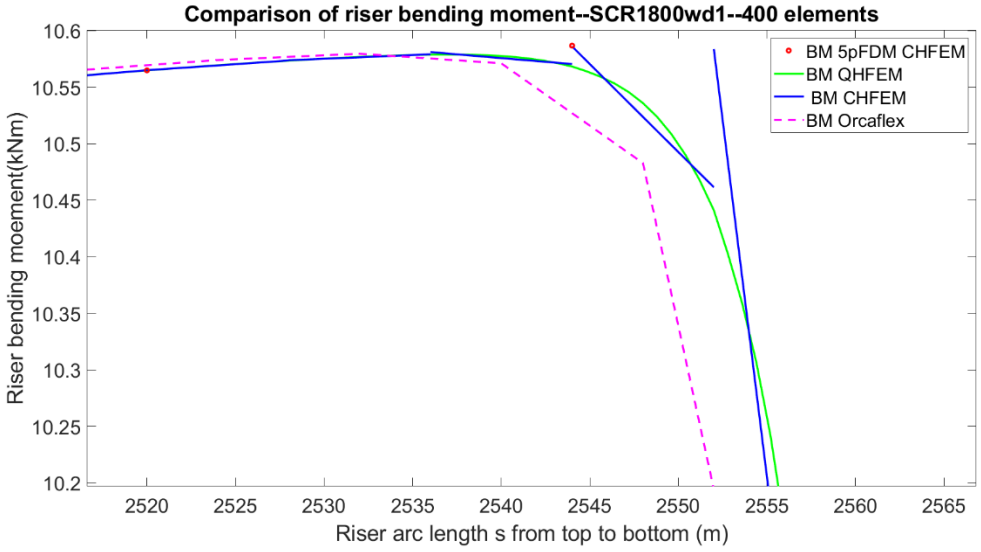

Figure 5.5 The 8'' SCR critical bending moment section zoom in

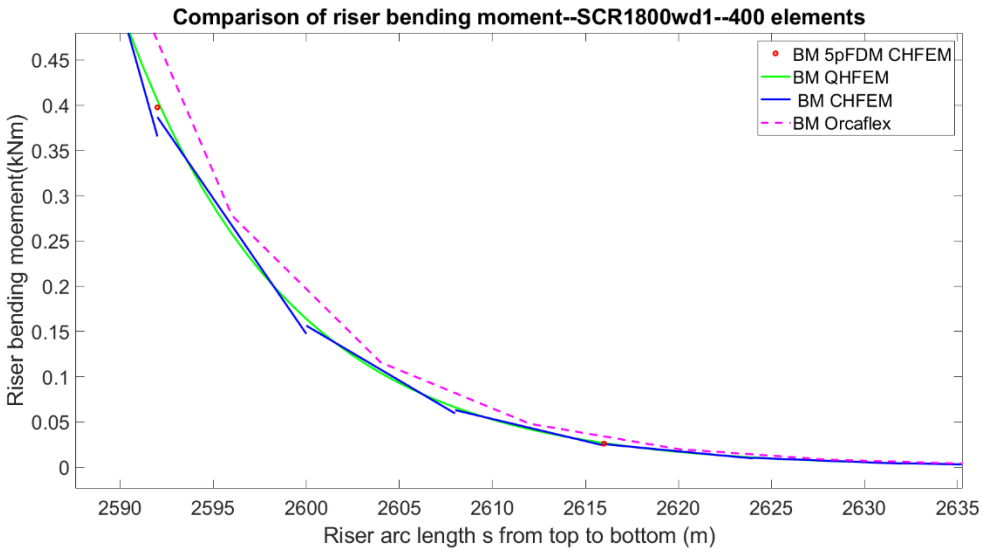

Figure 5.6 The 8'' SCR TDZ bending moment zoom in

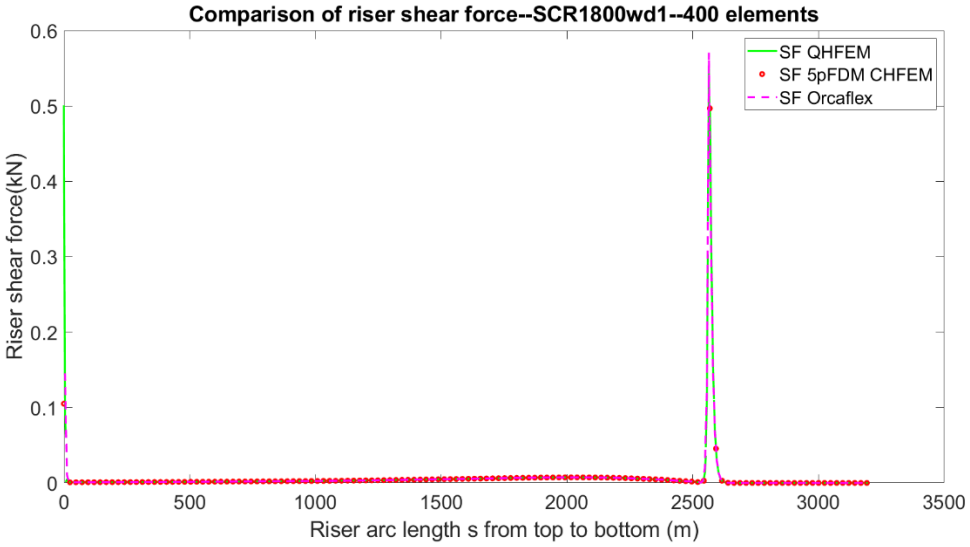

Figure 5.7 The 8'' SCR shear force distribution

As shown in Figure 5.1 to 5.3, the resulting curves of riser configuration, slope in horizontal direction, the effective tension by three different numerical methods agree very well with each other. From Figure 5.4 to 5.7, it can be seen that the bending moment distribution within the whole

domain predicted by CABLE3D and Orcaflex are piecewise discontinuous linearly distributed functions, while by using the new RISER3D program, the bending moment distribution are piecewise continuous cubic polynomial functions within the whole problem domain. The maximum bending moment predicted by CALBE3D are about 1% higher than RISER3D and Orcaflex for this element mesh. As for the shear force simulation, the shear force at the top end of the riser predicted by RISER3D are larger than CABLE3D and Orcaflex since RISER3D can apply the Dirichlet boundary conditions at the boundary of riser, which can produce more accurate bending moment and shear force at the near boundary sections.

5.2.2 SLWR Static In-place Analysis by RISER3D

In this section, a deep-water 1847.9m water depth 8'' SLWR static analysis is performed with RISER3D. The key parameters of the SLWR are referred to the literature (J.L. Wang, 2014) and summarized in Table 5.3. The non-available input data, such as the buoyancy module segment particulars, from the referred literature are assumed according to engineering experience and summarized in Table 5.4. The environmental conditions for this case are listed in Table 5.5.

Table 5.3 8'' 1847.9m water depth SLWR particulars of steel pipe segment

Designation	Symbol	Value	SI Unit
Outer diameter	D_o	0.2032	m
Internal diameter	D_i	0.1650	m
Young's modulus	E	2.060E+11	Pa
Outer cross-sectional area	A_f	3.24293E-02	m^2
Internal cross section	A_i	2.13825E-02	m^2
Mass per unit length in air	m_{air}	86.717	kg/m

Table 5.3 Continued

Designation	Symbol	Value	SI Unit
Buoyancy	B	325.652	N/m
Steel Density	ρ_s	7850.0	kg/m^3
Moment of Inertia	I	4.73047E-05	m^4
Bending Stiffness	EI	9.74477E+06	Nm^2
Axial Stiffness	EA	2.27564E+09	N
Internal Fluid Density	ρ_i	0.00	kg/m^3
Submerged Weight	W_{sub}	524.75	N/m
Hang-off segment	s_{ho}	1690	m
Buoyancy Module segment	s_{bm}	520	m
Touch down segment	s_{td}	590	m
Riser Total Length	L_r	2800.00	m

Table 5.4 8'' 1847.9m water depth SLWR particulars of BM segment

Designation	Symbol	Value	SI Unit
Outer diameter of steel pipe	D_o	0.2032	m
Internal diameter of steel pipe	D_i	0.1650	m
Buoyancy module diameter	D_{bm}	0.519422	m
Buoyancy module thickness	t_{bm}	0.158111	m
Buoyancy module density	ρ_{bm}	427.69395	kg/m^3
Young's modulus	E	2.060E+11	Pa

Table 5.4 Continued

Designation	Symbol	Value	SI Unit
Outer cross-sectional area	A_f	3.24293E-02	m^2
Internal cross section	A_i	2.13825E-02	m^2
Weight in air	W_{air}	163.476	kg/m
Buoyancy	B	2127.828	N/m
Steel density	ρ_s	7850.0	kg/m^3
Moment of inertia	I	4.73047E-05	m^4
Bending stiffness	EI	9.74477E+06	Nm^2
Axial stiffness	EA	2.27564E+09	N
Internal fluid density	ρ_i	0.00	kg/m^3
Submerged weight BM	W_{sub}	-524.73	N/m

Table 5.5 Environmental conditions for the 1800m water depth SLWR

Designation	Symbol	Value	Unit
Sea water density	ρ_{sw}	1024	kg/m^3
Water depth	H_{wd}	1847.9	m
Seabed soil stiffness	K_s	22.5	$kN/m/m^2$

The results extracted from the RISER3D numerical analysis, including the SLWR configuration, the riser horizontal slope, the effective tension distribution, the riser bending

moment distribution, the local zoom in of the bending moment at TDZ, the local zoom in of the bending moment at TDP, and the riser shear force distribution, are presented from Figure 5.8 to Figure 5.14 respectively. These results are compared to the two other numerical methods, i.e. CABLE3D and Orcaflex (Orcina, 2019).

For this case, a total number of 280 uniform-length elements are utilized to discretize the whole riser length of 2800m, so each element has a length of 10.0m. For Newton iteration method, the relaxation coefficient adopted is 0.8. The riser pipe is assumed to be empty during the analysis, and a top tension of 820.75kN are exactly matched among the three different numerical methods.

The touch down tension predicted by CABLE3D and RISER3D are both 78.14kN, which is a little bit higher than that of by Orcaflex 77.53kN. The top departure angle predicted by CABLE3D and RISER3D are 5.4717deg and 5.4714deg respectively, which is very close to Orcaflex result of 5.4415deg.

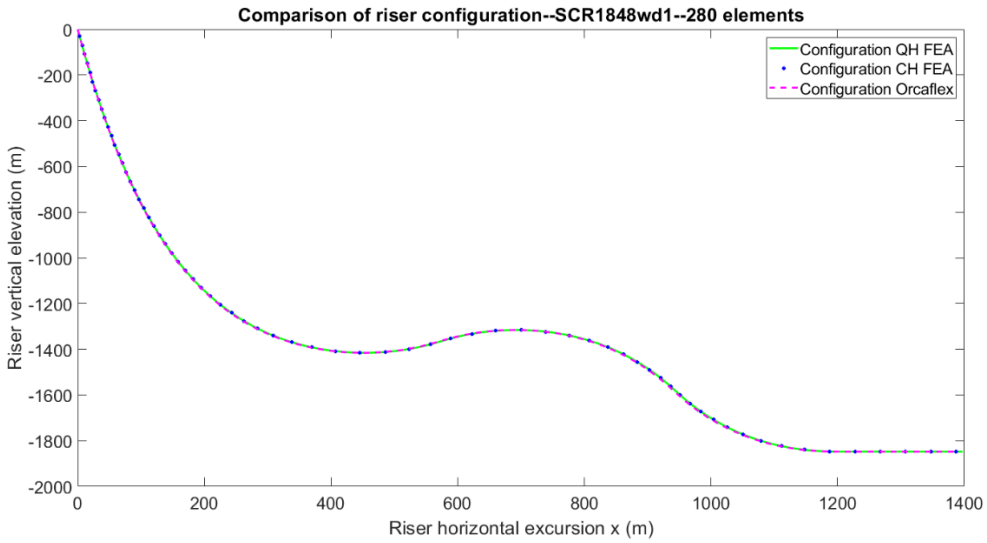

Figure 5.8 The 8’’ SLWR overall configuration

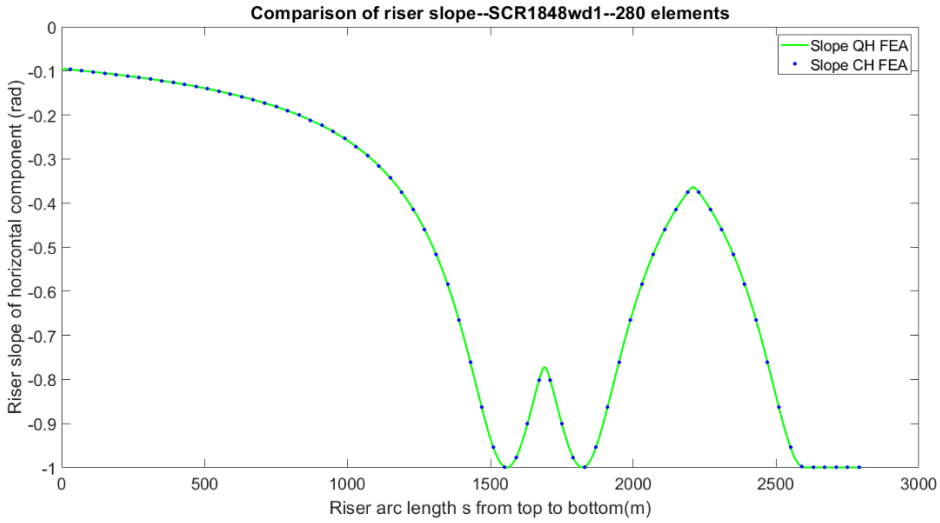

Figure 5.9 The 8'' SLWR horizontal component of slope

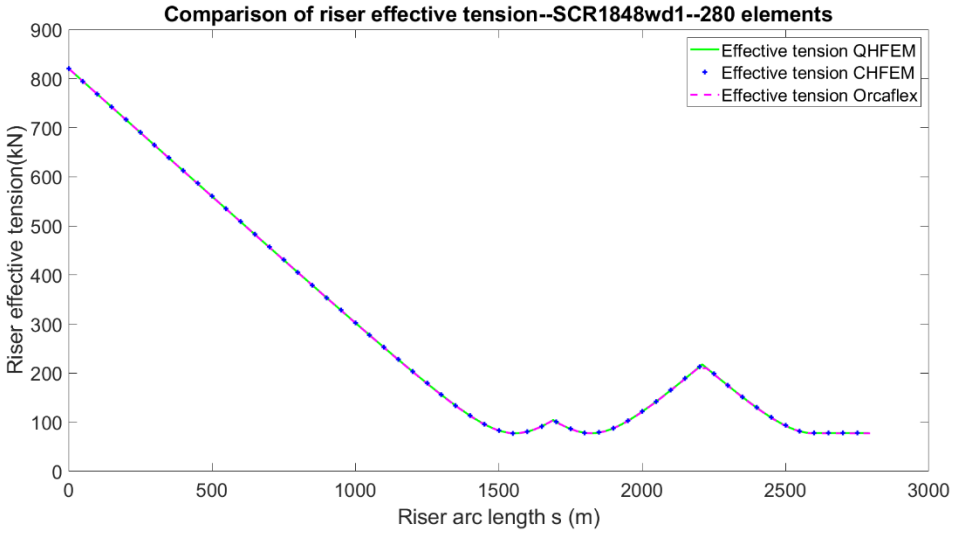

Figure 5.10 The 8'' SLWR effective tension distribution

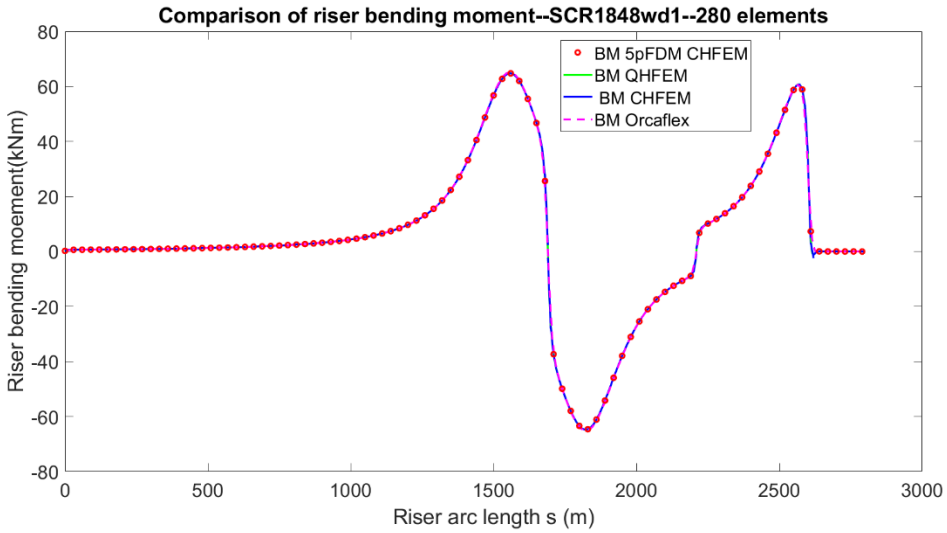

Figure 5.11 The 8'' SLWR overall bending moment distribution

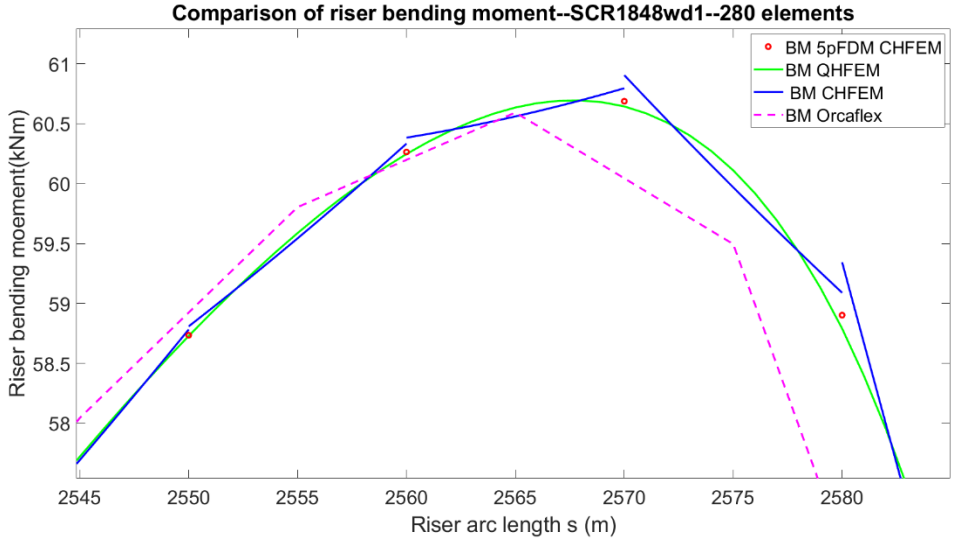

Figure 5.12 The 8'' SLWR peak bending moment at TDZ local zoom in

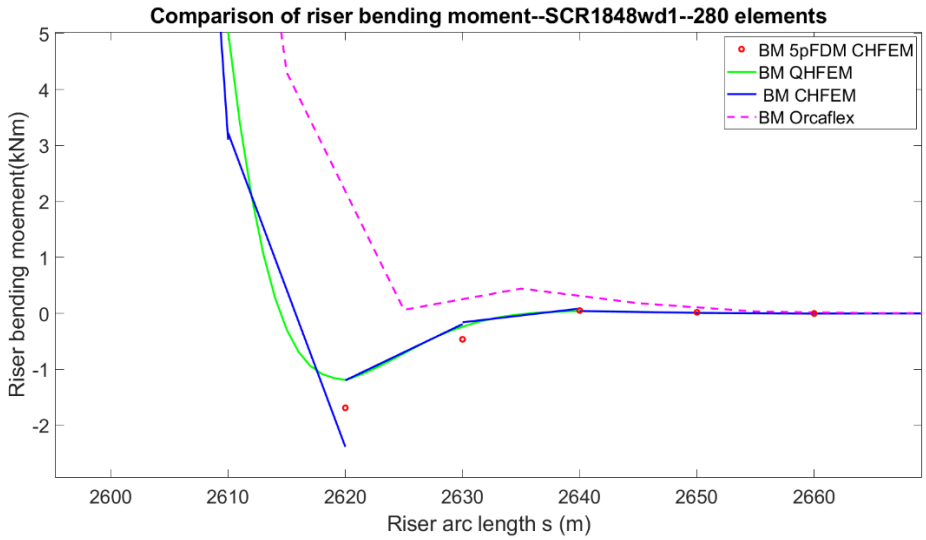

Figure 5.13 The 8'' SLWR bending moment at TDP local zoom in

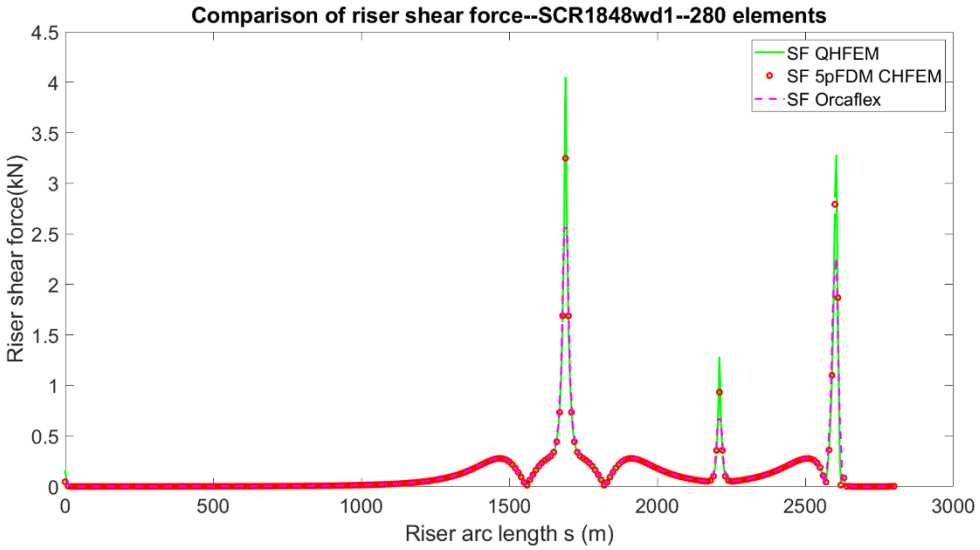

Figure 5.14 The 8'' SLWR shear force distribution

5.2.3 SLWR Static Analysis by RISER3D under Linear and Tidal Current Load

In this section, the same SLWR in section 5.2.2 are adopted for current load analyses. Two types of current load are considered here, the first one is a linearly distributed current with surface

velocity of 1.52m/s, linearly decreased to 0.0m/s at the sea bottom; the second one is a one-fifth power law decaying tidal current with surface velocity of 1.05m/s. The current velocity at arbitrary elevation can be evaluated based on equation (5.7). The current velocity profile related parameters for these two cases are summarized in Table 5.6, in which positive y-axis points vertically upward. The riser pipe normal and tangential drag coefficient for two types of current are summarized in Table 5.7.

Table 5.6 Current parameters for static SLWR analysis

Current Type	v_u **(m/s)**	v_b **(m/s)**	y_u **(m)**	y_b **(m)**	n_c
Linear current	1.52	0.0	0.0	1847.9	1
Tidal current	1.05	0.0	0.0	1847.9	5

Table 5.7 Assumed drag coefficients for static SLWR analysis

Drag Coefficient	**Linear Current**	**Tidal Current**
Normal direction C_{dn}	1.5	1
Tangential direction C_{dt}	0.1	0.05

A total of three subcases are studied for the SLWR in this section, the first one is the riser subjected to positive linear current load as relevant parameters depicted in Table 5.6 and Table 5.7; the second one is the riser subjected to positive tidal current load as relevant parameters depicted in Table 5.6 and Table 5.7; the third one is a parametric study for the riser subjected to current load in three different directions with the base case presented in section 5.2.2.

For positive linear current load case, i.e. subcase1, a total number of 280 uniform-length elements are utilized to discretize the whole riser length of 2800m, with element length of 10.0m. For Newton iteration method, the relaxation coefficient adopted is 0.5. The riser tube is assumed to be empty during the analysis, and a top tension of 843.7kN are exactly matched among the three different numerical methods, i.e. RISER3D, CABLE3D and Orcaflex.

The key results for subcase1 are presented from Figure 5.15 to Figure 5.22. Figure 5.15 is the SLWR configuration in equilibrium state and Figure 5.16 is the local room in of the riser configuration at around 400m water depth. The SLWR bending moment distribution and local zoom in plots are shown from Figure 5.17 to Figure 5.19 respectively. The SLWR shear force, critical shear force local zoom in and the effective tension are presented from Figure 5.20 to Figure 5.22 respectively. The tension at the touch down point predicted by CABLE3D and RISER3D is 114.52kN, which is a little bit larger than that of by Orcaflex 113.84kN. The riser top departure angle predicted by CABLE3D and RISER3D are 7.3685deg and 7.3665deg respectively, which is a little bit larger than Orcaflex result of 7.2755deg.

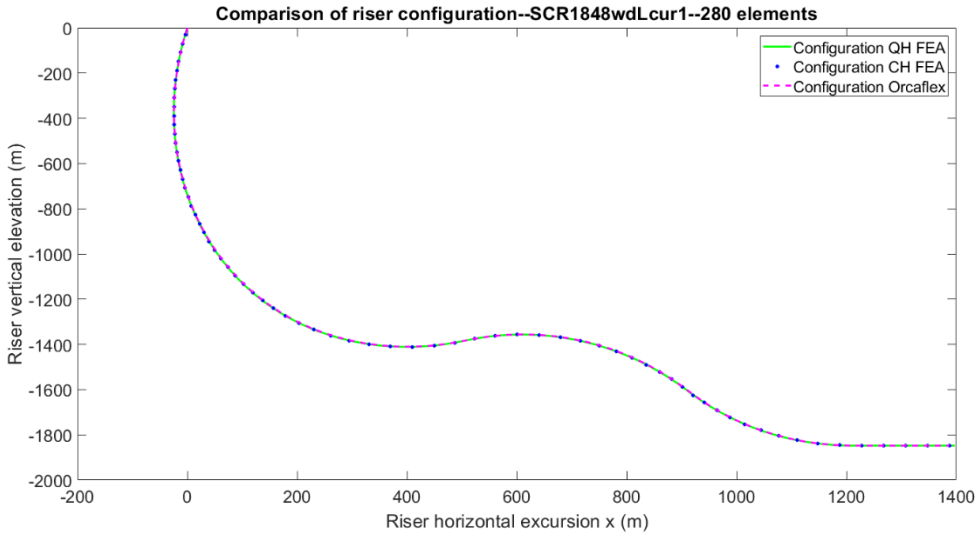

Figure 5.15 The SLWR configuration for subcase1

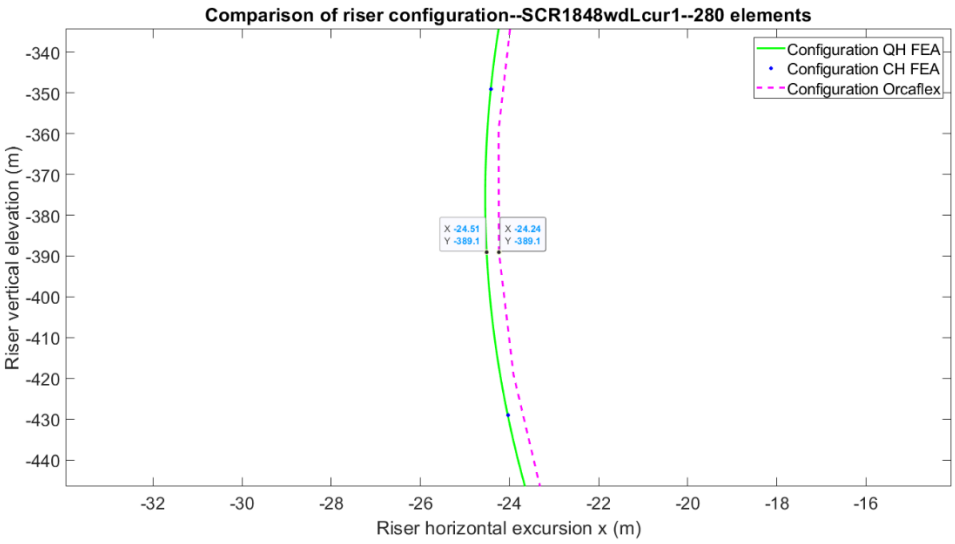

Figure 5.16 The SLWR configuration local zoom in for subcase1

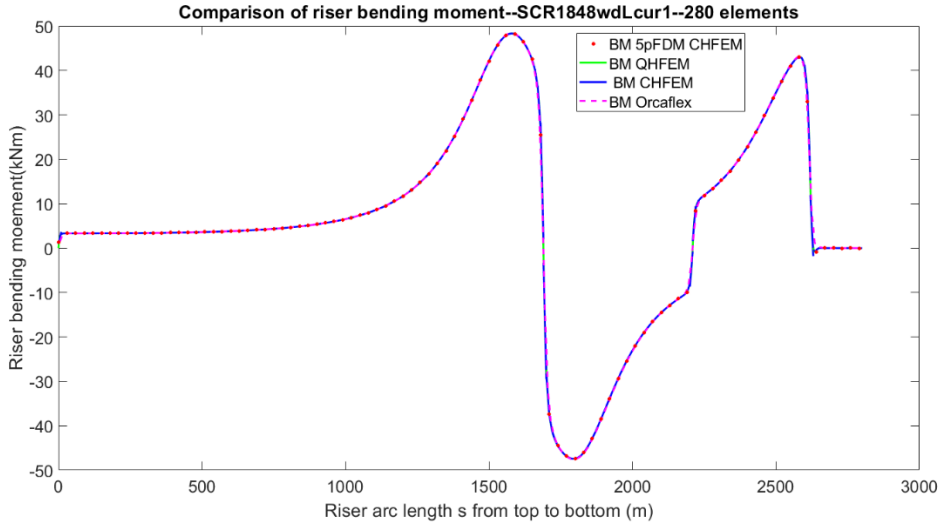

Figure 5.17 The SLWR bending moment distribution for subcase1

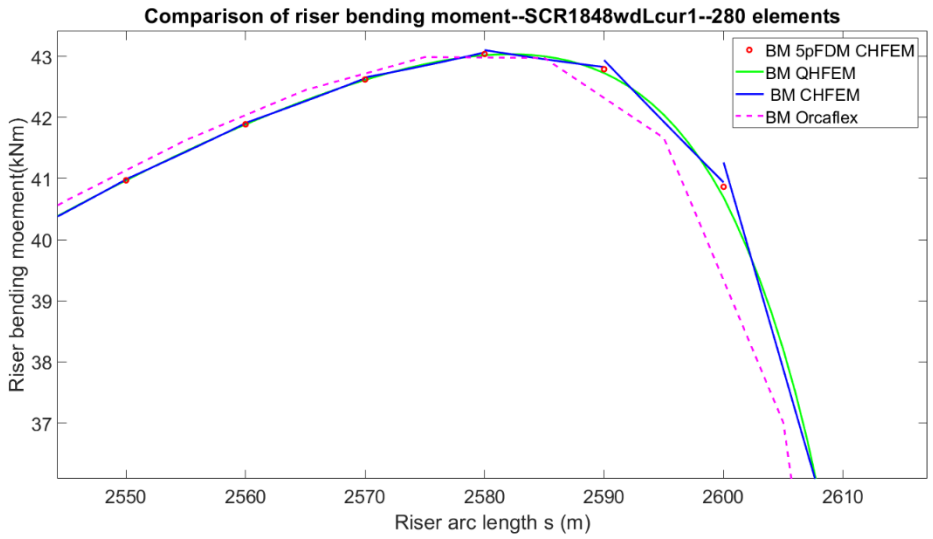

Figure 5.18 The SLWR peak bending moment at TDZ local zoom in for subcase1

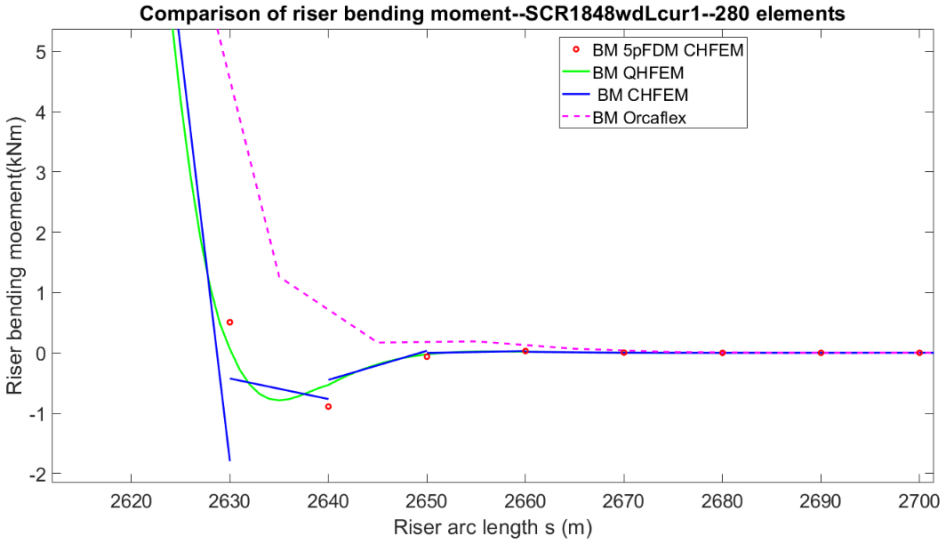

Figure 5.19 The SLWR bending moment at TDP local zoom in for subcase1

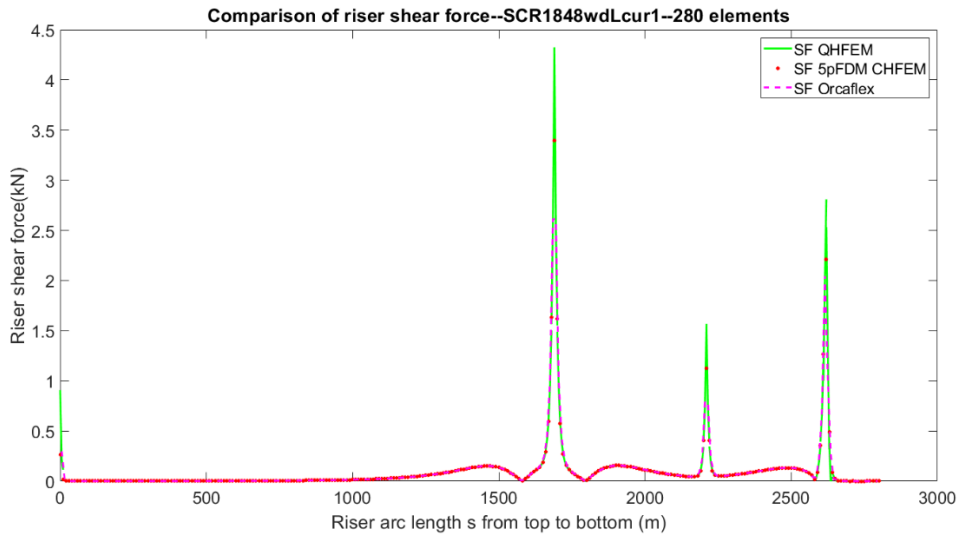

Figure 5.20 The SLWR shear force distribution for subcase1

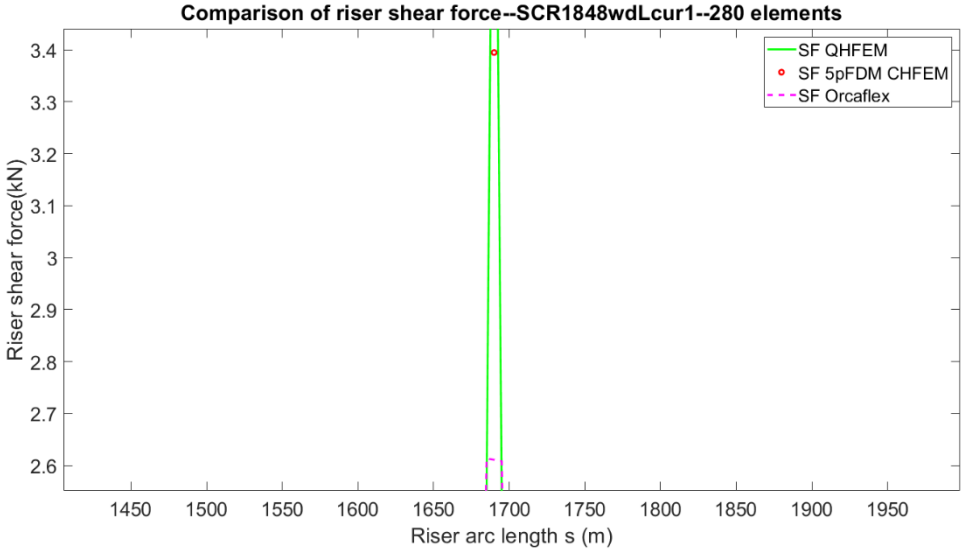

Figure 5.21 The SLWR critical shear force position local zoom in for subcase1

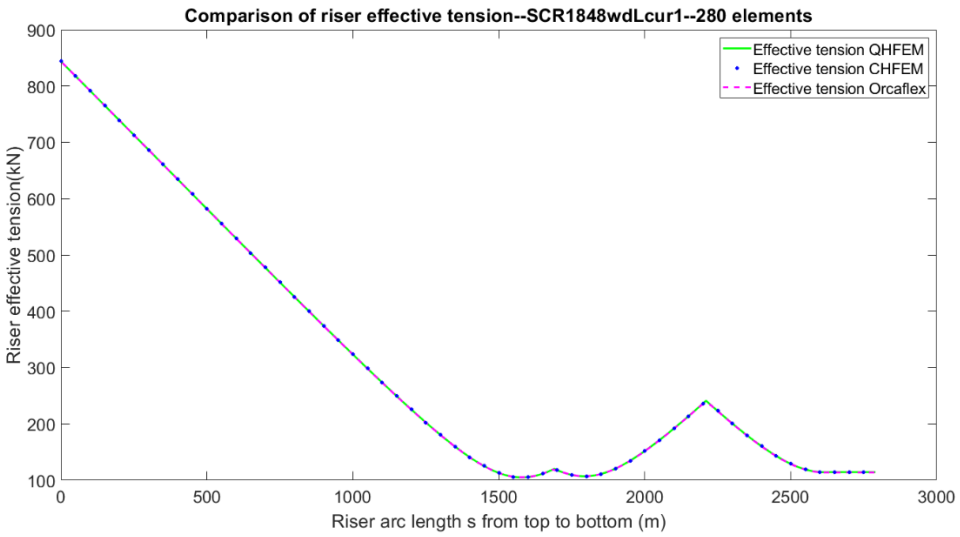

Figure 5.22 The SLWR effective tension distribution for subcase1

For subcase2, a total number of 280 uniform-length elements are also employed to discretize the whole riser length of 2800m, so each element has a length of 10.0m. For Newton iteration method, the relaxation coefficient adopted is 0.6. The riser tube is assumed to be empty during the analysis, and a top tension of 848.5kN are exactly matched among the three different numerical methods, i.e. RISER3D, CABLE3D and Orcaflex.

For subcase2, the key results for positive tidal current load case are presented from Figure 5.23 to Figure 5.29. Figure 5.23 is the riser configuration in equilibrium state and Figure 5.24 is the local room in of the riser configuration form surface to about 700m water depth. The riser bending moment distribution and local zoom in plots are shown from Figure 5.25 to Figure 5.27 respectively. The shear force and the effective tension of riser are presented in Figure 5.28 and Figure 5.29 respectively. The touch down tension predicted by CABLE3D and RISER3D is 131.28kN, which is a little bit larger than that of by Orcaflex 130.10kN. The riser top departure

angle predicted by CABLE3D and RISER3D are 1.9460deg and 1.9454deg respectively, which is a little bit larger than Orcaflex result of 1.8146deg.

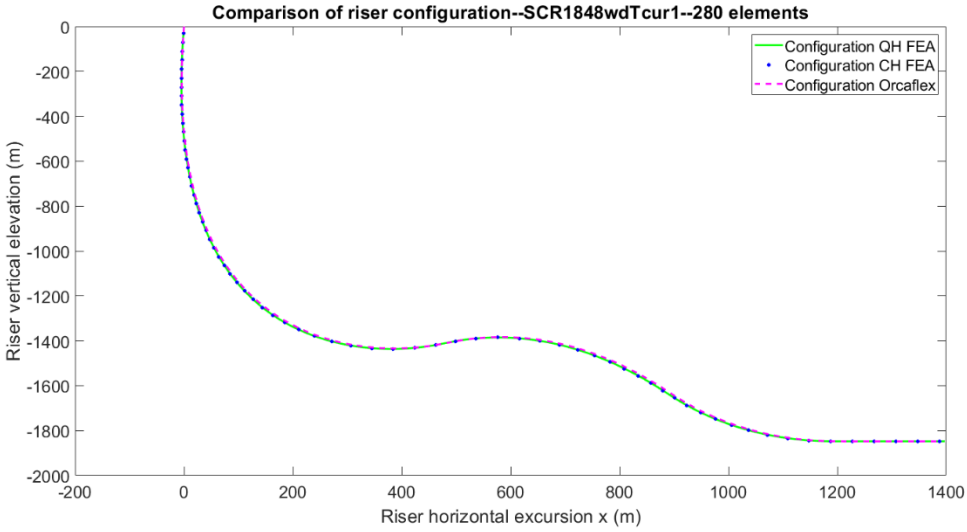

Figure 5.23 The SLWR configuration for subcase2

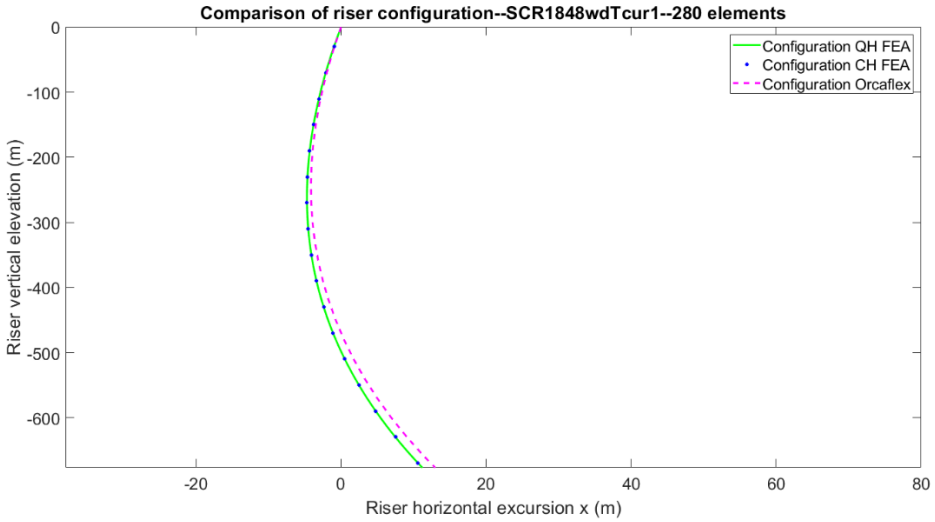

Figure 5.24 The SLWR configuration local zoom in for subcase2

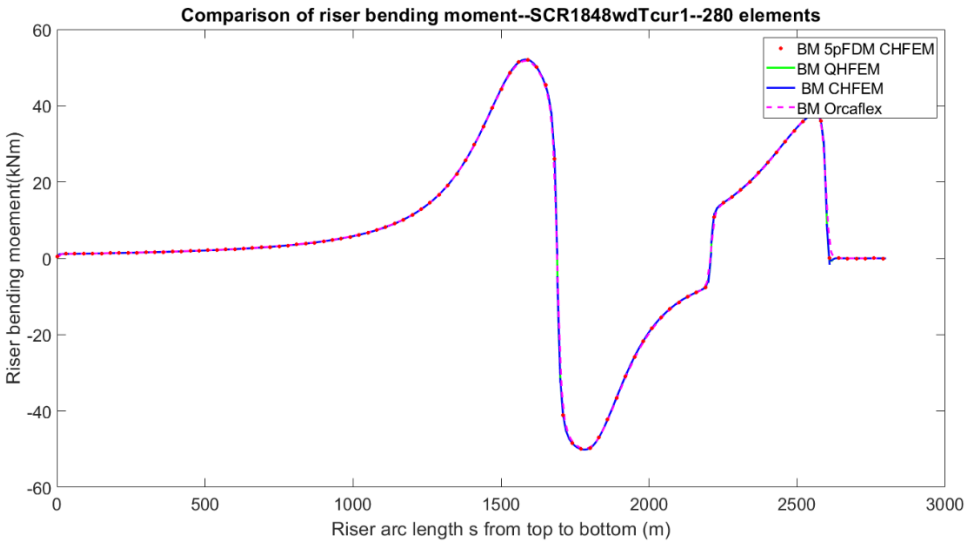

Figure 5.25 The SLWR bending moment distribution for subcase2

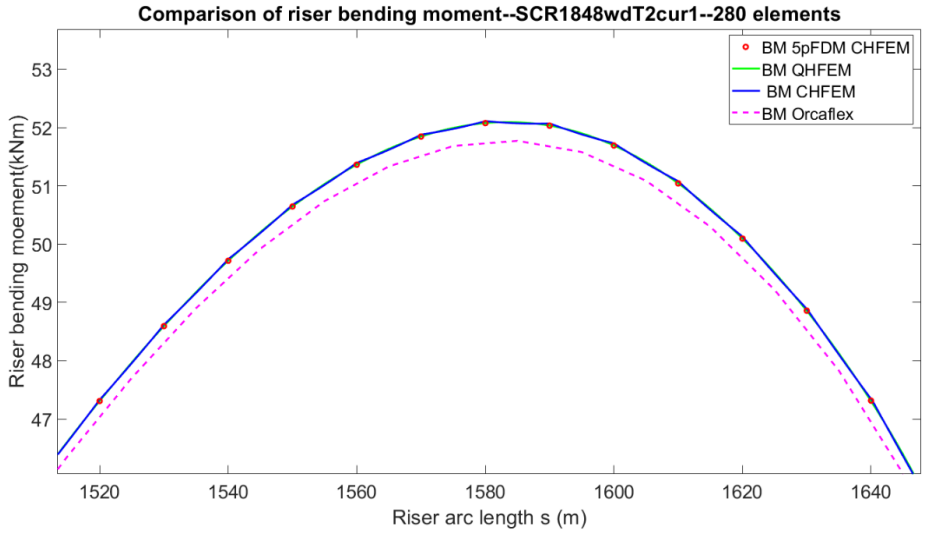

Figure 5.26 The SLWR maximum bending moment local zoom in for subcase2

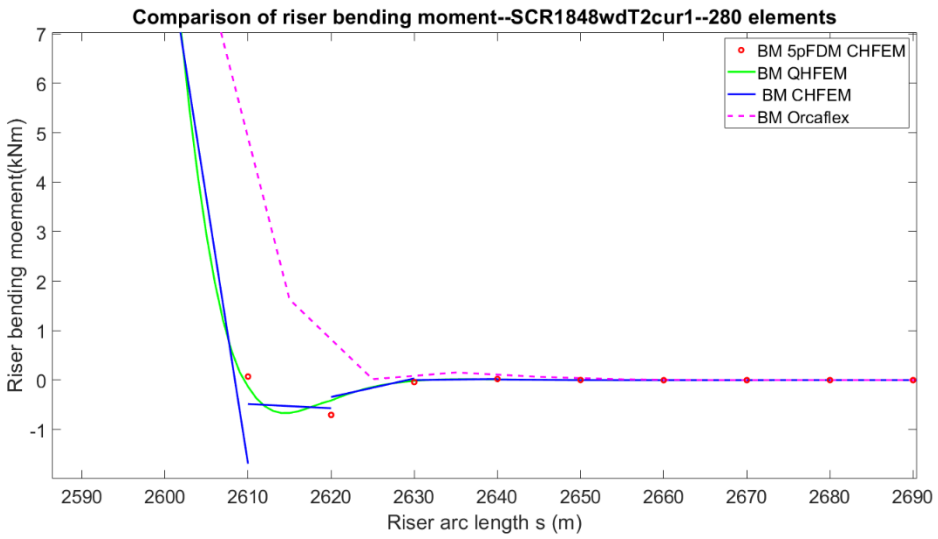

Figure 5.27 The SLWR bending moment TDP local zoom in for subcase2

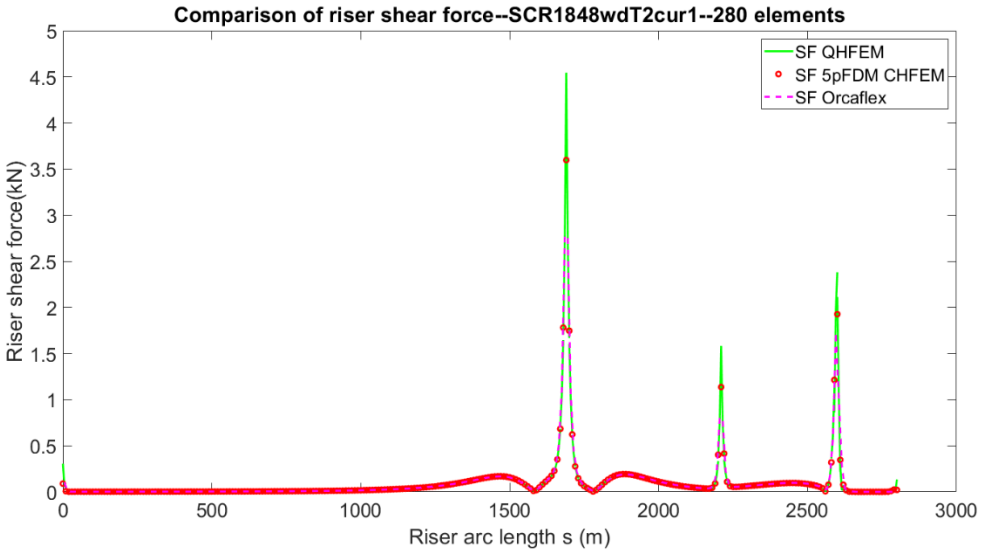

Figure 5.28 The SLWR shear force distribution for subcase2

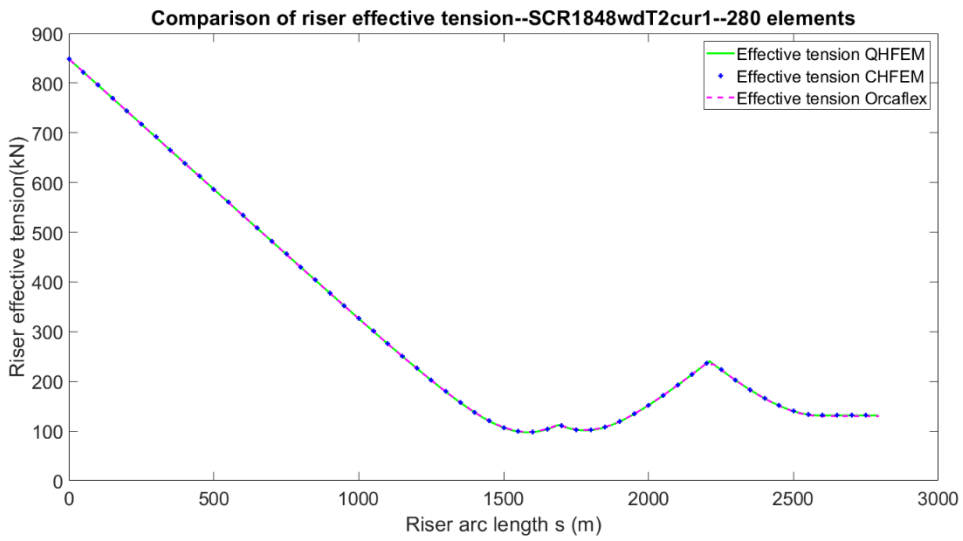

Figure 5.29 The SLWR effective tension distribution for subcase2

The third case is a parametric study on the influence of the current direction on the riser configuration and internal forces. The directions of the current load are set as -180deg, 0deg and 180deg respectively. The 180deg subcase denotes the SLWR subjected to positive linear current load, the parameters of which are already presented in Table 5.6 and Table 5.7; the 0deg subcase is the base with no current load; the -180deg subcase denotes the SLWR subjected to the same current loading but with an opposite direction to the 180deg subcase.

For this sensitivity analysis, a uniform mesh size is 10m are used for the domain mesh. The riser top end and bottom anchor point are assumed to be pinned with no horizontal offset under the influence the of current load. The results of the SLWR riser configuration, riser slope, bending moment distribution, shear force distribution and effective tension distribution are shown from Figure 5.30 to Figure 5.34 respectively.

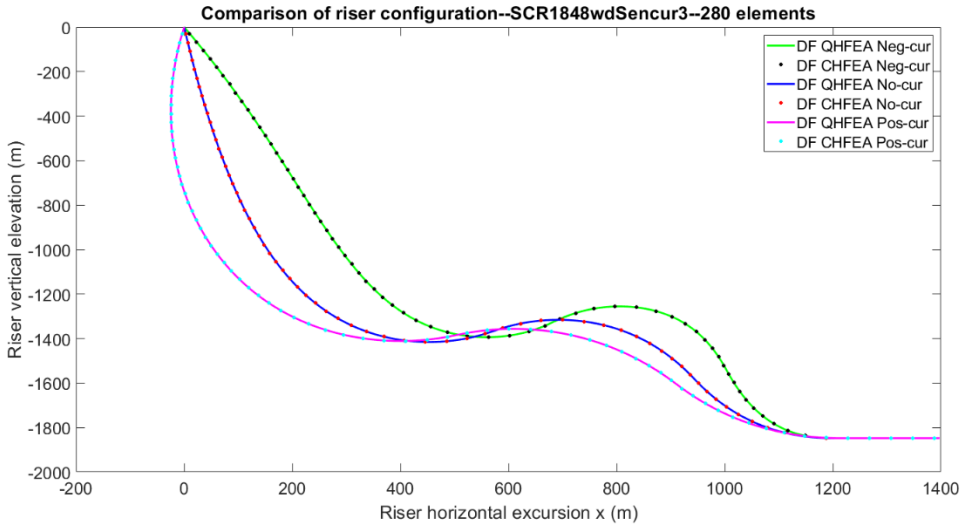

Figure 5.30 The SLWR configuration for current sensitivity analysis

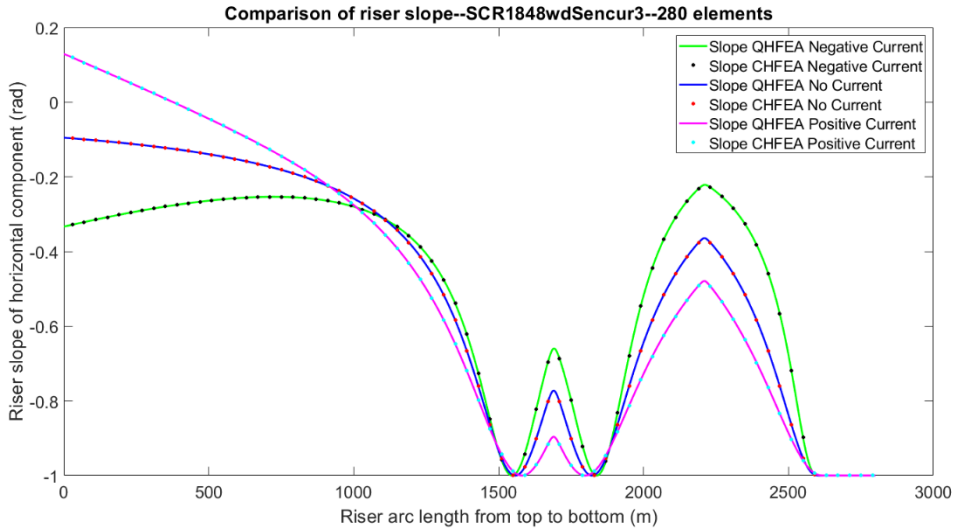

Figure 5.31 The SLWR horizontal slope component for current sensitivity analysis

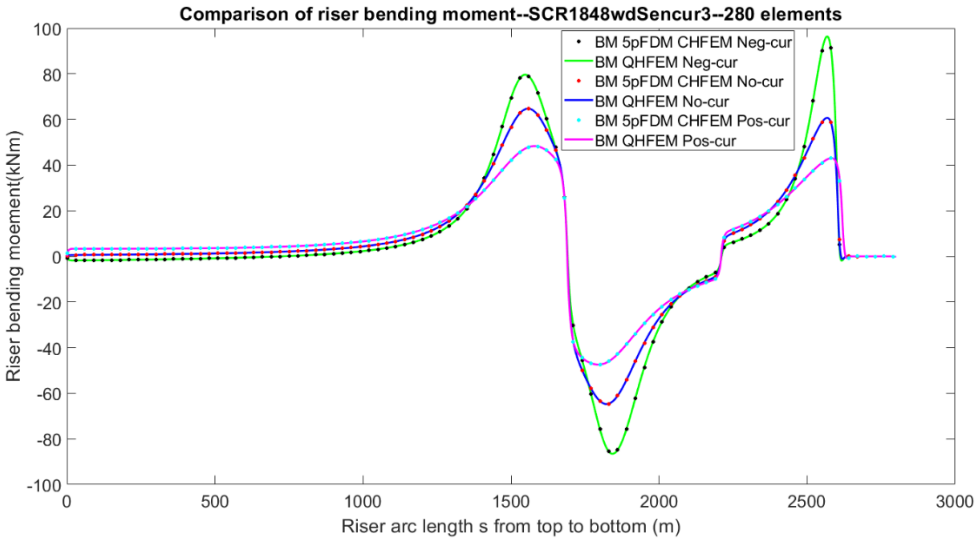

Figure 5.32 The SLWR bending moment distribution for current sensitivity analysis

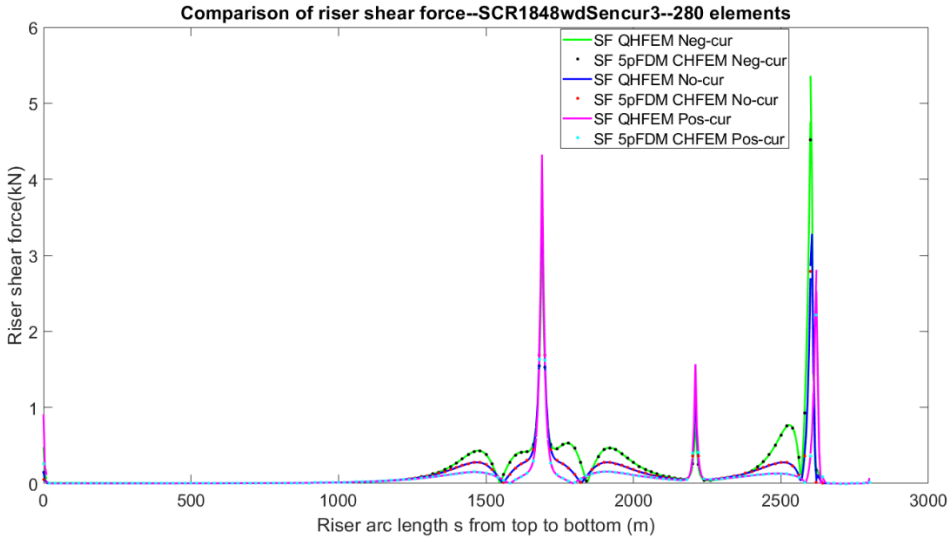

Figure 5.33 The SLWR shear force distribution for current sensitivity analysis

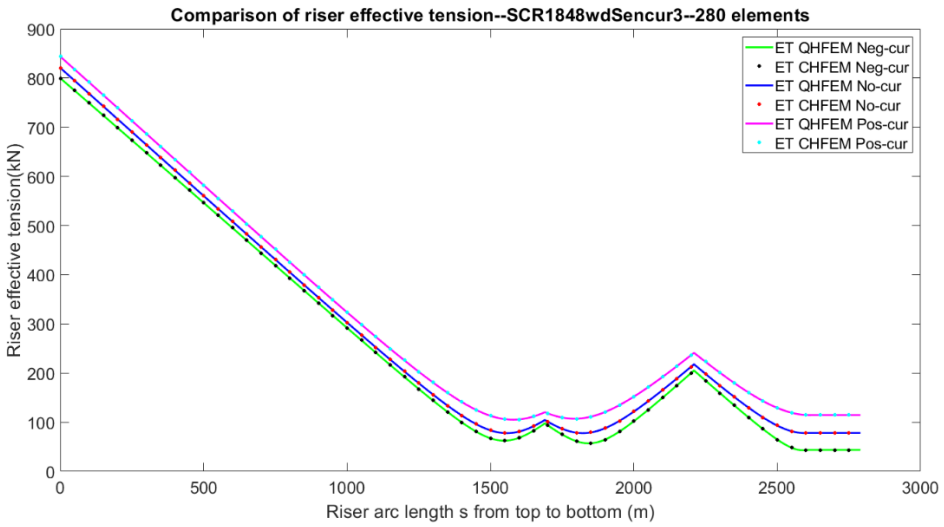

Figure 5.34 The SLWR axial effective tension distribution for current sensitivity analysis

From the current sensitivity analysis plots from Figure 5.30 to 5.34, it can be seen that the changes in current direction take a great hit on the riser configuration and internal force. Compared to the base case, positive current load will push the whole SLWR downward and increase both the top and TDP effective tension, while the peak bending moments can drop about 30% for this case; while the negative current load will push the whole SLWR configuration upward and decrease both the top and TDP effective tension, and the riser will suffer much larger curvature and the bending moment as shown in Figure 5.32. Especially at the touch-down zone (TDZ), the maximum bending moment has almost increased for about 60% for this case. Hence, during the design for the SLWR, the current loads, especially the current direction relative to the riser configuration plane should be paid great attention to.

5.2.4 SWR Static Analysis by RISER3D under Tidal Current Load

In this section, a deep-water 1500m water depth Steep Wave Riser (SWR) static analysis is performed by RISER3D. Compared to SCRs and SLWRs, SWR is a riser configuration that is suitable for deep water by connecting the bottom end directly to a subsea base. Therefore, there is

no touch down zone and pipe soil interaction section for this type of riser. Previous research work on this type of riser is very limited, which make this study on the SWR configuration and internal force subject to hydrodynamic load meaningful. Two cases are studied in this section, one is the base case, i.e. the SWR subject a positive tidal current load; the other one is the parametric study on the current load direction change. Moreover, the simulation results of the base case by RISER3D are also compared to that of by Orcaflex.

The main problem data of the SWR analysis are referred to a previous published paper (H.D. Qiao, et al., 2006), as listed in Table 5.8. The remaining input data not available in the referred literature are assumed according to engineering experience, as summarized in Table 5.9. The current loads and involved parameters are summarized in Table 5.10.

Table 5.8 Referred input data for 1500m water depth SWR analysis

Designation	**Symbol**	**Value**	**SI Unit**
Outer diameter	D_o	0.220	m
Bending stiffness	EI	4.736E+05	Nm^2
Axial stiffness	EA	1.652E+09	N
Sea water density	ρ_w	1025.0	kg/m^3
Water depth	H_{wd}	1500.0	m
Internal fluid density	ρ_i	0.00	kg/m^3
Submerged weight	W_{sub}	501.7	N/m
Submerged weight of BM segment	W_{bm}	-785.87	N/m

Table 5.9 Assumed input data for 1500m water depth SWR analysis

Designation	**Symbol**	**Value**	**SI Unit**
Outer diameter of BM	D_{bm}	0.57296	m
Buoyancy module material density	ρ_{bm}	427.7	Kg/m^3
Mass per unit length in air of pipe	m_r	90.1227	kg/m
Mass per unit length in air of BM section	m_{bm}	184.1396	kg/m
Upper hang-off segment	L_{us}	1080	m
Buoyancy module segment	L_{bm}	675	m
Lower segment	L_{ls}	450	m
Riser total length	L_r	2205.00	m

Table 5.10 Assumed input data of the tidal current load for the base case

Designation	**Symbol**	**Value**	**Unit**
Surface current velocity	v_u	1.1	m/s
Seabed current velocity	v_b	0.0	m/s
Current profile decay index	n_c	3	-
Normal drag coefficient	C_{dn}	0.7	-
Tangential drag coefficient	C_{dt}	0.07	-

For the base case, a total number of 490 uniform-length elements are utilized to discretize the whole riser length of 2205m, with an element length of 4.5m. For Newton iteration method,

the relaxation coefficient adopted is 0.15, considering this case is a nonlinear current and large deformation problem, large relaxation coefficient will have convergence problem. The riser tube is assumed to be empty during the analysis, i.e. with no internal fluid during the analysis.

For the key concerned simulation results of the base case, the top end tensions predicted by CABLE3D and RISER3D are both 459.66kN, and the bottom end tension predicted by CABLE3D and RISER3D are both 240.91kN. The top and bottom tension of the riser simulated by Orcaflex are 459.96kN and 241.22kN respectively. The top departure angle predicted by CABLE3D and RISER3D are 1.3521deg and 1.3533deg respectively, which is smaller than the Orcaflex result of 1.5564deg. The plots of the results for the base case, including the riser configuration, the local configuration zoom in, the riser horizontal slope, the riser bending moment , the maximum bending moment local zoom in, the riser shear force and the riser effective tension, are presented from Figure 5.35 to Figure 5.41 respectively.

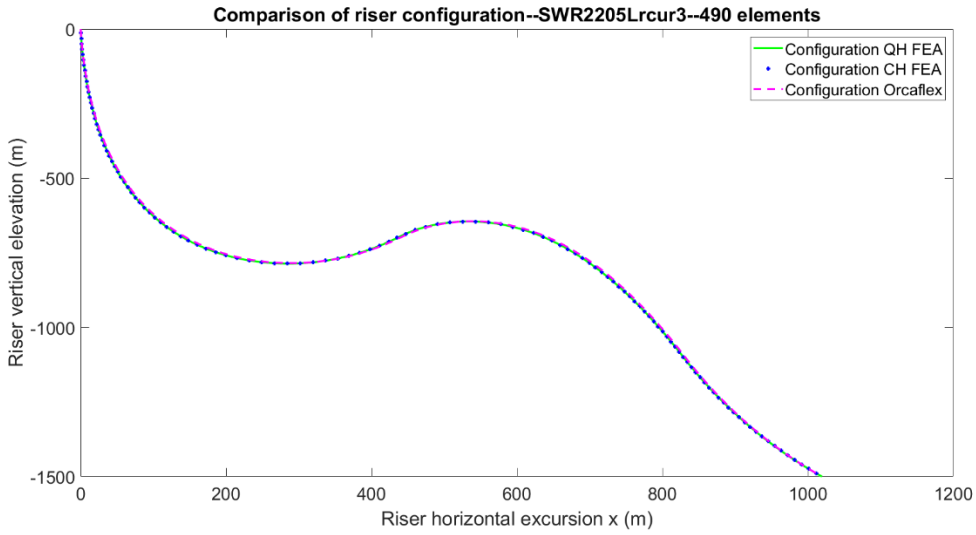

Figure 5.35 The SWR configuration for the base case analysis

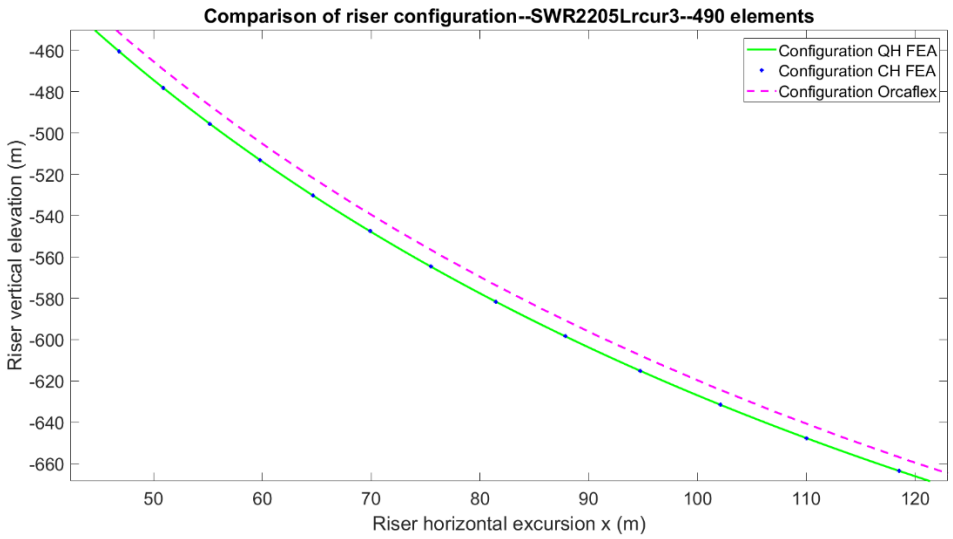

Figure 5.36 The SWR configuration local zoom in for the base case analysis

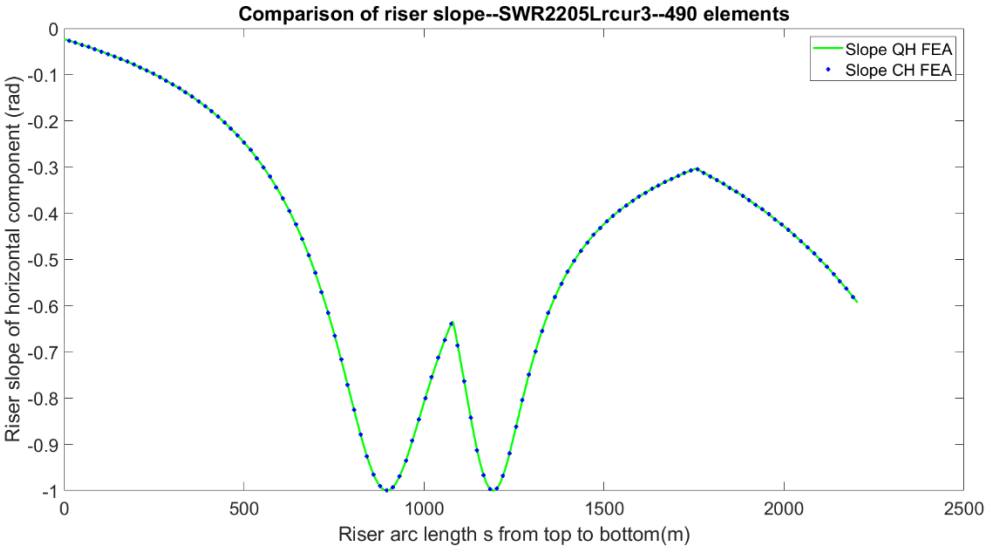

Figure 5.37 The SWR horizontal component of slope for the base case analysis

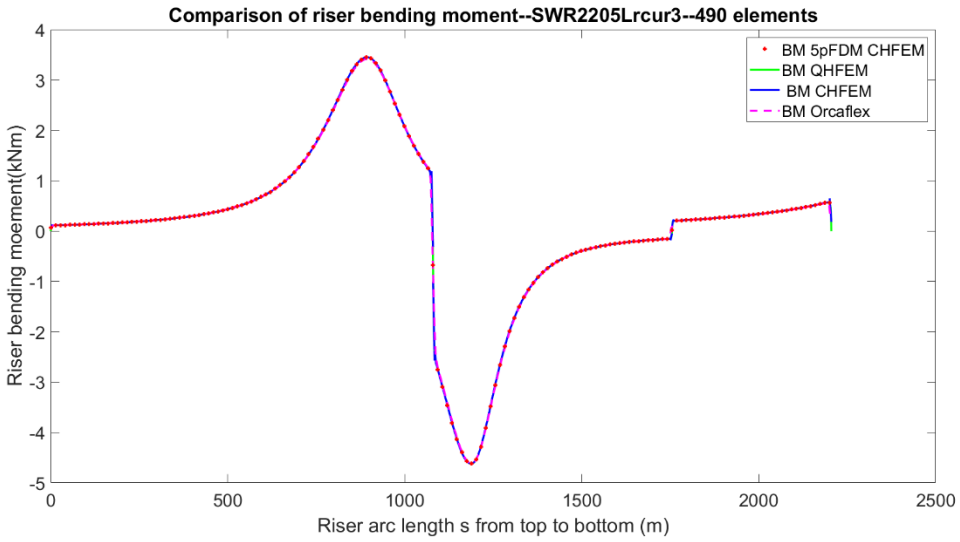

Figure 5.38 The SWR bending moment distribution for the base case analysis

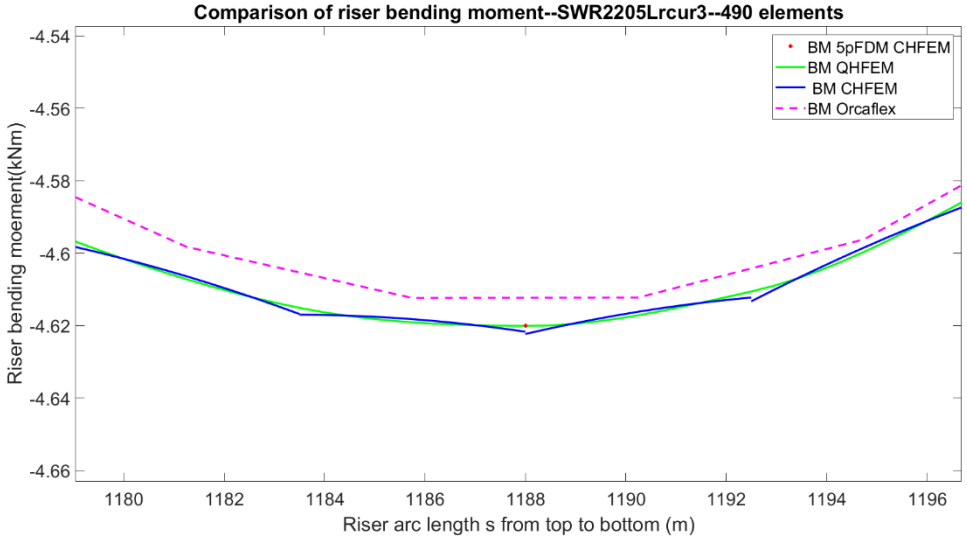

Figure 5.39 The SWR maximum bending moment local zoom in for the base case

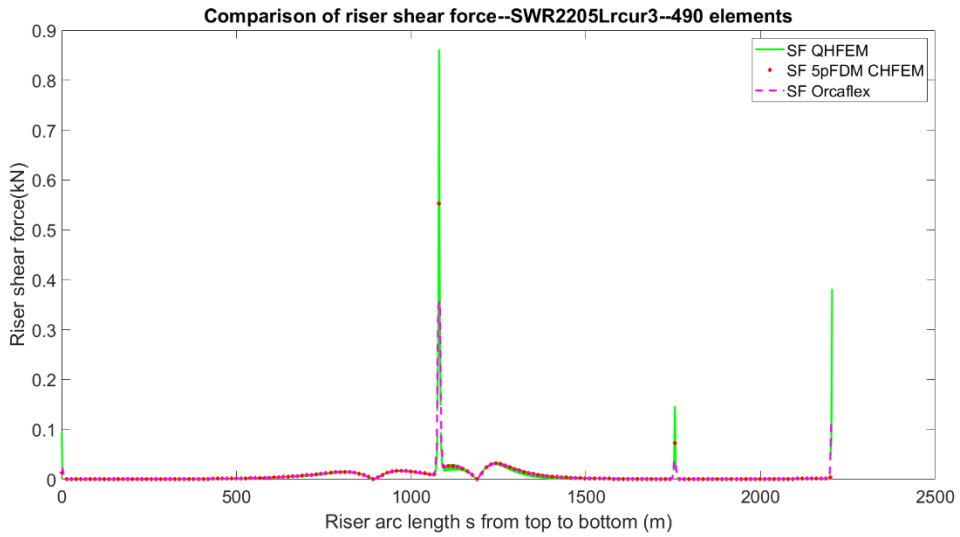

Figure 5.40 The SWR shear force distribution for the base case analysis

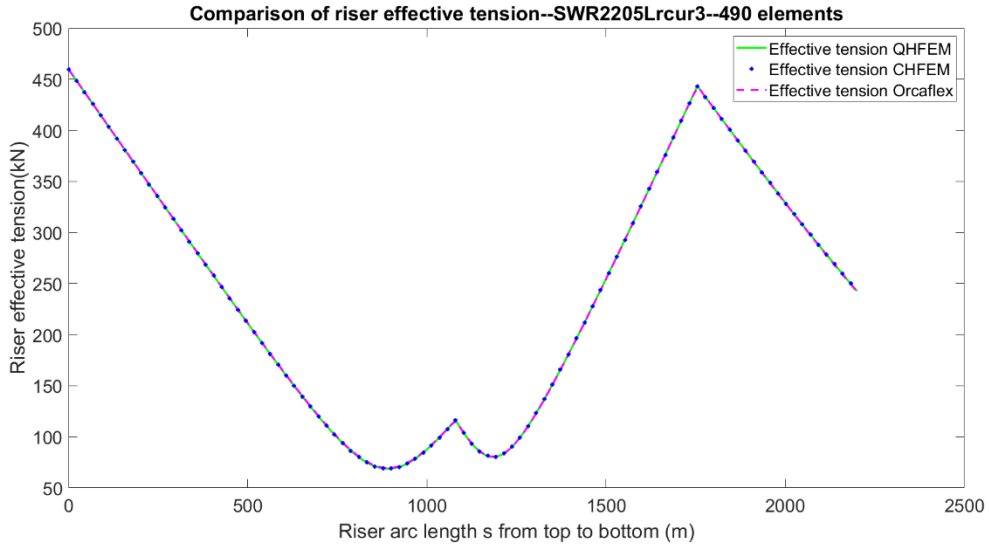

Figure 5.41 The SWR effective tension distribution for the base case analysis

For the current parametric study case, three scenarios are considered: the first scenario is exactly the same with the base case, i.e. the SWR subjected to positive current loads; the second scenario is the SWR subject to the same current velocities profile, but opposite direction to the

base case; the third scenario is the SWR subject to no current load. The simulation is performed with both CABLE3D and RISER3D. The main results of the parametric study, including the riser configuration, the horizontal riser slope, the riser bending moment, the riser shear force and the riser effective tension, are plotted from Figure 5.42 to Figure 5.46 respectively.

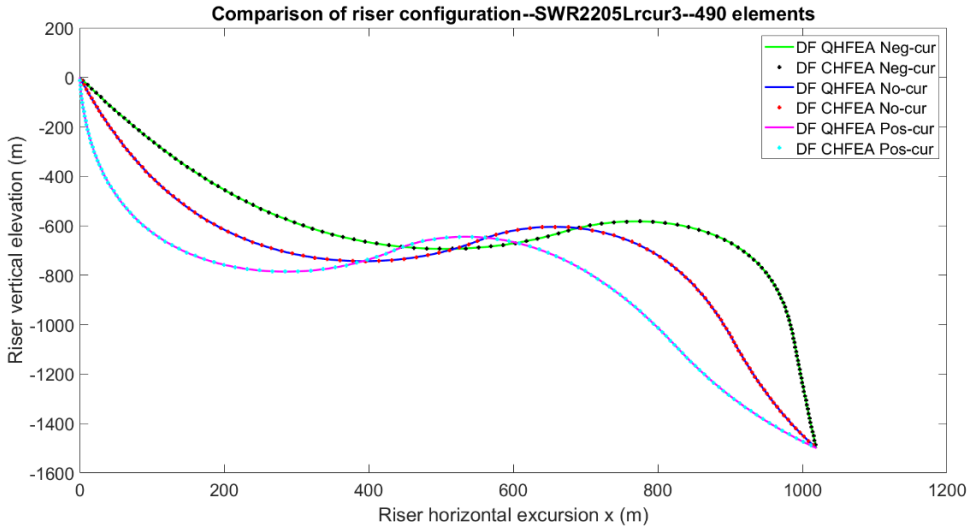

Figure 5.42 The SWR configuration for the parametric study case

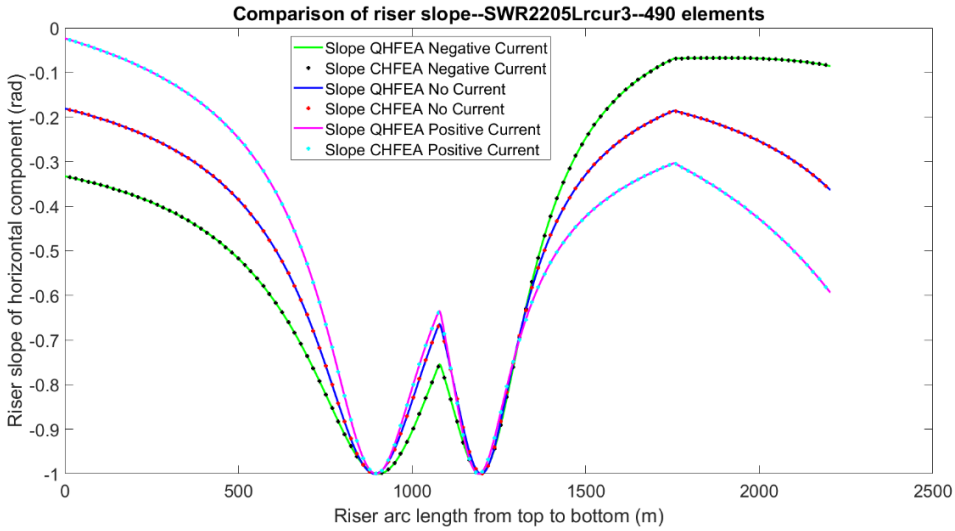

Figure 5.43 The SWR horizontal component of slope distribution for parametric study

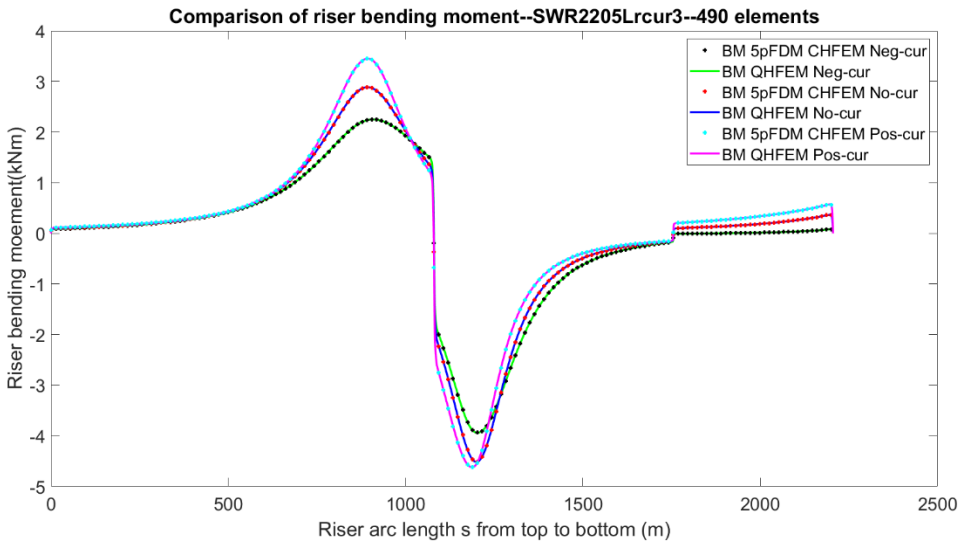

Figure 5.44 The SWR bending moment distribution for the parametric study case

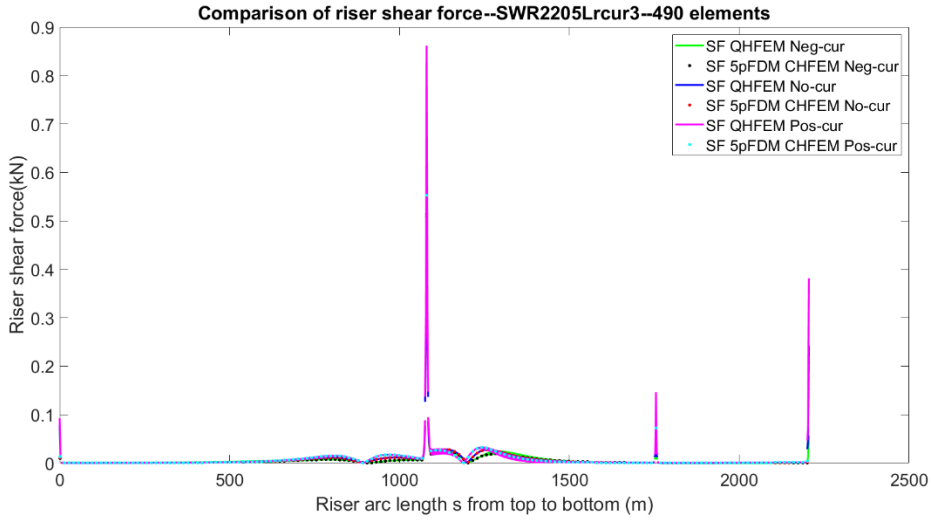

Figure 5.45 The SWR shear force distribution for the parametric study case

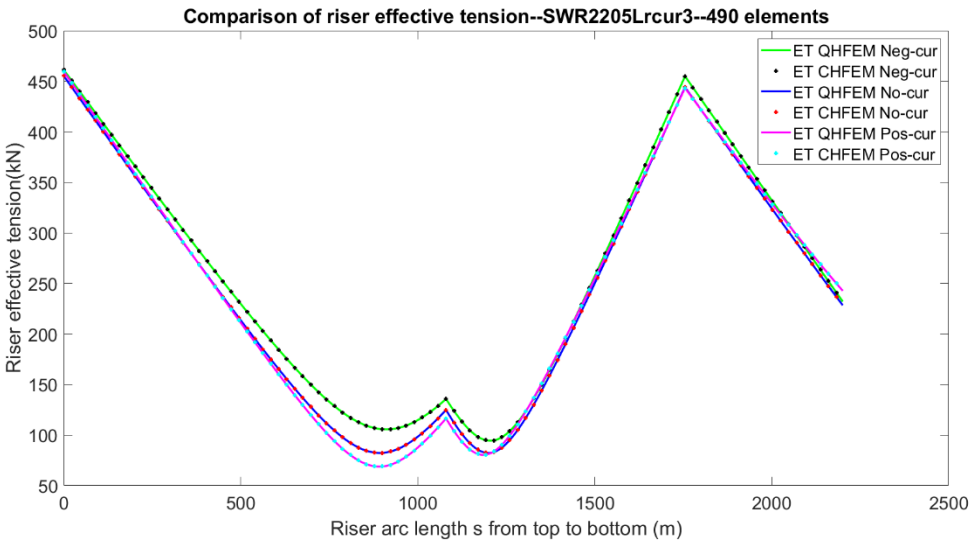

Figure 5.46 The SWR effective tension distribution for the parametric study case

According to the plotted results of the SWR parametric study case, the following conclusions, for the 4.5m element mesh, can be made:

- The difference between CABLE3D and RISER3D is very small, all the results between the two programs match well with each other
- The current load will drastically change the SWR configuration, declination angles along the riser arc length, and internal bending moment distribution
- The top and bottom effective tension does not change dramatically with the change of current direction and velocity

5.3 Application of RISER3D for Top Tension Risers (TTRs)

5.3.1 Deep-water Drilling Riser Subjected to Steady Current Load

When deep water drilling risers encounter the high external lateral current load, they will suffer large nonlinear deformation. Accurate prediction of the lateral deformation and internal force is of great importance for drilling riser design and analysis. Considering the high cost and

complexity of scaled model experiments for deep water drilling risers, the numerical finite element method becomes a feasible and cost-effective alternative for the prediction of their behaviors.

Considering the current load on deep water drilling riser is deformation dependent, i.e. the current load will initiate the deformation of riser. Moreover, the current load is a function of the local orientation of the deformed riser elements, the current loading and the riser deformation are coupled at all iteration step. Therefore, an initial vertical configuration will be guessed at the beginning of the analysis for vertical drilling riser, the current load at the first iteration will be computed according to the initial configuration. After solving the system of equations with current load by Newton iteration, a new equilibrium riser configuration will be obtained. And then the current load will be recalculated based on the newly obtained riser configuration. After recalculation, the system of equations with updated loads should be solved to achieve another new equilibrium riser configuration. These procedures will be repeated as much as required until the final equilibrium configuration has hit the preset convergence limit, which is usually a small positive number such as 10^{-6}. At this point, the analysis is considered as converged and can be terminated.

In this section, a previous three-dimensional drilling riser deformation study under current loads performed by Bernitsas et al. (1985) is reevaluated with both CABLE3D and RISER3D, the results of which are compared to those of published in one of his journal papers. All the three sub-cases in the literature are reanalyzed with RISER3D. The particulars of the riser are summarized in Table 5.11.

Table 5.11 The particulars of the riser for analysis

Designation	Symbol	Value	SI Unit
Outer Diameter	D_o	0.610	m
Internal Diameter	D_i	0.575	m
Young's Modulus	E	2.070E+11	Pa
Outer Cross-sectional Area	A_f	2.92247E-01	m^2
Internal Cross Section	A_i	2.59672E-01	m^2
Weight in Air	W_{air}	400.0873	kg/m
Buoyancy	B	5975.4818	N/m
Steel Density	ρ_s	7850.0	kg/m^3
Moment of Inertia	I	1.43067E-03	m^4
Bending Stiffness	EI	2.96148E+08	Nm^2
Axial Stiffness	EA	6.74290E+09	N
Drilling Internal Fluid Density	ρ_i	1250.323	kg/m^3
Submerged Weight	W_{sub}	1132.0	N/m
Density of steel pipes	ρ_s	8200.0	kg/m^3
Density of water	ρ_f	1025	kg/m^3
Density of Buoyancy Module material	ρ_{bm}	440	kg/m^3
Buoyancy Module Diameter	D_{bm}	0.870	m
Offset of riser upper end	d_0	0.0	m
Riser Total Length	L_r	2000.00	m
Gravitational constant	g	9.80665	m/s^2

Table 5.11 Continued

Designation	Symbol	Value	SI Unit
Hydrodynamic coefficient	C_d	1.0 or 0.7	-
Top tension load factor	C_{lf}	1.2	-
Applied top tension	T_t	$C_{lf} * W_{sub} * L_r$	N

For the first subcase, the riser is subject to a shear current load, which linearly decreases from the surface velocity 1.5m/s to the seabed velocity 0 m/s in positive global X-direction; for the second subcase, the riser is subject to a tidal current profile which decays proportionally to the one-seventh root of the water depth from the surface velocity 1 m/s to the sea bottom velocity 0m/s in positive global X-direction; for the third subcase, the riser is subject to both current profiles simultaneously as depicted in the first and second subcase, with shear current in global X-direction and tidal current in global Z-direction. The case matrices are summarized in Table 5.12.

Table 5.12 The current load case matrices

Case No	v_u (m/s)	v_b (m/s)	y_u (m)	y_b (m)	n_c	C_{dn}	C_{dt}
Subcase 1	1.5	0.0	0.0	2000.0	1	1.0	0.0
Subcase 2	1.0	0.0	0.0	2000.0	7	1.0	0.0
Subcase 3	Combined subcase 1 current in X-direction and Subcase 2 current in Z-direction					0.7	0.0

For the first subcase, a total of 80 uniform-length elements are employed to discretize the whole riser length of 2000m, with a uniform element length of 25m. The main simulation results of RISER3D and CABLE3D,consisting of deformed riser configuration, horizontal component of riser slope, riser bending moment, local zoom-in of the maximum bending moment (BM) section, riser shear force and effective tension, are compared from Figure 5.47 to Figure 5.52 respectively. After deformation, the top end riser effective tension is 2771.3kN and the bottom end effective tension is 520.2kN for both RISER3D and CABLE3D.

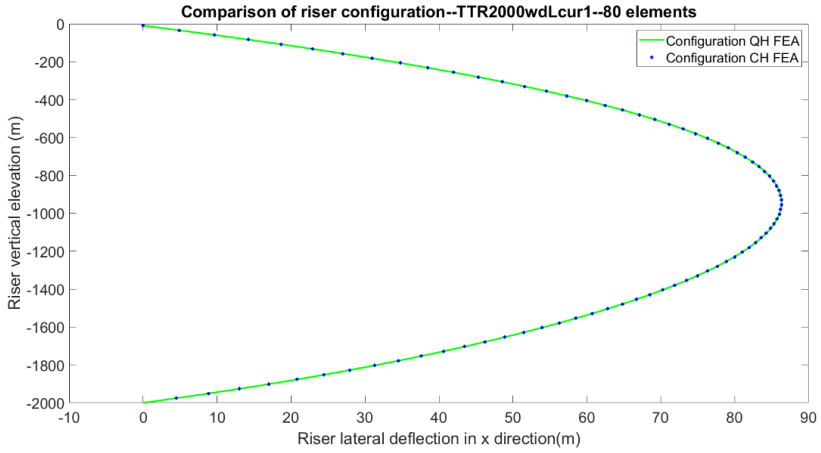

Figure 5.47 Deformed riser configuration for 2000m TTR subcase1

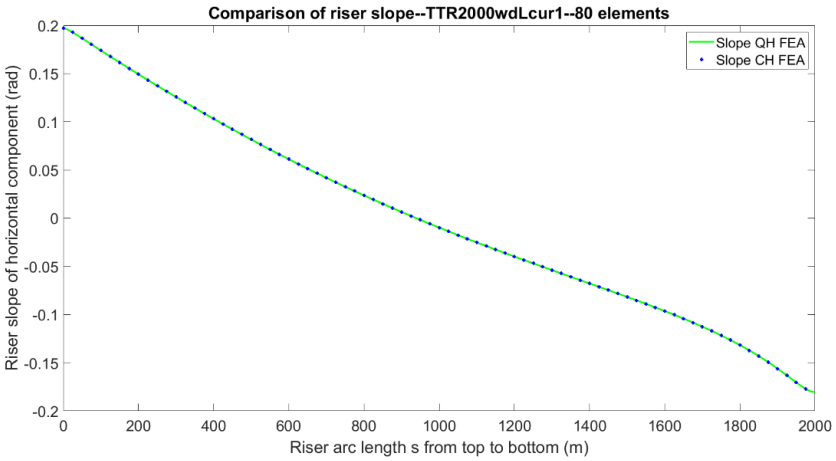

Figure 5.48 Deformed riser horizontal slope component for 2000m TTR subcase1

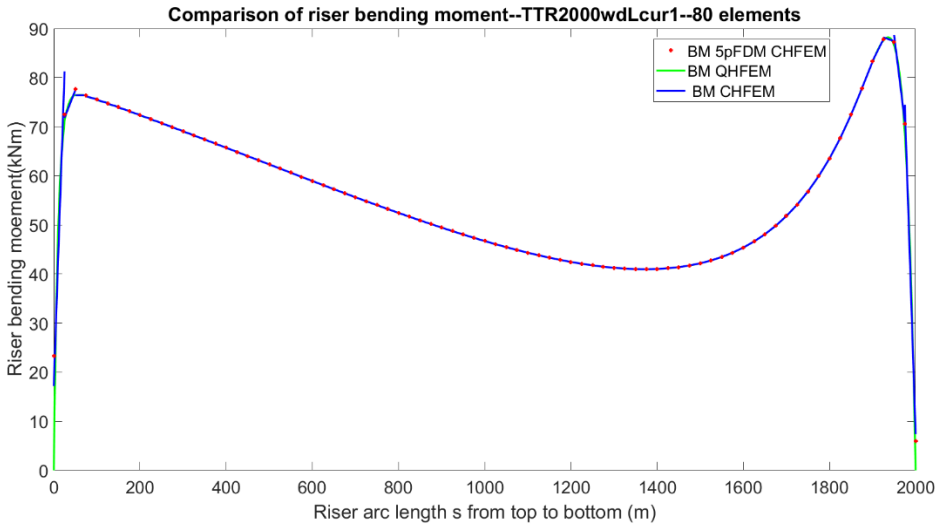

Figure 5.49 Riser bending moment distribution for 2000m TTR subcase1

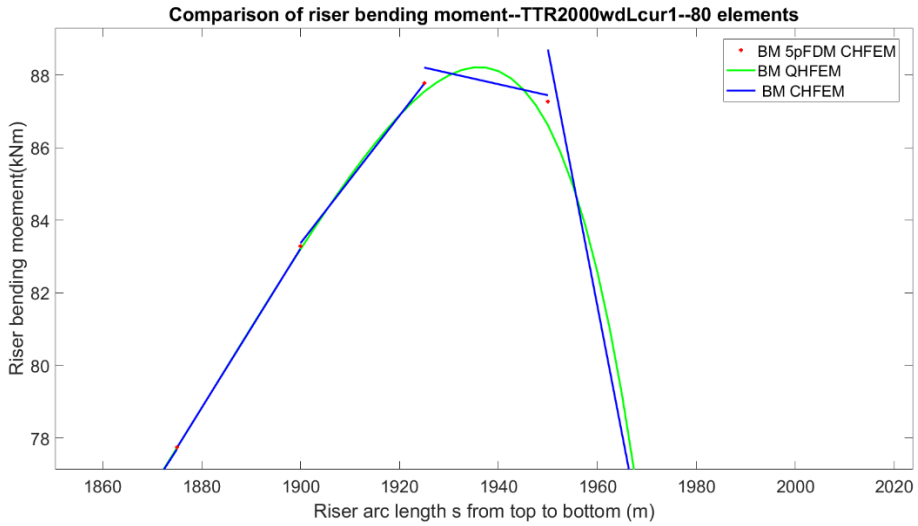

Figure 5.50 Riser maximum BM local zoom in for 2000m TTR subcase1

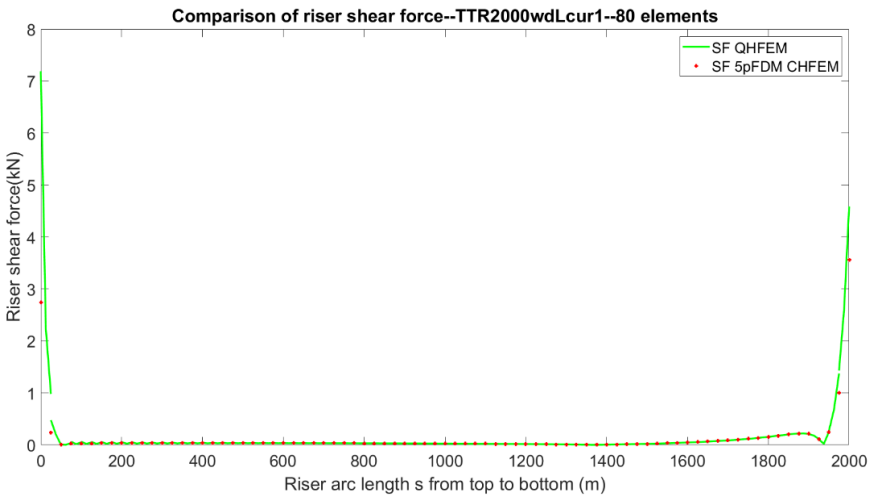

Figure 5.51 Riser shear force distribution for 2000m TTR subcase1

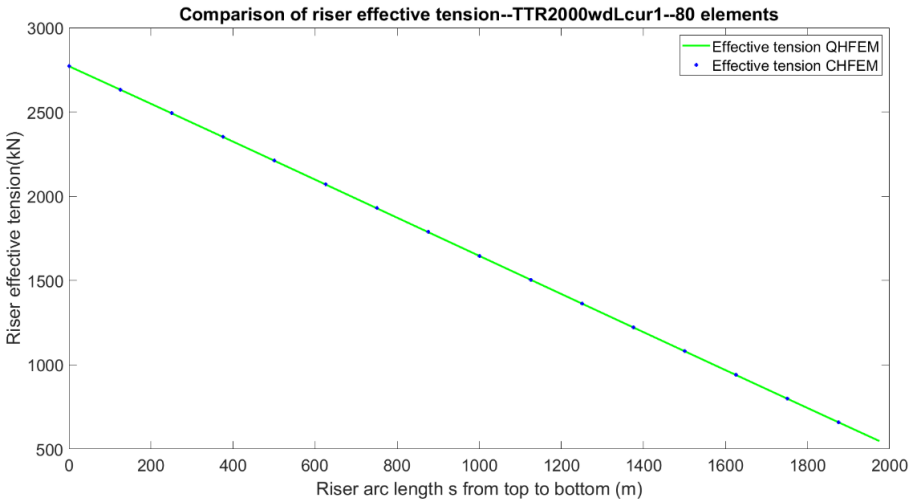

Figure 5.52 Riser effective tension distribution for 2000m TTR subcase1

Form Figure 5.47 to Figure 5.52, the riser lateral deflection, the riser x-component of slope and the riser effective tension match very well between RISER3D and CABLE3D respectively. As for the bending moment, RISER3D can accurately predict the distribution of bending moment at the neighborhood of the maximum bending moment point, while CALBE3D can only approximately predict the distribution of bending moment at that section. For the shear force

prediction, the shear forces predicted at both ends of riser by RISER3D are larger than those of by CALBE3D as illustrated in Figure 5.51, especially at the top end of the riser.

The comparison of riser deflection and slope between the results published by Bernitsas (1985) and by RISER3D are shown in Table 5.13 and 5.14 respectively. In the last column of tables in this section, the difference between RISER3D results, highlight in green color, and the best results provided by Bernitsas (1985), highlight in blue color, is presented.

Table 5.13 The comparison of the riser lateral deflection

z/L	RISER3D deflection (m)	Linear[3] (m)	Nonlinear[3] WODD[1] (m)	Nonlinear[3] WTDD[2] (m)	Diff. to the best (%)
0.000	**0.000**	0.00	0.00	**0.00**	-
0.125	**37.637**	40.45	40.04	**36.89**	2.02
0.250	**62.802**	66.46	66.01	**61.63**	1.90
0.375	**78.867**	82.62	82.21	**77.45**	1.83
0.500	**86.041**	89.51	89.11	**84.53**	1.79
0.625	**83.320**	86.28	85.84	**81.88**	1.76
0.750	**69.193**	71.47	70.79	**67.99**	1.77
0.875	**41.964**	43.35	42.88	**41.22**	1.80
1.000	**0.000**	0.00	0.00	**0.00**	-

Notes applied to all tables in section 5.3.1:

1. WODD= without deformation dependency;
2. WTDD=with deformation dependency;
3. Columns of result cited from the journal paper by Bernitsas (1985).

Table 5.14 The comparison of the riser horizontal slope

z/L	RISER3D slope (rad)	Linear (rad)	Nonlinear WODD[1] (rad)	Nonlinear WTDD[1] (rad)	Diff. to the best (%)
0.000	**0.1804**	0.1979	0.1939	**0.1759**	2.56
0.125	**0.1216**	0.1275	0.1270	**0.1194**	1.84
0.250	**0.0817**	0.0832	0.0832	**0.0803**	1.74
0.375	**0.0469**	0.0464	0.0465	**0.0462**	1.52
0.500	**0.0098**	0.0081	0.0081	**0.0097**	1.03
0.625	**-0.0326**	-0.0350	-0.0352	**-0.0320**	1.87
0.750	**-0.0816**	-0.0846	-0.0848	**-0.0802**	1.75
0.875	**-0.1374**	-0.1417	-0.1410	**-0.1350**	1.78
1.000	**-0.1968**	-0.2038	-0.2010	**-0.1937**	1.60

For the second subcase, a total of 80 uniform-length elements are employed to discretize the whole riser length, with an element length of 25m. The same numerical simulation results as the first subcase are presented from Figure 5.53 to Figure 5.58 respectively. After deformation, the top end riser effective tension is 2756.2kN and the bottom end effective tension is 517.8kN for both RISER3D and CABLE3D.

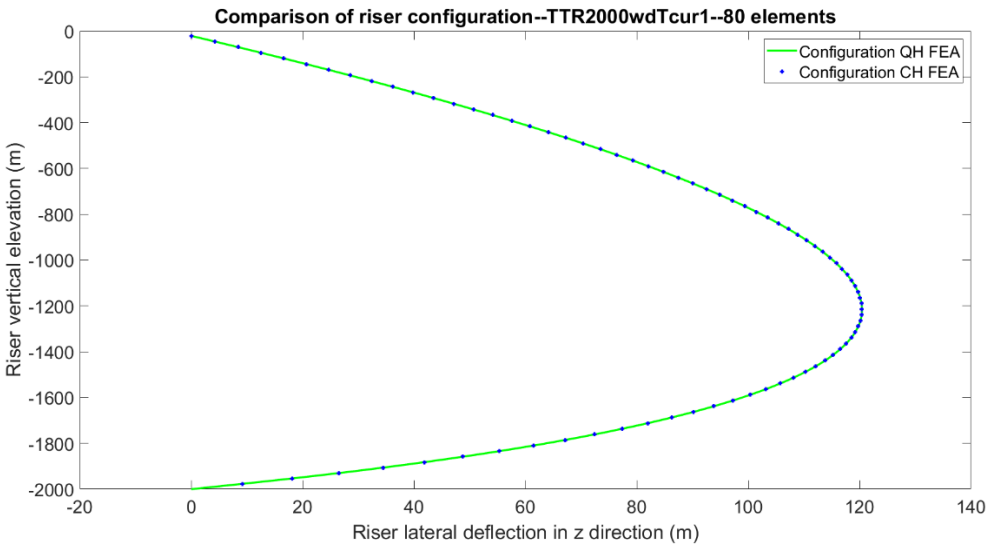

Figure 5.53 Deformed riser configuration for 2000m TTR subcase 2

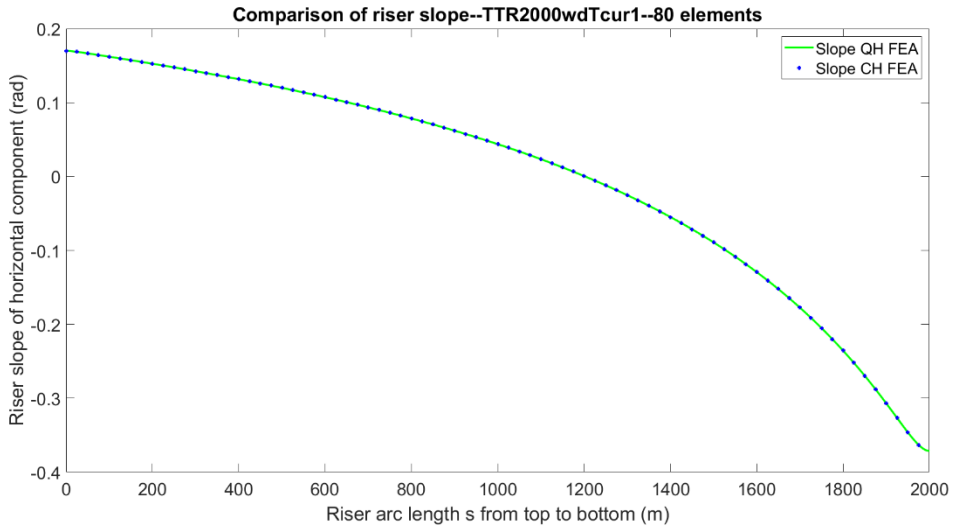

Figure 5.54 Deformed riser slope of x component for 2000m TTR subcase 2

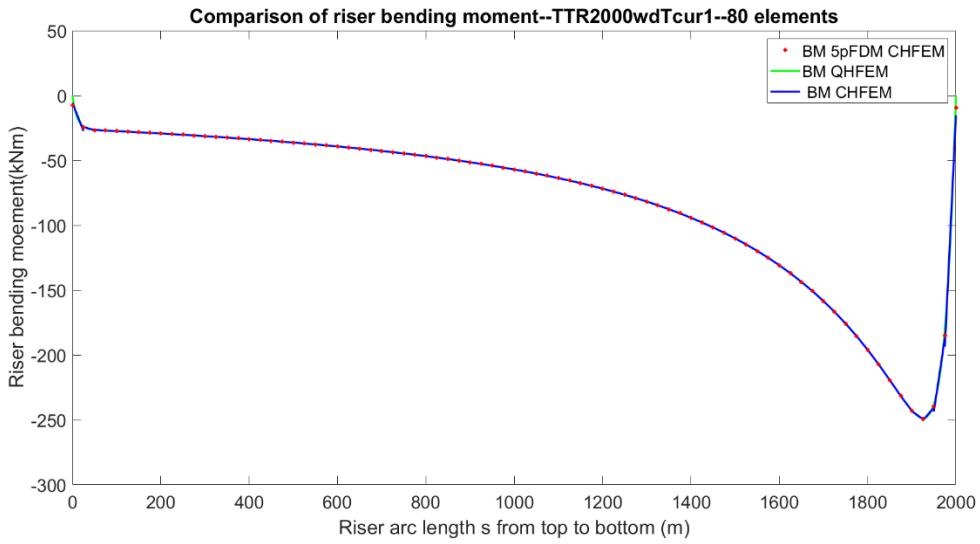

Figure 5.55 Riser bending moment distribution for 2000m TTR subcase 2

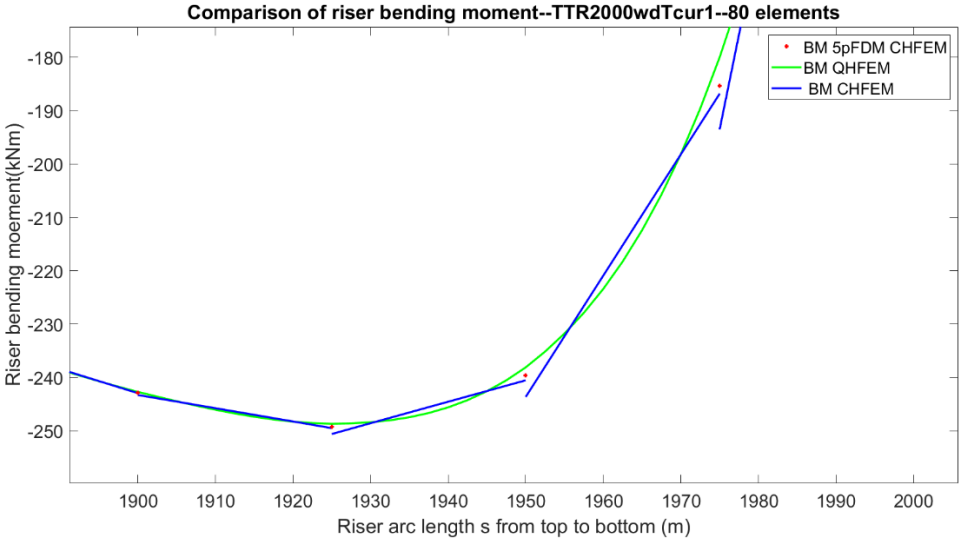

Figure 5.56 Riser maximum absolute BM local zoom in for 2000m TTR subcase 2

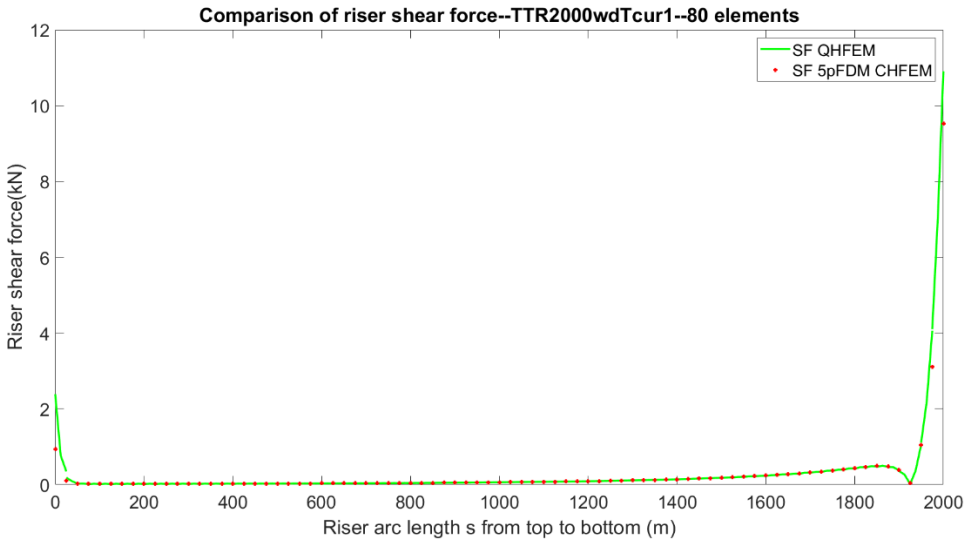

Figure 5.57 Riser shear force distribution for 2000m TTR subcase 2

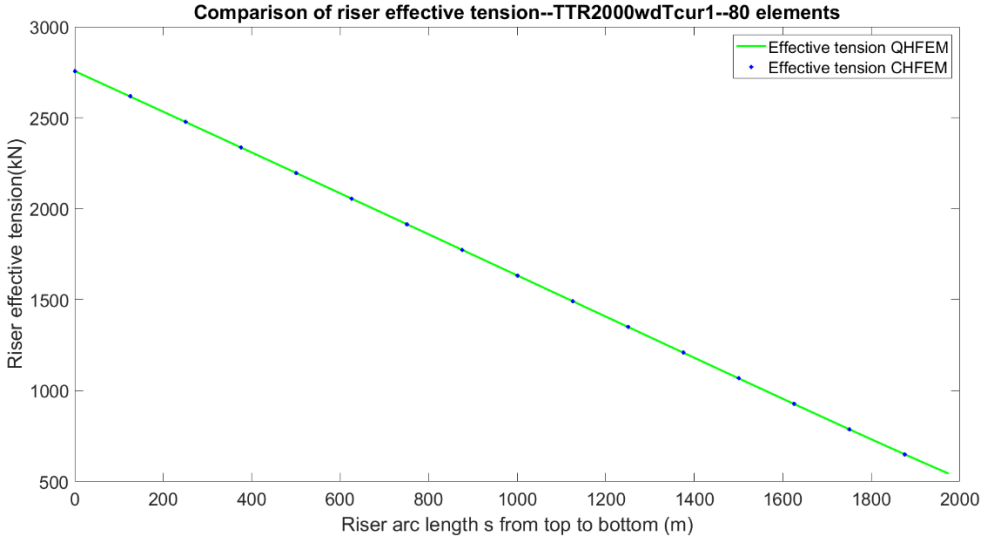

Figure 5.58 Riser effective tension distribution for 2000m TTR subcase 2

For the second subcase, the comparison of riser deflection and slope, between the results presented in the literature by Bernitsas (1985) and those of by RISER3D, are shown in Table 5.15 and 5.16 respectively.

Table 5.15 The comparison of the riser lateral deflection for subcase 2

z/L	RISER3D deflection (m)	Linear[3]	Nonlinear[3] WODD[1]	Nonlinear[3] WTDD[2]	Diff. to the best (%)
0.000	**0.000**	0.00	0.00	**0.00**	-
0.125	**72.423**	78.91	75.71	**70.74**	2.38
0.250	**108.106**	114.97	112.2	**105.9**	2.08
0.375	**120.150**	126.1	124	**117.9**	1.91
0.500	**115.824**	120.62	118.9	**113.7**	1.87
0.625	**99.360**	102.98	101.6	**97.54**	1.87
0.750	**73.443**	75.9	74.83	**72.1**	1.86
0.875	**39.889**	41.15	40.53	**39.16**	1.86
1.000	**0.000**	0.00	0.00	**0.00**	-

Notes applied to all tables in section 5.3.1:

1. WODD denotes without deformation dependency, applying to all tables in this section;
2. WTDD denotes with deformation dependency, applying to all tables in this section;
3. Columns of results cited from the paper by Bernitsas (1985).

Table 5.16 The comparison of the riser horizontal slope for subcase 2

z/L	RISER3D slope (rad)	Linear[3]	Nonlinear[3] WODD[1]	Nonlinear[3] WTDD[2]	Diff. to the best (%)
0.000	**0.3713**	0.4204	0.3890	**0.3603**	3.05
0.125	**0.2051**	0.2130	0.2122	**0.2014**	1.84
0.250	**0.0891**	0.0868	0.0895	**0.0881**	1.14
0.375	**0.0119**	0.0075	0.0095	**0.0121**	-1.65
0.500	**-0.0438**	-0.0485	-0.0470	**-0.0428**	2.34
0.625	**-0.0862**	-0.0909	-0.0896	**-0.0846**	1.89
0.750	**-0.1199**	-0.1246	-0.1231	**-0.1178**	1.78
0.875	**-0.1476**	-0.1525	-0.1504	**-0.1449**	1.86
1.000	**-0.1700**	-0.1753	-0.1728	**-0.1672**	1.67

For the subcase 3, a total of 80 elements are employed to discretize the whole riser length, with an element length of 25m. After deformation, the top end riser effective tension is 2801.5kN and the bottom end effective tension is 567.9kN for both RISER3D and CABLE3D.

For subcase 3, the comparison of riser deflections in x and z direction, between M. Bernitsas et al. (1985) and RISER3D, are shown in Table 5.17 and 5.18 respectively.

Table 5.17 The comparison of the riser lateral deflection in x direction for subcase 3

s/L	2D[3] WODD[1] x (m)	3D[3] WODD x (m)	2D[3] WTDD[2] x (m)	3D[3] WTDD x (m)	Cable3D x (m)	Riser3D x (m)	Cable3D Diff. (%)	Riser3D Diff. (%)
0	0	0	0	**0**	0.00	**0.00**	0.00	0.00
0.125	45.49	43.94	42.19	**38.65**	39.65	**39.65**	2.58	2.58
0.250	73.36	71.74	68.86	**64.13**	65.61	**65.61**	2.31	2.31
0.375	88.78	87.3	84.03	**79.07**	80.76	**80.76**	2.14	2.14
0.500	93.35	92.01	88.91	**84.19**	85.93	**85.93**	2.07	2.07
0.625	87.27	86.05	83.55	**79.41**	81.03	**81.03**	2.04	2.04
0.750	70.15	69.11	67.45	**64.23**	65.54	**65.54**	2.04	2.04
0.875	41.31	40.63	39.86	**37.98**	38.77	**38.77**	2.08	2.08
1.000	0	0	0	**0**	0.00	**0.00**	0.00	0.00

Table 5.18 The comparison of the riser lateral deflection in z direction for subcase 3

s/L	2D[3] WODD z (m)	3D[3] WODD z (m)	2D[3] WTDD z (m)	3D[3] WTDD z (m)	Cable3d z(m)	Riser3D z(m)	Cable3D Diff. (%)	Riser3D Diff. (%)
0.00	0.00	0.00	0.00	**0.00**	0.00	**0.00**	0.00	0.00
0.125	65.33	64.2	60.89	**56.65**	58.21	**58.21**	2.76	2.76
0.250	98.45	97.19	92.76	**87.32**	89.45	**89.45**	2.44	2.44
0.375	111.2	110	105.6	**100.2**	102.45	**102.45**	2.25	2.25
0.500	109.4	108.2	104.5	**99.6**	101.77	**101.77**	2.18	2.18
0.625	95.93	94.86	92.07	**88.01**	89.89	**89.89**	2.14	2.14
0.750	72.58	71.62	69.93	**66.9**	68.32	**68.32**	2.13	2.13
0.875	40.37	39.7	39.03	**37.3**	38.09	**38.09**	2.13	2.13
1.000	0.00	0.00	0.00	**0.00**	0.00	**0.00**	0.00	0.00

5.3.2 Shallow Water TTR Parametric Studies by RISER3D

In this section, three sets of sensitivity analyses have been performed using RISER3D and CABLE3D to identify the influence of some dominant parameters on the TTR configuration and internal force. The parameters chosen for sensitivity analysis including the uniform current velocity, the top tension of TTR and the Flex Joint stiffness at both end of the TTR.

The main properties of the shallow water TTR are referred to a previous literature published by M. Yazdchi and M.A. Crisfiled (2002). The referred and calculated particulars of the TTR are summarized in Table 5.19.

Table 5.19 Particulars for the shallow water TTR

Designation	Symbol	Value	SI Unit
Outer diameter	D_o	0.25	m
Internal diameter	D_i	0.21	m
Young's Modulus	E	2.00E+11	Pa
Outer cross-sectional area	A_f	0.0490874	m^2
Internal cross section	A_i	0.0346361	m^2
Weight in air	W_{air}	111.2752	kg/m
Buoyancy	B	503.146	N/m
Steel density	ρ_s	7700.0	kg/m^3
Internal fluid density	ρ_i	800.0	kg/m^3
Density of water	ρ_f	1025	kg/m^3
Moment of inertia	I	9.6282E-05	m^4
Bending stiffness	EI	1.92564E+07	Nm^2
Axial stiffness	EA	2.89027E+09	N
Submerged weight	W_{sub}	886.695	N/m
Riser total length	L_r	320.00	m
Gravitational constant	g	10.0	m/s^2
Normal hydrodynamic drag coefficient	C_{dn}	1.0	-
Tangential hydrodynamic drag coefficient	C_{dt}	0.01	-
Top tension load factor	C_{lf}	1.0	-
Applied top tension	T_t	510.0	kN

For the first sensitivity analysis, the TTR is subject to three different magnitudes of uniform current velocities, i.e. 1.0m/s, 1.5m/s and 2.0m/s. The tension load factor of 1.0 is adopted for this parametric study, which indicates the base case top tension 510.0kN is applied. A total of 32 equal size elements are used for the mesh of the whole TTR domain, with an element length of 10m. The main results compared between RISER3D and CABLE3D, including the riser horizontal deflection, the horizontal component of the riser slope and the distribution of riser bending moment, shear force and effective tension along the arc length, are plotted from Figure 5.59 to Figure 5.63 respectively.

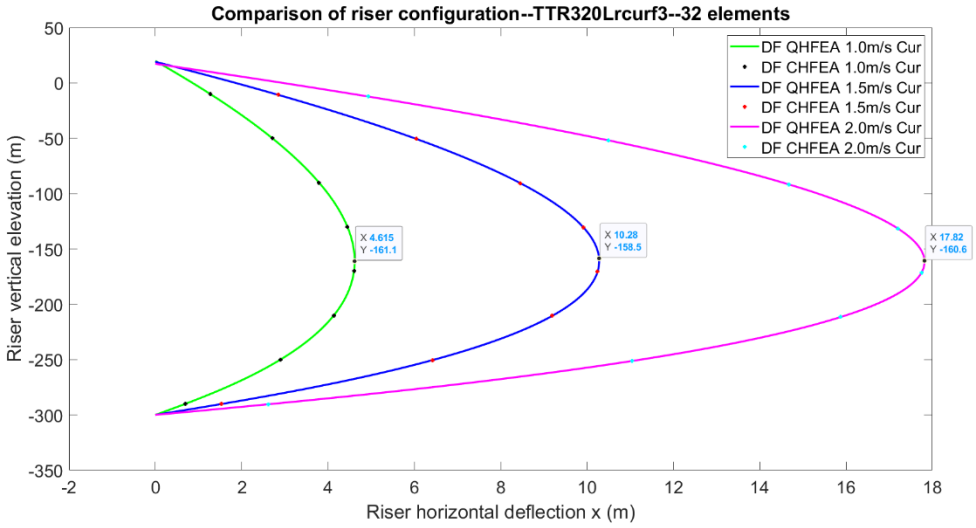

Figure 5.59 The 320m TTR horizontal deflection for current sensitivity analysis

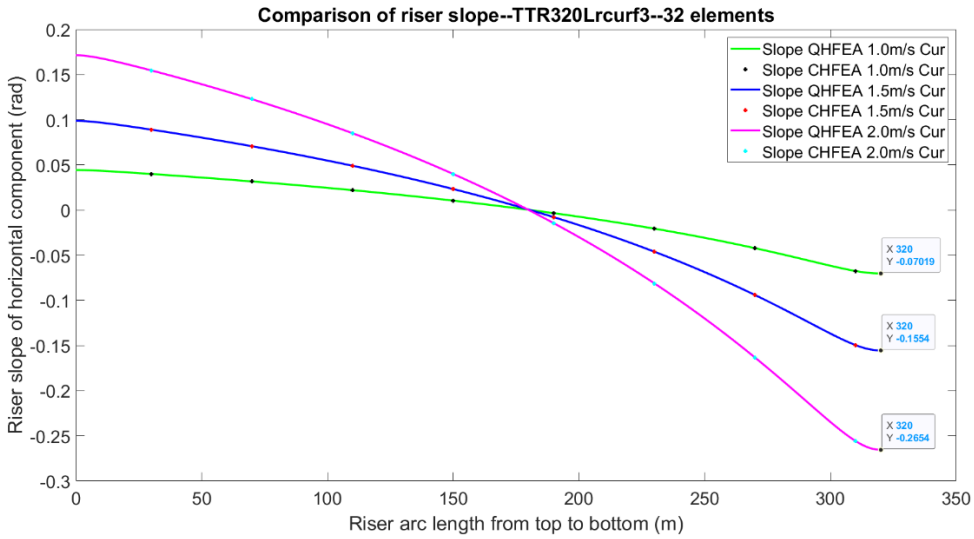

Figure 5.60 The 320m TTR horizontal slope for current sensitivity analysis

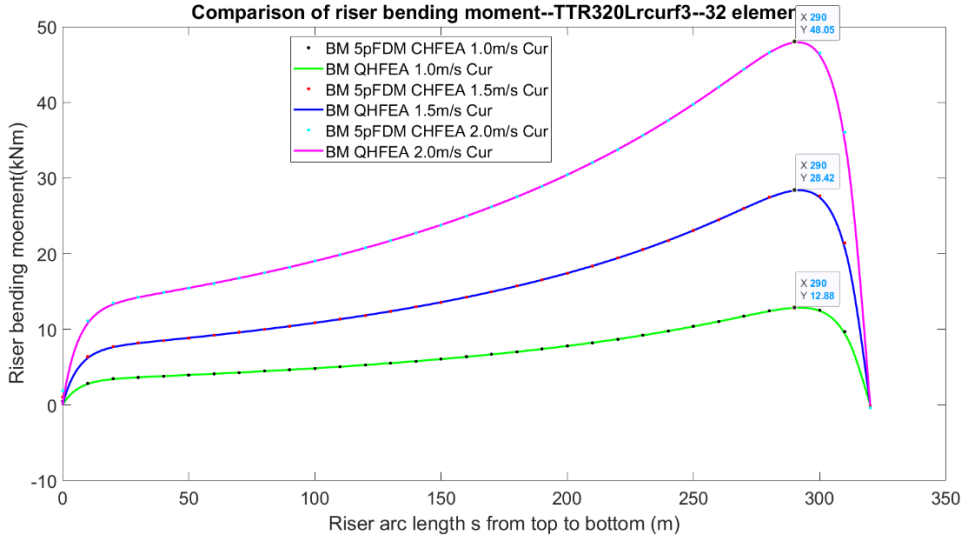

Figure 5.61 The 320m TTR bending moment distribution for current sensitivity analysis

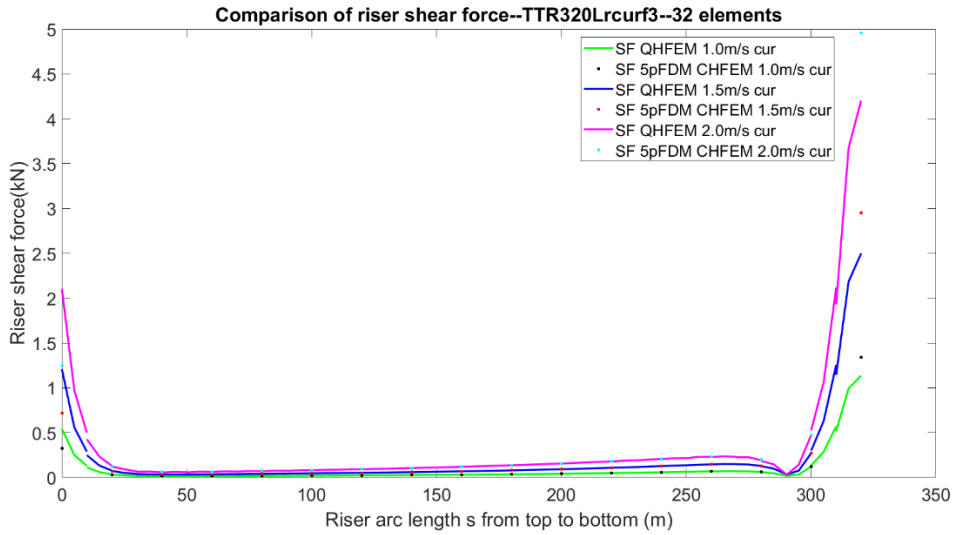

Figure 5.62 The 320m TTR shear force distribution for current sensitivity analysis

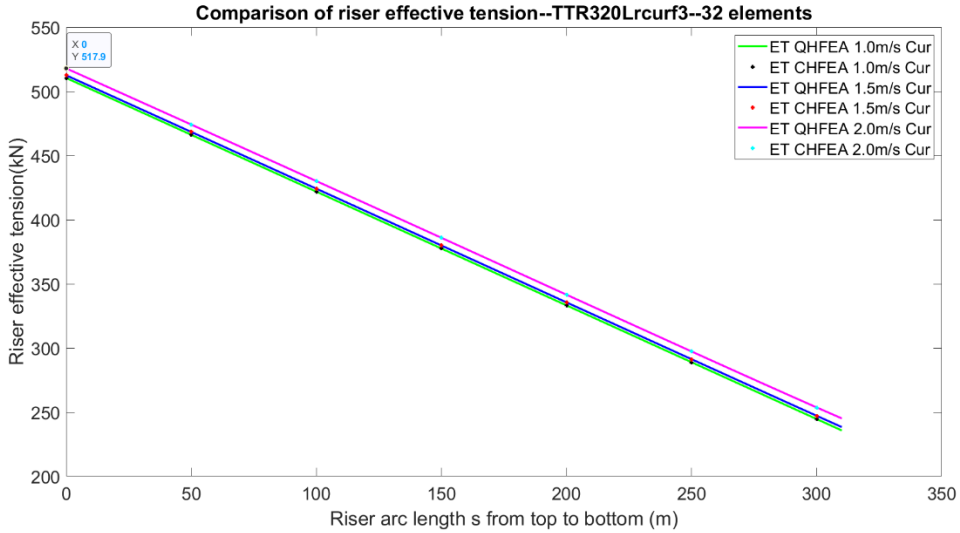

Figure 5.63 The 320m TTR effective tension distribution for current sensitivity analysis

According to the highlight data shown in the above sensitivity analysis figures, it can be concluded that with the increase of current velocity *a* (an arbitrary constant) times, the amplitude of the riser horizontal deflection, the maximum bending moment and shear force in the riser will

be amplified to about a^2 times, which is well consistent with the relationship between force and current velocity in the Morison equations.

For the second sensitivity analysis, the TTR is subject to varied top tensions by applying different top tension load factors, i.e. $0.75T_t$, $1.0T_t$ and $1.25T_t$. The current velocity adopted for this parametric study is uniform 2.0m/s current from sea surface to seabed. A total of 32 equal size elements are used for the mesh of the whole TTR domain, with an element length of 10m. The main results extracted and compared between RISER3D and CABLE3D, including the riser horizontal deflection, the horizontal component of the riser slope and the distribution of riser bending moment, shear force and effective tension along the riser arc length, are plotted from Figure 5.64 to Figure 5.68 respectively.

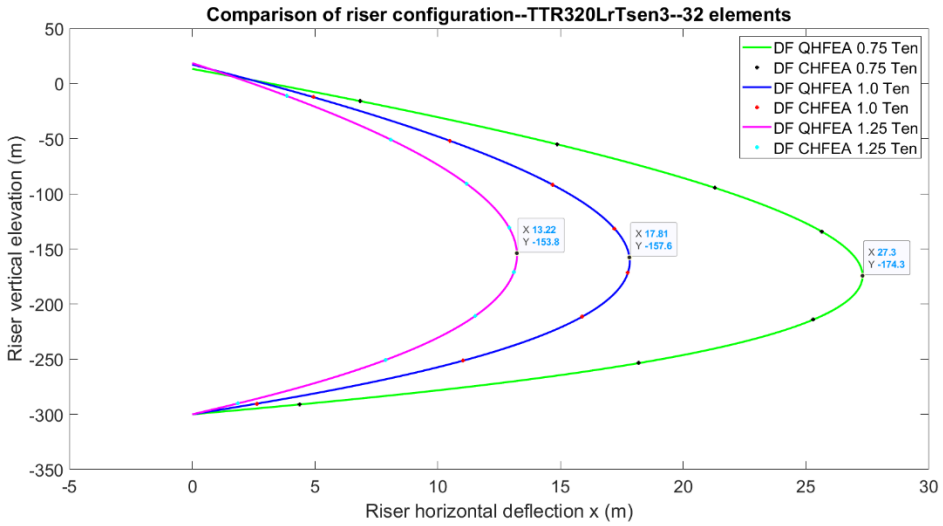

Figure 5.64 The 320m TTR horizontal deflection for top tension sensitivity analysis

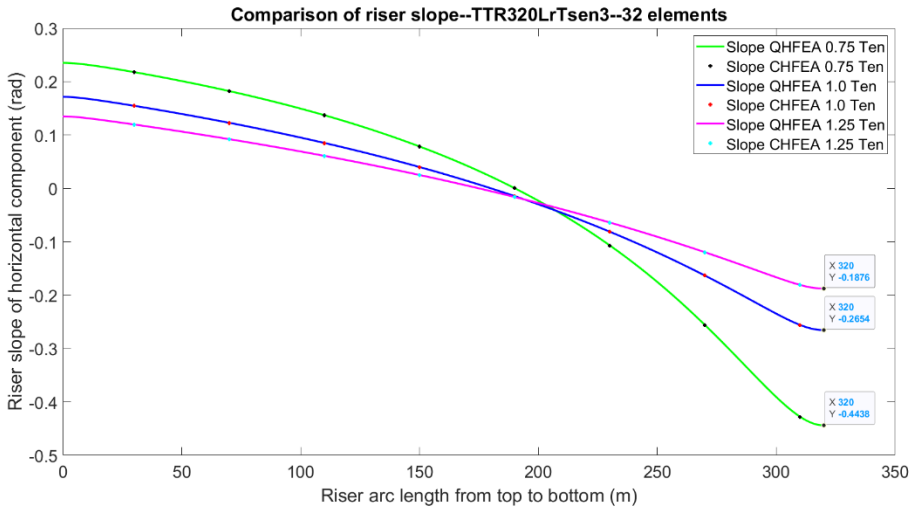

Figure 5.65 The 320m TTR horizontal slope for top tension sensitivity analysis

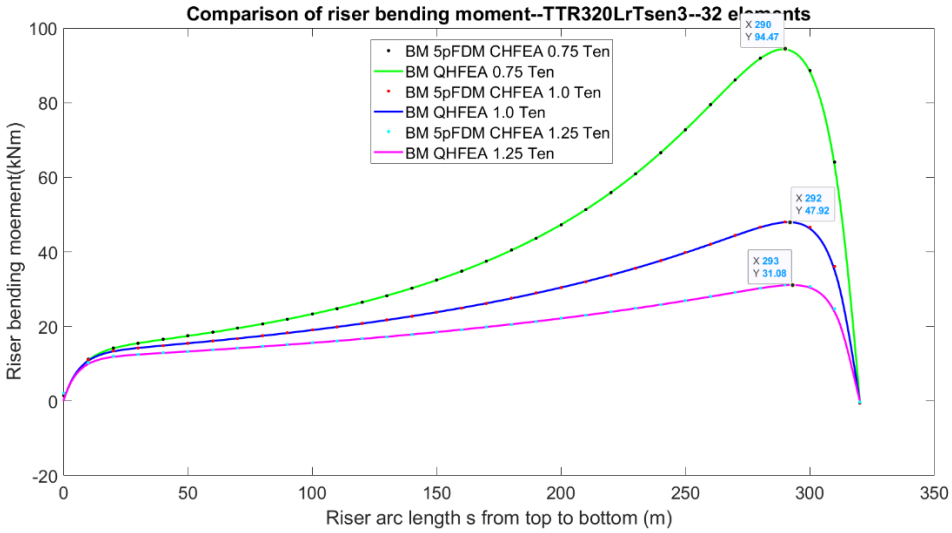

Figure 5.66 The 320m TTR bending moment distribution for top tension sensitivity analysis

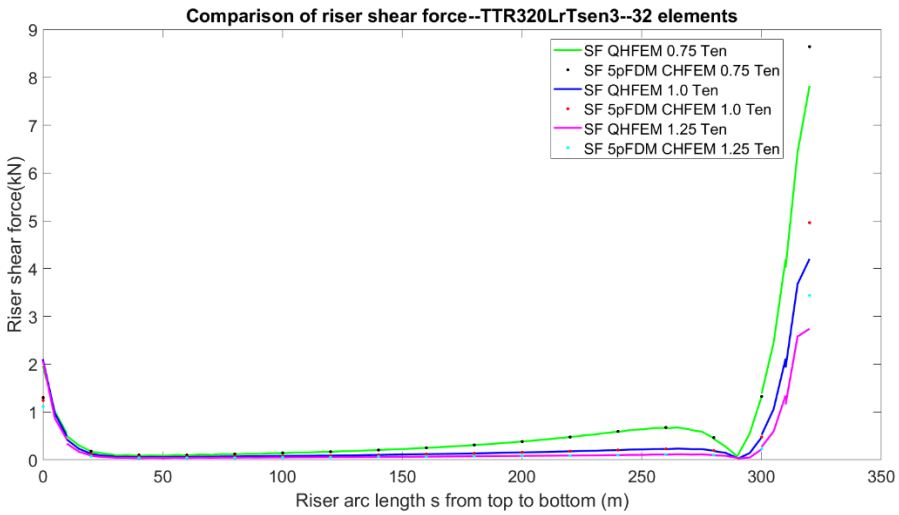

Figure 5.67 The 320m TTR shear force distribution for top tension sensitivity analysis

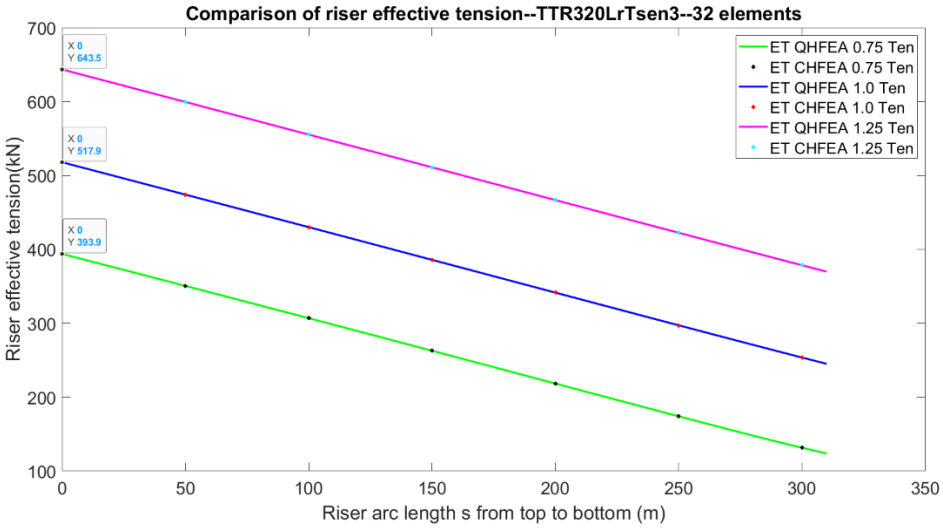

Figure 5.68 The 320m TTR effective tension distribution for top tension sensitivity analysis

According to the highlight results shown in the above figures, it can be concluded that with the increase of top tension, the amplitude of the riser horizontal deflection, the maximum bending moment and shear force in the riser will not decrease proportionally. Therefore, a large set of top tension sensitivities should be performed to identify an optimum top tension for a specific TTR.

Because if the designed top tension is too low, the riser deflection will rapidly increase with the loss of tension under current load; while if the tension is too high, it will not dramatically affect the riser deflection and bending moment, which makes the extra over-tension in the riser meaningless for riser deformation.

For the third sensitivity analysis, the TTR is subject to different magnitudes of linear rotational stiffnesses at both end of the riser, i.e. $0.0e6$Nm/rad, $1.0e6$Nm/rad and $2.0e6$Nm/rad. Zero rotational stiffness case means no flex-joint (FJ) effect is applied to the TTR. For this set of parametric study, the top tension load factor is set as 1.0 with uniform current velocity 2.0m/s. A total of 32 equal size elements are used for the mesh of the whole TTR domain, with an element length of 10m. The main results extracted and compared between RISER3D and CABLE3D, including the riser horizontal deflection, the horizontal component of the riser slope and the distribution of riser bending moment, shear force and effective tension along the riser arc length, are plotted from Figure 5.69 to Figure 5.73 respectively.

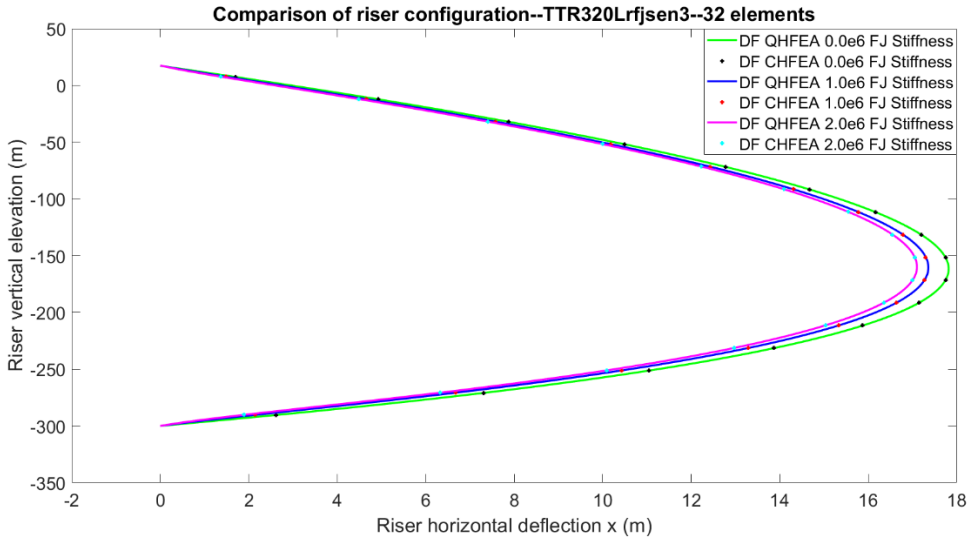

Figure 5.69 The 320m TTR horizontal deflection for Flex Joint sensitivity analysis

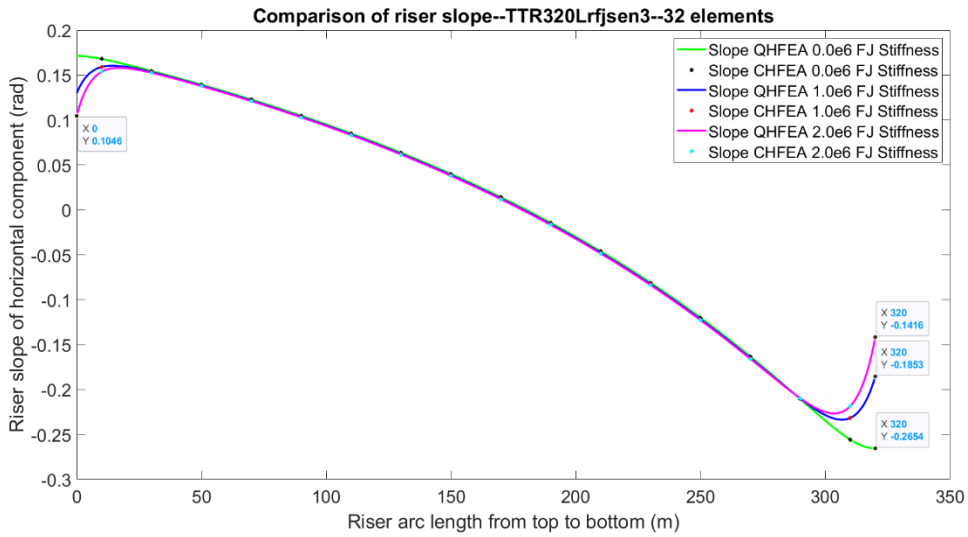

Figure 5.70 The 320m TTR horizontal slope for Flex Joint sensitivity analysis

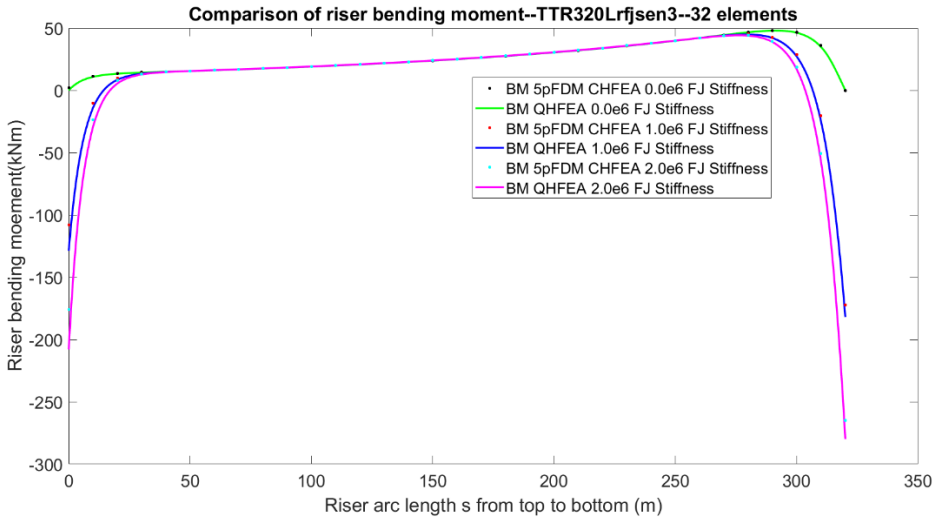

Figure 5.71 The 320m TTR bending moment distribution for Flex Joint sensitivity analysis

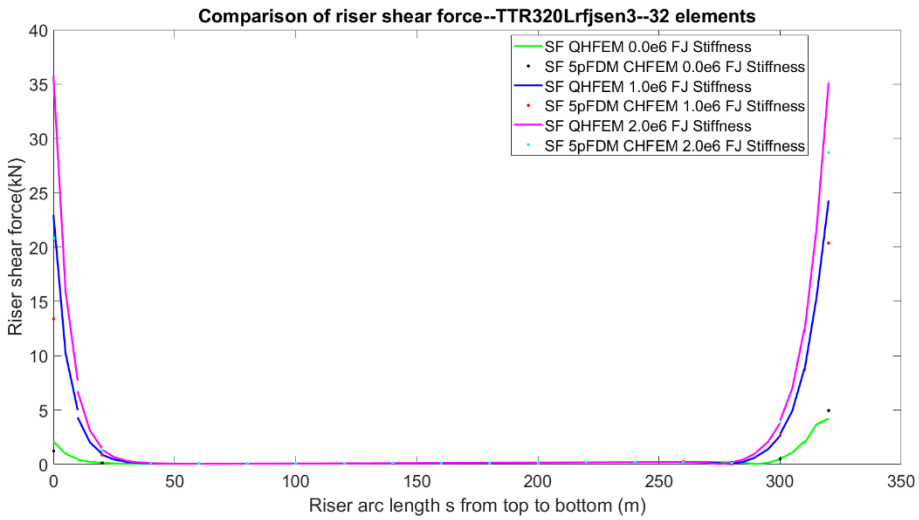

Figure 5.72 The 320m TTR shear force distribution for Flex Joint sensitivity analysis

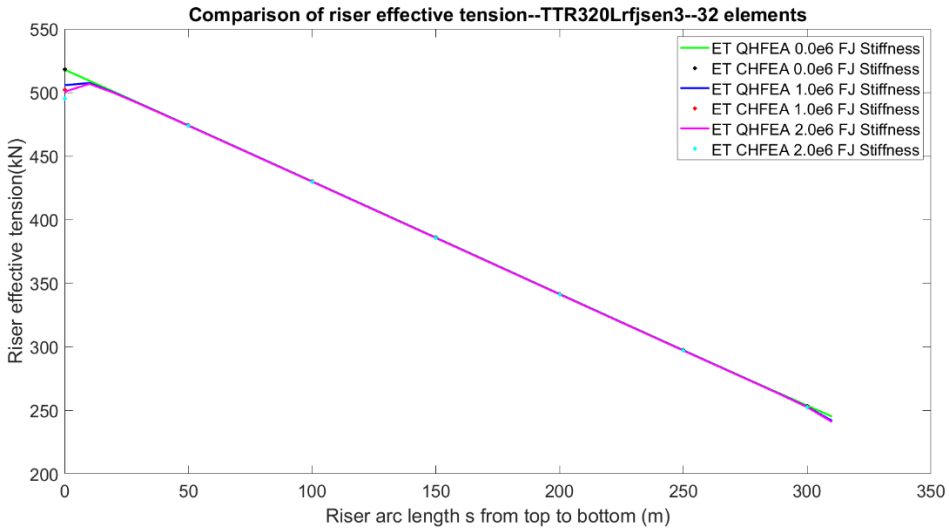

Figure 5.73 The 320m TTR effective tension distribution for Flex Joint sensitivity analysis

In Figure 5.69, the maximum TTR horizontal deflection with no rotational stiffness restraint is 17.82m. By increasing the linear rotational stiffness from 0Nm/rad to 1.0e6 Nm/rad and 2.0e6 Nm/rad respectively, the maximum deflection will slightly drop to 17.36m and 17.10m, which means the bending restraint by rotational stiffness at both ends will not drastically changed

the whole deformation of the TTR. Similarly, the top and bottom tension, as illustrated in Figure 5.73 will not change much after applying different rotational stiffness. However, the applied rotational stiffnesses at both ends of the TTR will dramatically change the distribution of the riser internal bending moment and shear force, as shown in Figure 5.71 and 5.72. The magnitude of the top and bottom bending moment is equal to the product of the linear rotational stiffness and the corresponding riser slope. Therefore, a properly designed rotational stiffness at the ends of a TTR can help to prevent local overbending by introducing an appropriate magnitude of bending moment to the riser, which can balance the unexpected locally applied large bending moments.

5.4 Application of RISER3D to Free Hanging Flexible Risers

For some riser systems, jumpers are an indispensable part for either used at the near surface zone or at the sea bottom flowline connection. Near surface jumper is usually in a catenary shape and is flexible, it can provide a flexible connection between submerged buoy or hybrid riser tower and surface FPSO or other types of platform. A view example of jumper's deployment is shown in Figure 5.74, the jumper is hung over the top of the hybrid riser tower to the FPSO.

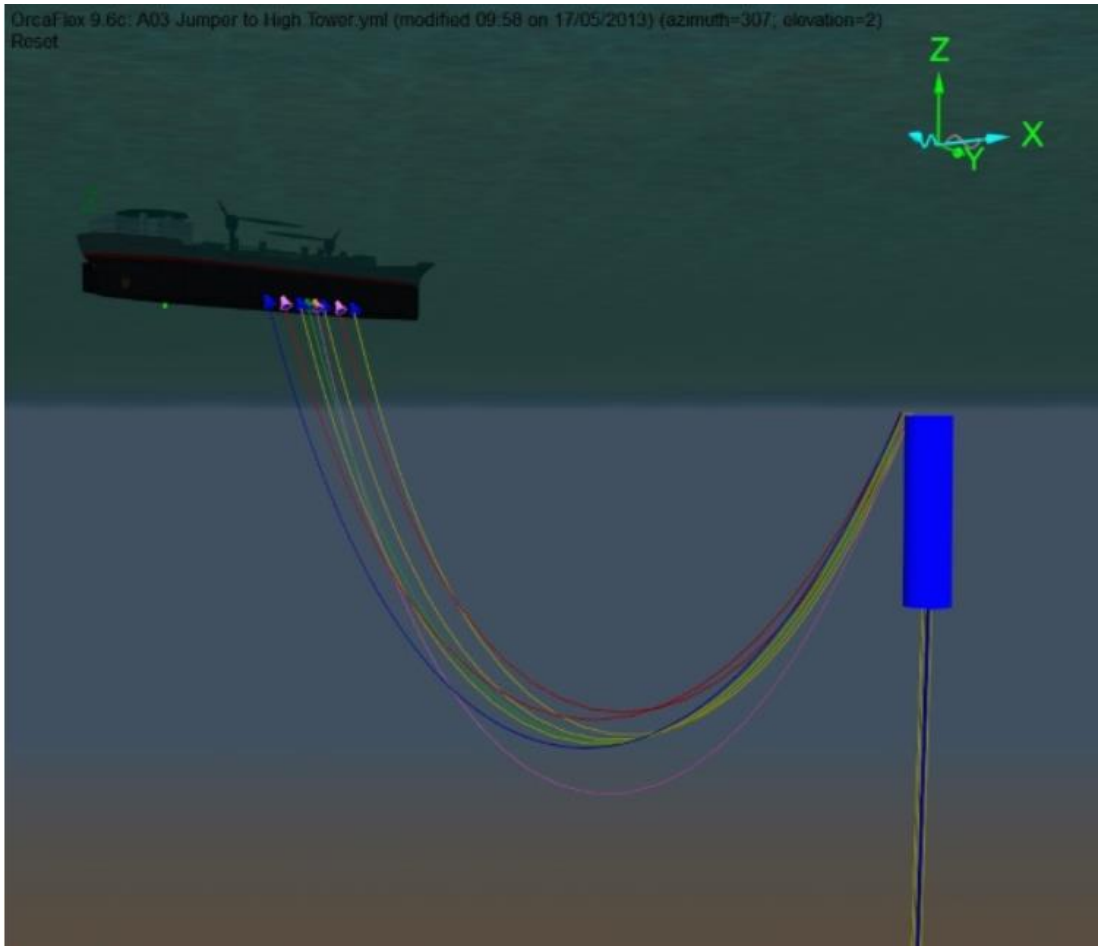

Figure 5.74 Multiple jumper connection between HR and FPSO (Reprinted from www.orcina.com)

Subsea rigid jumpers are mainly used as a connection between seabed flowlines and bottom end of risers. Jumpers should be flexible enough to accommodate the translation motions either comes from the flowline or riser. The loads which should be taken into consideration for subsea rigid jumper design consist of (B. Toleman, et al., OMAE 2019)

- Thermal and pressure load
- Environmental load such as strong bottom currents
- Slugging
- Interaction load between riser and flowline

A schematic view of a M-shape rigid jumper finite element model can be seen in Figure 5.75 (B. Toleman, et al., OMAE 2019)

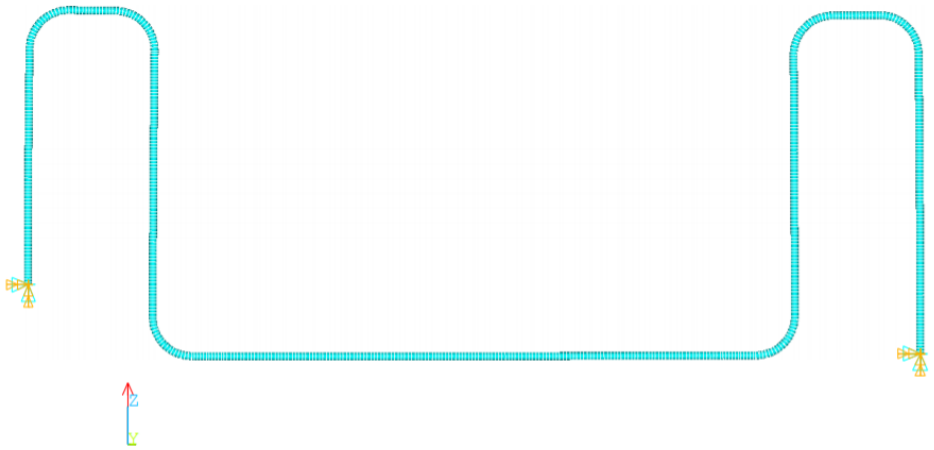

Figure 5.75 Finite element model of M-shape jumper (Reprinted from Toleman et al. 2019)

This research has only focused on the study of flexible jumpers and not performed any case study on subsea rigid jumpers due to the lack of detailed problem data. The rigid jumper analysis by using RISER3D is left for future research.

5.4.1 Analysis of a Catenary Flexible Jumper by RISER3D

In this section, a catenary jumper is simulated with both RISER3D and CABLE3D, the data of which, referred to a previous journal paper published by Connaire, et al. (2015), are summarized in Table 5.20.

Table 5.20 The properties of the 45m length catenary jumper

Designation	Symbol	Value	SI Units
Jumper length	L_r	45	m
Outer diameter	D_o	0.15	m
Inner diameter	D_i	0.09	m
Bending rigidity	EI	4000	Nm
Stretching rigidity	EA	3.0e8	N
Mass per unit length	M_{air}	200	Kg/m

The other required data for the analysis, not included in Table 5.20, are assumed and listed in Table 5.21.

Table 5.21 Assumed data for the 45m length catenary jumper

Designation	Symbol	Value	SI Units
Water depth	H_{wd}	1000	m
Water density	ρ_w	1025.0	Kg/m^3
Inner fluid density	ρ_i	0.0	Kg/m^3
Gravitational constant	g	9.80665	m/s^2

For static analysis, a total of 45 uniform-length elements are used to mesh the jumper, with an element length of 1.0m. Newton iteration are adopted for the static equilibrium iteration. The concerned results of the jumper from both CABLE3D and RISER3D static simulations, including the jumper configuration, horizontal component of slope, the distribution of the jumper bending moment, shear force and effective tension, are presented from Figure 5.76 to 5.80 respectively.

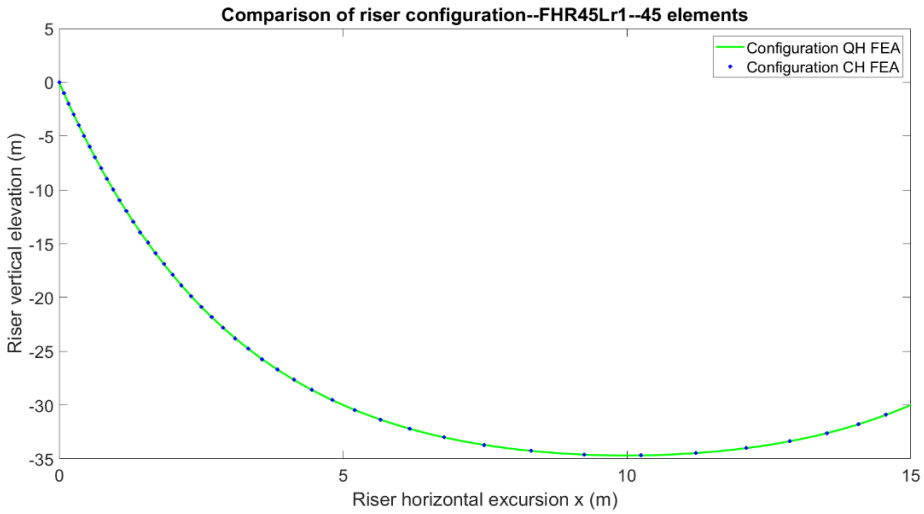

Figure 5.76 Static configuration of the catenary jumper

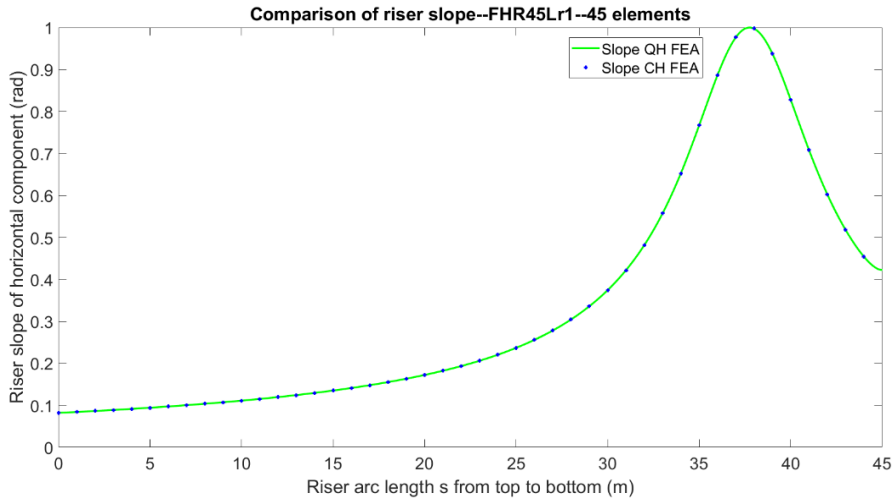

Figure 5.77 Jumper horizontal component of slope

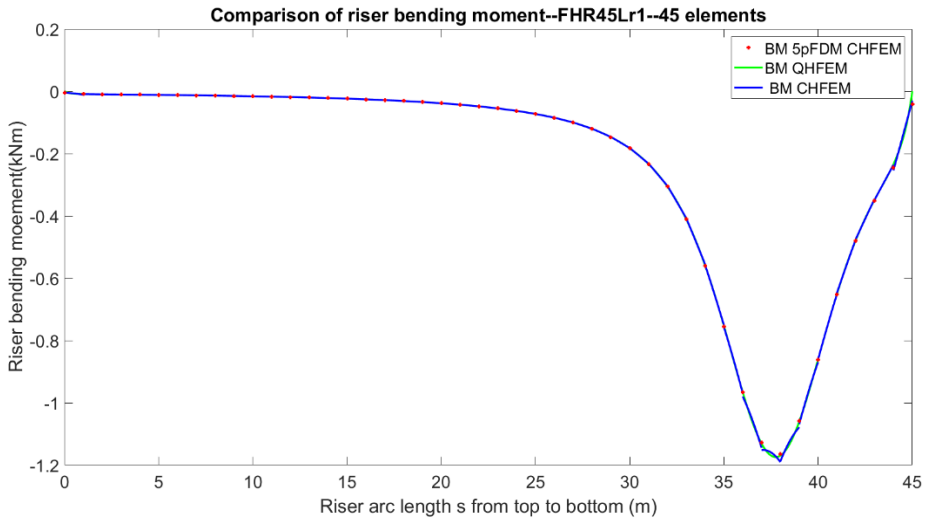

Figure 5.78 The bending moment distribution of the catenary jumper

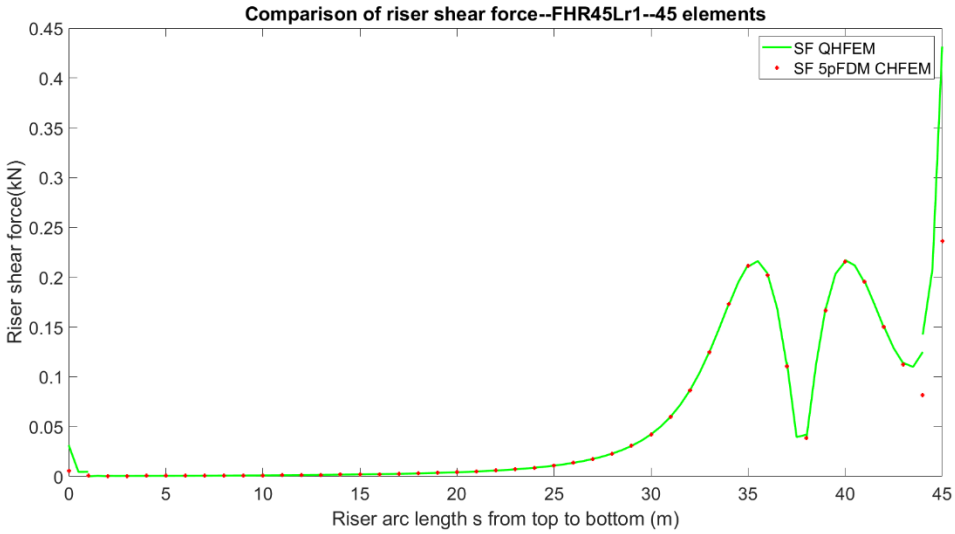

Figure 5.79 The shear force distribution of the catenary jumper

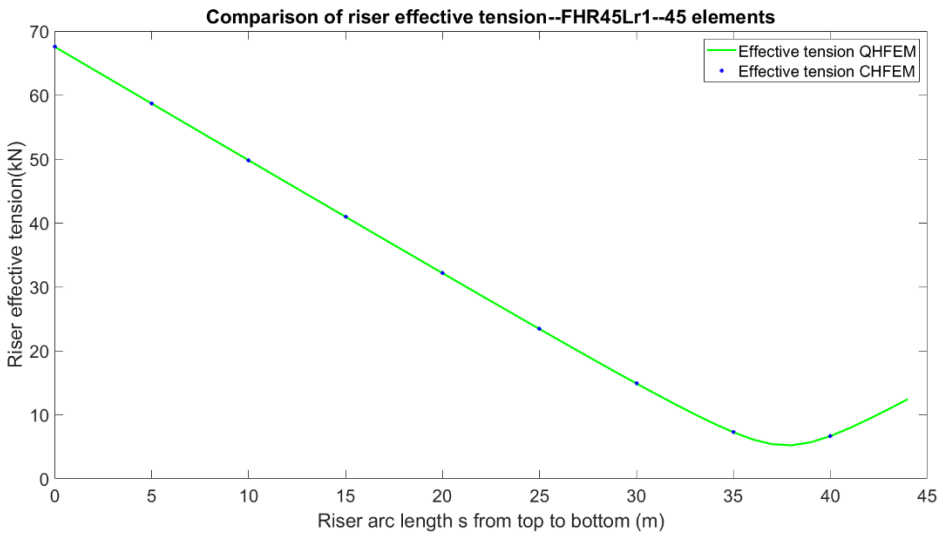

Figure 5.80 The effective tension distribution of the catenary jumper

The jumper top end offset analysis is also studied to compare the convergence speed between RISER3D and CALBE3D. For this analysis, the top end of the jumper is displaced from the static equilibrium place, as shown in Figure 5.76, to the positive global X-direction by a horizontal offset of 15m in a quasi-static manner, i.e. the top end will be displaced exactly above the lower end.

For the base case, a total of 90 uniform elements are used for domain mesh and each element has a length of 0.5m. The results of the jumper top end offset analysis, consisting of the deformed jumper configuration, the horizontal component of jumper slope, the bending moment distribution, the critical bending moment zone local zoom in, the distribution of jumper shear force and effective tension, are presented from Figure 5.81 to 5.86 respectively.

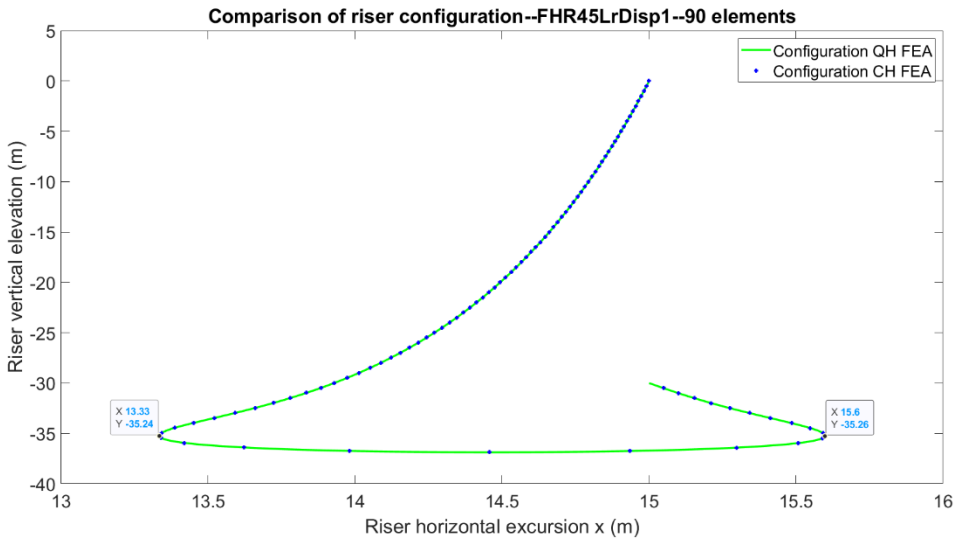

Figure 5.81 Jumper configuration of top end offset analysis

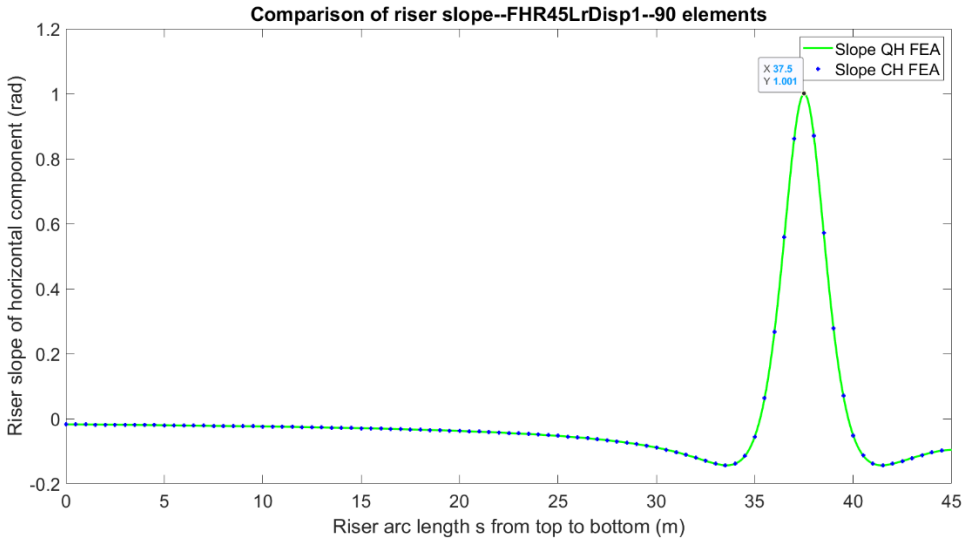

Figure 5.82 Jumper horizontal component of slope for top end offset analysis

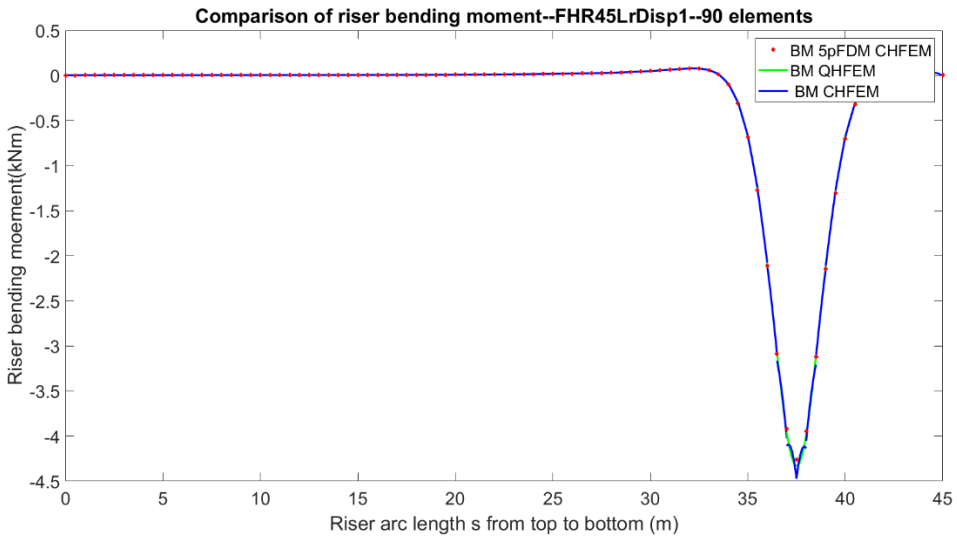

Figure 5.83 Jumper bending moment distribution for top end offset analysis

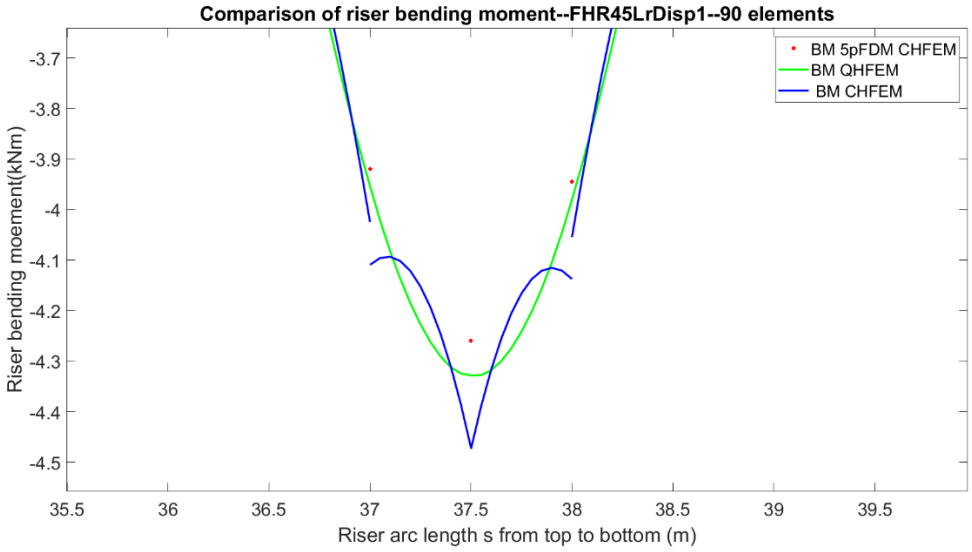

Figure 5.84 Critical bending moment local zoom in for top end offset analysis

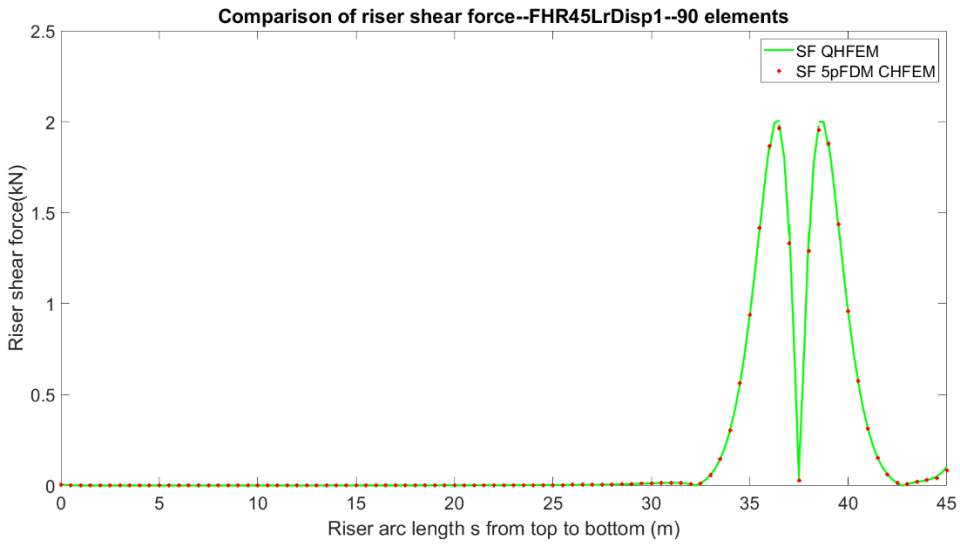

Figure 5.85 Jumper shear force distribution for top end offset analysis

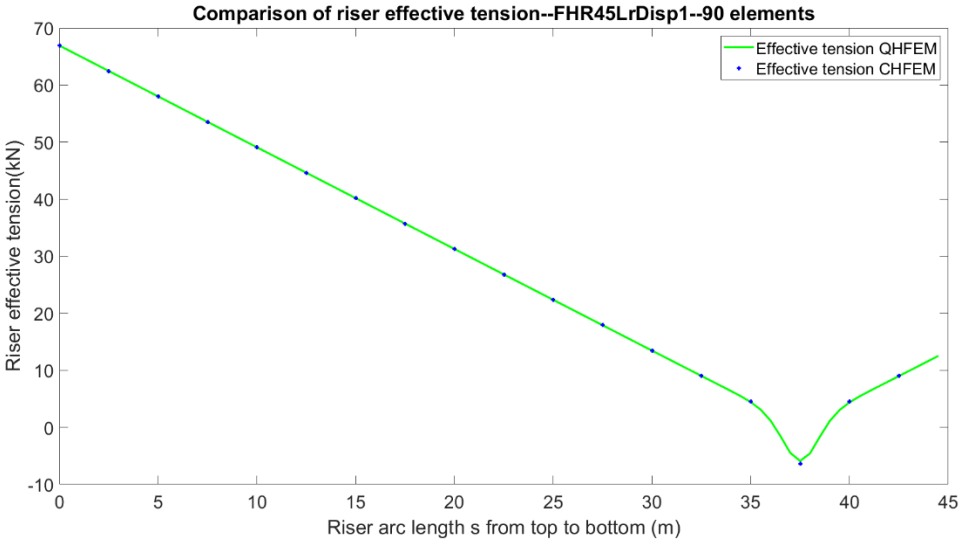

Figure 5.86 Jumper effective tension distribution for top end offset analysis

In order to test the convergence speed of the jumper top end offset analysis, a parametric study is performed by employing different element sizes while keeping the remaining input data

the same. The main concerned results are shown in Table 5.22 for the obtained maximum bending moment (BM) and Table 5.23 for the obtained maximum shear force (SF).

Table 5.22 The comparison of RISER3D and CABLE3D for BM convergence speed

Mesh Size	**BM_QH (kNm)**	**BM_CH (kNm)**	**BM_FDM (kNm)**	**BMQH_Dif (%)**	**BMCH_Dif (%)**	**BMFDM_Dif[2] (%)**	**CH_Time[1] (s)**	**QH_Time (s)**
1m	-4.3161	-4.5238	-3.5924	-0.314	4.483	-17.029	0.9103	1.4878
0.5m	-4.3281	-4.4734	-4.2596	-0.037	3.319	-1.619	1.7882	2.7241
0.25m	-4.3295	-4.3703	-4.3241	-0.005	0.938	-0.129	3.4799	5.2866
0.125m	**-4.3297**	-4.3401	-4.3292	-	0.240	-0.012	6.9276	10.644

Table notes in this section:

1. Time denotes the approximated CPU time for running the code on a laptop of Processor Intel(R) Core(TM) i7-7500U CPU @ 2.70GHz, 2904 Mhz, 2 Core(s), 4 Logical Processor(s).
2. Dif denotes the relative difference to the best obtained solution.

Table 5.23 The comparison of RISER3D and CABLE3D for SF convergence speed

Mesh Size	**SF_QH (kN)**	**SF_CHFDM (kN)**	**SFQH_Dif (%)**	**SFCH_Dif[2] (%)**	**CH_Time[1] (s)**	**QH_Time (s)**
1m	-2.0336	-1.8114	1.079	-9.966	0.9103	1.4878
0.5m	-2.0078	-1.9629	-0.204	-2.436	1.7882	2.7241
0.25m	-2.0117	-1.9928	-0.010	-0.949	3.4799	5.2866
0.125m	**-2.0119**	-2.0116	-	-0.015	6.9276	10.644

In Table 5.22, the bending moment of -4.3297 kNm is regarded as the best obtained solution by using the finest element size of 0.125m and RISER3D program. All the remaining bending moments are compared with this value by utilizing a relative difference percentage. From the fifth to seventh column, regardless of the mesh size adopted, the percentage of bending moment does not change much for RISER3D program. However, for CALBE3D program, if a course element size is adopted, the bending moment will have a large percentage difference to the best obtained solution.

From the data shown in Table 5.22, RISER3D can achieve equivalent accuracy to CABLE3D by using fewer element numbers, which can therefore save CPU time and computational effort. The same conclusion can be exactly drawn from Table 5.23 for the shear force results. Therefore, for flexible jumpers subject to large rotational deformation, RISER3D can converge much faster to the true solution than CALBE3D. Moreover, to achieve equivalent accuracy of concerned results, RISER3D cost less CPU time to CABLE3D by using larger size of mesh.

5.4.2 Static and Dynamic Analysis of a Free-hanging Flexible Riser by RISER3D

In this section, the static and dynamic analysis of a free-hanging flexible riser is performed with RISER3D. The problem data of which, referred to a previous paper published by Y.M. Low and R.S. Langley (2006), are listed in Table 5.24.

Table 5.24 The properties of the free-hanging flexible riser

Designation	**Symbol**	**Value**	**SI Units**
Riser length	L_r	170	m
Outer diameter	D_o	0.396	m
Density of water	ρ_w	1000	Kg/m^3
Bending rigidity	EI	1.208e5	Nm
Stretching rigidity	EA	5.0e8	N
Mass per unit length	M_{air}	165	Kg/m
Gravitational acceleration	g	9.807	m/s^2

The other required data for the analysis, not included in Table 5.24, are assumed and listed in Table 5.25. The riser top end is positioned at 5m below mean water level and the riser bottom end is positioned at 55m below the mean water level, the horizontal distance between the both end of the riser is 100m (Low and Langley, 2006).

Table 5.25 Assumed data for the free-hang flexible riser analysis

Designation	Symbol	Value	SI Units
Water depth	H_{wd}	1000	m
Inner fluid density	ρ_i	0.0	Kg/m^3
Top offset	U_t	0.0	m

For the jumper static in-place analysis, a total of 68 uniform-length elements are used to mesh the jumper, with an element length of 2.5m. Newton iteration are adopted for the static equilibrium iteration and the relaxation coefficient is set as 0.8 for static analysis. The concerned results of the free-hanging flexible riser extracted from both CABLE3D and RISER3D static simulations, including the deformed jumper configuration, the horizontal component of jumper slope, the distribution of jumper bending moment, shear force and effective tension, are presented from Figure 5.87 to 5.91 respectively.

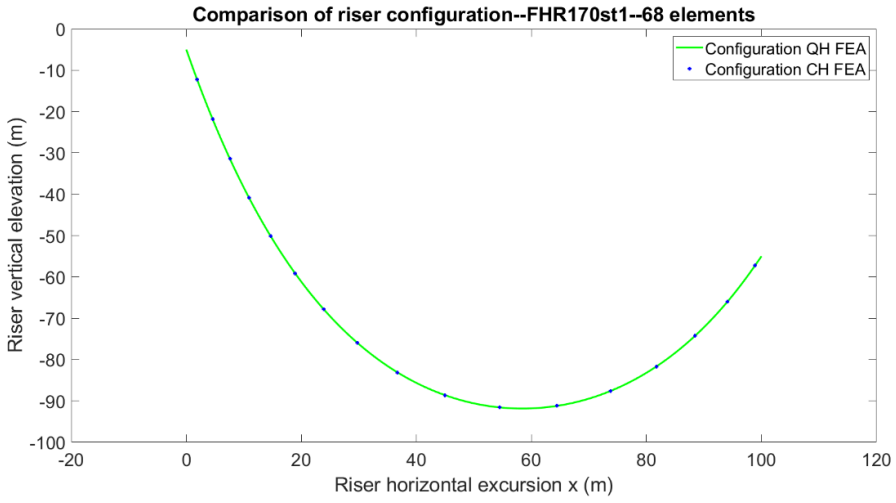

Figure 5.87 The equilibrium configuration of the free-hanging flexible riser

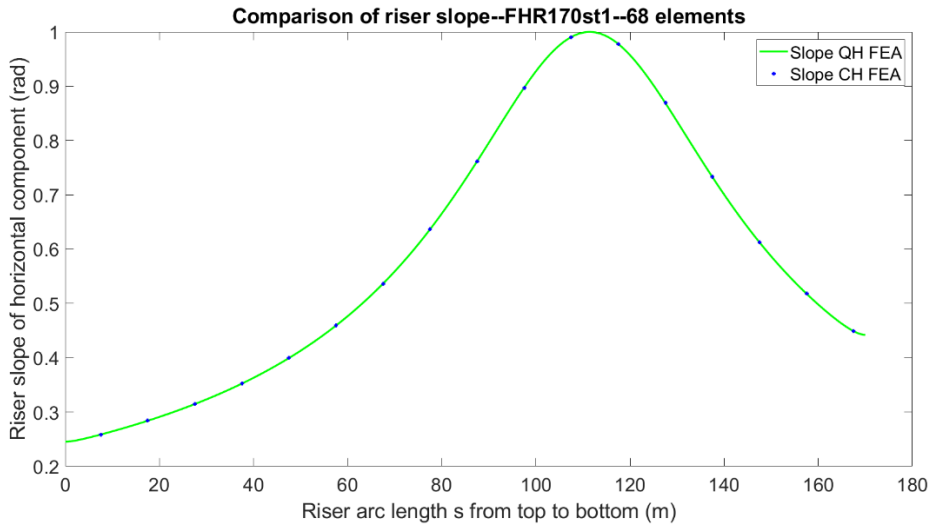

Figure 5.88 The horizontal component of the slope of the free-hanging flexible riser

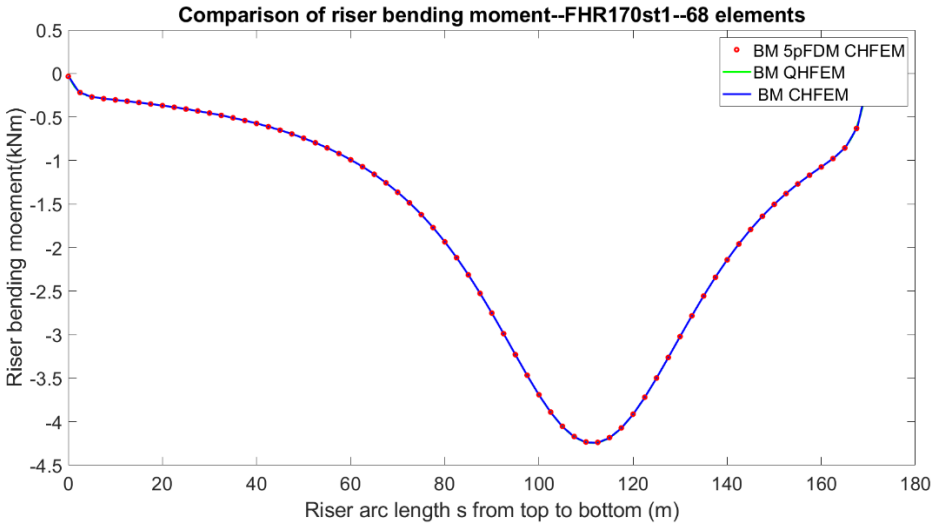

Figure 5.89 The bending moment distribution of the free-hanging flexible riser

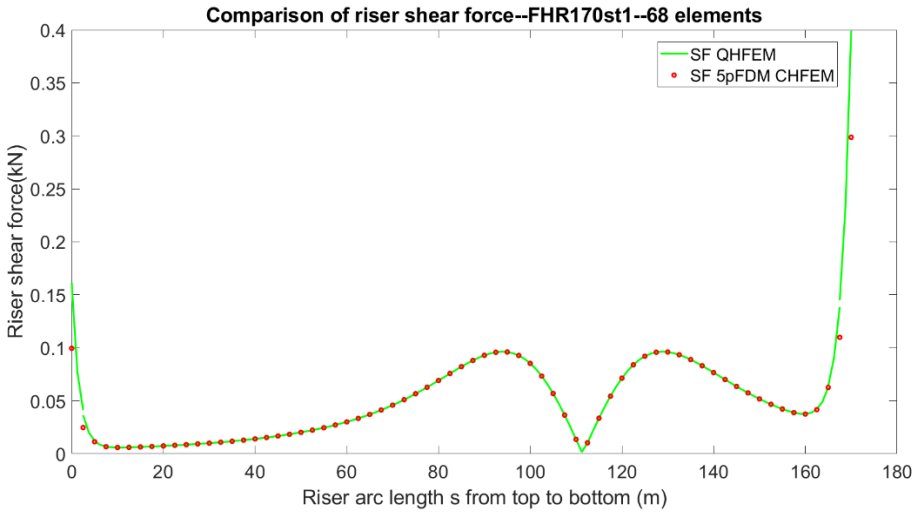

Figure 5.90 The shear force distribution of the free-hanging flexible riser

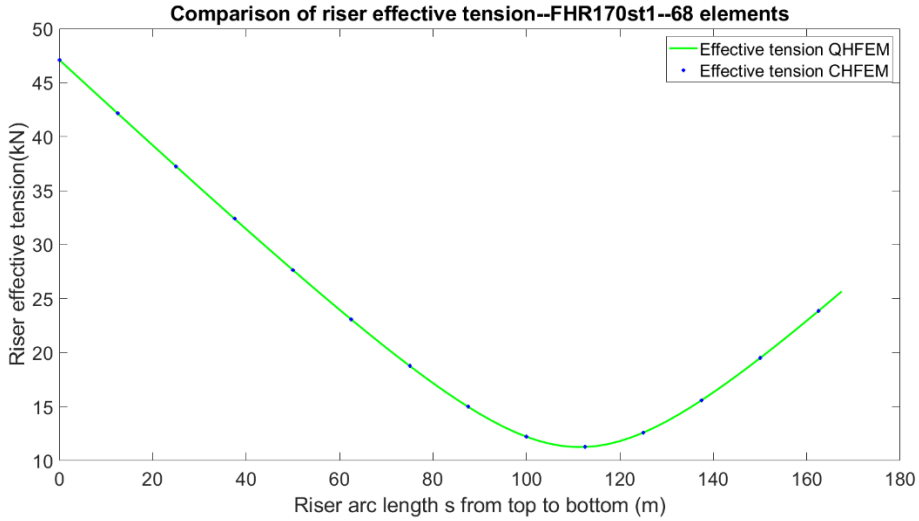

Figure 5.91 The effective tension of the free-hanging flexible riser

The top and bottom end of the effective tension are both 47.11kN and 26.60kN by RISER3D and CABLE3D, which exactly matches with the results presented in the published paper (Y.M. Low and R.S. Langley, 2006). By using the fine 2.5m element mesh, it can be seen from

Figure 5.89 and Figure 5.90 that both the bending moment and shear force predicted by RISER3D and CABLE3D matches well for this case study.

For the decoupled dynamic analysis, two top end excitation cases are simulated by RISER3D. For simplicity, no wave kinematics are considered for this study. The first case is the riser top end subjected to a harmonic surge motion (in global X-direction) and the second case is the riser top end subjected to a harmonic sway motion (in global Z-direction). For both cases, the amplitude of the imposed harmonic excitations is 10m and the periods of oscillation is 27s (Low and Langley, 2006). 80s of simulation is run and the load is ramped up in the first period for the dynamic analysis. The time series of the top end effective are compared between RISER3D and Orcaflex, which are shown in Figure 5.92 and Figure 5.93 below.

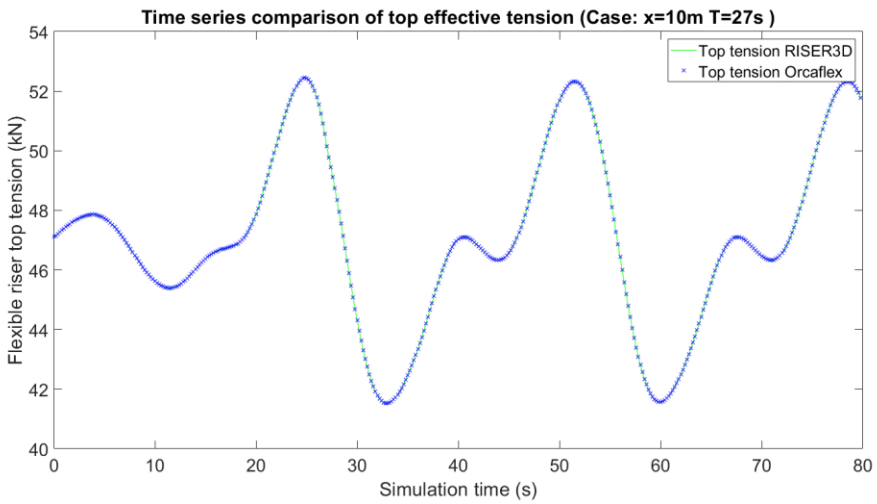

Figure 5.92 Time series of top end effective tension under surge motion

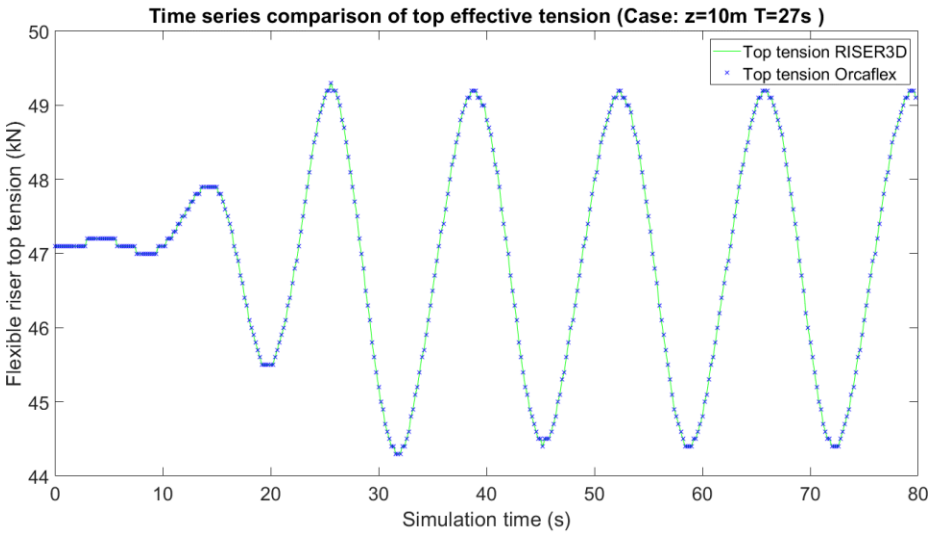

Figure 5.93 Time series of top end effective tension under sway motion

From the dynamic time series in Figure 5.92 and Figure 5.93, it can be seen that RISER3D can exactly match the response of riser to that of by Orcaflex. Due to time limitation for this research, more dynamic analysis cases using RISER3D program will be studied and published with journal papers in future research.

6 SUMMARY AND CONCLUSION

This research has placed on an emphasis on an improved numerical technique for marine riser strength analysis, i.e. by using quintic Hermite shape functions. A powerful and effective marine riser analysis tool called RISER3D, is formulated, developed using quintic Hermite shape functions, which has been verified to be applicable to almost all riser configurations, such as SCR, SLWR, Steep-wave riser, TTRs, HRs, free-hang flexible risers, etc. in this dissertation. RISER3D can, so far, handle well with three-dimensional nonlinear static and dynamic riser problems under steady linear or nonlinear currents and top end motion excitations. As for the linear wave loads, it is formulated in chapter 5 but no case is performed due to time limitation for this research.

6.1 Comparison of CALBE3D and RISER3D Program

Based on this research, for traditional CABLE3D, a gradually refined element mesh must be adopted for slender structures with large curvature gradient to improve the numerical simulation accuracy. Otherwise, analysts may fail to pinpoint the exact position of the peak curvatures in the whole problem domain, which will result in either an over conservative structural design or a non-conservative structural design. However, by doing so, twofold of drawbacks will occur, the first one is that more nodal degrees of freedom (DoFs) will be introduced to the finite element model, which will definitely increase the total number of the global system of equations and then the capacities of the computer storage, memory and the running time; the other one is an increased complexity for numerically postprocessing for the riser nodal bending moments. Because for CABLE3D, only nodal displacement and slope information are solved, and the nodal curvature of the riser shall be evaluated by either cubic Hermite interpolation method or five-point finite difference method based on the obtained nodal DoFs. If the multi-point finite difference method is used to approximate the riser nodal bending moments, a gradually refine element mesh

necessitate a non-uniform element mesh for segments with high curvatures, which can greatly increase the complexity for results postprocessing. What is worth mentioning is that if the element size is sharply changed during the element mesh process, a potential of ill-conditioning problem may be introduced into the riser global system of equations in CABLED3D program, and then the numerical divergence may be another headachy problem, which is definitely unacceptable for numerical simulations. Therefore, it is quite tricky for element mesh process by performing marine riser simulation with CALBE3D program, i.e. cubic Hermite interpolation functions finite method. Because too fine meshes mean improved accuracy but increased computational effort and complexity, while too coarse meshes suffers significant loss of the simulation accuracy and unacceptable simulation results.

On the contrary, with the excellent properties brought into RISER3D by the quintic Hermite shape functions. The beam or riser curvatures at discrete nodes can be directly handled as the nodal degrees of freedom (DoFs) and solved straightforwardly. For RISERED, at each internal node, the structure curvatures are continuous. Besides, by the application of the quintic Hermite interpolations with obtained nodal DoFs, the deformed deflection curves of slender structures in RISER3D are piecewise quintic polynomial functions in each element domain. Hence, the curvature curves, the second derivative of the deflection curves, are piecewise cubic polynomial functions and the rate change of curvatures with respect to arc length, i.e. the third derivative of the deflection curves, are piecewise quadratic polynomial functions. As is known by structural mechanics, the magnitudes of second and third derivative of the deflection curves are proportional to the structural bending moment and shear force in the element domain respectively. Therefore, the riser bending moment predicted with RISER3D are piecewise continuous cubic polynomial functions in the whole problem domain. Moreover, by examining the third derivatives of the

deflection curves in each element domain, if a zero point can be identified in an element, then there must be a peak value for the bending moment in that element, i.e. either the maximum bending moment or the minimum bending moment. With the existence of these properties for the deflection curves predicted by RISER3D in the problem domain, analysts can adopt uniform and relatively large size of elements for computing the distribution of the bending moment and shear force in slender structures without worrying the loss of accuracy at all. Which means the foregoing twofold drawbacks enrooted in CALBE3D do not exist in RISER3D anymore.

One may intuitively think that RISER3D has a total of 21 DoFs per element for riser, which is more than the 15 DoFs per element for CABLE3D; hence, RISER3D will definitely need more CUP time and computational effort than CABLE3D for marine riser simulation. This argument is straightforwardly true if both programs utilize the same element size for the same problem domain. And according to experience of running CABLE3D and RISER3D, the RISER3D program usually cost about an extra 30% of simulation time than CALBE3D. Nevertheless, for the same problem, to achieve equivalent accuracy, RISER3D does not need so many of element numbers as required by CALBE3D, especially for segments where the expected solutions have large gradients. From this perspective, RISER3D can actually decrease the total required DoFs by using a smaller number of meshed elements, and therefore can save simulation time when compared to CABLE3D.

6.2 Research Summaries

By comparison between CABLE3D and RISER3D, i.e. by comparison of traditional cubic Hermite finite element method with the new quintic Hermite finite element method, the following bullet points can be summarized according to all the studies performed in this dissertation.

- RISER3D can guarantee the continuity of the curvatures of the slender structures, such as beams, risers, etc., at the discrete nodes while CALBE3D cannot.
- RISER3D can accurately pinpoint the critical bending moment position in an element domain with a relatively large size elements while CABLE3D cannot. CABLE3D has to dramatically refine element mesh to achieve a closer solution to the critical bending moment by bringing about issues for increased computational effort and difficulties for data postprocessing. If locally refine the element size, ill-conditioning of the global matrix may be of another problem for CABLE3D, especially for high nonlinear three-dimensional problems.
- For pinned or hinged boundary conditions, RISER3D can yield more accurate results for the internal bending moment and shear force at the near boundary sections, while CALBE3D cannot. This is because RISER3D can apply essential boundary conditions on the curvatures at the boundary points while CALBE3D cannot.
- For dynamic beam vibration problems, RISER3D can produce more accurate dynamic time series of the internal bending moment and shear force than CALBE3D, especially for the shear force response of structures.
- For eigenvalue problems, by using the same element mesh, RISER3D can yield much more accurate natural frequencies than CABLE3D. As modes go higher, CABLE3D could yield a considerable amount of error while RISER3D will not.
- RISER3D can show better effectiveness for flexible jumper simulation, especially for those jumpers subjected to large rotation angles

- RISER3D can produce more accurate prediction for bending moment and shear force for slender structure subjected to transverse loads with large gradient, such as high-order polynomial load and high frequency harmonic loads

To be brief, compared to traditional cubic Hermite finite element methods, RISER3D has been proved to be an effective general tool for numerical simulations of slender Euler-Bernoulli beams and almost all configurations of marine risers. It can use less elements to achieve much better accuracy and it can easily identify the position of the maximum bending moment and stress in the slender structure problem domain, which can greatly enhance the confidence of analysts and designers before making big decisions. Therefore, the quintic Hermite finite element method are highly recommend other researches or scholars for performing finite element analysis of almost all of slender structures, no matter it is static, dynamic or eigenvalue analyses.

Although RISER3D can have so many advantages over the traditional finite element methods (utilizing cubic Hermite shape functions), it should be confessed that this new method is much more complicated to implement than traditional cubic Hermite finite element method. No matter it is from the perspectives of math formulation or numerical programming. Besides, RISER3D admits smaller rooms of error during the whole procedures of finite element analysis because the fifth-order polynomials can easily amplify any mistakes to numerical divergence. Therefore, analysts should make sure the math formulation and boundary conditions are exactly correct to get high accurate solutions to practical slender structure problems by RISER3D. Moreover, a point should be emphasized is that RISER3D can handle problems with continuous curvatures in the finite element domain. If the problem domains have non-continuous curvatures physically, special treatments or measures must be taken to avoid any potential mistakes, such as problems with sudden change of cross sectional area or with internal concentrated moments, etc.

A reasonable judgment is that quintic Hermite shape functions shall show great advantages for solving more and more complicated slender structural problems and a lot of future research shall be performed to explore the great benefits that quintic Hermite shape functions can bring us for finite element simulations.

6.3 Topics for Future Research

Due to time limitations for this research, some of the less important factors are neglected and some of the riser topics are not covered. However, for some of special problems, these neglected factors and topics may have to be considered. For the sake of completeness, the following topics are recommended for future research by using quintic Hermite shape functions for RISER3D:

- Problems of riser deformation with torque
- Problems of riser with steady and unsteady internal flow
- Riser seabed lateral and longitudinal frictional forces
- Simulate the fluctuational lift forces caused by riser VIV
- Coupled riser and host platform dynamic finite element analysis
- Riser fatigue analysis
- Flexible Steep-S and W-shape riser finite element analysis
- M-shaped rigid jumper finite element analysis
- Multi-layer composite riser finite element analysis
- Titanium riser finite element analysis

REFERENCES

Love, A.E.H., 1944. *A treatise on the mathematical theory of elasticity*. Fourth edition, Dover Publications, New York.

Roveri, F.E., Martins, C.A. et al., 2005. Parametric analysis of a lazy-wave steel riser. OMAE 2005-67128

Kim, S., Kim, M.H., Shim, S., Im, S., 2014. Structural performance of deepwater lazy- wave steel catenary risers for FPSOs. In: Proceeding of the Twenty-fourth International Offshore and Polar Engineering Conference. ISOPE.

Timoshenko, S., Young, D.H., W. Weaver, JR. 1974.*Vibration problems in engineering*. John Wiley & Sons, Inc.

Dareing, D.W., Huang, T., 1976. Natural frequency of marine drilling riser. J. Pet. Tech 28, 813-818.

Garrett, D. L., 1982. Dynamic analysis of slender rods. Journal of Energy Resources Technology, Transaction of ASME 104, 302-307.

Bernitsas, M.M., J.E. Kokarakis, and A. Imron, 1985. Large deformation three-dimensional static analysis of deep water marine risers. Applied Ocean Research, Vol. 7, No.4, pp.178-187.

Egeland, O., 1981. Verification of analysis of marine risers. Eauib Reliab in Hydrocarbon Process, ASME, pp.133-140.

Ertas, A., and Kozik, T.J., 1987. Numerical solution technique for dynamic analysis of marine riser. ASME Journal of Energy Resources Technology, Vol.109, No.1, pp.1-5.

Ertas, A., and Kozik, T.J., 1987. A review of current approaches to riser modelling. Journal of Energy Resources Technology, Vol. 109, pp.155-160.

Kim, Y.C., 1985. Derivation of three dimensional equation of motion of a marine riser for large deflection. ASME, Energy Sources Technology Conference and Exhibition, PD-Vol. 1, pp.1-10.

Konuk, I., 1981. Application of adaptive numerical technique to 3D pipeline problems with strong nonlinearities. ASME, Pet-106.

Nordgren, R.P. , 1982. Dynamic analysis of Marine risers with vortex excitation. ASME Journal of Energy Resources Technology, Vol.104, pp.14-19.

Young, R.D., Fowler, J.R., Fisher, E.A., and Luke, R.R., 1977. Dynamic analysis as an aid to the design of Marine Risers", Energy-Sources Technology Conference and Exhibition, ASME, Pet-82.

Patel, M.H., Sarohia, S., 1984. Finite-element analysis of the marine risers. Engng Struct., Vol. 6, pp.175-184.

Huang, T., and Chucheepsakul, S., 1985. Large displacement analysis of a marine riser. ASME, Vol. 107, pp.54-59.

Patel, M.H., and Jesudasen, A.S., 1987. Theory and model tests for the dynamic response of free hanging risers. Journal of Sound and Vibration 112(1), pp. 149-166.

Ghadimi, R., 1988. A simple and efficient algorithm for the static and dynamic analysis of flexible marine risers. Computers & Structures Vol. 29, No.4, pp. 541-555.

McNamara, J.F., O'Brien, P.J., Gilroy, S.G., 1988. Nonlinear analysis of flexible risers using hybrid finite elements. ASME, Vol. 110, pp. 197-204.

Vlahopoulos, N., Bernitsas, M.M., 1988. Static, dynamic and eigen analysis of non-integral production risers. Applied Ocean Research, Vol. 10, No.3, pp. 144-154.

O'Brien, P.J., McNamara, J.F., 1989. Significant characteristics of three-dimensional flexible riser analysis. Eng. Struct., Vol. 11, pp. 223-233.

Sakamoto, T., Hobbs, R.E., 1995. Nonlinear static and dynamic analysis of three-dimensional flexible risers. International Offshore and Polar Engineering Conference, ISBN 1-880653-18-4 (Vol. II), pp. 227-235.

Pesce, C.P., Fujarra, A.L.C., Simos, A.N., Tannuri, E.A., 1999. Analytical and closed form solutions for deep water riser-like eigenvalue problem. International Offshore and Polar Engineering Conference, ISBN 1-880653-41-9 (Vol. II), pp. 255-264.

Fernandes, A.C., Jacob, B.P., Silva, R.M.C., Carvalho, R.A., Lemos C. A.D., 2001. Alternative design of flexible jumpers for deepwater hybrid riser configurations. ASME, Vol. 123, pp. 57-64.

Yazdchi, M., Crisfield, M.A., 2002. Non-linear dynamic behavior of flexible marine pipes and risers. International Journal for Numerical Methods in Engineering, 54: pp. 1265-1308.

Yazdchi, M., Crisfield, M.A., 2002. Buoyancy forces and 2D finite element analysis of flexible offshore pipes and risers. International Journal for Numerical Methods in Engineering, 54: pp. 61-88.

Raman-Nair, W., Baddour, R.E., 2003. Three-dimensional dynamics of a flexible marine riser undergoing large elastic deformations. Multibody System Dunamics, 10: pp. 393-423.

Senjanovic, I., Ljustina, A.M., Parunov, J., 2006. Natural vibration analysis of tensioned risers by segmentation method. Oil & Gas Science Technology, Vol. 61, pp. 647-659.

Chai, Y.T., Varyani, K.S., 2006. An absolute coordinate formulation for three-dimensional flexible pipe analysis. Ocean Engineering 33, pp. 23-58.

Santillan, S.T., Virgin, L.N., Plaut, R.H., 2010. Static and dynamic behavior of highly deformed risers and pipelines. ASME, Vol. 132, 021401 1-6.

Chatjigeorgiou, I.K., 2010. On the effect of internal flow on vibrating catenary risers in three dimensions. Engineering Structures, Vol. 32, pp. 3313-3329.

Santillan, S.T., Virgin, L.N., 2011. Numerical and experimental analysis of static behavior of highly deformed risers. Ocean Engineering 38, pp. 1397-1402.

Miller, C.A., 2017. Riser Introduction. Encyclopedia of Marine and Offshore Engineering, John Wiley & Sons. Ltd. ISBN: 978-1-118-47635-2.

Yoo, D.H., Jang, B.S., Yim, K.H., 2017. Nonlinear finite element analysis of failure modes and ultimate strength of flexible pipes. Marine Structures 54, pp. 50-72.

Zhang, C., Kang, Z., Ma, G., Xu, X., 2019. Mechanical modeling of deepwater flexible structures with large deformation based on absolute nodal coordinate formulation. Journal of Marine Science and Technology, 24: pp. 1241-1244.

Cheng, Y., Tang, L.Y., Fan, T.H., 2020. Dynamic analysis of deepwater steel lazy wave riser with internal flow and seabed interaction using a nonlinear finite element method. Ocean Engineering 209, 107498.

Bomfimsilva, C.T.P. , Netto, T.A., 2020. On the feasibility of a novel concept for a free standing riser. Ocean Engineering 214, 107731.

Ruan, W.D. Bai, Y. et al., 2016. Nonlinear dynamic analysis of deep water steel lazy wave riser subjected to imposed top-end excitations. OMAE 2016-54111

Det Norske Veritas, 2010. DNV-OS-F201, Dynamic Risers. Høvik, Norway.

Nordgren R. P., 1974. On computation of the motion of elastic rods. Journal of Applied Mechanics, 41(3):777-780.

Chen, X.H., 2002. Studies on dynamic interaction between deep-water floating structures and their mooring/tendon Systems. Ph.D. Dissertation, Ocean Engineering Program, Civil Engineering Department, Texas A&M University, College Station, Texas, USA.

Orcina, 2011. OrcaFlex User Manual, Version 9.4a. Cumbria, UK.

Wang, J.L., Duan, M.L., et al., 2014. Numerical solutions for nonlinear large deformation behavior of deepwater steel lazy-wave riser. Ships and Offshore Structures, 9(6): 655-668.

Wang, J.L., Duan, M.L., 2014. A nonlinear model for deepwater steel lazy-wave riser configuration with ocean current and internal flow. Ocean Engineering 94, pp. 155–162

Seyed, F.B., Patel, M.H., 1992. Mathematics of flexible risers including pressure and internal flow effects. Marine Structures 5 (1992), pp. 121-150.

Torres, A.L., Gonzalez, E.C., Ferreira, M.D.S., et al. 2003. Lazy wave steel rigid riser for FSO with spread mooring anchoring system, OMAE 2003-37068

Qiao, H.D., Bai Y., et al., 2016. Non-linear Static Analysis of Offshore Steep Wave Riser. MATEC Web of Conferences 65 01009.

Reddy, J.N., 2006. *An introduction to the finite element method*. Published by McGraw Hill Education (India) Private Limited, ISBN 978-0-07-060741-5

Low Y.M., Langley, R.S., 2006. Dynamic analysis of a flexible hanging riser in the time and frequency domain. OMAE2006-92171.

Cheng, Y., Vandiver, J.K., Moe, 2002. The linear vibration analysis of marine risers using WKB-based dynamic stiffness method. J. Sound Vibr 251 (4), 750-760.

Sparks, C.P., 2007. *Fundamentals of Marine Riser Mechanics: Basic Principles and Simplified Analysis*. PennWell Corp.

Chen, Y.F., Chai, Y.H., Li, X., Zhou, J., 2009. An extraction of the natural frequencies and mode shapes of marine risers by the method of differential transformation. Comput. Strct 87 (21-22),1384-1393.

Chen, Y.F., Zhuang, J., et al., 2015. Re-examination of natural frequencies of marine risers by variational iteration method. Ocean Engineering 94 (2015) 132-139.

Connaire, A., O'Brien P., Harte A., O'Connor, A., 2015. Advancements in subsea riser analysis using quasi-rotations and the Newton-Raphson method. International Journal of Non-linear Mechanics 70, pp.47-62.

Toleman B., Huang, C.J., Shankaran R., Foster D., 2019. Seabed rigid jumper design optimization for sour service application. OMAE2019-95536.

Ma, W., Webster, W.C., 1994. An analytical approach to cable dynamics: theory and user manual. SEA GRANT PROJECT R/OE-26.

Wu, M.C., Lou, J.Y.K., 1991. Effects of rigidity and internal flow on marine riser dynamics. Applied Ocean Research, Vol. 13, No. 5, pp. 235-244.

Kamermans M., 2011. https://pomax.github.io/bezierinfo/legendre-gauss.html

Orcina, A03 Jumper to high tower. https://www.orcina.com/wp-content/uploads/examples/a/a03/A03%20Jumper%20to%20high%20tower.pdf

Sun L.P., Qi, B., 2011. Global analysis of a flexible riser. J. Marine. Sci. Appl. (2011) 10: 478-484.

Zhen, X.W., Han, Y., Huang, Y., Yao, J.J., Wu, J.H., 2018. Analytical approach for the establishment of critical length criterion for the safe and economical design of the flexible jumper in deepwater applications. Applied Ocean Research 75 (2018), pp. 193-200.

APPENDIX A

DERIVATION OF QUINTIC HERMTIE SHAPE FUNTIONS

For the implementation of quintic Hermite shape functions for finite element model establishment, a total of six conditions have to be considered in a one-dimensional two-node beam element (three primary variables per end, i.e. the beam displacement r, slope r' and curvature r''). Therefore, a complete six-parameter polynomial must be chosen to perform the interpolation, which takes a form of

$$r^{qh}(x) = c_0 + c_1 x + c_2 x^2 + c_3 x^3 + c_4 x^4 + c_5 x^5 \tag{A.1}$$

where c_i $(i = 0{\sim}5)$ are unknown coefficients.

What is worth mentioning it that a total 18 degrees of freedom, for a three-dimensional beam element, have to be considered for one element. A schematic figure for three dimensional beam element, consisting of 18 degrees of freedom, are shown in Figure A.1 below.

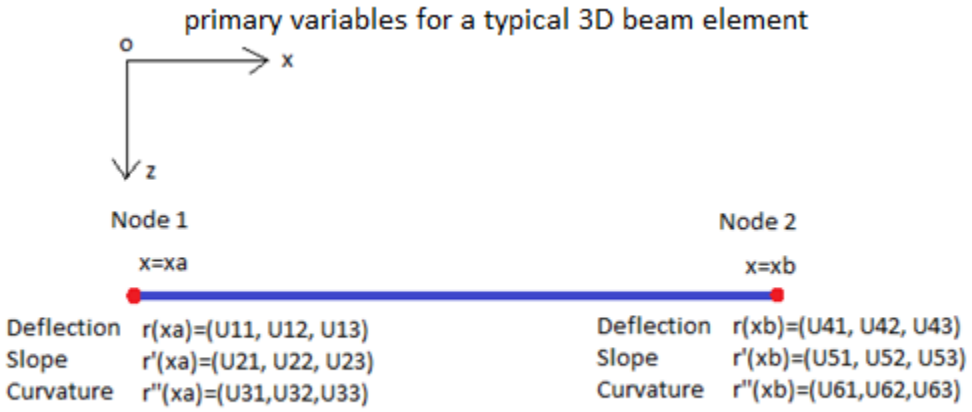

Figure A.1 Primary variables for typical three dimensional beam element

The derivation of the expressions of the quintic Hermite shape functions can be simply based on the one-dimensional beam problem. The approximation function of the transverse

deflection at eth beam element, assuming that the interval for e^{th} element being $x \in [x_a, x_b]$, can be written as

$$r(x) \approx {r_{ap}}^e(x) = C_0 + C_1 x + C_2 x^2 + C_3 x^3 + C_4 x^4 + C_5 x^5 = \sum_{i=1}^{6} {u_i}^e {a_i}^e(x) \quad \text{(A.2)}$$

This approximated function must satisfy the quintic Hermite interpolation properties, i.e. satisfying the following essential boundary conditions in the element, which form the basis for derivation of the quintic Hermite shape functions.

$$\begin{gathered} {u_1}^e = {r_{ap}}^e(x_a), {u_2}^e = {r'_{ap}}^e(x_a), {u_3}^e = {r''_{ap}}^e(x_a) \\ {u_4}^e = {r_{ap}}^e(x_b), {u_5}^e = {r'_{ap}}^e(x_b), {u_6}^e = {r''_{ap}}^e(x_b) \end{gathered} \quad \text{(A.3)}$$

where ${u_1}^e$ and ${u_4}^e$ are the beam displacement at the left and right end respectively, ${u_2}^e$ and ${u_5}^e$ are the beam slope at the left and right end respectively, and ${u_3}^e$ and ${u_6}^e$ are the beam curvature at the left and right end respectively; x_a and x_b are the starting and end x-coordinate of the e^{th} beam element, the simple ‘’’ denotes taking derivative with respect to x-coordinate.

Substitution the approximation function expression in equation (A.2) into the equation (A.3), leads to

$$\begin{gathered} {u_1}^e = {r_{ap}}^e(x_a) = C_0 + C_1 x_a + C_2 {x_a}^2 + C_3 {x_a}^3 + C_4 {x_a}^4 + C_5 {x_a}^5 \\ {u_2}^e = {r'_{ap}}^e(x_a) = C_1 + 2C_2 x_a + 3C_3 {x_a}^2 + 4C_4 {x_a}^3 + 5C_5 {x_a}^4 \\ {u_3}^e = {r''_{ap}}^e(x_a) = 2C_2 + 6C_3 x_a + 12C_4 {x_a}^2 + 20C_5 {x_a}^3 \\ {u_4}^e = {r_{ap}}^e(x_b) = C_0 + C_1 x_b + C_2 {x_b}^2 + C_3 {x_b}^3 + C_4 {x_b}^4 + C_5 {x_b}^5 \\ {u_5}^e = {r'_{ap}}^e(x_b) = C_1 + 2C_2 x_b + 3C_3 {x_b}^2 + 4C_4 {x_b}^3 + 5C_5 {x_b}^4 \\ {u_6}^e = {r''_{ap}}^e(x_b) = 2C_2 + 6C_3 x_b + 12C_4 {x_b}^2 + 20C_5 {x_b}^3 \end{gathered} \quad \text{(A.4)}$$

For further simplicity, the coefficients for quintic Hermite shape functions can be derived in a normalized local coordinate system ξ, here $\xi = \frac{x - x_a}{x_b - x_a}$. Obviously, if $x = x_a, \xi = 0$ and

if $x = x_b, \xi = 1$. Therefore, equation (A.4) can be expressed in the normalized local coordinate system can be simply expressed as

$$
\begin{aligned}
{u_1}^e &= {r_{ap}}^e(0) = C_0 + C_1 0 + C_2 0^2 + C_3 0^3 + C_4 0^4 + C_5 0^5 \\
h^e {u_2}^e &= {r'_{ap}}^e(0) = C_1 + 2C_2 0 + 3C_3 0^2 + 4C_4 0^3 + 5C_5 0^4 \\
h^{e2} {u_3}^e &= {r''_{ap}}^e(0) = 2C_2 + 6C_3 0 + 12C_4 0^2 + 20C_5 0^3 \\
{u_4}^e &= {r_{ap}}^e(1) = C_0 + C_1 1 + C_2 1^2 + C_3 1^3 + C_4 1^4 + C_5 1^5 \\
h^e {u_5}^e &= {r'_{ap}}^e(1) = C_1 + 2C_2 1 + 3C_3 1^2 + 4C_4 1^3 + 5C_5 1^4 \\
h^{e2} {u_6}^e &= {r''_{ap}}^e(1) = 2C_2 + 6C_3 1 + 12C_4 1^2 + 20C_5 1^3
\end{aligned}
\tag{A.5}
$$

where $h^e = x_b - x_a$ is the element length of eth beam element.

Rewrite equation (A.5) in a compact matrix form as

$$
\begin{bmatrix}
1 & 0 & 0 & 0 & 0 & 0 \\
0 & 1 & 0 & 0 & 0 & 0 \\
0 & 0 & 2 & 0 & 0 & 0 \\
1 & 1 & 1 & 1 & 1 & 1 \\
0 & 1 & 2 & 3 & 4 & 5 \\
0 & 0 & 2 & 6 & 12 & 20
\end{bmatrix}
\begin{Bmatrix} C_0 \\ C_1 \\ C_2 \\ C_3 \\ C_4 \\ C_5 \end{Bmatrix}
=
\begin{Bmatrix} {u_1}^e \\ h^e {u_2}^e \\ h^{e2} {u_3}^e \\ {u_4}^e \\ h^e {u_5}^e \\ h^{e2} {u_6}^e \end{Bmatrix}
\tag{A.6}
$$

Since the coefficient matrix in equation (A.6) is invertible, the six constant unknowns can be solved in terms of the inverse coefficient matrix and the nodal degrees of freedom, i.e. the primary variables as

$$
\begin{bmatrix}
1 & 0 & 0 & 0 & 0 & 0 \\
0 & 1 & 0 & 0 & 0 & 0 \\
0 & 0 & 0.5 & 0 & 0 & 0 \\
-10 & -6 & -1.5 & 10 & -4 & 0.5 \\
15 & 8 & 1.5 & -15 & 7 & -1 \\
-6 & -3 & -0.5 & 6 & -3 & 0.5
\end{bmatrix}
\begin{Bmatrix} {u_1}^e \\ h^e {u_2}^e \\ h^{e2} {u_3}^e \\ {u_4}^e \\ h^e {u_5}^e \\ h^{e2} {u_6}^e \end{Bmatrix}
=
\begin{Bmatrix} C_0 \\ C_1 \\ C_2 \\ C_3 \\ C_4 \\ C_5 \end{Bmatrix}
\tag{A.7}
$$

Therefore, the eth beam deflection can be expressed in terms of the nodal primary variables as

$$r_{ap}{}^{e}(\xi) = C_0 + C_1\xi + C_2\xi + C_3\xi^3 + C_4\xi^4 + C_5\xi^5$$

$$= u_1{}^{e} + h^e u_2{}^{e}\xi + \frac{1}{2}h^{e2}u_3{}^{e}\xi^2$$

$$+ \left(-10u_1{}^{e} - 6h^e u_2{}^{e} - \frac{3}{2}h^{e2}u_3{}^{e} + 10u_4{}^{e} - 4h^e u_5{}^{e} + \frac{1}{2}h^{e2}u_6{}^{e}\right)\xi^3$$

$$+ \left(15u_1{}^{e} + 8h^e u_2{}^{e} + \frac{3}{2}h^{e2}u_3{}^{e} - 15u_4{}^{e} + 7h^e u_5{}^{e} - h^{e2}u_6{}^{e}\right)\xi^4$$

$$+ \left(-6u_1{}^{e} - 3h^e u_2{}^{e} - \frac{1}{2}h^{e2}u_3{}^{e} + 6u_4{}^{e} - 3h^e u_5{}^{e} + \frac{1}{2}h^{e2}u_6{}^{e}\right)\xi^5 \quad \text{(A.8)}$$

Now by collecting the coefficients of the same primary variable together in equation (A.8), the beam deflection function can be eventually written as

$$r_{ap}{}^{e}(\xi) = (1 - 10\xi^3 + 15\xi^4 - 6\xi^5)u_1{}^{e} + (\xi - 6\xi^3 + 8\xi^4 - 3\xi^5)h^e u_2{}^{e} +$$

$$\frac{1}{2}(\xi^2 - 3\xi^3 + 3\xi^4 - \xi^5)h^{e2}u_3{}^{e} + (10\xi^3 - 15\xi^4 + 6\xi^5)u_4{}^{e} + (-4\xi^3 + 7\xi^4 - 3\xi^5)h^e u_5{}^{e} +$$

$$\frac{1}{2}(\xi^3 - 2\xi^4 + \xi^5)h^{e2}u_6{}^{e} = \sum_{i=1}^{6} u_i{}^{e} a_i{}^{e}(\xi) \quad \text{(A.9)}$$

According to the results obtained in equation (A.9), the expressions of the quintic Hermite interpolation functions $a_i{}^{e}(\xi)$ for the eth beam element becomes

$$a_1{}^{e}(\xi) = 1 - 10\xi^3 + 15\xi^4 - 6\xi^5$$

$$a_2{}^{e}(\xi) = h^e(\xi - 6\xi^3 + 8\xi^4 - 3\xi^5)$$

$$a_3{}^{e}(\xi) = \frac{h^{e2}}{2}(\xi^2 - 3\xi^3 + 3\xi^4 - \xi^5)$$

$$a_4{}^{e}(\xi) = 10\xi^3 - 15\xi^4 + 6\xi^5$$

$$a_5{}^{e}(\xi) = h^e(-4\xi^3 + 7\xi^4 - 3\xi^5)$$

$$a_6{}^e(\xi) = \frac{h^{e2}}{2}(\xi^3 - 2\xi^4 + \xi^5) \tag{A.10}$$

which are functions of the eth beam element length and normalized local coordinate $\xi = \frac{x-x_a}{h^e}$ ($x \in [x_a, x_b]$ and $\xi \in [0,1]$).

APPENDIX B

NUMERICAL RESULTS OF FINITE ELEMENT MODEL COEFFICIENTS FOR RISER3D

The key coefficient matrices in equation (2.29) by quintic Hermite finite element method have relatively large dimensions, i.e. 6x6x3. Besides, the integrand of the integration formulas for quantifying these coefficients are very high order polynomials. Therefore, it is time-consuming and complicated to get the analytical results of these coefficients.

Hence, the coefficient matrices are numerically evaluated with the Gaussian Legendre quadrature and the numerical results of these matrices are presented here in Fortran language matrix storing format in double precision.

The numerical values of the coefficient of $\bar{\alpha}_{ik1}, \bar{\alpha}_{ik2}, and\ \bar{\alpha}_{ik3}$ are summarized in data block (B.1), (B.2) and (B.3) respectively:

```
      data ((alpha(i,k,1),i=1,6),k=1,6)
     c/ 0.000000000000000d0,  0.428571428571429d0,  0.285714285714286d0,
     c -0.000000000000000d0, -0.428571428571429d0,  0.142857142857143d0,
     c -4.142857142857145d0, -2.700000000000001d0, -0.807142857142857d0,
     c  4.142857142857145d0, -1.442857142857143d0,  0.178571428571429d0,
     c -0.142857142857143d0, -0.107142857142857d0, -0.040476190476190d0,
     c  0.142857142857143d0, -0.035714285714286d0,  0.004761904761905d0,
     c -0.000000000000000d0, -0.428571428571429d0, -0.285714285714286d0,
     c  0.000000000000000d0,  0.428571428571429d0, -0.142857142857143d0,
     c  0.142857142857144d0,  0.128571428571429d0,  0.092857142857143d0,
     c -0.142857142857144d0,  0.014285714285715d0, -0.035714285714286d0,
     c -0.000000000000000d0, -0.007142857142857d0, -0.009523809523810d0,
     c  0.000000000000000d0,  0.007142857142857d0,  0.002380952380952d0/
```

(B.1)

```
      data ((alpha(i,k,2),i=1,6),k=1,6)
     c/-17.142857142857157d0,-8.571428571428573d0, -0.571428571428572d0,
     c 17.142857142857157d0, -8.571428571428577d0,  0.571428571428572d0,
     c -4.571428571428575d0, -2.800000000000002d0, -0.542857142857143d0,
     c  4.571428571428575d0, -1.771428571428572d0,  0.028571428571428d0,
     c -0.285714285714286d0, -0.200000000000000d0, -0.047619047619048d0,
     c  0.285714285714286d0, -0.085714285714286d0, -0.009523809523810d0,
     c 17.142857142857157d0,  8.571428571428573d0,  0.571428571428572d0,
     c-17.142857142857157d0,  8.571428571428577d0, -0.571428571428572d0,
     c -4.571428571428574d0, -1.771428571428572d0, -0.028571428571429d0,
     c  4.571428571428574d0, -2.800000000000001d0,  0.542857142857143d0,
     c  0.285714285714286d0,  0.085714285714286d0, -0.009523809523809d0,
     c -0.285714285714286d0,  0.200000000000000d0, -0.047619047619048d0/
```

(B.2)

```
      data ((alpha(i,k,3),i=1,6),k=1,6)
     c/ -0.000000000000011d0, -0.428571428571432d0,-0.142857142857143d0,
     c   0.000000000000011d0,  0.428571428571423d0, -0.285714285714284d0,
     c   0.142857142857147d0,  0.014285714285716d0,  0.035714285714286d0,
     c  -0.142857142857147d0,  0.128571428571431d0, -0.092857142857144d0,
     c   0.000000000000003d0, -0.007142857142856d0,  0.002380952380952d0,
     c  -0.000000000000003d0,  0.007142857142859d0, -0.009523809523810d0,
     c   0.000000000000011d0,  0.428571428571432d0,  0.142857142857143d0,
     c  -0.000000000000011d0, -0.428571428571423d0,  0.285714285714284d0,
     c  -4.142857142857139d0, -1.442857142857140d0, -0.178571428571428d0,
     c   4.142857142857139d0, -2.699999999999998d0,  0.807142857142857d0,
     c   0.142857142857142d0,  0.035714285714286d0,  0.004761904761905d0,
     c  -0.142857142857142d0,  0.107142857142857d0, -0.040476190476190d0/
```

(B.3)

The numerical values of the coefficient of $\bar{\beta}_{ik1}, \bar{\beta}_{ik2}, and\ \bar{\beta}_{ik3}$ are summarized in data block (B.4), (B.5) and (B.6) respectively:

```
      data ((beta(i,k,1),k=1,6),i=1,6)
     c/ 0.064935064935065d0, -0.050865800865801d0, -0.006493506493507d0,
     c  -0.064935064935065d0,  0.044372294372294d0, -0.005411255411255d0,
     c  -0.050865800865801d0,  0.107503607503608d0,  0.005681818181818d0,
     c   0.050865800865801d0, -0.010750360750361d0,  0.001064213564214d0,
     c  -0.006493506493507d0,  0.005681818181818d0,  0.000450937950938d0,
     c   0.006493506493507d0, -0.001461038961039d0,  0.000144300144300d0,
     c  -0.064935064935065d0,  0.050865800865801d0,  0.006493506493507d0,
     c   0.064935064935065d0, -0.044372294372294d0,  0.005411255411255d0,
     c   0.044372294372294d0, -0.010750360750361d0, -0.001461038961039d0,
     c  -0.044372294372294d0,  0.002741702741703d0, -0.000523088023088d0,
     c  -0.005411255411255d0,  0.001064213564214d0,  0.000144300144300d0,
     c   0.005411255411255d0, -0.000523088023088d0,  0.000054112554113d0/
```

(B.4)

```
      data ((beta(i,k,2),k=1,6),i=1,6)
     c/ 1.298701298701299d0,  0.220779220779221d0,  0.012987012987013d0,
     c  -1.298701298701299d0,  0.220779220779221d0, -0.012987012987013d0,
     c   0.220779220779221d0,  0.118326118326119d0,  0.010461760461760d0,
     c  -0.220779220779221d0,  0.007215007215007d0,  0.002236652236652d0,
     c   0.012987012987013d0,  0.010461760461760d0,  0.001082251082251d0,
     c  -0.012987012987013d0, -0.002236652236652d0,  0.000505050505051d0,
     c  -1.298701298701299d0, -0.220779220779221d0, -0.012987012987013d0,
     c   1.298701298701299d0, -0.220779220779221d0,  0.012987012987013d0,
     c   0.220779220779221d0,  0.007215007215007d0, -0.002236652236652d0,
     c  -0.220779220779221d0,  0.118326118326118d0, -0.010461760461760d0,
     c  -0.012987012987013d0,  0.002236652236652d0,  0.000505050505051d0,
     c   0.012987012987013d0, -0.010461760461760d0,  0.001082251082251d0/
```

(B.5)

```
      data ((beta(i,k,3),k=1,6),i=1,6)
     c/ 0.0649350649350650d0,  0.0443722943722950d0,  0.0054112554112550d0,
     c -0.0649350649350650d0, -0.0508658008658010d0,  0.0064935064935060d0,
     c  0.0443722943722950d0,  0.0027417027417030d0,  0.0005230880230880d0,
     c -0.0443722943722950d0, -0.0107503607503610d0,  0.0014610389610390d0,
     c  0.0054112554112550d0,  0.0005230880230880d0,  0.0000541125541130d0,
     c -0.0054112554112550d0, -0.0010642135642140d0,  0.0001443001443000d0,
     c -0.0649350649350650d0, -0.0443722943722950d0, -0.0054112554112550d0,
     c  0.0649350649350650d0,  0.0508658008658010d0, -0.0064935064935060d0,
     c -0.0508658008658010d0, -0.0107503607503610d0, -0.0010642135642140d0,
     c  0.0508658008658010d0,  0.1075036075036070d0, -0.0056818181818180d0,
     c  0.0064935064935060d0,  0.0014610389610390d0,  0.0001443001443000d0,
     c -0.0064935064935060d0, -0.0056818181818180d0,  0.0004509379509380d0/
```

(B.6)

The numerical values of the coefficient of $\bar{\gamma}_{ik1}, \bar{\gamma}_{ik2}, and\ \bar{\gamma}_{ik3}$ are summarized in data block (B.7), (B.8) and (B.9) respectively:

```
      data ((gamma(i,k,1),k=1,6),i=1,6)
     c /0.1849261849261850d0, 0.0207459207459210d0,   0.0011849261850000d0,
     c  0.0055500055500060d0, -0.0024864024864020d0,  0.0003121878122000d0,
     c  0.0207459207459210d0,  0.0033022533022530d0,  0.0002136752137000d0,
     c  0.0006826506826510d0, -0.0004134754134750d0,  0.0000568875568900d0,
     c  0.0011849261850000d0,  0.0002136752137000d0,  0.0000145687645700d0,
     c  0.0000055500055500d0, -0.0000208125208100d0,  0.0000034687534690d0,
     c  0.0055500055500060d0,  0.0006826506826510d0,  0.0000055500055500d0,
     c -0.0293595293595290d0,  0.0048673548673550d0, -0.0003121878122000d0,
     c -0.0024864024864020d0, -0.0004134754134750d0, -0.0000208125208100d0,
     c  0.0048673548673550d0, -0.0008824508824510d0,  0.0000568875568900d0,
     c  0.0003121878122000d0,  0.0000568875568900d0,  0.0000034687534690d0,
     c -0.0003121878122000d0,  0.0000568875568900d0, -0.0000034687534690d0/

      data ((gamma(i,k,2),k=1,6),i=1,6)
     c /0.2362082362082360d0,  0.0514374514374510d0,  0.0041958041960000d0,
     c  0.0971250971250970d0, -0.0295149295149300d0,  0.0029470529470000d0,
     c  0.0514374514374510d0,  0.0125874125874130d0,  0.0010878010880000d0,
     c  0.0295149295149300d0, -0.0087690087690090d0,  0.0008602508603000d0,
     c  0.0041958041960000d0,  0.0010878010880000d0,  0.0000971250971300d0,
     c  0.0029470529470000d0, -0.0008602508603000d0,  0.0000832500832500d0,
     c  0.0971250971250970d0,  0.0295149295149300d0,  0.0029470529470000d0,
     c  0.2362082362082360d0, -0.0514374514374510d0,  0.0041958041960000d0,
     c -0.0295149295149300d0, -0.0087690087690090d0, -0.0008602508603000d0,
     c -0.0514374514374510d0,  0.0125874125874130d0, -0.0010878010880000d0,
     c  0.0029470529470000d0,  0.0008602508603000d0,  0.0000832500832500d0,
     c  0.0041958041960000d0, -0.0010878010880000d0,  0.0000971250971300d0/
```

(B.7)

(B.8)

```
      data ((gamma(i,k,3),k=1,6),i=1,6)
     c/-0.029359529359529d0, -0.004867354867355d0, -0.000312187812200d0,
     c  0.005550005550006d0, -0.000682650682651d0,  0.000005550005550d0,
     c -0.004867354867355d0, -0.000882450882451d0, -0.000056887556890d0,
     c  0.002486402486402d0, -0.000413475413475d0,  0.000020812520810d0,
     c -0.000312187812200d0, -0.000056887556890d0, -0.000003468753469d0,
     c  0.000312187812200d0, -0.000056887556890d0,  0.000003468753469d0,
     c  0.005550005550006d0,  0.002486402486402d0,  0.000312187812200d0,
     c  0.184926184926185d0, -0.020745920745921d0,  0.001184926185000d0,
     c -0.000682650682651d0, -0.000413475413475d0, -0.000056887556890d0,
     c -0.020745920745921d0,  0.003302253302253d0, -0.000213675213700d0,
     c  0.000005550005550d0,  0.000020812520810d0,  0.000003468753469d0,
     c  0.001184926185000d0, -0.000213675213700d0,  0.000014568764570d0/
```

(B.9)